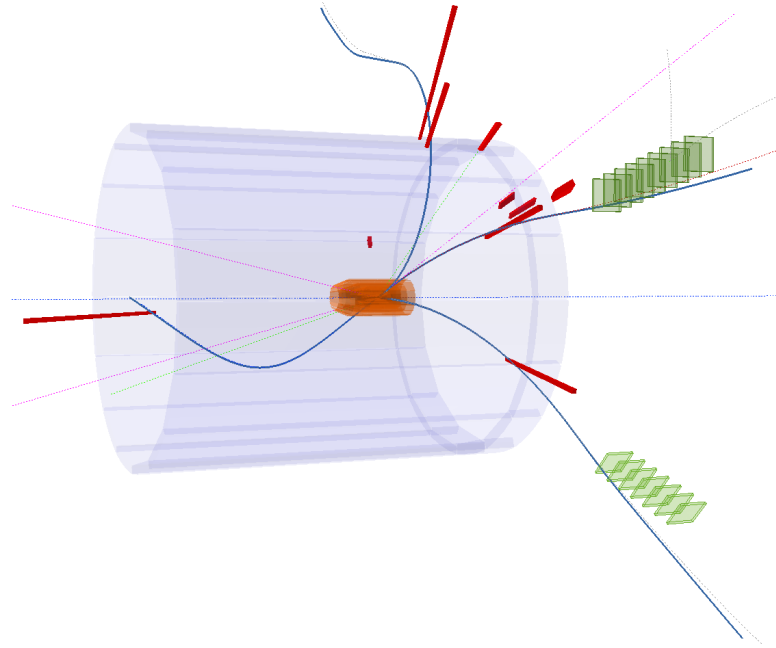




Universität Hamburg
DER FORSCHUNG | DER LEHRE | DER BILDUNG

τ -Lepton Lifetime Measurement and Working Point Optimization for the Pixel Vertex Detector at Belle II



DISSERTATION

zur Erlangung des Doktorgrades
an der Fakultät für Mathematik, Informatik und Naturwissenschaften
Fachbereich Physik
der Universität Hamburg

vorgelegt von
Anselm Baur
aus Tübingen

Hamburg
2025

Gutachter/innen der Dissertation:	Prof. Dr. Kerstin Tackmann Dr. Daniel Pitzl
Zusammensetzung der Prüfungskommission:	Prof. Dr. Kerstin Tackman Dr. Daniel Pitzl Prof. Dr. Jochen Liske Prof. Dr. Ingrid-Maria Gregor Prof. Dr. Gudrid Moortgat-Pick
Vorsitzender der Prüfungskommission:	Prof. Dr. Jochen Liske
Datum der Disputation:	14.05.2025
Vorsitzender Fach-Promotionsausschusses PHYSIK:	Prof. Dr. Wolfgang J. Parak
Leiter des Fachbereichs PHYSIK:	Prof. Dr. Markus Drescher
Dekan der Fakultät MIN:	Prof. Dr.-Ing. Norbert Ritter

Zusammenfassung

Im Standardmodell der Teilchenphysik haben alle Leptonen die gleiche Kopplungsstärke an die schwache Wechselwirkung. Der Vergleich des theoretischen Modells mit experimentellen Beobachtungen zeigt jedoch eine leichte Abweichung im elektronischen Verzweungsverhältnis von τ -Lepton-Zerfällen. Die Präzision dieses Tests ist durch die Genauigkeit der gemessenen τ -Lepton-Lebensdauer limitiert. Diese Arbeit präsentiert eine neuartige Messung der τ -Lepton-Lebensdauer unter Verwendung eines Template-Fit-Ansatzes bei Belle II. Die Lebensdauer wird für τ -Leptonen bestimmt, die in drei geladene Teilchen zerfallen. Hierzu werden Daten verwendet, in denen ein τ -Lepton-Paar erzeugt wird, wobei ein τ -Lepton in drei und das andere in ein geladenes Teilchen zerfällt. Die Zerfallslänge wird in der xy -Ebene vom SuperKEKB-Kollisionspunkt bis zum Zerfallsvertex des τ -Leptons bestimmt. Ein robustes Software-Framework wurde entwickelt, um die Datenverarbeitung, Validierung und systematischen Studien zu vereinheitlichen und so die Reproduzierbarkeit sowie Flexibilität für zukünftige Verbesserungen sicherzustellen. Die Auflösung der Vertexrekonstruktion beträgt $31.43 \pm 0.01 \mu\text{m}$ und nutzt dabei die Präzision des Pixel-Vertex-Detektors.

Zur Bestimmung der τ -Lebensdauer im aufgenommenen Datensatz wird dieser mit Vorhersagen von rekonstruierten Zerfallslängen für verschiedene τ -Lepton-Lebensdauern (Templates) verglichen. Die τ -Lepton-Lebensdauer des Templates mit der besten Übereinstimmung zu den Messdaten entspricht der gemessenen Lebensdauer. Die alternativen Templates werden aus einem vollständig generierten Template durch Umgewichtung der Generator-Lebensdauern erzeugt. Zur Validierung dieser Umgewichtungsmethode wurden Studien durchgeführt, um die umgewichteten Templates mit vollständig generierten Templates mit der entsprechenden Lebensdauer zu vergleichen. Diese Studien haben die Zuverlässigkeit der Methode bestätigt. Systematische Unsicherheiten werden über Störgrößenparameter in das Likelihood-Fit-Modell integriert. Um den Einfluss dominanter Modellierungsunsicherheiten zu reduzieren, wird eine zweidimensionale, datenbasierte Korrektur durchgeführt. Durch diese Korrektur konnte die Größe der systematischen Unsicherheiten signifikant verringert werden. Die finale erwartete Präzision der Messung beträgt $\pm 0.08 \text{ fs}$ statistische Unsicherheit und $\pm 0.18 \text{ fs}$ systematische Unsicherheit. Damit ist die erwartete totale Unsicherheit der Messung mit $\pm 0.2 \text{ fs}$ mehr als um den Faktor 2 besser als der aktuelle Weltmittelwert.

Im Jahr 2023 wurde ein neuer, zweilagiger Pixel-Vertex-Detektor in Belle II installiert, der den vorherigen, unvollständigen Detektor gleichen Designs ersetzte. Die Effizienz des Detektors, ein Teilchen zu detektieren, hängt von der korrekten Kalibrierung der Arbeitsspannungen und -ströme ab. Die Effizienz des Pixel-Vertex-Detektors beeinflusst maßgeblich die Auflösung der Vertexinformationen des Belle II-Detektors und ist somit entscheidend für die darauf basierenden zukünftigen Analysen. In einer Testphase vor der Inbetriebnahme wurden detaillierte, multidimensionale Optimierungsmessungen mit einer externen radioaktiven Quelle an der Hälfte der Pixel-Vertex-Detektor-Module durchgeführt, um die Sensoreinstellungen zu bewerten und abzustimmen. Diese Messungen identifizierten stabile Arbeitspunkte, die die Detektionseffizienz einzelner Sensoren signifikant um bis zu 14 % steigerten und Effekte wie Clusteranomalien in unterdepletierten Modulen verhinderten. Anschließend wurden vereinfachte Optimierungsmessungen mit allen Pixel-Vertex-Detektor-Modulen durchgeführt, was zu geeigneten Betriebspa-

rametern führte, die auch als Ausgangswerte für zukünftige In-situ-Kalibrierungen während des Beschleunigerbetriebs dienen. Die Analyse von Daten, die während der ersten Phase des Beschleunigerbetriebs im Jahr 2024 aufgenommen wurden, zeigte Verbesserungen der Detektionseffizienz einzelner Module von bis zu 8 % durch die optimierten Betriebsparameter.

Abstract

In the Standard Model of Particle Physics, all leptons have the same coupling strength to the weak interaction. Comparing the theoretical model with experimental observations reveals a slight deviation in the electron branching fraction of τ -lepton decays. However, the precision of the measurement is limited by the precision of the measured τ -lepton lifetime. This work presents a novel measurement of the τ -lepton lifetime using a template fitting approach applied to 3×1 -prong $\tau^+\tau^-$ decays at Belle II. The decay length is determined in the xy -plane from the precisely known SuperKEKB interaction point to the 3-prong τ -lepton decay vertex. A robust software framework was developed to unify data processing, validation, and systematic studies, ensuring reproducibility and flexibility for future improvements. The vertex reconstruction achieves a resolution of $31.43 \pm 0.01\mu\text{m}$, leveraging the precision of the pixel vertex detector. Templates corresponding to different lifetime hypotheses are generated using a re-weighting method. The reliability of this approach is confirmed through comparisons with templates produced from shifted generator lifetimes and pseudo-data fits. Systematic uncertainties are incorporated into the likelihood fit model via nuisance parameters. To address dominant modeling uncertainties, a dedicated two-dimensional re-weighting strategy was developed, resulting in an expected total precision of 0.2 fs, including a statistical uncertainty of 0.08 fs and a systematic uncertainty of 0.18 fs. With this, the expected precision of the analysis exceeds the current world average by more than a factor of two.

In 2023, the Belle II experiment upgraded its pixel vertex detector by replacing the previous single-layer configuration with a new two-layer detector, based on the same sensor design. Optimized sensor working points are crucial for the success of future analyses relying on precise vertex information with the new two-layer pixel vertex detector. To maximize hit efficiency, dedicated optimization studies were conducted. During pre-commissioning, detailed multi-parameter source scans were performed to evaluate and tune the sensor settings across half of the pixel vertex detector modules. These scans identified stable operation points that significantly improved hit efficiency, with gains of up to 14 %, and mitigated effects such as cluster anomalies in under-depleted modules. Simplified high-voltage scans with all pixel vertex detector modules were subsequently performed, resulting in suitable operating parameters that also serve as starting values for future in-situ calibration during beam collisions. Early data following the resumption of beam operations in 2024 revealed individual module improvements of up to 8 % from refined operation parameters.

Contents

1. Introduction	13
2. Foundations	15
2.1. The Standard Model of Particle Physics	15
2.2. Mean Lifetime and Decay Length	18
2.2.1. Exponential Decay	18
2.2.2. Decay Time and Decay Length	18
2.2.3. Decay Length Distribution and Detector Resolution	19
2.3. Particle Interactions in Matter	20
2.4. Silicon Semiconductors	23
2.4.1. Doping	23
2.4.2. pn-Junction - A Diode and Particle Detector	24
2.4.3. MOSFET	26
3. τ-Lepton Lifetime Measurement	29
3.1. τ -Lepton Decay	29
3.2. Precise Measurement of Standard Model Parameters	31
3.2.1. Lepton Flavour Universality Test	31
3.2.2. Extraction of $\alpha(s)$	31
3.3. Decay Length Measurement of Tau-Lepton Decays	34
3.3.1. Overview of Measurement Methods	34
3.3.2. Previous Measurements	35
4. The Belle II Experiment	41
4.1. The SuperKEKB Accelerator	41
4.2. The Belle II Detector	45
4.2.1. Vertex Detector	46
4.2.2. Central Drift Chamber	47
4.2.3. Time of Propagation Detector	48
4.2.4. Aerogel Ring Imaging Cherenkov Detector	49
4.2.5. Electromagnetic Calorimeter	49
4.2.6. K-Long and Muon Detector	50
4.3. Trigger	53
4.4. Belle II Analysis Software Framework	54
4.4.1. Charged Particles	54
4.4.2. Neutral Particles	54
4.4.3. Neutrinos	55
4.4.4. Tree Fitter	55
4.5. Data Production	56

5. The Pixel Vertex Detector	57
5.1. DEPFET Pixels	57
5.1.1. DEPFET Working Principle	58
5.1.2. DEPFET Sensor Matrix	59
5.2. PXD Module	64
5.2.1. Structure	64
5.2.2. Readout	65
5.3. PXD Ladder and Half-Shell	67
5.4. From PXD1 to PXD2: Completion and Advantages	69
6. τ-Lepton Lifetime Measurement Using Template Fits	71
6.1. Simulated and Experimental Data Samples	71
6.1.1. τ -Lepton Pair Production	71
6.1.2. Simulated Data	71
6.1.3. Experimental Data	73
6.2. Measurement Method	77
6.2.1. 3x1 Vertex Method	77
6.2.2. Template Fit	79
6.2.3. Model Parameters	81
6.2.4. Decay Length Models from Re-Weighting	82
6.2.5. Properties of the Generator Decay Length Weights	84
6.3. Low Level Selections	86
6.3.1. L1 Trigger Selection	86
6.3.2. TauThrust Skim	87
6.4. Particle Reconstruction and Event Selection	92
6.4.1. Track Selection and Kinematic Correction	92
6.4.2. Photon and π^0 Selection and Correction	92
6.4.3. Selection of 3x1-Topology	92
6.4.4. Background and Mismodeling Suppression	92
6.4.5. Expected $\tau^+\tau^-$ Background	99
6.4.6. Selection Summary	102
6.5. Vertex Fit	105
6.5.1. Measuring the Vertex Resolution	105
6.5.2. Impact of PXD Hit Requirements	106
6.5.3. Mismodeling of the Vertex Residual	108
6.5.4. Vertex Requirements	110
6.5.5. Alignment	111
6.6. Template Configuration and Fit Setup	115
6.6.1. Validation of the Template Re-Weighting Method	115
6.6.2. Fit Regions and Normalization	116
6.6.3. Template Variations to Address Systematic Uncertainties	118
6.6.4. Mismodeling and Template Correction	118
6.6.5. Lifetime Fit Stability	122
6.7. Lifetime Analysis Framework	127
6.7.1. General Overview	127
6.7.2. Reconstruction	127

6.7.3.	Event Selection	128
6.7.4.	Template Creation	129
6.7.5.	Lifetime Fit	130
6.7.6.	Framework Summary	130
6.8.	Estimated Precision	132
6.8.1.	Statistical Uncertainty	132
6.8.2.	Simulated Data Statistical Uncertainty	133
6.8.3.	Template Correction Uncertainty	133
6.8.4.	Remaining Mismodeling of Observables	133
6.8.5.	Misalignment	135
6.8.6.	Material Budget	136
6.8.7.	Background Contribution	137
6.8.8.	Trigger	138
6.8.9.	Kaon Contribution	139
6.8.10.	Reconstruction Corrections	140
6.8.11.	Normalization Uncertainties	141
6.8.12.	NP Pulls and Correlations	142
6.8.13.	Total	146
7.	PXD2 DEPFET Biasing Optimization	149
7.1.	Previous Optimization Efforts for PXD Modules During Series Testing	149
7.2.	Revised Figure of Merit for DEPFET Biasing Optimization	152
7.3.	Charge Collection Dependency on Incident Angle	154
7.4.	Simulation and Construction of a Half-Shell Source Setup	156
7.4.1.	Source Setup Simulation	156
7.4.2.	Validation of the Simulation	161
7.4.3.	Expected Hitmap and Measurement Time	161
7.4.4.	DESY Half-Shell Test Setup	163
7.4.5.	KEK Commissioning Setup	164
7.5.	Half-Shell Source Scans	166
7.5.1.	Multi-Parameter Source Scan	166
7.5.2.	HV Source Scan	179
7.6.	First Run 2 PXD2 Hit Efficiency Improvements	182
8.	Summary and Outlook	185
A.	Appendix	199
A.1.	Production Cross-Section	199
A.2.	Scaling of Simulated Data Samples	199
A.3.	ECL Trigger Bits	200
A.4.	π^0 Efficiency Correction	201
A.5.	Applying Event Selection	204
A.5.1.	Observable Distributions with All Selections Applied	204
A.6.	π_{3p}^{\pm} Momentum	209
A.7.	Analysis Framework Task Trees	209
A.7.1.	Template Creation Task Tree	209
A.7.2.	Lifetime Fit Task Tree	210

Contents

A.8. Full Uncertainty Breakdown	212
A.9. MC Stat. NP Correlations	213
A.10.Pseudo Data Fit Pulls	215
A.11.Mechanical Issues Observed with PXD2	216
A.12.Multi-Parameter Source Scan Results	217
A.13.HV Scan Results	238

1. Introduction

The *Standard Model of Particle Physics* is one of the most successful theoretical frameworks describing the universe and the laws of nature. It encompasses elementary particles on one hand and their interactions via fundamental forces on the other. The Standard Model has made remarkably accurate predictions about new particles before their experimental discovery, such as the top quark [1] and the Higgs boson [2][3].

Despite its successes, the Standard Model remains an incomplete theory. Phenomena such as dark matter, neutrino masses, the baryon asymmetry of the universe, and gravity are not yet incorporated. Although extensive experimental efforts have been undertaken, no direct evidence for *New Physics* capable of explaining these phenomena has been observed to date. High-energy collider experiments have placed stringent constraints on various New Physics scenarios, including the existence of new massive particles.

For this reason, one of the central tasks of particle physics is to test the Standard Model with the highest possible precision, searching for discrepancies between theoretical predictions and experimental results. Such deviations could provide crucial insights into the nature of New Physics and guide the development of extensions to the Standard Model. The ultimate objective is to formulate a unified theory that consistently describes all fundamental interactions and observations.

The τ -lepton is the third and final known generation of the lepton family, discovered in 1975 at the Stanford Linear Accelerator Center [4]. It is the only lepton massive enough to decay into mesons. This offers a unique opportunity to study the hadronization of quantum chromodynamics and perform rigorous New Physics tests. The τ -lepton is an ideal candidate for precise property measurements. One key property is the τ -lepton lifetime. With a lifetime of approximately 290 fs, the τ -lepton travels only about 90 μm before decaying.

The Belle II experiment [5], operating at the SuperKEKB collider [6] in Japan, offers a clean experimental environment designed to collect large datasets for precision studies of particles such as B mesons and τ -leptons. The Belle II pixel vertex detector is particularly well-suited to resolve the short decay length of the τ -lepton, making it a key instrument for lifetime measurements.

The pixel vertex detector is based on the DEPFET technology, which requires multiple biasing voltages with complex interdependencies to operate the sensors reliably. The optimal working points can vary from sensor to sensor, requiring careful calibration. Between 2022 and 2024, the Belle II detector underwent an upgrade, during which the original single-layer pixel vertex detector was replaced with the two-layer configuration. Optimizing the sensor working points of the new detector is a central challenge to ensure optimal performance of vertex measurements in future data-taking.

This thesis focuses on two key aspects: It introduces a novel method for measuring the τ -lepton lifetime using a template fitting approach and discusses the working point optimization

1. Introduction

of the two-layer pixel vertex detector.

The thesis is structured as follows: Chapter 2 provides a brief overview of the theoretical foundations for this work. Chapter 3 introduces the τ -lepton decay, its measurement, and summarizes previous τ -lepton lifetime measurements. Chapter 4 gives an overview of the Belle II detector and the SuperKEKB accelerator, while Chapter 5 introduces the pixel vertex detector. The two main chapters are Chapter 6, which presents the novel τ -lepton lifetime measurement method, and Chapter 7, which discusses the working point optimization of the two-layer pixel vertex detector sensors. Finally, Chapter 8 provides a brief summary and outlook.

The τ -lepton lifetime analysis described in this work (see Chapter 6) was carried out within an analysis group of four people. Many tasks and analysis steps were the result of iterative, collaborative efforts. To complete this thesis, the analysis was frozen at its state as of September 2024.

The following list summarizes the personal contributions of the author to the τ -lepton lifetime measurement:

- development of the main analysis framework;
- reconstruction and correction of the simulated and experimental datasets;
- studies to determine the trigger and skim efficiencies;
- background suppression studies and examination of the $\tau^+\tau^-$ background;
- analysis of the vertex resolution and modeling of the pixel vertex detector;
- implementation and verification of the re-weighting method for template creation;
- studies on the impact of observable mismodeling and template corrections;
- validation studies of the template fit stability; and
- a comprehensive study of the uncertainties and correlations of the nuisance parameters.

The optimization studies for the pixel vertex detector sensors discussed in Chapter 7 were entirely performed by the author of this thesis.

2. Foundations

This chapter discusses the theoretical foundations of various topics covered in this work. Section 2.1 provides a brief overview of the building blocks of the Standard Model, which is the fundamental theory for all the discussion in this thesis, including the τ -lepton. Section 2.2 formally introduces the mean lifetime and decay length derived from exponential decays of particle ensembles. The section provides fundamental theoretical concepts of the τ -lepton lifetime measurement, which are detailed in Chapter 3. Section 2.3 gives a short overview of the interaction of charged particles with absorber materials, which is relevant for multiple scattering and the measurements with ionizing radiation discussed in Chapter 7. Section 2.4 provides an introduction to silicon semiconductors, the basis of silicon tracking detectors.

2.1. The Standard Model of Particle Physics

The *Standard Model (SM)* is a *quantum field theory (QFT)* based on local gauge invariance, defined by the symmetry group $SU(3) \times SU(2) \times U(1)$. It describes very successfully the *elementary particles* that constitute the fundamental building blocks of the experimentally accessible universe and three of the four *fundamental forces* governing their interactions. The fourth fundamental force, the *gravitational force*, is not (yet) included in the SM.

In the SM, elementary particles are described as excitations of quantum fields at specific space-time points. They are grouped into three generations of spin- $\frac{1}{2}$ *fermions*, each consisting of four particles and their corresponding antiparticles; five spin-1 *gauge bosons*, which mediate the *electromagnetic (EM)*, *weak*, and *strong* interactions; and one spin-0 *scalar boson*, responsible for generating the masses of fermions and bosons. The fermions are further classified into six *quarks* and six *leptons*. Quarks interact via the strong force, whereas leptons do not. The quark and lepton flavors are distinguished solely by their masses. Figure 2.1 provides a summary of the elementary particles and their interactions.

Each fundamental force is described by its own QFT. *Quantum electrodynamics (QED)* is based on $U(1)$ gauge symmetry and introduces the photon, γ , as the gauge boson mediating the electromagnetic interaction, which couples to the *electric* charge. The weak interaction is mediated by the W^\pm and Z gauge bosons, introduced by $SU(2)$ gauge symmetry, coupling to the *weak isospin*, as described by the weak theory. *Quantum chromodynamics (QCD)* is based on $SU(3)$ gauge symmetry and introduces eight gluons, g , as the gauge bosons mediating the strong interaction, which couples to the *color* charge. The electromagnetic and weak interactions are unified in the $SU(2) \times U(1)$ *electroweak (EW)* theory.

The spin-0 scalar boson is the so-called *Higgs boson*, the excitation of the scalar *Higgs field*, responsible for generating the masses of the elementary particles. The Higgs boson couples to all massive gauge bosons via the Higgs mechanism [7] and to the massive fermions via the Yukawa [8] couplings. Owing to their tiny masses, the neutral leptons, called *neutrinos*, ν , are considered in the SM as massless.

2. Foundations

In the SM, all leptons have the same coupling strength to the W^\pm boson. This is referred to as *lepton flavour universality (LFU)*.

The (d, s, b) quark *mass eigenstates* (free quarks) are not the same as when the (d', s', b') quarks interact in their *weak eigenstates* with the weak interaction. The weak eigenstates are linear combinations of the mass eigenstates. This so-called quark mixing is defined by:

$$\begin{pmatrix} d' \\ s' \\ b' \end{pmatrix} = \begin{pmatrix} V_{ud} & V_{us} & V_{ub} \\ V_{cd} & V_{cs} & V_{cb} \\ V_{td} & V_{ts} & V_{tb} \end{pmatrix} \begin{pmatrix} d \\ s \\ b \end{pmatrix}, \quad (2.1)$$

where V_{ij} are the elements of a 3×3 *Cabibbo-Kobayashi-Maskawa (CKM) unitary matrix*.

In total, the SM has 19 free parameters which are the three charged lepton and six quark masses, four quark mixing related parameters, the three coupling constants to each of the fundamental forces, and three parameters related to the vacuum and Higgs boson. These parameters need to be experimentally measured.

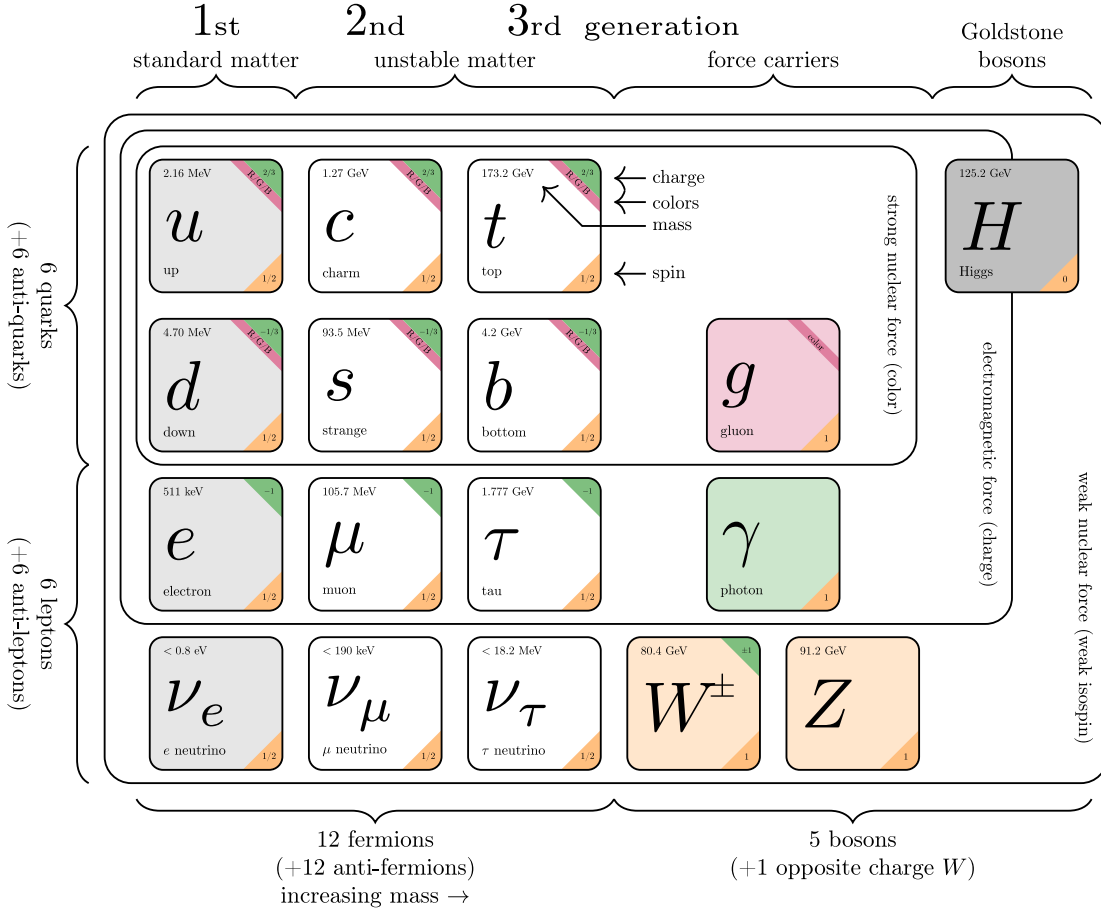


Figure 2.1.: Overview of the particles of the SM. The three fermion generations differ only by their masses. (Figure adapted from [9], values updated to [10])

Hadron	Quark content	Mass in MeV/c ²	Mean lifetime in ps
π^+	$u\bar{d}$	140	2.6×10^{-4}
π^0	$1/\sqrt{2}(u\bar{u} - d\bar{d})$	135	8.4×10^{-5}
K^+	$u\bar{s}$	494	1.2×10^{-4}
K^0	$d\bar{s}$	498	-
K_S^0	$1/\sqrt{2}(d\bar{s} + s\bar{d})$	-	89
K_L^0	$1/\sqrt{2}(d\bar{s} - s\bar{d})$	-	5.1×10^{-4}
D^+	$c\bar{d}$	1870	1.0
D_s^+	$c\bar{s}$	1968	0.5

Table 2.1.: List of hadrons and their compositions frequently appearing in this work. [10]

Leptons exist freely in isolation, whereas quarks can only exist in quark-antiquark pairs (*mesons*) or as a combination of three quarks or three antiquarks (*baryons*) due to *confinement*. Particles constituted from quarks are also called *hadrons*. Table 2.1 lists the most relevant hadrons for this work.

Only the first generation quarks and the electron are considered as stable particles. All other particles decay over time. The weak interaction can change the fermion flavours via so-called *flavour changing currents*.

The unstable particles are characterized by the lifetime, which is associated with the inverse *decay width* Γ :

$$\tau = \hbar \frac{1}{\Gamma} = \hbar \frac{1}{\sum_f \Gamma_{if}}, \quad (2.2)$$

where \hbar is the reduced Planck constant and Γ_{if} the partial decay widths. The partial decay widths for each Γ_{if} transition from an initial state $|i\rangle$ to a final state $|f\rangle$ can be calculated with *Fermi's golden rule*. The *branching ratio* B is defined as:

$$B_{if} = \frac{\Gamma_{if}}{\Gamma} \quad (2.3)$$

Section 3.1 discusses the τ -lepton decay specifically in more detail.

A comprehensive discussion about the SM can be found in the following literature [11][12].

2.2. Mean Lifetime and Decay Length

Since particle decays are probabilistic processes, the observables like mean lifetime and mean decay length must be determined from a statistical ensemble. This section gives a brief overview of how to measure particle mean lifetimes via their decay lengths.

2.2.1. Exponential Decay

Exponential decay is a common phenomenon in nature that describes the decrease of a population – such as a group of particles – at a constant rate, assuming no new particles are produced. Each particle in the population has the same probability of decaying at any given time. Consequently, the probability of observing a decay event is directly proportional to the size of the population. At the initial time ($t = 0$), the population is at its maximum size, so the number of particles decaying per unit of time is also at its highest. As time progresses, the population decreases due to continuous decay events, leading to fewer particles available to decay in each subsequent time step.

In general, the decay rate of a set of N unstable particles in their rest frame within infinitesimal small time steps dt is defined by:

$$\frac{dN}{dt} = -\lambda N, \quad (2.4)$$

where λ is the decay constant. The solution of the differential Equation (2.4) is:

$$N(t) = N_0 e^{-\frac{t}{\tau}}, \quad (2.5)$$

where N_0 is the number of particles at time $t = 0$, and $\tau = 1/\lambda$ is the mean lifetime. Combining Equation (2.4) and Equation (2.5), the decay rate is described by:

$$\frac{dN(t)}{dt} = -\frac{N_0}{\tau} e^{-\frac{t}{\tau}}. \quad (2.6)$$

The mean lifetime τ represents the time after which the population has decreased to $1/e$ of its original size.

2.2.2. Decay Time and Decay Length

The lifetime T' of a particle in its *proper time* (in the particle's rest frame) defines the time span between its production time T'_0 and the time t' when it decays:

$$T' = t' - T'_0. \quad (2.7)$$

Let the particle move with a velocity v relative to an observer at rest in the *laboratory frame* (*lab frame*). If v is close to the speed of light c in vacuum, the observed time t and position x of the particle in the lab frame need to be transformed using the *Lorentz transformation* to

describe the relation between the two coordinate systems:

$$t = \gamma \left(t' + \frac{vx'}{c^2} \right), \quad (2.8)$$

$$x = \gamma (x' + vt'), \quad (2.9)$$

where x' is the position of the particle in its rest frame, and γ is the relativistic Lorentz factor. During the particle's lifetime, the observer sees it travelling a distance d , which corresponds to the decay length:

$$d = c\beta\gamma T', \quad (2.10)$$

where $\beta = v/c$. Replacing T' by the mean lifetime τ , one obtains the common relation

$$c\tau = \frac{d}{\beta\gamma} = \frac{m}{p}d \quad (2.11)$$

$$= \frac{m}{p} \frac{d_{xy}}{\sin \theta} \quad (2.12)$$

with $p = \beta\gamma m$, θ is the polar angle of the particle's momentum direction, and d_{xy} is the decay length in the xy -plane.

2.2.3. Decay Length Distribution and Detector Resolution

Considering again a particle population, and transferring the decay time to the decay length by combining Equation (2.6) and Equation (2.10), resulting in the differential decay length distribution:

$$\frac{dN(d)}{dd} = -\frac{N_0}{c\beta\gamma\tau} e^{-\frac{d}{c\beta\gamma\tau}}. \quad (2.13)$$

This describes the number of observed decays within an infinitesimal small distance dd , called the decay length distribution. If the distribution of Equation (2.13) is divided in macroscopic bins, the number of observed decays (entries) in the i -th bin is given by:

$$n_i = -\frac{N_0}{c\beta\gamma\tau} \int_{d_i}^{d_{i+1}} dd e^{-\frac{d}{c\beta\gamma\tau}} \quad (2.14)$$

However, such a distribution would only be observed with an infinitely precise detector. In a real measurement, the finite resolution of the detector must be taken into account. A straightforward approach to incorporate this effect is to convolve the distribution with a *resolution function* $R(d)$:

$$\frac{dN(d)}{dd} \propto -\frac{1}{\tau} e^{-\frac{d}{c\beta\gamma\tau}} \otimes R(d) \quad (2.15)$$

The τ -lepton specific decay length measurement will be further discussed in Chapter 3.

2.3. Particle Interactions in Matter

This section gives a short overview of the interaction of charged particles with absorber materials, which is relevant for multiple scattering and the measurements with ionizing radiation discussed in Chapter 7.

When fast, heavy charged particles (heavier than electrons) traverse matter, they interact with the atoms of the absorber material through ionization, atomic excitation, or collective excitation. The energy loss along a path x in a material consists of many small contributions from individual interactions. Statistical fluctuations in the number of interactions and the magnitude of each energy loss lead to a so-called *Landau* distribution. Rare collisions with very high energy transfer create a long tail toward higher energy loss values.

The most probable energy loss, Δ_p , in moderately thick materials for moderately relativistic charged particles is well described by [13]:

$$\Delta_p = \xi \left[\ln \left(\frac{2m_e c^2 \beta^2 \gamma^2}{I} \right) + \ln \frac{\xi}{I} + 0.20 - \beta^2 - \delta(\beta\gamma) \right], \quad (2.16)$$

where the explanation of the variables is summarized in Table 2.2.

Variable	Description
x^*	mass per unit area
ξ	$(K/2) \langle Z/A \rangle z^2 (x^*/\beta^2)$
K	unit-dependent coefficient
z	charge number of incident particle
Z	atomic number of absorber
A	atomic mass of absorber
β	velocity of the incident particle relative to the speed of light
γ	Lorentz factor of the incident particle
I	mean excitation energy
δ	density effect correction to ionization energy loss
m_e	electron mass
c	speed of light in vacuum

Table 2.2.: Summary of variables used in Equation (2.16). (Table adopted from [10])

The Landau-shaped energy loss distribution for 500 MeV π^\pm in silicon is shown in Figure 2.2. For thinner materials, the skewness of the Landau distribution increases.

For electrons and positrons, energy loss in matter follows a slightly different behavior. Electrons and positrons undergo additional interactions that contribute to the energy loss. The most significant of these are bremsstrahlung, with smaller contributions from Møller scattering for electrons and annihilation and Bhabha scattering for positrons. Figure 2.3 illustrates the energy-dependent contributions of various interactions for electrons and positrons.

For high-energy electrons and positrons, bremsstrahlung is the dominant interaction, with

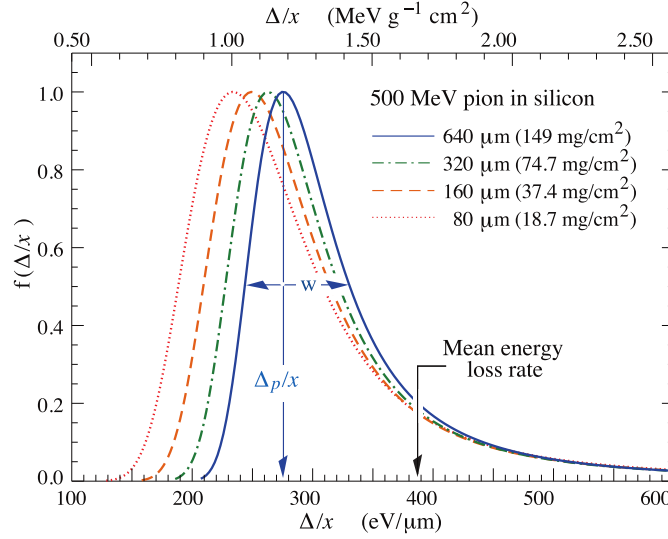


Figure 2.2.: Landau-shaped energy loss functions for 500 MeV π^\pm in silicon, normalized to unity at the most probable value Δ_p/x . The width w of the energy loss function is the full width at half maximum. (Figure taken from [10])

energy loss proportional to the particle's energy E :

$$\left\langle -\frac{dE}{dx} \right\rangle_{\text{brems}} = -\frac{E}{X_0}, \quad (2.17)$$

where the proportionality factor is a material-dependent quantity known as the radiation length, X_0 . In silicon, the radiation length is $X_0^{\text{Si}} = 9.36 \text{ cm}$ [10].

On their way through the material, the charged incident particles undergo small-angle Coulomb scattering¹ with the charged material nuclei, which deflects their trajectories. The Coulomb scattering process can be described by the Rutherford cross-section. The successive execution of such scattering processes is called *multiple scattering*. Figure 2.4 shows the deflection of the particle in the multiple scattering process.

Using the central limit theorem, the net scattering displacement angle is described by [14]:

$$\theta_{\text{plane}}^{\text{rms}} = \frac{13.6 \text{ MeV}}{\beta pc} z \sqrt{\frac{x}{X_0}} \left(1 + 0.038 \ln \frac{x z^2}{X_0 \beta^2} \right), \quad (2.18)$$

where $\theta_{\text{plane}}^{\text{rms}}$ is the width of a Gaussian distribution, $\frac{x}{X_0}$ is the material thickness in terms of radiation length, and p is the momentum of the incident particle. Multiple scattering increases with larger material thickness or lower momentum and velocity.

¹For hadronic incident particles, the strong interaction also contributes to the scattering processes.

2. Foundations

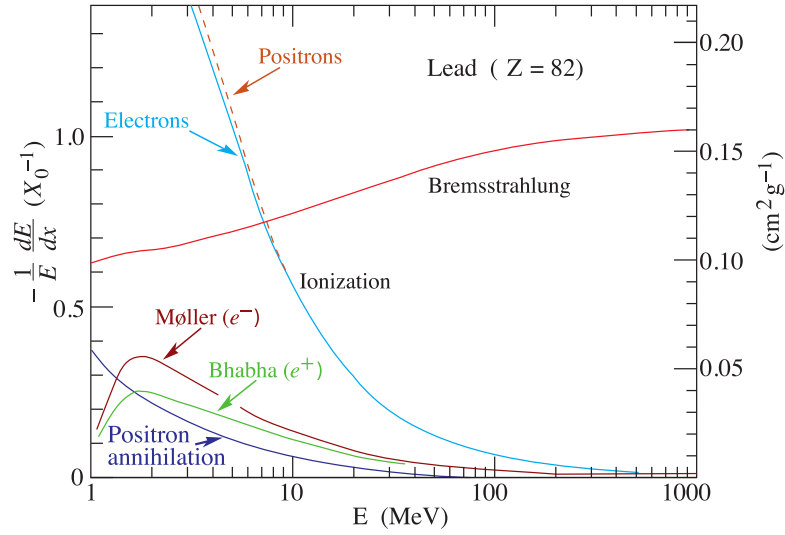


Figure 2.3.: Fractional energy loss per radiation length in lead as a function of electron or positron energy. (Figure taken from [10])

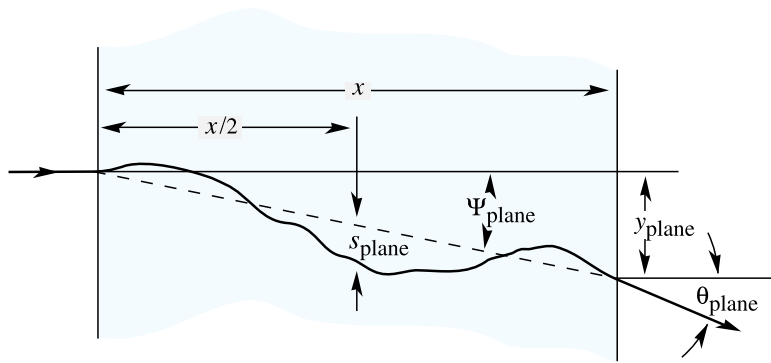


Figure 2.4.: Deflection of a particle trajectory caused by multiple scattering. (Figure taken from [10])

2.4. Silicon Semiconductors

This section provides an introduction to silicon semiconductors, the basis of silicon tracking detectors.

Semiconductors are elements or chemical compounds forming single crystals with diamond or zinc-blende lattice structures. Unlike conductors, semiconductors do not have e^- in the conduction band in their ground state. However, in contrast to insulators, they have a smaller band gap between the conduction and valence bands. This allows valence e^- to be thermally excited and elevated to the conduction band. Figure 2.5 illustrates the band structures for insulators, semiconductors, and conductors.

In semiconductors, when e^- are excited into the conduction band, they leave behind vacancies called *holes* (h^+) in the valence band. These h^+ can be filled by e^- from neighboring covalent bonds, allowing the holes to migrate through the lattice. This phenomenon enables both e^- and h^+ to move freely within the semiconductor.

While Si is the most commonly used semiconductor material, others include germanium (Ge) and gallium arsenide (GaAs) [15]. This thesis focuses on the principles of semiconductors used in particle detectors, using Si as the primary example. Like most semiconductor-based detectors in experimental particle physics, the Belle II pixel vertex detector is based on Si sensors (see Chapter 5).

Silicon has a diamond lattice structure and a band gap of 1.12 eV. Each Si atom has four valence e^- , each forming a covalent bond with a neighboring Si atom's valence e^- . At 300 K, Si has an electrical conductivity of $5 \times 10^{-4} \Omega^{-1} \text{m}^{-1}$, which is 11 orders of magnitude smaller than copper ($58.1 \times 10^6 \Omega^{-1} \text{m}^{-1}$) but six orders of magnitude larger than insulating SiO_2 ($\mathcal{O}(10^{-10} \Omega^{-1} \text{m}^{-1})$).

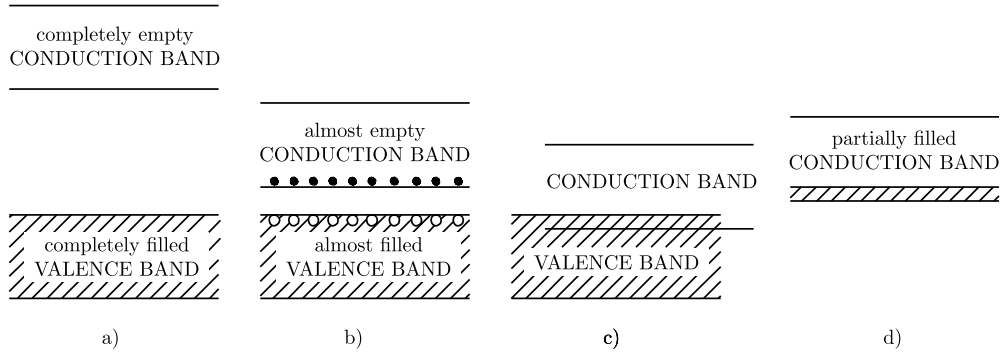


Figure 2.5.: Schematic examples of different band configurations for: a) insulators with a band gap $\sim 9 \text{ eV}$, b) semiconductors with a band gap of $\sim 1 \text{ eV}$, and c)/d) conductors with partially filled conduction bands. (Adapted from [16])

The following paragraphs are primarily based on the comprehensive work of [17] and [16].

2.4.1. Doping

The conductivity properties of a Si crystal lattice can be modified by introducing impurities. These impurities are typically atoms with either one additional valence e^- (*n-doping*) or one fewer valence e^- (*p-doping*) compared to Si. Such atoms can either donate (*donors*) or accept

2. Foundations

(*acceptors*) an e^- within the covalent bonds of the lattice. The doping process increases the number of charge carriers available for conduction, depending on the concentration of dopants.

For n-doping, the energy level E_D of the additional valence e^- is located near the conduction band. This shifts the intrinsic *Fermi level*² (E_f) from the center of the band gap (in undoped Si) towards the conduction band, reaching a new level E_F . Conversely, p-doping introduces an energy level E_A slightly above the valence band, shifting the Fermi level closer to the valence band.

2.4.2. pn-Junction - A Diode and Particle Detector

When a Si crystal contains an n-doped region adjacent to a p-doped region with an abrupt transition, it forms a *pn-junction*. This structure acts as a diode in microelectronics. In p-type Si, the primary charge carriers are h^+ , whereas in n-type Si, the charge carriers are e^- . At the interface of the p- and n-regions, e^- and h^+ recombine, forming a *depletion zone* devoid of free charge carriers.

The concentration gradient of e^- and h^+ across the junction generates a diffusion current, I_{diff} , which moves the charge carriers to the opposite sides of the junction. As the depletion zone expands, the immobile ions within the zone create an electric field, resulting in a drift current, I_{drift} , in the opposite direction of I_{diff} . The depletion zone grows until thermal equilibrium is reached, where $I_{\text{diff}} + I_{\text{drift}} = 0$. This process is illustrated in Figure 2.6a, which also shows the associated bending of the energy bands near the junction.

The resulting electric field, $E(x)$, within the depletion zone, depends on the position x and the concentrations of positive donor ions (N_D) on the n-side and negative acceptor ions (N_A) on the p-side [17]:

$$E(x) = \begin{cases} -eN_A(x + x_p), & -x_p < x < 0, \\ +eN_D(x - x_n), & 0 < x < x_n. \end{cases} \quad (2.19)$$

The electric field reaches its maximum magnitude at $x = 0$, as depicted in Figure 2.6b. The depth of recombination on the p- and n-sides depends on the doping density $\rho(x) = \frac{N}{x}$, which is determined by the number of acceptors or donors per unit volume.

In thermal equilibrium, the depletion zone prevents charge transport across the junction. However, applying a *forward bias*³ voltage, V_{ext} , reduces the depletion zone, restoring conductivity.

Conversely, applying a *reverse bias*⁴ voltage increases the width of the depletion zone. As the reverse bias voltage rises, the depletion zone extends further until the entire bulk is depleted. The current-voltage characteristic of a pn-junction under reverse bias is shown in Figure 2.7.

When $e^- h^+$ -pairs are generated within the Si bulk, either by thermal excitation or by an ionizing particle passing through (see Section 2.3), the charges are separated by the electric field. Thermally generated charges contribute to a constant *leakage current*, while ionization-induced charges produce a measurable current pulse.

An additional external drift voltage can be applied to steer the direction of charge collection. Readout can be performed through conductive contacts (commonly made of aluminum or

²The Fermi level is the chemical potential of e^- in a solid.

³Forward biasing: a positive voltage is applied to the p-side and a negative voltage to the n-side.

⁴Reverse biasing: a positive voltage is applied to the n-side and a negative voltage to the p-side.

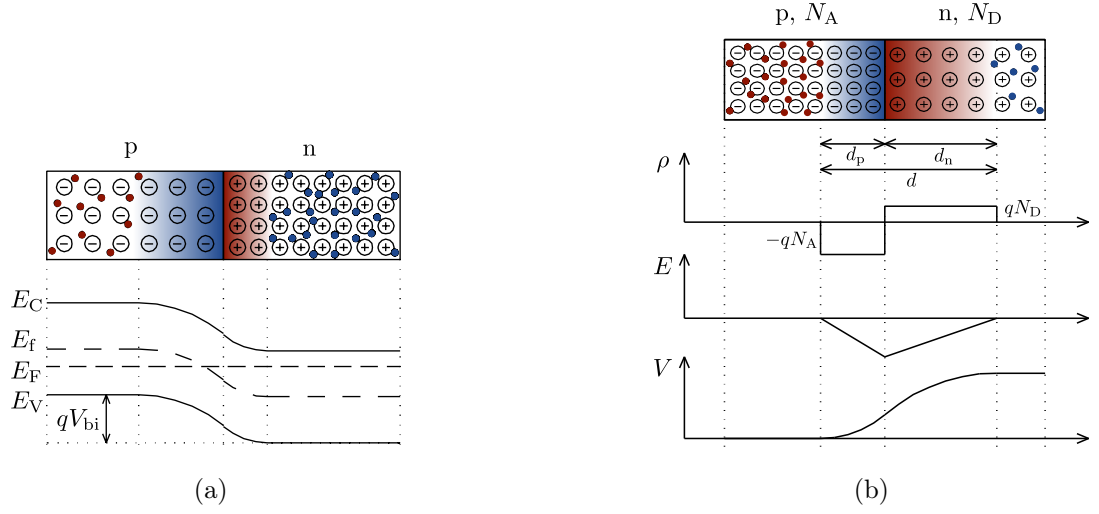


Figure 2.6.: (a) Energy band bending around the pn-junction at thermal equilibrium, where the Fermi levels align. The diffusion current is determined by the diffusion potential V_{bi} . (b) Electric potential and field across the pn-junction. (Both figures adapted from [16])

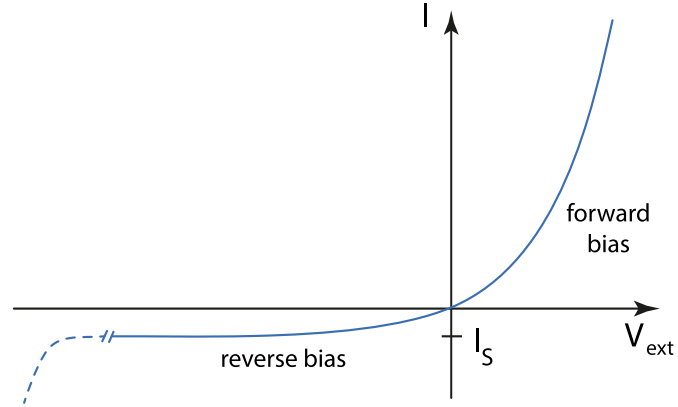


Figure 2.7.: Under forward bias, the depletion zone collapses, restoring conductivity. Under reverse bias, apart from a small saturation current caused by thermal excitation, no significant charge transport occurs. (Figure taken from [17])

2. Foundations

polysilicon) attached to highly doped Si⁵, or by capacitive coupling, where readout contacts are insulated from the Si.

2.4.3. MOSFET

The *metal oxide semiconductor (MOS)* structure is a junction composed of three materials: a conductive metal layer, an insulating oxide layer, and a semiconductor layer. The oxide layer electrically isolates the metal from the semiconductor, preventing charge flow between them. Silicon dioxide (SiO₂) is commonly used as the oxide layer.

The MOS structure is the foundation of the FET, a fundamental component in microelectronics. A FET consists of three terminals: the *drain*, *source*, and *gate*. The source-drain current is controlled by an external voltage applied at the gate terminal.

PMOS and NMOS configurations are distinguished by the type of doping used for the source and drain contacts and the substrate channel. In a PMOS-FET, the source and drain contacts are p^+ wells in an n-type substrate, while in an NMOS-FET, the source and drain are n^+ wells in a p-type substrate. In both configurations, the metal layer, insulated by the oxide layer, serves as the gate contact. Fabrication technologies that use PMOS and NMOS transistors symmetrically and complementarily are referred to as *complementary metal oxide semiconductor (CMOS)* technology. Since this work focuses solely on PMOS-FETs, their operating principles are described below (NMOS operation works similarly by inverting dedicated charges and potentials).

In the PMOS structure at thermal equilibrium, the Fermi level of the metal, E_F^M , aligns with the Fermi level of the n-doped semiconductor, E_F^S , as shown in Figure 2.8a. Due to differences in the work functions, $e\phi_M$ and $e\phi_S$, between the metal and semiconductor, and the energy level of free e^- in a vacuum, E_{vac} , the energy bands in the semiconductor bend downward near the oxide interface. This bending results from charge redistribution (accumulation or depletion) in the semiconductor. The metal, with its freely moving e^- , does not develop an electric field, keeping its energy bands flat. Through the oxide layer, where no charges are present, the energy bands transit linearly, while within the semiconductor, the bending becomes quadratic due to displaced charges at the boundary. No current flows through the oxide or semiconductor.

When a sufficiently negative external voltage, V_{ext} , is applied to the metal layer, the energy bands of the semiconductor bend upward at the oxide interface, as illustrated in Figure 2.8b. If V_{ext} becomes sufficiently negative, E_F^S drops below the intrinsic Fermi level of the pure semiconductor, E_f . Consequently, the semiconductor near the oxide boundary transitions from n-type to p-type, a process called *inversion*. In this state, holes accumulate at the oxide boundary while thermally excited electrons are pushed deeper into the semiconductor. This inversion enables the formation of a conductive *p-channel* between the source and drain, controlled by the gate voltage, $V_g := V_{ext}$.

The described principles also apply to NMOS-FETs, but with the charges and the polarity of V_{ext} inverted.

Radiation damage can trap charges within the oxide layer, causing a shift in the threshold voltage required to achieve inversion [18].

⁵Highly doped Si is necessary to form ohmic contacts; otherwise, the Si-metal junction would act as a Schottky diode.

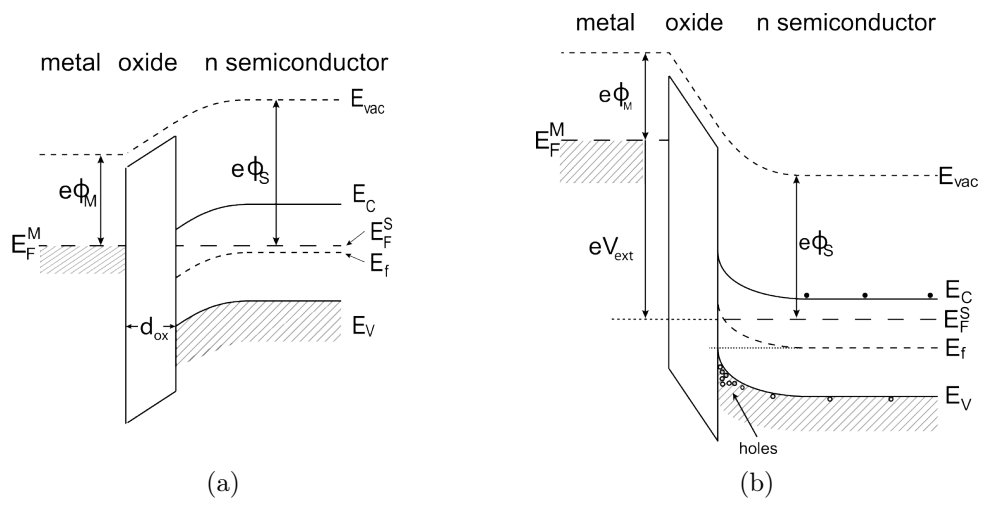


Figure 2.8.: (a) Band structure at the oxide-semiconductor interface without external voltage. (b) Band structure at the oxide-semiconductor interface with external voltage applied, leading to inversion. (Figures adapted from [17])

3. τ -Lepton Lifetime Measurement

The τ -lepton lifetime is a property of the τ -lepton that is not predicted by the SM. This chapter provides an overview of the τ -lepton decay in Section 3.1 and explains in Section 3.2 why measuring the τ -lepton lifetime with greater precision is of interest. Section 3.3.1 introduces two methods for measuring the τ -lepton lifetime, while Section 3.3.2 presents a brief overview of previous measurements that contribute to the current PDG average value.

3.1. τ -Lepton Decay

While the electron is considered stable, muons and τ -leptons decay via the weak interaction. The lifetime of a lepton is defined by Equation (2.2). The τ -lepton has several decay channels, and the τ -lepton lifetime τ_τ is determined by the sum of the partial decay widths of each channel:

$$\tau_\tau = \hbar \frac{1}{\Gamma_\tau} = \hbar \frac{1}{\Gamma_{\tau e} + \Gamma_{\tau \mu} + \Gamma_{\tau h}}, \quad (3.1)$$

where $\Gamma_{\tau l}$ (with $l \in \{e, \mu\}$) denotes the partial leptonic decay width for $\tau \rightarrow l$, $\Gamma_{\tau h}$ denotes the hadronic decay width, \hbar is the reduced Planck constant, and c is the speed of light in a vacuum.

The decay width $\Gamma_{\tau l}$, is defined by the *Fermi theory*:

$$\Gamma_{\tau l} = \frac{G_\tau G_l}{192\pi^3} \cdot m_\tau^5 \cdot F(\rho) \cdot (1 + \varepsilon_{\tau l}), \quad (3.2)$$

where G_l and G_τ are the coupling constants of l and the τ -lepton to the weak interaction, $\rho = m_l^2/m_\tau^2$, $F(\rho) = 1 - 8\rho + 8\rho^2 - \rho^4 - 12\rho^2 \ln \rho$ are corrections due to the mass of the final leptons, $\varepsilon_{\tau l}$ accounts for radiative corrections. In the case of LFU, the electroweak couplings in Equation (3.2) are equal: $G_e = G_\mu = G_\tau = G_F$. The Fermi weak coupling constant G_F is defined as:

$$G_F = \sqrt{2} \frac{g_W^2}{M_W}, \quad (3.3)$$

where M_W is the mass of the W boson, and g_W is the fundamental coupling constant of the weak interaction.

Possible τ -lepton decay modes are shown in Figure 3.1.

3. τ -Lepton Lifetime Measurement

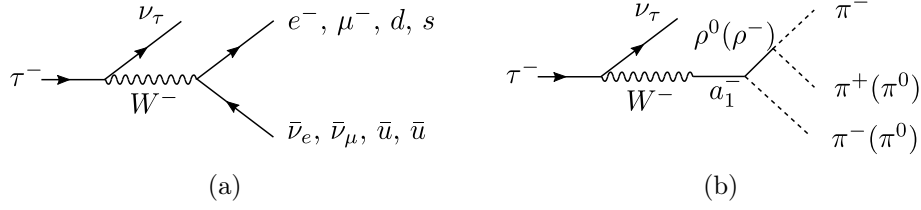


Figure 3.1.: Feynman diagrams of weak τ -lepton decays. The τ -lepton couples to a W boson. (a) The τ -lepton decays into a lighter charged lepton, $\bar{\nu}_l$, and ν_τ , or into a charged hadron and ν_τ . (b) The τ -lepton decays via the a_1^- resonance and the ρ^0 or ρ^- meson into pions and ν_τ : $\tau^- \rightarrow \pi^+\pi^-\pi^-\nu_\tau$, $\tau^- \rightarrow \pi^-\pi^0\pi^0\nu_\tau$.

3.2. Precise Measurement of Standard Model Parameters

Precise measurements of lepton properties provide stringent tests of the SM and enable accurate determinations of its parameters. Table 3.1 lists the experimental values of lepton masses and lifetimes. It is evident that the values for the τ -lepton are the least precisely measured, primarily due to its short lifetime.

Lepton	Mass in MeV/c ²	Mean lifetime in s
Electron (e)	$0.51099895000 \pm 0.00000000015$	$>2.03 \times 10^{36}$ with 90 % CL
Muon (μ)	$105.6583755 \pm 0.0000023$	$(2.1969811 \pm 0.0000022) \times 10^{-6}$
Tau (τ)	1776.93 ± 0.09	$(290.3 \pm 0.5) \times 10^{-15}$

Table 3.1.: The masses and lifetimes of the three charged lepton generations [10].

In the following, two fundamental SM tests are discussed which require a precise measurement of the τ -lepton lifetime.

3.2.1. Lepton Flavour Universality Test

LFU leads to unambiguous and simple relationships among the lepton lifetime, mass, and leptonic branching fractions. The SM prediction of the τ -lepton leptonic branching fractions, $B_{\tau\ell} = B(\tau^- \rightarrow \ell^- \bar{\nu}_\ell \nu_\tau)$ is given by

$$B_{\tau\ell}^{SM} = B_{\mu e} \frac{\tau_\tau}{\tau_\mu} \frac{m_\tau^5}{m_\mu^5} \frac{F_{\tau\ell}}{F_{\mu e}} (1 + \varepsilon'_{\tau\ell}), \quad (3.4)$$

with the muon lifetime τ_μ , muon mass m_μ , and the radiative corrections $\varepsilon'_{\tau\ell}$, including those arising from the muon decay. This relation is sensitive to the τ -lepton mass value and the τ -lepton lifetime value.

To test LFU, the SM-predicted branching fraction can be compared with the directly measured branching fraction, as shown in Figure 3.2 for $B_{\tau e} = B(\tau^- \rightarrow e^- \bar{\nu}_e \nu_\tau)$.

It is clearly visible that there is a slight tension between the experimentally measured value and the SM prediction within their 1σ uncertainty bands. However, the limited precision of the measurements prevents any definitive conclusions at this stage. It is evident that the uncertainty is dominated by the measured branching fraction and the global average of τ_τ . Therefore, achieving higher precision in the experimental measurement of these properties is essential. Significant deviations from the predictions could indicate the presence of physics beyond our current understanding, offering hints of New Physics.

3.2.2. Extraction of $\alpha(s)$

Another fundamental parameter of the SM is the *strong interaction coupling constant*, α_s . The strength of this coupling varies with the *energy scale*, a phenomenon known as the running of α_s , which is fully predicted by the SM. However, its value at a chosen reference energy scale must be determined experimentally.

3. τ -Lepton Lifetime Measurement

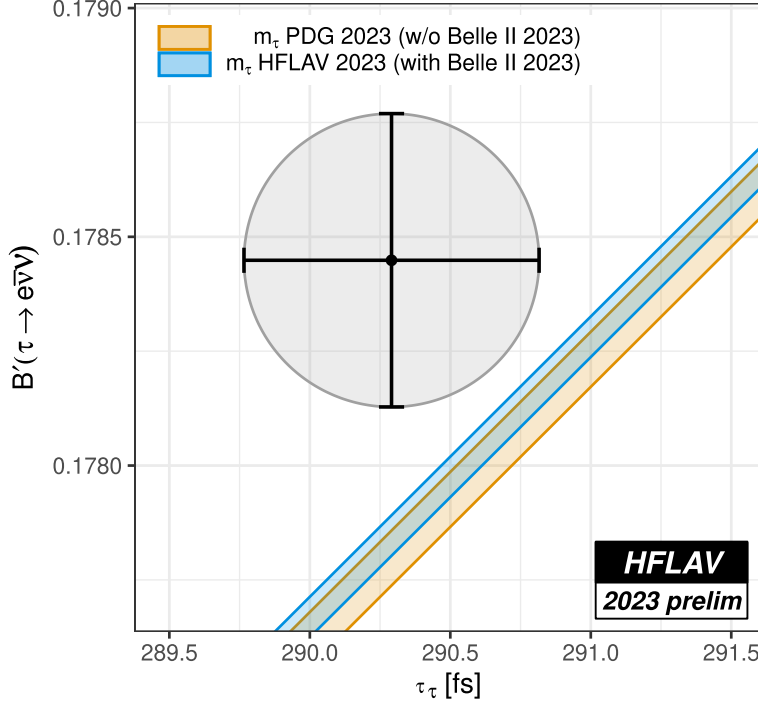


Figure 3.2.: Comparison of the SM prediction for τ -lepton leptonic branching fractions with the direct measurement. The data point represents the statistical average $B'_{\tau e}$ of the direct measurement of $B_{\tau e}$ and the $B_{\tau e}$ SM prediction derived from the $B_{\tau \mu}$ measurement, $B_{\tau e} = B_{\tau \mu} \cdot (f_{\tau e}/f_{\tau \mu})$, with $f_{\tau l}$ being the respective phase space factors. The data point incorporates the precision of the leptonic branching fraction and the current world average of τ_τ . The linear colored band shows the SM prediction as a function of different τ -lepton lifetimes and includes the PDG value of m_τ , with its width reflecting the uncertainty in m_τ . The blue band includes the latest τ -lepton mass measurement from Belle II [19]. (Figure adapted from [20])

The determination of the strong coupling $\alpha_s(M_Z)$ at the Z mass peak can be affected by the presence of New Physics. A powerful crosscheck is the determination of $\alpha_s(m_\tau)$ from the τ_τ and the leptonic branching fractions, which are less affected by many types of New Physics as summarized in [10].

The relation between τ_τ and the theoretically calculated partial decay width $\Gamma_{\tau\{u,d\}}$ of the hadronic branching fraction (excluding the s quark channel), using the SM predictions, is defined by [21]:

$$\tau_\tau = \frac{1 - B_{\tau s}}{\Gamma_{\tau e} + \Gamma_{\tau \mu} + \Gamma_{\tau\{u,d\}}}, \quad (3.5)$$

with the theoretical calculation of the partial decay widths $\Gamma_{\tau l}$ of the leptonic branching fractions. The s quark channel is excluded from the theoretical calculation due to a large uncertainty

3.2. Precise Measurement of Standard Model Parameters

on the s quark mass entering the calculations. Instead, the measured branching fraction $B_{\tau s}$ is used.

The hadronic decay width can be calculated by [22][23]:

$$\Gamma_{\tau\{u,d\}} = \frac{G_F^2 m_\tau^5 |V_{ud}|^2}{64\pi^3} S(m_\tau, M_Z) \left(1 + \frac{3}{5} \frac{m_\tau^2 - m_\mu^2}{M_W^2} \right) \times \left[1 + \frac{\alpha_s^{(3)}(m_\tau)}{\pi} + \frac{5.202 \alpha_s^2}{\pi^2} + \frac{26.37 \alpha_s^3}{\pi^3} + \frac{127.1 \alpha_s^4}{\pi^4} + \frac{\hat{\alpha}}{\pi} \left(\frac{85}{24} - \frac{\pi^2}{2} \right) + \delta_{\text{NP}} \right], \quad (3.6)$$

where V_{ud} is the CKM matrix element, $S(m_\tau, M_Z)$ is an electroweak correction factor, M_W is the W boson mass, $\hat{\alpha}$ is the electromagnetic coupling constant, and δ_{NP} accounts for non-perturbative and quark-mass suppressed contributions.

With the methods described in [21] and [24] one obtains [10]

$$\alpha_s(m_\tau) = 0.312_{-0.013}^{+0.016} \text{ and } \alpha_s(M_Z) = 0.1171_{-0.0017}^{+0.0018}. \quad (3.7)$$

The current PDG average value [10] is $\alpha_s(M_Z) = 0.1180 \pm 0.0009$. To have a precise test from the low energy measurement, the precision of the $\alpha_s(m_\tau)$ needs to be increased. This requires a precise measurement of τ_τ . However, the current precision of the extrapolated $\alpha_s(M_Z)$ is dominated by theoretical uncertainties originating from perturbative QCD and non-perturbative corrections [25]. Nevertheless, if the theory is better understood, the precision of the τ -lepton lifetime becomes relevant.

3.3. Decay Length Measurement of Tau-Lepton Decays

There are several methods to measure the τ -lepton lifetime via the decay length distribution. The choice of method depends on the decay topology of the $\tau^+\tau^-$ pair, the statistical precision afforded by the dataset, and the precision of the experimental setup. This section gives an overview of the common methods and summarizes the measurements of the τ -lepton lifetime included in the current PDG world average value.

3.3.1. Overview of Measurement Methods

In the $e^+e^- \rightarrow \tau^+\tau^-$ CMS, the τ -leptons are boosted back-to-back. As a result, their decay products are well-separated into two opposite hemispheres. To distinguish between these hemispheres, the thrust axis \hat{n}_{thrust} is defined as the vector that maximizes the thrust value V_{thrust} :

$$V_{\text{thrust}} \equiv \max_i \sum_j \frac{\mathbf{p}_i^* \cdot \hat{n}_{\text{thrust}}}{\sum_j |\mathbf{p}_j^*|}, \quad (3.8)$$

where \mathbf{p}_i^* are the CMS momenta of all final state particles of the collision in the event. The value of V_{thrust} reaches 1 when the momenta sum of the respective daughter particles are exactly back-to-back. Since neutrino(s) remain undetected, their momentum is not accounted for, resulting in V_{thrust} being slightly less than 1.

The *decay topologies* are categorized by the number of charged particles produced in the decay of the respective τ -lepton. The possible decay channels lead to 1, 3, or 5 charged daughter particles (*prongs*) per τ -lepton. For the decay of the τ -lepton pair, this results in 1x1-prong, 3x1-prong, 3x3-prong, 5x1-prong, 5x3-prong, or 5x5-prong decay topologies¹. Hereafter, the particles associated with the 1-prong (3-prong) decay are denoted with a 1p (3p) index.

A major challenge in τ -lepton decay length measurements is the accurate reconstruction of the τ -lepton flight direction due to the presence of invisible neutrino(s) ν . Two concepts for measuring the τ -lepton decay, based on [26], are discussed. These methods use the production point, such as the interaction point (IP) in particle collisions, as a constraint. The two methods are illustrated in Figure 3.3 and described in the bullet points below.

- **Impact parameter method:** If one τ -lepton decays via the 1-prong mode, the *distance of closest approach (DOCA)* d_0 , relative to the IP, can be measured (Figure 3.3a). This distance is orthogonal to the direction \mathbf{p}_{1p} of the charged daughter particle's trajectory t^\pm . The decay length d is not measured directly by this method; however, d_0 is related to the angle ψ between \mathbf{p}_{1p} and \mathbf{d} :

$$d_0 = d \sin \psi \quad (3.9)$$

Negative values can occur due to resolution effects if $\sin \psi < 0$. Equation (3.9) is related to the proper lifetime by Equation (2.11). However, ψ is unknown since the true τ -lepton direction is unknown. Therefore, in the fit to the experimental data, the average d_0 is calculated from the mean proper lifetime and the mean ψ , which needs to be estimated from simulations.

¹The 5-prong decay modes have such a low branching fraction that they are not considered in this work.

- **Decay length or vertex method:** If at least one τ -lepton decays via the 3-prong mode, the decay vertex V can be directly reconstructed from the charged daughter particle trajectories t^\pm , as shown in Figure 3.3b. The distance of V to the IP (the production vertex) is the decay length $|\mathbf{d}|$. Since the beam size is typically large in the beam direction, the measurement is usually performed in the transverse plane to the beam direction. Again, the challenge is the accurate reconstruction of the τ -lepton direction \mathbf{d} , which can be approximated from the thrust. The boost factor $\beta\gamma$ can be estimated from simulations, including radiative influences, and the average decay length can be obtained from a fit to the experimental data, with the lifetime then derived from Equation (2.11).

More advanced methods exist that incorporate the entire event into the measurement, such as the **momentum-dependent impact parameter sum method** and the **impact parameter difference method**, which reduce the dependence on the unknown τ -lepton direction compared to the single-hemisphere impact parameter measurement. Their applications and extensions are discussed in Section 3.3.2.

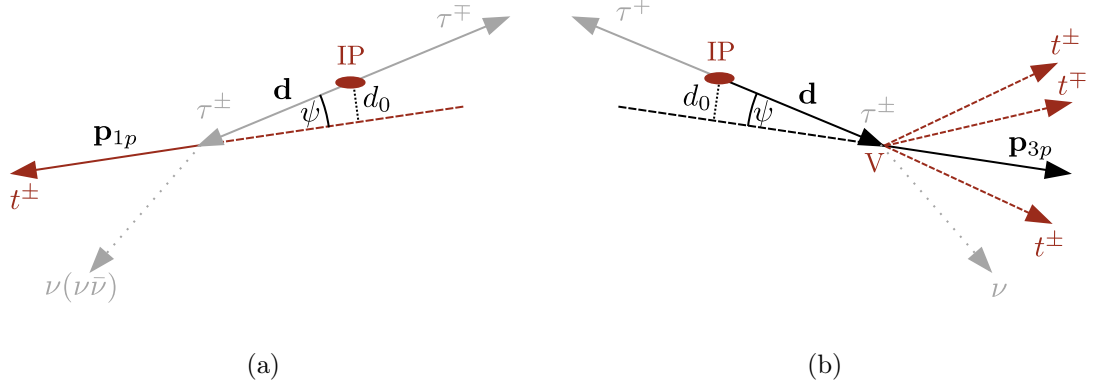


Figure 3.3.: (a): Measurement of the DOCA using the trajectory and the IP. (b): Measurement of the decay length using the reconstructed vertex and the IP.

3.3.2. Previous Measurements

The τ -lepton lifetime measurement has advanced over the past decades. Since the first measurement at Mark II in 1982 [27], which reported (490 ± 190) fs, precision has steadily improved, culminating in the most accurate measurement to date, achieved by the Belle experiment in 2014 [28]. Figure 3.4 provides an overview of the measurements that contribute to the PDG average of the mean τ -lepton lifetime.

These experiments were conducted at the Cornell Electron Storage Ring (CESR), Large Electron-Positron Collider (LEP), and KEKB. CESR was an e^+e^- collider operating, like KEKB, at the $\Upsilon(4S)$ resonance. At LEP, τ -leptons were produced in symmetric e^+e^- collisions, resulting in highly back-to-back boosted $\tau^+\tau^-$ pairs in the lab frame. LEP operated near the mass peak of the Z -boson, yielding a mean decay length of $\beta\gamma c\tau_\tau \approx 2.2$ mm. The following subsections provide an overview of the methods used to measure τ -lepton lifetimes, as shown in Figure 3.4.

3. τ -Lepton Lifetime Measurement

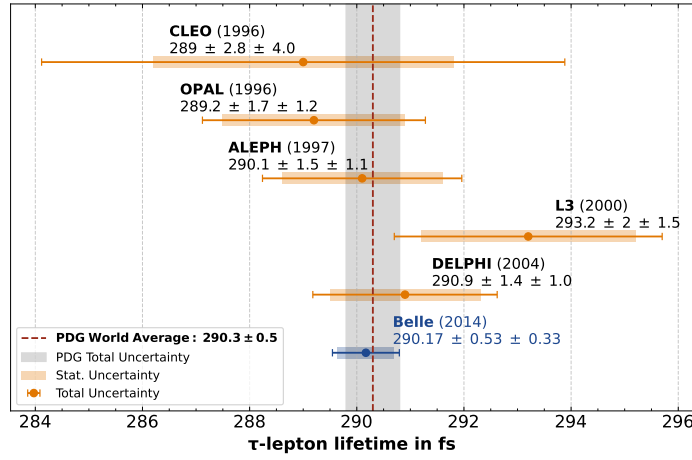


Figure 3.4.: Previous τ -lepton lifetime measurements combined to yield the world average value of the PDG [10]. The measurement method(s) of each experiment are discussed in the text.

CLEO II

At the CESR experiment CLEO II, the τ -lepton decay length was measured using the 1x3-prong and 3x3-prong decay topologies with the **decay length method** in the transverse plane to the beam direction [29]. Applying Equation (2.12), $\beta\gamma$ and the τ -lepton transverse momentum are obtained from the beam energy. The τ -lepton polar angle is obtained from the reconstructed momentum vector of the three charged tracks. For the 1x3-prong topology, the IP is used as the production point. In contrast, for the 3x3-prong topology, the production point is determined using the center of the difference vector between the two reconstructed vertices, eliminating the need for knowledge of the IP position. The lifetime is derived from the weighted average of the respective $c\tau$ distributions.

OPAL

At LEP, the OPAL experiment measured the τ -lepton lifetime using two different techniques [30]:

- **Decay length method:** Events which contain a 3-prong decay in a hemisphere were selected. The decay length was determined from the distance between the decay vertex and the IP. The event thrust axis was used as τ -lepton flight direction constraint. The mean decay length was obtained from a maximum likelihood fit of the decay length distribution. The beam energy boost factor $\beta\gamma c$ was then applied to calculate the mean lifetime.
- **Impact parameter method:** Events which contain a 1-prong decay in a hemisphere were selected. The τ -lepton lifetime was extracted from the distribution of the measured signed DOCAs. The mean DOCA values \bar{d}_0 were calculated from the simulated (sim)

3.3. Decay Length Measurement of Tau-Lepton Decays

and measured (data) distributions, where a portion of the positive and negative tails were truncated. The lifetime is determined by:

$$\tau_{\text{data}} = \bar{d}_{\text{data}} \cdot \frac{\tau_{\text{sim}}}{\bar{d}_{\text{sim}}} \quad (3.10)$$

ALEPH

The ALEPH experiment at LEP measured the τ -lepton lifetime [31] using three distinct methods [32]–[34]:

- **Momentum-dependent impact parameter sum method:** In the transverse plane to the beam axis, the sum δ of the 1x1-prong track signed DOCAs was calculated, resulting in two exponential functions with means dependent on the τ -lepton decay angles, τ -lepton polar angles, and mean decay length. A likelihood function was constructed, which takes on an event-by-event basis the momentum dependence of δ into account. The lifetime was determined from an unbinned maximum likelihood fit of the δ distribution, convoluted with two resolution functions. The first resolution function is a double Gaussian distribution accounting for tracking uncertainty and beam size, while the second accounts for misreconstructed τ -lepton flight directions, obtained from simulation.
- **Impact parameter difference method:** Events with a 1x1-prong decay topology were selected. This method leverages the near back-to-back nature of the two τ -lepton flight directions, with thrust axis polar angle, θ , yielding nearly zero decay angle differences $\Delta\phi = (\sin\psi^+ - \sin\psi^-)$. In the transverse plane to the beam axis, the average difference of the two DOCAs $\langle d_0 \rangle$ relates to the average projected decay length $\langle d_{xy} \rangle$:

$$\begin{aligned} \langle d_0 \rangle &= \langle d_{xy} \rangle \cdot \Delta\phi \\ &= \frac{p_\tau}{m_\tau} \tau_\tau \cdot \Delta\phi \sin\theta, \end{aligned} \quad (3.11)$$

yielding a linear relation to the τ -lepton lifetime, with the boost factor p_τ/m_τ as proportional constant. The lifetime is obtained from a linear fit of the $\langle d_0 \rangle$ distribution, with resolution effects incorporated as event weights.

- **Decay length method:** This method is applied to the 1x3-prong and 3x3-prong decay topologies in three-dimensional space. For each decay, the τ -lepton decay length is obtained from a least-squares fit with adjustable production and decay vertices, constrained by the beam size and vertex fit uncertainty. The mean decay length, including the LEP beam energy boost factor, is obtained from a maximum likelihood fit of the decay length distribution, convoluted with a Gaussian resolution function (see Equation (2.15)).

L3

At the LEP experiment L3, the τ -lepton lifetime was measured employing two different techniques [35]:

- **Decay length method:** Events which contain a 3-prong decay in a hemisphere were selected. The decay length was obtained from the center of the IP and a vertex fit.

3. τ -Lepton Lifetime Measurement

The lifetime was extracted by an unbinned maximum likelihood fit of the decay length distribution (see Equation (2.15)).

- **Impact parameter method:** Events which contain a 1-prong decay in a hemisphere were selected. The distribution of signed DOCAs in the transverse plane to the beam direction was measured. From simulations, it was found that the generator-level DOCA distribution can be described by three exponential functions with lifetime-dependent slopes for both positive and negative DOCA values. An unbinned maximum likelihood fit of the observed DOCA distribution, convoluted with a double Gaussian resolution function, was then performed to determine the lifetime.

DELPHI

At the LEP experiment DELPHI, the τ -lepton lifetime was measured using three different methods [36]:

- **Decay vertex method:** This method corresponds to the decay length method. Events with 3x3-prong or 3x1-prong decay topologies were selected. The decay length was measured from the IP to the 3-prong decay vertex in the transverse plane to the beam direction. The decay time was calculated from Equation (2.12), incorporating the boost factor based on the beam energies, corrected for initial state radiation (ISR) and final state radiation (FSR) effects estimated from simulations. The lifetime was extracted by an unbinned maximum likelihood fit of the decay time distribution similar to Equation (2.15). The function used in the fit was convoluted with three Gaussian resolution functions obtained from simulations.
- **Miss distance method:** Applied for 1x1-prong decay topology, similar to the ALEPH *momentum-dependent impact parameter sum method*.
- **Impact parameter difference method:** Applied for 1x1-prong decay topology, similar to the ALEPH measurement.

Belle

At the Belle experiment, the τ -lepton lifetime measurement was performed for the 3x3-prong decay topology [28]. The reconstruction of the τ -lepton flight directions was conducted in the CM frame. The angle θ^* between the reconstructed τ -lepton momentum from the daughter particles \mathbf{P}^* and the true τ -lepton flight direction \mathbf{n}^* , in conjunction with the beam energies, was used to set up a system of three equations. This approach yielded two distinct solutions for the τ -lepton momentum direction in the CM frame, which were then averaged. Using the beam energies and the τ -lepton mass, the four-momentum vector was reconstructed and boosted to the lab frame. This procedure was applied to both τ -leptons. The resulting τ -lepton momentum vectors \mathbf{n}_\pm were required to pass through their respective measured decay vertices \mathbf{V} . Due to finite detector resolution, the vectors, extended as straight lines, typically did not intersect precisely at the $\tau^+\tau^-$ production point but crossed at a distance $d\mathbf{l}$. The decay lengths l_1 and l_2 were measured from the DOCA \mathbf{V}_0 to their decay vertices. This method is illustrated in Figure 3.5.

The proper decay time was calculated using Equation (2.11) with the necessary replacements. The mean proper time distribution was measured by fitting an exponential function convoluted

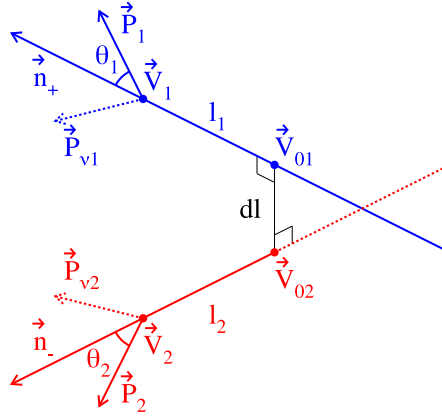


Figure 3.5.: Reconstruction of the τ -lepton flight directions and production vertex at Belle in the lab frame. Figure taken from [28].

with a resolution function to the measured proper time distribution. The smearing of the proper time distribution was studied with simulations. The largest systematic uncertainty arose from the SVD alignment, though the total uncertainty was dominated by statistical precision.

Belle II

This thesis presents a novel method using a template fitting approach applied to the decay length distribution measured from the 3-prong side of the 3×1 -prong $\tau^+ \tau^-$ decays. The 3×1 -prong topology, combined with an optimized event selection, results in a high-statistics dataset that will limit the precision to systematic uncertainties. The most sensitive measurement to date is expected, as discussed in Section 6.8.

4. The Belle II Experiment

The Belle II experiment consists of the asymmetric SuperKEKB double-ring e^+e^- collider and the Belle II detector. It is located at the High Energy Physics research center (KEK) in Tsukuba (Japan), 60 km north of Tokyo. Since 2019, the Belle II experiment has been collecting data.

By the summer of 2022, Belle II had completed its first major data-taking period (*Run 1*), accumulating an integrated luminosity of 428 fb^{-1} . 363 fb^{-1} were collected while operating at the energy of the $\Upsilon(4S)$ resonance [37]. *Run 2* started at the beginning of 2024.

This chapter provides an overview of the SuperKEKB accelerator and the Belle II detector.

4.1. The SuperKEKB Accelerator

SuperKEKB, the successor of KEKB [38], is a second generation asymmetric *B-Factory*¹, mainly operating at a *center of mass (CM) energy*, \sqrt{s} , of 10.58 GeV, which corresponds to the energy of the $\Upsilon(4S)$ resonance [6]. This resonance is a bound state of a $b\bar{b}$ quark pair, and decays with over 96 % probability into a $B\bar{B}$ meson pair [10]. The $\Upsilon(4S)$ production cross-section at $\sqrt{s} = 10.58 \text{ GeV}$ is $\sigma[\Upsilon(4S)] = 1.11 \text{ nb}$ [39].

Alongside $\Upsilon(4S)$ mesons, other particles are also produced in e^+e^- collisions. With a $\tau^+\tau^-$ production cross-section of $\sigma[\tau\tau] = 0.919 \text{ nb}$ [39], the accelerator serves as an ideal τ -*Factory*. The largest production cross-section occurs for e^+e^- (Bhabha scattering), which is approximately 300 times higher than the production cross-sections of $\sigma[\Upsilon(4S)]$ and $\sigma[\tau\tau]$. The full spectrum and fraction of produced particles at SuperKEKB is shown in Figure 4.1.

A schematic overview of SuperKEKB is shown in Figure 4.2. The accelerator operates with an e^- -beam and an e^+ -beam counter circulating in a storage ring. The beams are divided into small particle *bunches* and guided by electric and magnetic fields along beam orbits through evacuated *beam pipes (BPs)*. At the *interaction region (IR)*, the beams cross, and at the *interaction point (IP)* the e^+ and e^- in the bunches interact.

The beams have asymmetric energies of 7 GeV (*high-energy ring (HER)*) and 4 GeV (*low-energy ring (LER)*). The CM energy is calculated by:

$$\begin{aligned}\sqrt{s} &= \sqrt{(p_{\text{HER}} + p_{\text{LER}})^\mu (p_{\text{HER}} + p_{\text{LER}})_\mu} \\ &= \sqrt{(7 + 4)^2 - (7 - 4)^2} \\ &\approx 10.58 \text{ GeV},\end{aligned}\tag{4.1}$$

where p are the four momentum vectors of the colliding particles and μ are the sum indices.

¹A B-Factory is an accelerator designed to produce a large number of $B\bar{B}$ meson pairs. The first generation of asymmetric B-Factories were KEKB (Belle experiment, Japan) and PEP-II (BaBar experiment, USA). Experiments like CLEO and ARGUS collected data at symmetric e^+e^- accelerators, which are considered as predecessors of B-Factories.

4. The Belle II Experiment

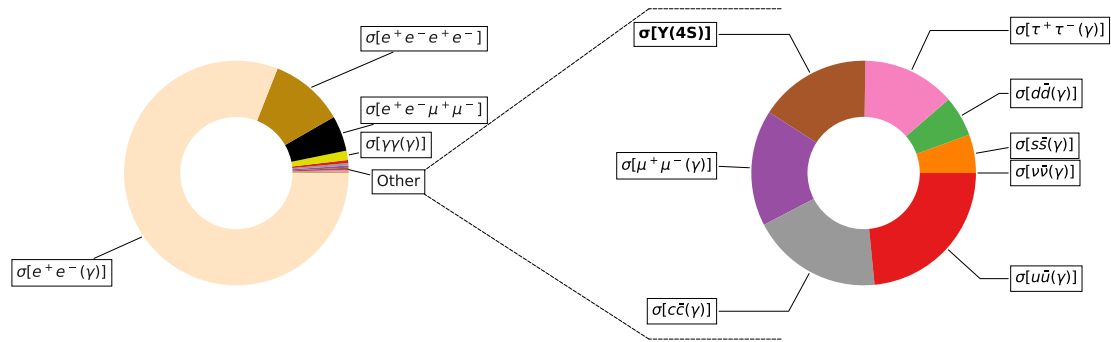


Figure 4.1.: Relative production cross-sections at $\sqrt{s} = 10.58 \text{ GeV}$. The actual numbers can be found in Table A.1. (Figure taken from [40])

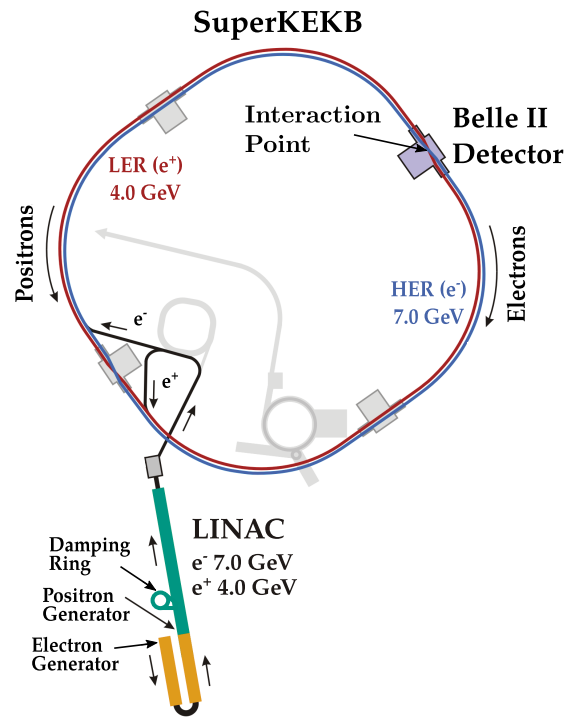


Figure 4.2.: Schematic overview of the SuperKEKB accelerator. (Figure adapted from [41])

Owing to the asymmetric beam energies, the created particles are boosted in direction of the higher energetic beam by a relativistic *Lorentz-boost* of $\beta\gamma = 0.28$ in z -direction (*forward direction*). As a consequence, the boosted particles have a longer lifetime in the *laboratory (lab) system* of the Belle II detector. This allows a precise decay length measurement of particles with lifetimes down to $\mathcal{O}(\text{fs})$, decaying already within the BP into charged secondary particles. The beam energy asymmetry in Belle II was optimized compared to its predecessor, Belle, to mitigate Touschek scattering² in the LER, thereby reducing beam background and increasing beam lifetime, though at the cost of a reduced Lorentz boost.

The e^+ and e^- are injected by a linear accelerator (LINAC) into the LER and HER storage rings. The e^- are seeded into the LINAC by an Yttrium doped laser shot on an Ir_5Ce photocathode, which emits low emittance e^- created by the photoelectric effect. Subsequently, the e^- are accelerated to 7 GeV before they are injected into a bunch in the HER. To generate the e^+ , an electron-gun emits an additional e^- -beam, which is guided onto a 14 mm tungsten target. The e^- interact with the material and generate Bremsstrahlung. High energetic photons are converted into e^+e^- -pairs. In a magnetic field, the e^- and e^+ are separated. The obtained e^+ -beam has a large emittance, which is cooled down in a 1.1 GeV damping ring before the e^+ are further accelerated to 4 GeV and injected into the LER bunches.

At the IR, the beams are squeezed to a vertical size of ~ 50 nm, at a crossing angle of 83 mrad. Figure 4.3 illustrates this so-called *nano-beam scheme* for the e^+ and e^- beams.

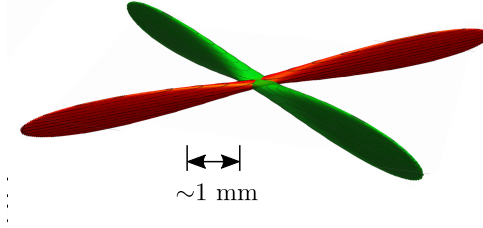


Figure 4.3.: Illustration of the nano-beam scheme at the IP. The design beam size in vertical direction at the IP is 50 nm. (Figure adapted from [42])

The design instantaneous luminosity L of SuperKEKB is $8 \times 10^{-35} \text{ cm}^{-2} \text{ s}^{-1}$, 40 times higher than KEKB. It is defined as:

$$L = \frac{\gamma_{\pm}}{2er_e} \left(1 + \frac{\sigma_y^*}{\sigma_x^*} \right) \left(\frac{I_{\pm} \xi_{y\pm}}{\beta_y^*} \right) \left(\frac{R_L}{R_{\xi_{y\pm}}} \right), \quad (4.2)$$

where, “+” denotes e^+ -beam and “-” denotes e^- -beam. Furthermore, γ_{\pm} corresponds to the Lorentz factor of the respective beam, r_e to the classical electron radius, and $\sigma_{x/y}$ to the transverse beam sizes at the IP in the respective transverse plane. The beam currents are given by I_{\pm} , while $\xi_{y\pm}$ represents the vertical beam-beam parameters incorporating electric and magnetic forces of the opposite bunch at the IP, and β_y^* denotes the vertical beta function at the IP. Additionally, R_L and $R_{\xi_{y\pm}}$ are correction factors that account for geometric losses caused by the hourglass effect, where the beam’s transverse size increases as it moves away from the IP. Table 4.1 shows the machine parameters of SuperKEKB. Low emittance and high beam currents as well as a contentious top-up injection scheme are fundamental to reach the desired target

²Intra-bunch Coulomb scattering repels particles with the same charge sign.

4. The Belle II Experiment

luminosity. During the end of Run 1, SuperKEKB achieved a record-breaking instantaneous luminosity of $4.7 \times 10^{34} \text{ cm}^{-2} \text{ s}^{-1}$ [43].

	SuperKEKB 2020 May 1st		SuperKEKB 2022 June 22nd		SuperKEKB Design	
	LER	HER	LER	HER	LER	HER
I_{beam} [A]	0.438	0.517	1.363	1.118	3.6	2.6
# of bunches	783		2249		2500	
I_{bunch} [mA]	0.5593	0.6603	0.606	0.497	1.440	1.040
β_y^* [mm]	1.0		1.0		0.27	0.30
ξ_y	0.0236 ^b	0.0219 ^b	0.0398 ^b	0.0278 ^b	0.0881 ^c	0.0807 ^c
			0.0565 ^d	0.0434 ^d	0.069 ^b	0.061 ^b
L [$10^{34} \text{ cm}^{-2} \text{ s}^{-1}$]	1.57		4.71		80	
$\int L dt$ [ab^{-1}]	0.03		0.424		50	

^{b,c,d} different equations were used to calculate the values of ξ_y .

Table 4.1.: SuperKEKB machine parameters at the beginning of Run 1, the end of Run 1, and the design parameters. (Table taken from [43])

4.2. The Belle II Detector

The Belle II detector is an asymmetric detector covering almost 4π of solid angle, located around the IP of SuperKEKB. Its purpose is to detect the primary and secondary produced particles after an e^+e^- -collision.

Several subsystems with various detection purposes form the onion-like structured detector [5] (Figure 4.4). The innermost subsystem is the *vertex detector (VXD)* composed of the *pixel vertex detector (PXD)* and the *silicon strip detector (SVD)*. The VXD is surrounded by the *central drift chamber (CDC)* which is the main tracking system. Outside the CDC, the charged *particle identification (PID)* system is located: The *time of propagation counter (TOP)* in the barrel region, and the *aerogel ring imaging Cherenkov detector (ARICH)* in the forward end-cap region (the detector regions are described below). The PID system is enclosed in the *electromagnetic calorimeter (ECL)* to measure the energy of e.g. e^- and γ utilizing particle showers created in the thallium doped cesium iodide (CsI(Tl)) crystals. Around the ECL, a *superconducting coil* is installed to provide a homogeneous magnetic field inside the detector along the beam axis (z -direction). It is used for momentum measurements and charge identification of charged particles. The outermost subsystem is the K_L and muon detector consisting of resistive plate chambers and scintillators.

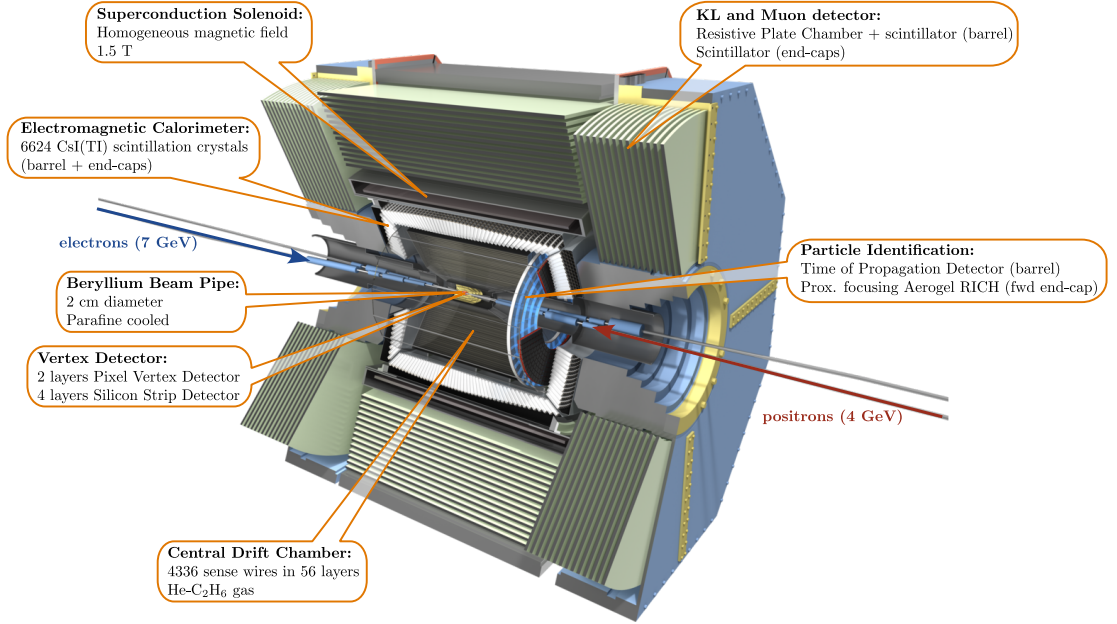


Figure 4.4.: The Belle II detector with its subsystems. (Figure adapted from [44])

The *Belle II coordinate system* [45][5] is depicted in Figure 4.5. It is right-handed, Cartesian, and with the origin in the nominal IP. The x -axis points radial outwards of the storage ring, the y -axis to the detector top, and the z -axis in direction of the HER beam. The polar angle θ is defined in the yz -plane with $\theta = 0 \parallel z$, and the azimuthal ϕ is defined in the xz -plane with $\phi = 0 \parallel x$. The three detector regions are defined based on the ECL acceptance regions as: *forward* ($12^\circ \leq \theta < 31^\circ$), *barrel* ($32^\circ \leq \theta \leq 129^\circ$), and *backward* ($130^\circ \leq \theta \leq 155^\circ$).

The following subsections describe the individual subsystems and the Belle II trigger system

4. The Belle II Experiment

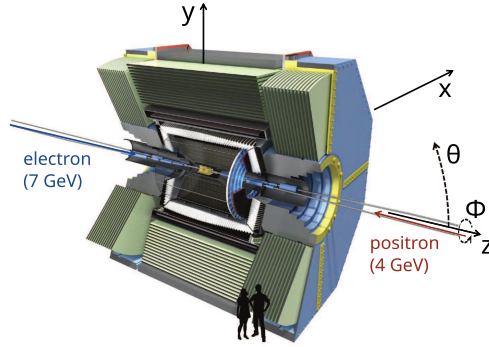


Figure 4.5.: Belle II coordinate system. (Figure adapted from [45])

in more detail.

4.2.1. Vertex Detector

The VXD consists of two different detector-systems. The innermost two-layer PXD and the enclosing four-layer SVD [46]. While the PXD consists of monolithic DEPFET pixels (Section 5.1), the SVD is made up of double-sided silicon strip sensors. The system is designed and utilized for high precision vertex measurements, and to reconstruct low- p_T tracks at the level of $\mathcal{O}(\text{MeV})$. The PXD is described in more detail in Chapter 5. A picture of the open VXD is shown in Figure 4.6.

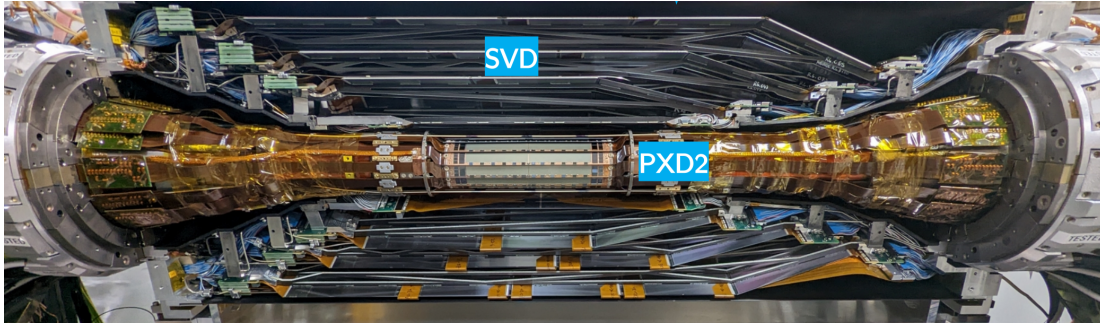


Figure 4.6.: The mounted PXD2 inside a SVD-half. (Figure taken from [47])

The six layers of VXD ladders are positioned parallel to the z -axis at radii of 14, 22, 38, 80, 115 and 140 mm around the IP. In direction of the boost, the three outer layer SVD ladders have a 17° inclined sensor towards the BP at the forward end. This increases the acceptance region on the one hand, and on the other hand, the necessary number of wafers is reduced compared to a plain cylindrical geometry. A 3D model of the mechanical structure of an SVD-half is shown in figure 4.7b.

The SVD ladders are built from so-called *double-sided strip detectors (DSSD)*. These sensors consist of n-doped Silicon (Si) bulk. Structured p-doped strips are implanted parallel to the BP on the backside. In contrast to the backside strips, on the front side n-doped strips are implanted perpendicular to them. Charged particles traversing the sensor ionize the bulk,

creating electron-hole-pairs. In the depleted bulk, the electrons drift towards the n-doped strips while the holes drift to the opposite p-doped strips (Figure 4.7a). The sensors are 300 - 320 μm thick and the strip pitch is 50 - 75 μm in R - ϕ and 160 - 240 μm in z .

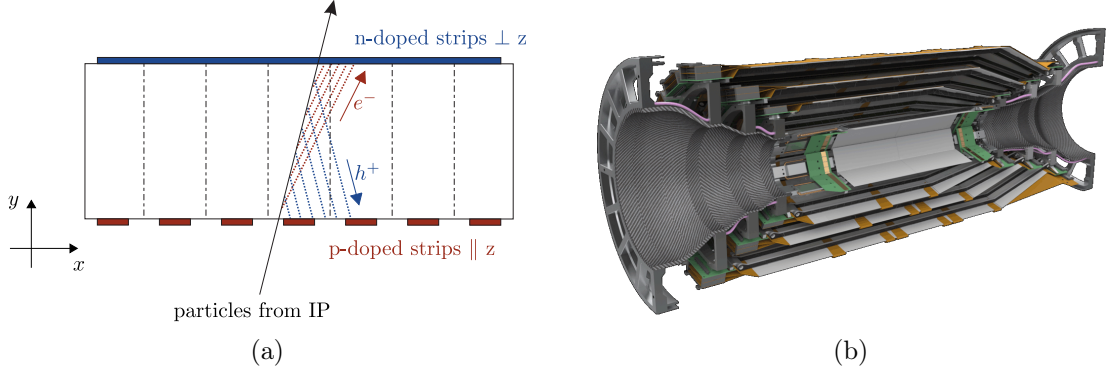


Figure 4.7.: (a) Schematic cross-section of a double-sided SVD sensor working principle. (Figure adapted from [5]) (b) 3D model of the mechanical structure of an SVD-half (Credit to the SVD Collaboration).

DSSDs have an intrinsic drawback in high occupancy environments like the operation at high luminosity close to the IP. The positions of particles that traverse a sensor at the same time cannot be resolved unambiguously, resulting in ghost hits. Since the occupancy increases at smaller radii, the number of ghost hits also rises, resulting in a higher load on the data readout system. For that reason, the two innermost layers of the VXD consists of pixel sensors. Under high luminosity background conditions, the SVD is utilized to extrapolate reconstructed tracks into the PXD. The expected PXD hits associated with a track are in a defined search window (*region of interest (ROI)*).

4.2.2. Central Drift Chamber

The main Belle II tracking system is the CDC, utilized to measure in the xy -plane curved trajectories of charged particles traversing the 1.5 T magnetic field. It provides a coverage of 17° - 150° in the θ direction and 2π in the ϕ direction. In addition to the tracking, the CDC signals enter the hardware trigger (L1) decisions and its collision time (T_0) calculations.

The CDC consists of 14336 30 μm thick *sense wires* and 42240 126 μm thick *field wires*. They are taut along the z -axis in 56 sense wire layers grouped into nine *superlayers* with different wire configuration. A single drift cell consists of a sense wire in the center, surrounded by several field wires. Different potentials put on the field wires and sense wires create radial electric fields around the sense wires.

The innermost superlayer consists of eight sense wire layers, each with a smaller drift cell configuration compared to the seven outer superlayers, which consist of six sense wire layers each. This denser small-cell superlayer mitigates the performance impact caused by wall effects and higher occupancy at smaller radii. The superlayers are alternating between *stereo* and *axial wire configurations*. In the axial configuration, the wires are all parallel in z -direction, while in the stereo configuration the wires are tilted 45 mrad with respect to the z -axis. The latter allows the measurement of the z -component of a trajectory. Figure 4.8 schematically shows in

4. The Belle II Experiment

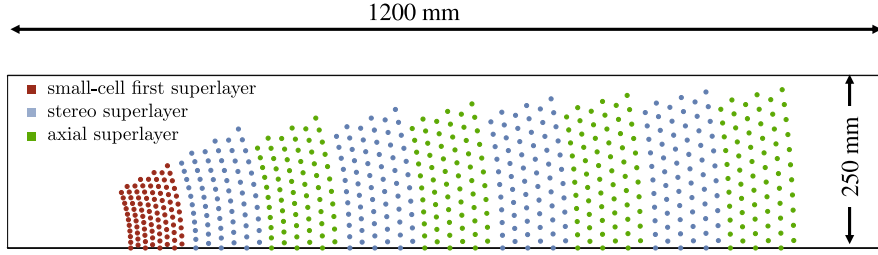


Figure 4.8.: CDC wire configuration in the xy -plane. (Figure adapted from [5])

the xy -plane the wire configuration.

The CDC volume is filled with helium-ethane ($\text{He-C}_2\text{H}_6$) gas. Charged particles traversing the gas volume of the CDC cylinder, are ionizing the He atoms. The free e^- and ions drift inside the radial electrical fields in opposite directions. The ions recombine already after a short drift length owing to their mass, while the e^- drift all the way to the sense wires in the centers of the drift cells. The force on the e^- grows by factor $1/r^2$ with the distance r towards the center of the sense wires. Reaching a certain momentum, the e^- ionize further He atoms and an avalanche effect sets in. A rising slope in the current at the sense wire is detected by the read-out electronics.

The total collected charge in the CDC of associated tracks is related to the energy loss dE/dx of the particle due to ionization. The dE/dx measurement in combination with the particle momentum p measurement is also used for PID.

4.2.3. Time of Propagation Detector

The TOP detector is the main PID system of Belle II in the barrel region. When the velocity of a charged particle traversing a transparent medium exceeds the speed of light in that medium, *Cherenkov* photons are emitted. The characteristic Cherenkov angle θ_c , at which the photons are radiated, depends on the particle's velocity β and is given by

$$\theta_c = \frac{1}{n \cdot \beta}, \quad (4.3)$$

where n is the refractive index of the medium.

The TOP detector consists of 16 transparent quartz bars. When a charged particle passes through a quartz bar, Cherenkov photons are generated and propagate through the bar via total internal reflection at the surfaces. One end of each quartz bar is equipped with a spherical mirror, while the other end is instrumented with a photo-detector. Cherenkov photons emitted toward the mirror are reflected back toward the photo-detector, ensuring efficient photon collection.

Each quartz bar module is 2.6 m long, 45 cm wide, 2 cm thick, and equipped with a 10 cm long extension wedge at one end. That extension wedge serves as a prism and functions like a pinhole camera for improved ring imaging and wavelength discrimination [5]. On the exit window of the wedge, a photo-detector is mounted, consisting of 16 fast multi-anode photon detectors, arranged in two rows. The photon detectors are microchannel plate photomultiplier tubes (MCP PMTs) with a single-photon time resolution of about 100 ps. They detect emitted *Cherenkov radiation*, which is used to distinguish between different particle types, mainly between K^\pm and

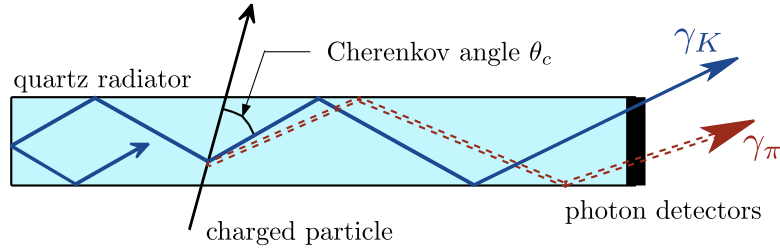


Figure 4.9.: Schematic working principle of a TOP quartz bar. (Figure adapted from [5])

π^\pm (Figure 4.9).

With the knowledge of T_0 and the incident angle of the passing particle, the photon propagation time through the quartz bar and the impact position at the photo-detector are a function of θ_c . In combination with the momentum measurement of the track curvature in the CDC, this enables particle identification.

4.2.4. Aerogel Ring Imaging Cherenkov Detector

The proximity focusing ARICH detector is the main PID system of Belle II in the forward end-cap region to distinguish tracks from K^\pm and π^\pm . As well as the TOP detector, described in Section 4.2.3, the ARICH PID principle is based on Cherenkov radiation. The ARICH information can also be used for general PID for the likelihood calculation of different particle hypotheses. Figure 4.10 shows a schematic of the working principle and the detector disk.

Two stacked disks of 2 cm thick SiO_2 aerogel with different refractive indices for each plane are placed in front of a photon detector disk. Each of the aerogel disk is built from 124 170 mm x 170 mm tiles with a refractive index n of 1.045 (1.055) for the inner (outer) plane. The photon detector disk is equipped with 420 hybrid avalanche photon detector (HAPAD) sensors, arranged in seven concentric rings with radii from 56 cm to 114 cm. Each HAPAD sensor measures 73 mm x 73 mm and has 144 channels (12×12).

The two stacked aerogel disks increase the number of Cherenkov photons, and ensure a good Cherenkov angle resolution. The distance between the aerogel disks and the photon detector disk, as well as the arrangement of the refractive indices, are chosen so that the emitted Cherenkov photons focus on the photon detectors, as illustrated in figure 4.10a.

For Bhabha electrons in the 6 - 8 GeV regime, an average angular resolution of 14 mrad was measured with an average yield of 10 photons [48].

In combination with the dE/dx measurement of the CDC, TOP and ARICH can be used for PID in a general manner, assigning likelihoods to particle hypotheses.

4.2.5. Electromagnetic Calorimeter

The ECL is utilized to measure the energy of γ and e^- in a range of 20 MeV and 4 GeV. Especially for the reconstruction of π^0 decaying into two γ , the ECL is essential for the γ detection and energy measurement. It consists of 6624 CsI(Tl) scintillation crystals pointing in direction to the IP³. Each crystal has the shape of a truncated pyramid with an average size

³The crystals are deliberately oriented slightly away from the IP to minimize efficiency losses caused by photons escaping through the tiny gaps between the crystals.

4. The Belle II Experiment

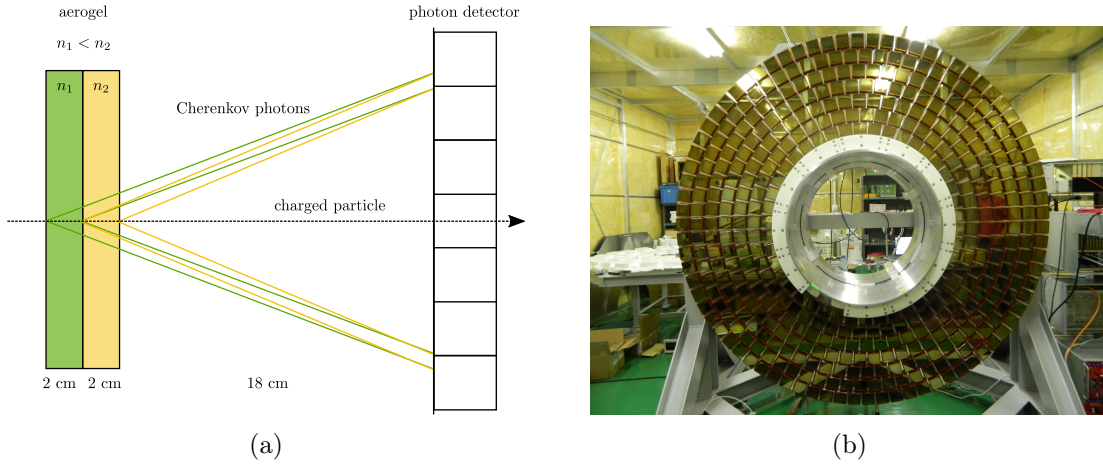


Figure 4.10.: (a) Schematic working principle of the proximity focusing ARICH (Figure adapted from [5]). (b) HAPAD photon detector disk (Figure taken from [39]).

of 6 cm x 6 cm x 30 cm. The radiation length amounts to $X_0 = 16.1$ along the long crystal edge. Figure 4.11 shows a schematic cross-section of the crystal arrangement in the barrel and end-cap regions.

The ECL can detect e^\pm , hadrons (h) or, γ due to their interactions with the crystal nuclei, which generate electromagnetic (EM) and/or hadronic showers. Within an EM shower, more and more photons are created until the lower energy threshold is reached. The number of created photons is proportional to the energy of the initial particle. Photodiodes are mounted on the end of the crystals to detect the created photon showers.

In addition to the energy, the angular coordinates can be determined. Furthermore, the ECL signals enter the L1 global decision logic (GDL) for triggering.

4.2.6. K-Long and Muon Detector

The KLM is the outermost subsystem of the Belle II detector [5]. Its purpose is to detect muons, as well as long-lived neutral K_L^0 mesons. Muons are *minimum ionizing particles (MIPs)* at the momentum range of $\mathcal{O}(\text{MeV} - \text{GeV})$ and can therefore traverse all sub-detectors. An interaction length of $3.9 \lambda_0$ for K_L^0 lead to hadronic showers while μ will only lose some energy by ionization. K_L^0 do not leave any signal in the CDC but create isolated clusters in the KLM.

The KLM consists of 14 layers of fast plastic scintillator strips in the end-caps (Figure 4.12a). In the barrel region, the first two layers are also made of fast plastic scintillator strips, while the outer 13 layers are composed of *resistive plate chambers (RPCs)* (Figure 4.12b). Fast plastic scintillator strips offer better efficiency in high-background environments due to the absence of dead time, which affects RPCs. The higher background originates primarily from neutrons, e.g. created in showers caused by e^+e^- from radiative Bhabha scattering. Between the active detector layers, passive 4.7 cm thick iron layers are installed, serving as a return yoke for the 1.5 T magnetic field generated by the superconducting solenoid. They provide $\geq 3.9 X_0$ of material (on top of $0.8 X_0$ from the ECL) to initiate the particle showers for the K_L^0 .

The KLM RPCs consist of two layers of resistive-glass electrodes separated by a gap filled with a gas mixture. High voltage is applied to the electrodes to create an electric field of up to

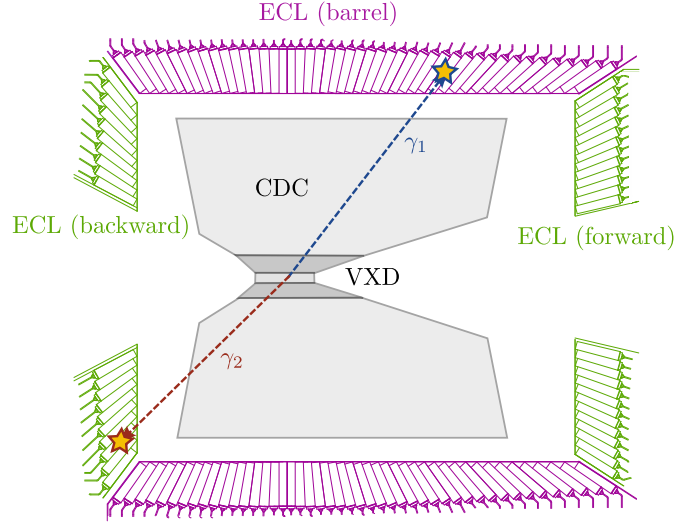
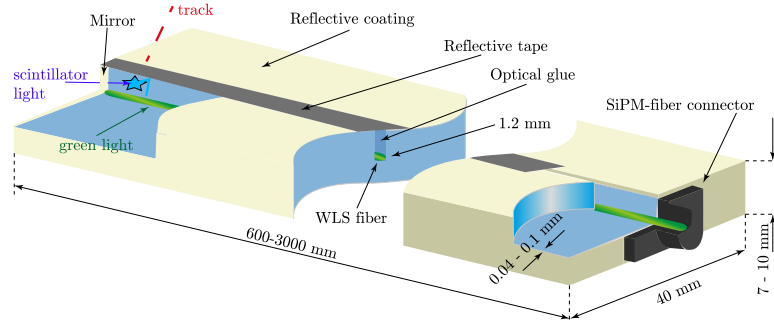


Figure 4.11.: Schematic cross-section through the ECL crystals and photo diodes. (Figure adapted from [5])


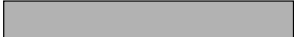











4.3 kV mm^{-1} . A traversing charged particle ionizes the gas between the electrodes. Due to the high electric field, additional photons are emitted, further ionizing gas molecules and initiating an avalanche that creates a discharge (streamer). This leads to a temporary breakdown of the electric field. Until the electric field is restored, the efficiency of the RPC is significantly reduced. The discharge pulse induces mirror charges in 5 cm conducting pickup strips, which are isolated from the outer ground plates by dielectric foam. The schematic layout of the RPC is illustrated in figure 4.12b.

When high energetic particles traverse the plastic scintillator strips, scintillation light is generated. The scintillation light is caught by wavelength shifting (WLS) fiber and transported to silicon photodiodes. A schematic illustration of a scintillator strip is shown in figure 4.12a.

4. The Belle II Experiment



(a)

Ground plane		0.25 mm Mylar 0.035 mm Copper
Dielectric foam		7 mm
Cathode plane		0.035 mm Copper 0.25 mm Mylar
+HV		3.00 mm
Gas gap		2.00 mm
-HV		3.00 mm
Insulator		0.5 mm Mylar
+HV		3.00 mm
Gas gap		2.00 mm
-HV		3.00 mm
Cathode plane		0.25 mm Mylar 0.035 mm Copper
Dielectric foam		7 mm
Ground plane		0.035 mm Copper 0.25 mm Mylar
		31.6 mm total

(b)

Figure 4.12.: (a) Schematic illustration of the fast plastic scintillator strips [49] (b) Schematic structure of an RPC module [5]

4.3. Trigger

As shown in Figure 4.1, only a small fraction of processes is of interest. The purpose of trigger system is to reduce the data which is recorded to a reasonable level. The Belle II subsystem signals are processed in the *Level 1 (L1) hardware trigger* utilizing field-programmable gate arrays (FPGAs). The detector readout (all subsystems except PXD) is triggered by the L1, when relevant signatures in the sub-detector systems (mainly CDC and ECL) are found. A set of *trigger bits* is defined, each with specific conditions tuned to detect specific event signatures. When a dedicated signature is detected, the respective trigger bit is set (enabled).

A second stage *software trigger* based on a CPU farm, the *high level trigger (HLT)*, is used to reconstruct events on online analysis level [5][50]. The HLT uses the information from all subsystems whose readout was triggered by the L1. ROIs are defined for the subsequent PXD readout when the decision is made to keep the event. The PXD information is incorporated into the event data and finally stored.

The maximum output rate of the L1 trigger is 30 kHz while the HLT has a lower maximum output rate of 10 kHz. The trigger system is optimized on $B\bar{B}$ signatures and low multiplicity events, such as those with a small number of tracks, like $\tau^+\tau^-$ events.

4.4. Belle II Analysis Software Framework

The *Belle II Analysis Software Framework* (*basf2*) [51][52] is an open source software project developed by the Belle II collaboration to reconstruct collision data, simulate collisions, perform analyses, and many other tasks around the physical interpretation of Belle II data.

One major task is the reconstruction of physics objects from the detector signals. The following subsections briefly describe the reconstruction of particles relevant for this work.

4.4.1. Charged Particles

Charged particles generate specific electrical signals (hits) in the CDC and in the VXD. This information allows the reconstruction of charged particle trajectories [53]. A reconstructed trajectory, called *track*, is described by a helix defined by five parameters:

- d_0 : the distance of the point of closest approach (POCA) to the z axis in the $r\phi$ -plane,
- ϕ_0 : the angle between the transverse momentum and the x axis at the POCA in the $r\phi$ -plane,
- ω : the track curvature, signed according to the particle charge,
- z_0 : the z coordinate at d_0 ,
- $\tan \lambda$: the tangent of the track dip angle in the rz -plane.

These five helix parameters are illustrated in Figure 4.13.

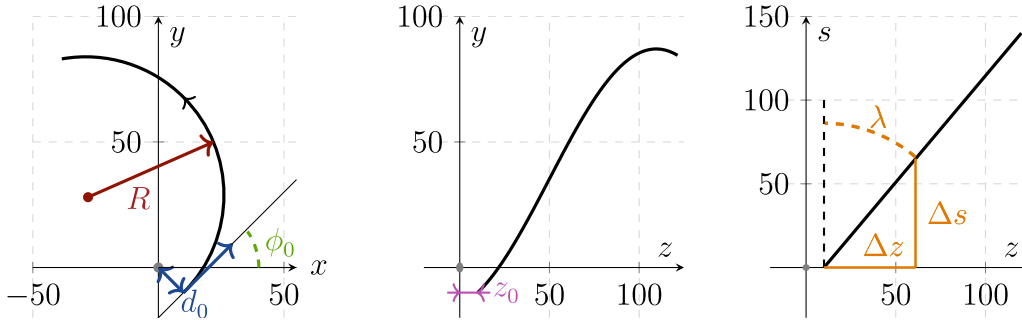


Figure 4.13.: Definition of the five track helix parameters. (Figure adapted from [53])

In *basf2*, track reconstruction is performed using three hypotheses – π , K , and p – to calculate mass-dependent energy loss and material effects.

4.4.2. Neutral Particles

Photons are identified by their EM showers in the ECL crystals, while not creating a track. The deposited energy and the time of energy deposition are measured. Showers created by a single particle, which extend over several neighboring crystals, are combined into clusters. Photons are identified by the round cluster shape and the exponential decay of the energy deposit from the cluster center (photon incident axis) outward.

π^0 are not measured directly but are reconstructed from their decay into two photons (see Section 6.4.2).

4.4.3. Neutrinos

In Belle II, neutrinos are invisible and cannot be directly detected by the detector. However, they can be indirectly observed in reconstructed events by identifying missing quantities—such as *missing energy*, *missing mass*, and *missing momentum*—when applying energy and momentum conservation.

4.4.4. Tree Fitter

The τ_{3p} decay vertex is determined using the `basf2` built-in module `TreeFitter`, which employs an *Extended Kalman Filter (EKF)* algorithm [54][55]. This method iteratively optimizes the particle properties of the state vector \mathbf{x} , considering constraints and uncertainties, to locate the most likely vertex position. The EKF provides a computationally efficient alternative to traditional least-squares fitting methods, such as the Newton-Raphson approach [56]. Here, only a brief overview is provided, focusing on aspects relevant to this analysis.

The relevant constraints for the τ -lepton decay vertex fit are:

- **Reconstructed track:** Defined for each of the three π^\pm tracks (see Section 6.2.1) by its five track helix parameters (see Section 4.4.1).
- **Kinematic constraint:** Enforces conservation of four-momentum between the π^\pm and the reconstructed τ -lepton (neutrinos are not considered).

The χ^2 value at each filter iteration step α is defined as the sum of the χ^2 values of each constraint k :

$$\chi_\alpha^2 = \sum_k \chi_k^2, \quad (4.4)$$

with

$$\chi_k^2 = (\mathbf{x}_k - \mathbf{x}_{k-1})^T \mathbf{C}_{k-1}^{-1} (\mathbf{x}_k - \mathbf{x}_{k-1}) + (\mathbf{m}_k - \mathbf{h}_k(\mathbf{x}_k))^T \mathbf{W}_k^{-1} (\mathbf{m}_k - \mathbf{h}_k(\mathbf{x}_k)). \quad (4.5)$$

Here, \mathbf{x} denotes the state vector of the particles, which is optimized during the fitting process. The state vector has the general form $\mathbf{x} = \{\mathbf{V}_1, d_1, \mathbf{p}_1, E_1, \dots, \mathbf{V}_n, d_n, \mathbf{p}_n, E_n\}$, where \mathbf{V}_i represents the 3D decay vertex, d_i the decay length, \mathbf{p}_i the momentum, and E_i the energy, for the i -th of n particles. The vector \mathbf{m} contains the measured parameters of the π^\pm tracks, and \mathbf{W} is the covariance matrix of the measurements. The hypothesis vector is represented by \mathbf{h} , with its associated covariance matrix \mathbf{C} .

The state vector is updated iteratively for each k , incorporating the state from the previous constraint $k - 1$. This process is repeated at each step α until convergence or divergence is observed. Minimizing Equation (4.5) results in:

$$\mathbf{x}_k^\alpha = \mathbf{x}_{k-1}^\alpha - \mathbf{K}_k^\alpha \mathbf{r}_k^\alpha, \quad (4.6)$$

where \mathbf{K}_k is the gain matrix to project the residuals \mathbf{r}_k on a correction of the state. The residuals are defined as $\mathbf{r}_k^\alpha = \mathbf{m}_k - \mathbf{h}_k(\mathbf{x}_{k-1}^\alpha)$, which represents the difference between the measurement and the hypothesis. The hypothesis for each constraint depends on the state of the previous constraint. The gain matrix incorporates the linearized hypothesis around a reference state from

4. The Belle II Experiment

the previous filter step $\alpha - 1$, the covariance matrix of the previous constraint $k - 1$, and the measurement covariance matrix of the current constraint k , serving as a weight. The updated hypothesis covariance matrix \mathbf{C}_k is obtained by propagating uncertainties.

The vertex fit is successful if it converges, meaning the change in χ^2 between two iteration steps is less than 2 %, and the p -value (χ^2_{prob}) is less than 0.1 %. After the vertex fit, the particle objects are updated with the parameter values derived from the final state vector. The updated momentum still contains the momentum corrections (see Section 6.4.1). However, the energy loss corrections are not further applied, since this is not yet implemented in **basf2**.

4.5. Data Production

The experimental dataset used in this work (see Section 6.1.3) was collected with the Belle II detector during Run 1. The experimental data is recorded in units called *runs* (not to be confused with, e.g., Run 1). A new run begins whenever data-taking is resumed after an interruption. The data from multiple runs over several consecutive days of stable operation is combined into a *bucket*, each with a size of 9 fb^{-1} .

The bucket data undergoes a so-called *prompt calibration* where calibration constants, such as alignment (see Section 6.5.5), are estimated before the offline Belle II data reconstruction can be started. The data taking period comprising several buckets on a larger timescale ($\mathcal{O}(\text{months})$) is called an “experiment (exp.)”. In *official major data processing campaigns (procs)* the data of several experiments is combined in so-called *chunks* which are then reprocessed with the latest **basf2** release.

5. The Pixel Vertex Detector

The PXD is the innermost detector, mounted on the BP, near the IP. Its primary purpose is to allow high-precision measurements of decay vertices for particles that decay within the BP, such as the τ -lepton.

The full detector consists of 40 *modules* arranged into 20 *ladders*. The ladders are organized in two cylindrical layers, forming a windmill-like structure parallel to the BP along the z -axis around the IP. The complete PXD setup is shown in Figure 5.1.

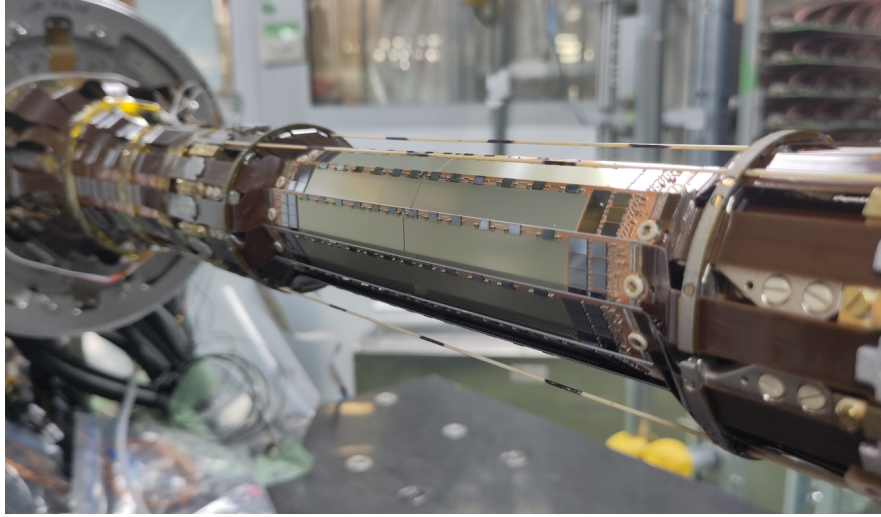


Figure 5.1.: Picture of the complete PXD setup (PXD2) mounted on the beam pipe.

This chapter provides a description of the PXD's working principle and mechanical structure. It first explains the working principle of the pixel cells, followed by the mechanical structure and the readout system, and closes with the comparison of the incomplete with the complete setup.

5.1. DEPFET Pixels

The PXD is based on the *DEpleted P-channel Field Effect Transistor (DEPFET)* technology. This technology originated in 1986 from studies of silicon (Si) drift chambers [57]. The fundamental concept was to modulate the current of a FET using charge carriers trapped in a potential minimum (for e^- a potential maximum) within a fully depleted Si-bulk (see Section 2.4).

5.1.1. DEPFET Working Principle

The PXD sensors are segmented into pixel cells, each constructed from p-type MOSFETs (referred to as FETs) implanted atop a fully depleted, lightly doped n^- -type Si bulk¹. The backside of the bulk features a highly doped p^+ contact. Less than $1\text{ }\mu\text{m}$ beneath the FET's oxide layer, an additional n doped region, known as the *internal gate*, is implanted, as shown in Figure 5.2. This internal gate creates a potential maximum within the bulk, attracting the e^- generated by traversing ionizing particles, while the h^+ drift toward the p^+ backside and are removed. The e^- can be removed from the internal gate via an n^+ -doped clear implant.

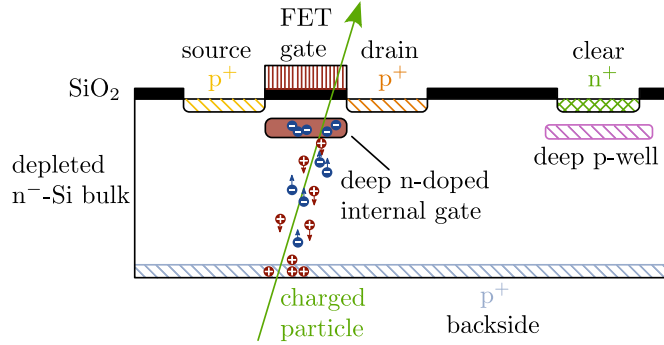


Figure 5.2.: Simplified projected cross-section of a DEPFET pixel cell illustrating the e^-h^+ pair creations by an ionizing charged particle. In real, the source, drain, and clear are not inline. The e^- drift into the internal gate, the h^+ drift toward the back plane. (Figure adapted from [59])

Charges accumulated in the internal gate modulate the drain current by inducing mirror charges in the conductive p-channel. This modulation is equivalent to altering V_g by ΔV_g [16]:

$$\Delta V_g = \frac{\alpha q_{\text{sig}}}{C_g} = \frac{\alpha q_{\text{sig}}}{WLC_{\text{ox}}}, \quad (5.1)$$

where α is the fraction of charges in the internal gate, q_{sig} , that induce mirror charges in the p-channel. Here, C_g denotes the oxide capacitance, W and L are the width and length of the channel, respectively, μ_h is the hole mobility, C_{ox} is the capacitance per unit area of the oxide layer, and V_{th} is the threshold voltage required to form the conductive channel. The modulated drain current is expressed as [16]:

$$I_d + \Delta I_d = \frac{W}{2L} \mu_h C_{\text{ox}} \left(V_g + \frac{\alpha q_{\text{sig}}}{WLC_{\text{ox}}} - V_{\text{th}} \right)^2 \quad (5.2)$$

$$= \frac{W}{2L} \mu_h C_{\text{ox}} \left((V_g - V_{\text{th}})^2 + \frac{2\alpha q_{\text{sig}}}{WLC_{\text{ox}}} (V_g - V_{\text{th}}) + \mathcal{O}(q_{\text{sig}}^2) \right), \quad (5.3)$$

where the higher-order term $\mathcal{O}(q_{\text{sig}}^2)$ is negligible. The gain factor g_q per accumulated charge

¹In the DEPFET context, doping levels are as follows: “-”: 10^{13} cm^{-3} (weakly doped, fully depletable); no sign: 10^{16} cm^{-3} (moderately doped, fully depletable); “+”: 10^{19} cm^{-3} (highly doped, not fully depletable) [58].

on the drain current is [16][60]:

$$g_q = \frac{d(I_d + \Delta I_d)}{dq_{\text{sig}}} = \alpha \mu_h \frac{W}{L} (V_g - V_{\text{th}}) = \alpha \sqrt{\frac{2\mu_h I_d}{WL^3 C_{\text{ox}}}} \quad (5.4)$$

$$\approx 80 \text{ pA/e to } 1700 \text{ pA/e.} \quad (5.5)$$

The Belle II PXD DEPFET pixel cells have a g_q of approximately 500 pA/e.

The amplification of the modulated drain current is proportional to the energy deposited by the traversing particle. The charges in the internal gate persist, enabling the drain current to be read out non-destructively at any time. After the readout, the charges in the internal gate must be cleared to allow detection of subsequent particles.

For charge clearance, the n^+ *clear* implant is placed adjacent to the internal gate (Figure 5.3a). A polysilicon cleargate layer is placed atop the oxide layer between the clear implant and the internal gate. The cleargate and the clear implant are capacitively coupled, as shown in Figure 5.3b. The cleargate is connected to a constant voltage supply through a high resistor. Thus, switching the clear contact switches also the cleargate.

In *clear-off* mode, the clear contact is held at a lower potential, $V_{\text{clear-off}}$, than the internal gate. This creates a potential barrier in the bulk under the cleargate, preventing e^- from escaping the internal gate. A deep p-well beneath the clear implant shields the Si bulk during the clear-off phase, ensuring charge collection is unaffected by the clear mechanism.

Switching to *clear-on* mode by applying a high positive voltage to the clear contact removes the potential barrier, allowing e^- to drain into the clear implant. This mode removes all signal charges and thermally generated charges from the internal gate, preventing any reset noise.

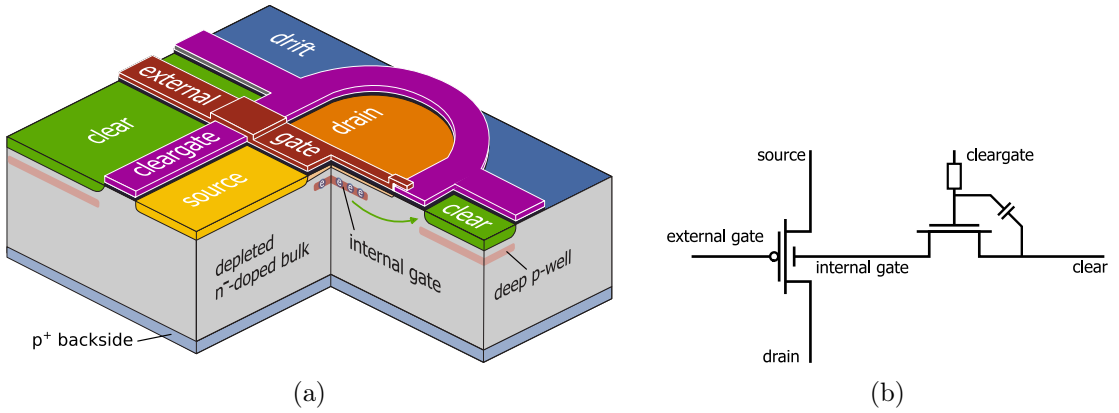


Figure 5.3.: (a) 3D representation and cross-section of a DEPFET pixel cell (adapted from [61]).
(b) Circuit diagram of the DEPFET pixel, illustrating drain current modulation and the clear mechanism (Figure from [61]).

5.1.2. DEPFET Sensor Matrix

The DEPFET sensor matrix used for the PXD modules consists of 192k pixels arranged geometrically in 250 columns and 768 rows, forming a spatially segmented sensitive area. Each

5. The Pixel Vertex Detector

pixel comprises a DEPFET cell, as described in Section 5.1.1. The pixel sizes vary depending on their position within the sensor and the specific sensor type (see Section 5.2.1).

The pixels are organized in a double-row structure as illustrated in Figure 5.4. In this configuration, the pixels in the first row share a common source and clear implant with the pixels in the second row. Furthermore, two adjacent pixel columns also share a common clear implant.

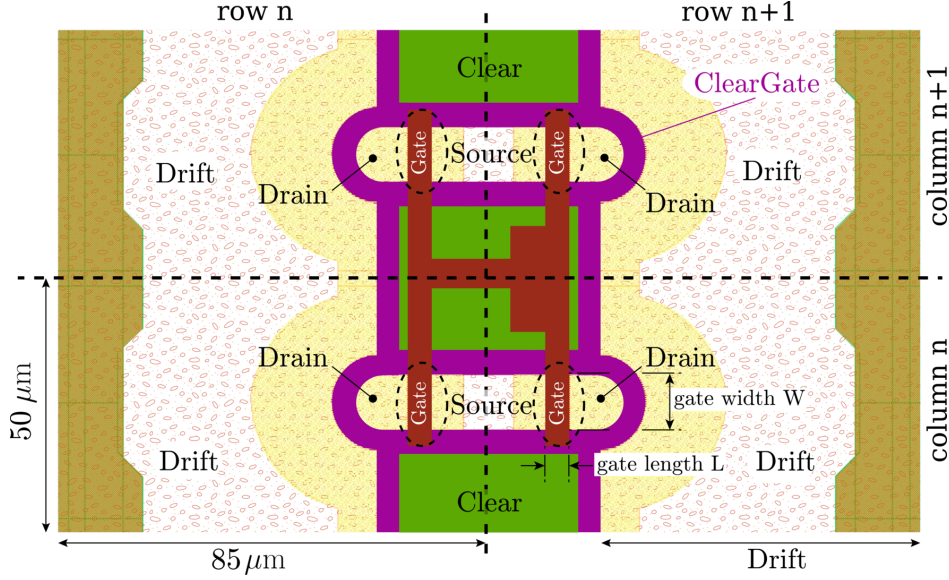


Figure 5.4.: Illustration of a 2x2 pixel array in the PXD DEPFET sensor matrix: Left to right represents the pixel rows, while top to bottom corresponds to the pixel columns. Pixels are visually separated by black dotted lines. *Purple*: polysilicon 1; *red*: polysilicon 2; *green*: n^+ implant; *light yellow*: n implant for additional space charges for drift and the internal gate, separated by polysilicon 2; *black ellipse*: location of the internal gate beneath the FET gate. The absence of a p^+ layer below the FET gate (only a shallow p implant to reduce V_{th} is present) in combination with the deep n implant forms the potential maximum. *Red pattern*: p^+ implant; *orange/brown*: additional deeper p drift implant to create a small negative potential. (Figure adapted from [62])

The whole pixel cell (excluding the FET structures) is provided with a full-surface, $0.4\mu\text{m}$ deep p^+ -implanted *drift* structure. This implant depletes the bulk of the sensor from the front-side surface and forms a negative potential surface, creating a potential maximum in the depth below the surface. Additionally, the double rows are separated by $\sim 1\mu\text{m}$ deep, p -implanted drift structures. These drift implants are connected to a voltage supply (V_{drift}) at the end of each row. By applying a negative voltage² to V_{drift} , a potential gradient is established, becoming more positive toward the internal gate. This gradient enables faster lateral drift of the e^- into the internal gate. Figure 5.5 illustrates the e^- drift trajectories within the potential landscape of a pixel cell, while Figure 5.6 only shows the e^- drift trajectories.

The vertical drift field through the bulk is mainly generated by applying a high negative voltage, V_{HV} , to the backside of the bulk, while maintaining the bulk at a positive voltage. This

²Relative to the source voltage.

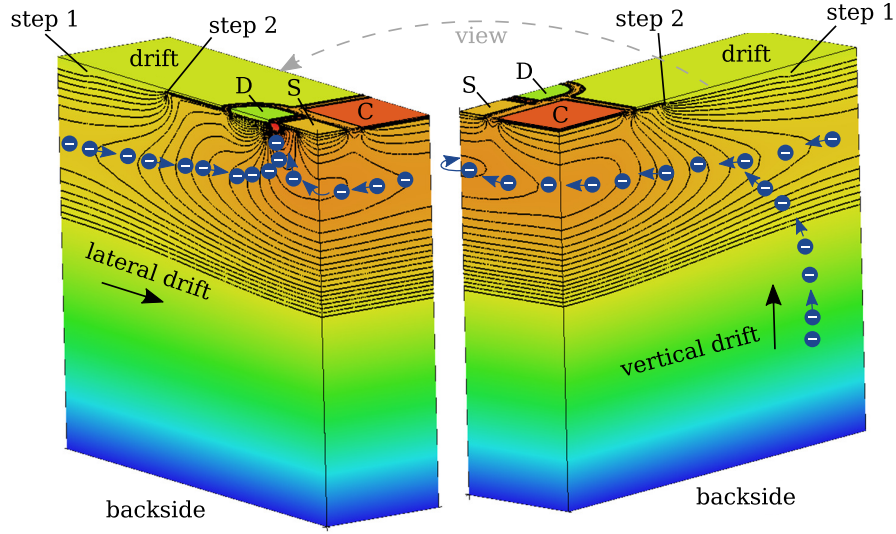


Figure 5.5.: Cross-section of a pixel cell with a cut through the FET structure, illustrating the vertical and lateral drift paths of the e^- during charge collection mode. The deep p-drift implant creates a small potential step (step 1), while the additional n-doped space charge implant generates a stronger potential step (step 2) in the potential landscape. e^- drifting beneath the drain implant (D) move directly into the internal gate, whereas e^- beneath the clear structure (C) follow a curved trajectory under the source implant (S) before entering the internal gate. The right cross-section shows the backside of the left cross-section. The small vertical cross-sections in both figures represent the same cross-section. (Figure adapted from [62])

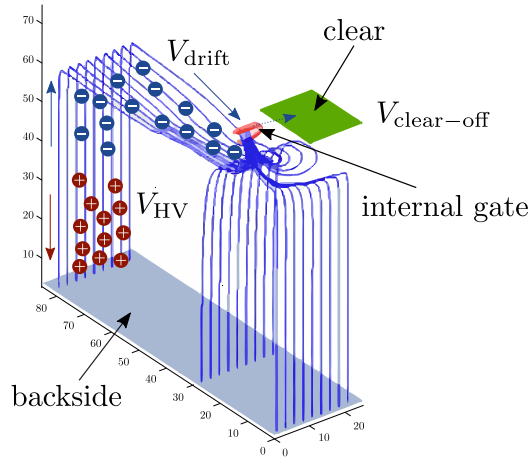


Figure 5.6.: Drift trajectories of e^- in a fully depleted pixel cell operated in clear-off mode: The e^- drift toward the internal gate (potential maximum). The vertical drift field is determined by the backside voltage V_{HV} , while the lateral drift field is created by the voltage V_{drift} applied to the drift implants. Dimensions are in μm . (Figure adapted from [62])

5. The Pixel Vertex Detector

configuration also depletes the bulk (sensor).

To apply the voltage to the backside, the so-called *punch-through* mechanism is employed, as shown in Figure 5.7. A p^+ implant on the front side of the sensor connects to the bias electrode of the voltage supply V_{HV} . This method eliminates the need for an additional contact on the p^+ backside.

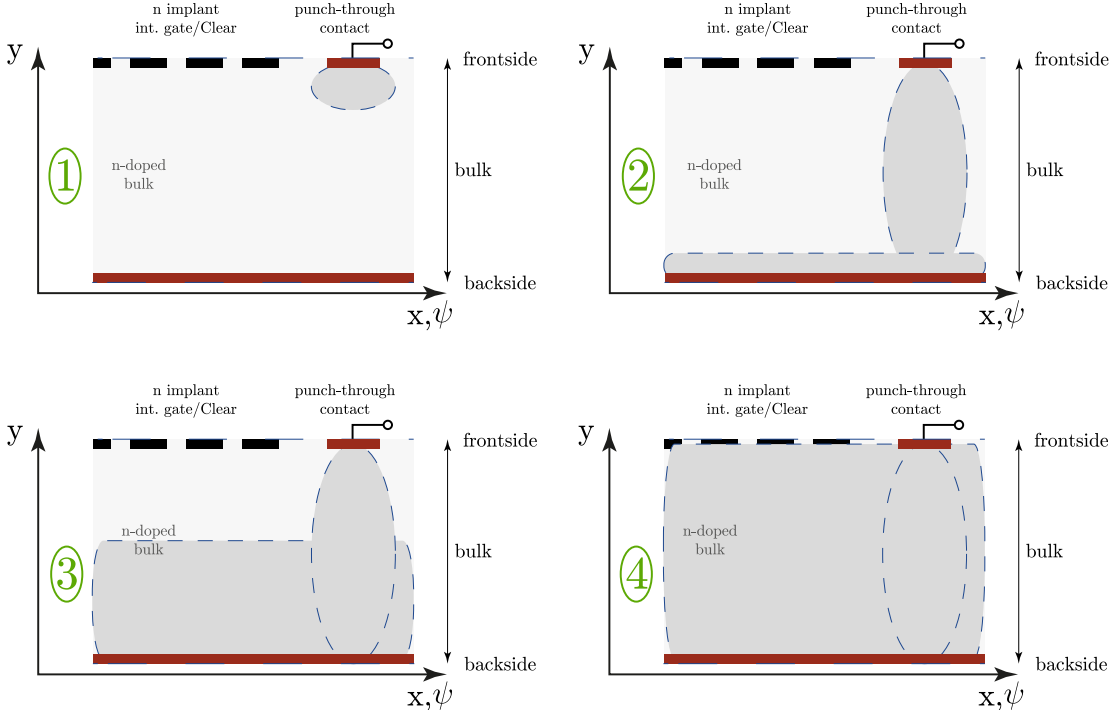


Figure 5.7.: Four phases of punch-through for bulk depletion. *Phase 1:* Applying a negative voltage (V_{HV}) starts to deplete the area underneath the implant. *Phase 2:* For Si with a thickness of $75\ \mu\text{m}$, the depletion zone reaches the backside at $V_{HV} \sim -35\ \text{V}$. *Phase 3:* Further decreasing V_{HV} initiates bulk depletion. *Phase 4:* The bulk is fully depleted at $V_{HV} \sim -70\ \text{V}$. (Adapted from [62])

If V_{HV} is not negative enough (*under-depletion*), the bulk is not fully depleted and the created e^-h^+ are not fully separated. As a result, not all e^- are drifted towards the internal gate. If V_{HV} is reduced further than necessary to reach full depletion, the potential maximum for the e^- within the bulk begins to shift toward the FET structure. In both cases, the charge collection efficiency is decreased.

To prevent e^- from outside the sensor matrix from entering the sensitive bulk volume, an n^+ guard ring surrounding the DEPFET matrix is implemented and biased with a negative potential, V_{guard} .

A DEPFET pixel cell requires 11 different voltages for operation, many of which exhibit complex interdependencies. However, only three voltages dominate charge collection in the internal gate: V_{HV} , V_{drift} , and $V_{\text{clear-off}}$ (which is applied almost continuously during charge collection). Typical voltage values are provided in Table 5.1. These dominant voltages must be fine-tuned for each sensor.

Voltage	Value [V]	Comment
V_{HV}	-60	Depletion high-voltage (punch-through)
V_{bulk}	10	N-doped depletion contact
V_{source}	6	DEPFET source potential
V_{drain}	1	DEPFET drain potential
$V_{\text{gate-on}}$	-2	DEPFET gate potential during charge sampling
$V_{\text{gate-off}}$	5	DEPFET gate potential during charge collection
$V_{\text{clear-on}}$	19	Clear pulse potential for charge removal
$V_{\text{clear-off}}$	5	Shielded clear contact
$V_{\text{cleargate}}$	0	Clear FET gate potential
V_{drift}	-5	Supporting drift field
V_{guard}	-5	Guard ring

Table 5.1.: Typical values for the DEPFET operation voltages. (Table from [63])

The operational sequence of the DEPFET matrix is divided into three steps:

1. **Charge collection:** $V_{\text{gate-off}}$ and $V_{\text{clear-off}}$ are applied to the external gates and clear contacts. Generated h^+ drift to the backside, while e^- drift to the internal gate.
2. **Signal readout:** $V_{\text{gate-on}}$ is applied to the external gate, while $V_{\text{clear-off}}$ remains applied to the clear contact. The FET channel becomes conductive, and I_d is sampled (see Section 5.2.2).
3. **Signal clearing:** $V_{\text{clear-on}}$ is applied to the clear contact, while $V_{\text{gate-on}}$ remains applied to the external gate. The e^- in the internal gate are removed.

Due to their low input capacitance and intrinsic charge-to-current amplification, DEPFET sensors operate with low noise. This enables the construction of thin detectors with minimal material budget. Furthermore, DEPFET cells can be read out at any time, allowing for switchable readout sequences. This flexibility reduces power consumption, which is advantageous for simplifying cooling designs and further lowering the material budget.

5.2. PXD Module

The PXD consists of individual modules. Each module is its own entity and operates independently of the others. The PXD modules were designed at the *MPG Semiconductor Lab (HLL)* in Munich and the *University of Heidelberg* and were produced at HLL.

5.2.1. Structure

A PXD module comprises an almost entirely silicon monolithic die with an active area integrating the DEPFET sensor matrix, as illustrated in Figure 5.8. The module includes a thin metal layer that connects the DEPFET sensor matrix to surface-mounted devices (SMDs) and application-specific integrated circuits (ASICs). Structurally, the module consists of a sensor wafer containing the DEPFET matrix and a handle wafer serving as a support structure, bonded to the bottom of the sensor wafer.

In the sensitive DEPFET area, the module is thinned down to $75\,\mu\text{m}$. The remainder of the module forms a $\sim 500\,\mu\text{m}$ -thick Si support frame surrounding the sensitive DEPFET area. This design results in a low average material budget of only $\sim 0.21\,\% X_0$ per module within the Belle II physics acceptance region.

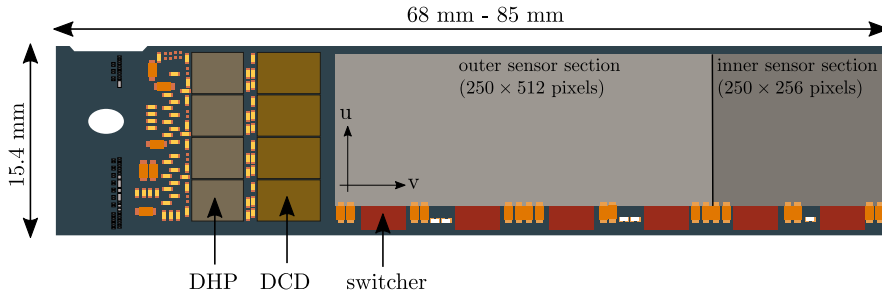


Figure 5.8.: Schematic illustration of a single PXD module (top view). The sensor region (gray area) is thinned down to $75\,\mu\text{m}$ from the backside.

Along the long edge of the DEPFET sensor matrix, the support frame features a 2.3 mm-wide balcony that accommodates six *switcher* ASICs and several SMD capacitors. On the opposite edge, the frame is narrower, measuring only 0.6 mm in width. The $\sim 23\,\text{mm}$ -long *end of stave (EOS)* region of the support frame provides space for four *drain current digitizer (DCD)* ASICs and four *data handling processor (DHP)* ASICs arranged parallel to one another. These ASICs handle sensor configuration, digitization, and data processing (see Section 5.2.2). Since the EOS region contains a significantly higher material budget, it is located outside the Belle II physics acceptance region. The DEPFET sensor matrix is divided into four column segments, each read out by a pair of DCD and DHP ASICs.

At the very end of the EOS, a Kapton³ cable is soldered to the module. Electrical contacts on the Kapton cable enable power supply and data transfer, connecting to the module's circuits via wire bonds.

Four module flavors are used in the PXD based on their position: *inner-forward (IF)*, *inner-*

³Kapton is a polyimide film used in flexible printed circuits. It is a registered trademark of DuPont de Nemours, Inc.

Property	Inner layer	Outer layer
pixel size (inner section) in μm^2	50×55	50×70
pixel size (outer section) in μm^2	50×60	50×85
active sensor length (inner section) in mm	14.08	17.92
active sensor length (outer section) in mm	30.72	43.52
active sensor thickness in μm		75
active sensor width in mm		12.5
Si support frame thickness μm		525 or 450
module length in mm	67.575	84.575

Table 5.2.: Dimensions of PXD modules.

backward (IB), *outer-forward (OF)*, and *outer-backward (OB)*. The modules differ slightly in dimensions depending on whether they are positioned in the inner or outer layer, resulting in different pixel sizes. The azimuthal (column) pixel size is consistently $50\mu\text{m}$, while the longitudinal (row) pixel size varies between $55\mu\text{m}$ (inner section with 256 rows) and $85\mu\text{m}$ (outer section with 512 rows), as shown in Figure 5.8. The smaller pixel sizes are beneficial for higher resolution near the IP, covering a large solid angle. Table 5.2 summarizes the basic dimensions of the inner and outer module flavors. Forward and backward modules differ only in their mirrored geometry.

In the module production process, each Si wafer is fabricated with six modules of all flavors (1 IF, 1 IB, 2 OF, and 2 OB). Each wafer has a unique wafer number, thus the modules are named *WXX-IF*, *WXX-OB1*, ..., where *XX* is the two digit wafer number.

5.2.2. Readout

The DEPFET matrix is read out in *rolling shutter* mode, which sequentially switches groups of pixel rows. Four pixel rows are always sampled and then cleared simultaneously. These four pixel rows together form one *electrical row*. All gate and clear contacts within an electrical row are connected, as shown in Figure 5.9. Dedicated switcher ASIC output channels control each gate and clear line of every electrical row.⁴

Since the drain currents are only switched on with $V_{\text{gate-on}}$ when the corresponding electrical row is selected, each pixel column in the DEPFET sensor matrix requires only four drain lines. The drain currents of 250 pixels are simultaneously converted into digital units within a single DCD. As a result, four DCDs are needed to process one electrical row (1000 drain lines).

As each electrical row is read out, the next one is selected sequentially, continuing the process until all 192 electrical rows have been sampled. The cycle then repeats from the beginning.

With the current PXD settings, reading out and clearing one electrical row takes approximately 100 ns [64]. Consequently, the total readout time for the entire matrix is about 20 μs , which corresponds to two full bunch revolutions in the SuperKEKB accelerator rings.

The DCDs convert the drain currents into 256 analog-to-digital units (ADUs). The magnitude of the drain currents is typically on the order of $100\mu\text{A}$. These digitized values are then sent to the DHPs. To reduce the data rate, only pixels that exceed a certain threshold relative to their

⁴Each switcher ASIC has 32 output channels and can therefore control 32 electrical rows.

5. The Pixel Vertex Detector

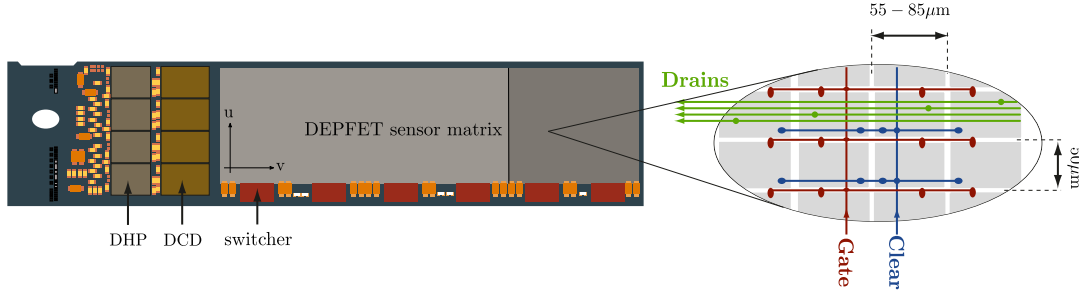


Figure 5.9.: Gate, clear and drain connection lines of an electrical row. The gate and clear lines are connected to the switcher ASICs, the drain lines are connected to the DCDs. (Figure adapted from [62])

pedestal currents are transmitted to the DAQ system (*zero suppression*).

The average pedestal current of each pixel is determined through dedicated pedestal calibration measurements, and the pedestal values are stored in an internal DHP memory. During each readout cycle, the pre-recorded pedestal currents are subtracted from the received drain currents in the DHP. Additionally, the pedestal-subtracted signals must surpass a defined threshold to further suppress noise (referred to as *signal hit*). The signal hits are formatted and transmitted to the FPGA-based *data handling hub (DHH)* [65][66] upon receiving a Level 1 trigger signal. If no trigger signal is received, the data is discarded after a certain period.

Each DHH unit is connected to five PXD modules. From the DHH, the data is forwarded to the *online selector node (ONSEN)* [67] and/or the local PXD *data acquisition (DAQ)* system. Each DHH unit has a dedicated ONSEN node where the data is buffered. If an event, defined by the level 1 trigger, passes also the HLT selection after online reconstruction, the HLT requests the corresponding PXD data to be stored alongside the event data in the central storage system. If the HLT discards an event, its PXD data is removed from ONSEN memory.

Due to the high data load of approximately 17 GB s^{-1} [68], the PXD has a dedicated DAQ system separate from the DAQ system of all other Belle II subsystems. The PXD DAQ system is used in laboratory setups, during development and commissioning phases, calibrations (e.g. pedestal measurements), and for independent and parallel monitoring in the setup at KEK.

Each PXD module is powered by a custom-made power supply (PS) [69], which provides 23 distinct voltage channels. To mitigate voltage drops along the cables, 16 of these channels are equipped with remote sensing capabilities.

5.3. PXD Ladder and Half-Shell

Each forward and backward module pair is glued together along the short edge of the support frame opposite the EOS to form a *ladder*. These ladders are mounted at their EOS onto *support and cooling blocks (SCBs)*, as shown in Figure 5.10.

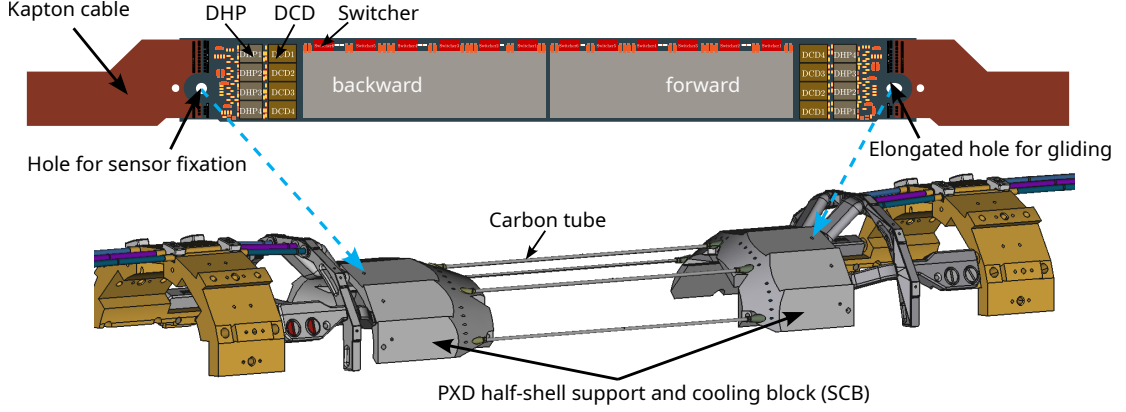


Figure 5.10.: 3D drawing of the PXD half-shell mount and support structure. PXD ladders are mounted onto the SCBs from the outside and from the inside on the SCBs. The SCBs are attached to brass mount blocks fixed to the beam pipe (BP). The elongated hole in the ladder allows mechanical relaxation caused by thermal stress.

Ladders mounted on the *inner layer (L1)* have their topside facing the IP, whereas ladders mounted on the *outer layer (L2)* have their topside facing away from the IP. This design allows L1 and L2 ladders to be mounted on the same SCB from opposite sides without requiring completely different designs. The entire PXD is constructed as two identical *half-shells*, each containing ten ladders. Four L1 ladders are mounted at a radius of 14 mm, while six L2 ladders are mounted at a radius of 22 mm. The half-shells are attached directly to the beam pipe, forming the windmill structure. The ladder arrangement including both half-shells is illustrated in Figure 5.11a.

Property	Inner layer	Outer layer
ladder length in mm	136	170
ladder width in mm	15.4	

Table 5.3.: Dimensions of PXD ladders.

The power consumption of a single module is approximately 9 W, with the majority (~ 8 W) consumed by the DCD and DHP ASICs. The remaining power (1 W) is used by the switcher ASICs and the sensor matrix⁵. For the entire PXD, this results in a total power consumption of 360 W for a fully populated system.

⁵Due to the rolling shutter readout, only the currently selected electrical row contributes to the power consumption of the DEPFET sensor matrix, which is approximately 0.5 W. The rest of the sensor is inactive and doesn't consume any power.

5. The Pixel Vertex Detector

To manage heat dissipation, a two-fold cooling system is employed. Most of the heat generated by the DCD and DHP ASICs is removed via the SCBs using *active cooling*, where two-phase CO₂ circulates through cooling channels at temperatures between -20°C and -30°C . The remaining heat is dissipated through *passive cooling* using cooled N₂ gas streaming out of the SCBs ends and the carbon tubes connecting the SCBs.

5.4. From PXD1 to PXD2: Completion and Advantages

When data collection began in 2019, only a subset of the PXD ladders, necessary to build the full system, had been produced. The first installed system, PXD1, consisted of a complete inner layer. However, to complete the inner layer, one L1 ladder containing a non-functional module had to be installed. To compensate, two already available L2 ladders were mounted to cover the affected region, as shown in Figure 5.11b. With the subsequent upgrade to PXD2, a fully populated PXD system is available. PXD2 was installed into the Belle II detector in summer 2023 and the Run2 operation started in February 2024.

The components required for PXD1 and their adaptations for PXD2 are listed in Table 5.4.

Table 5.4.: Number of sensor-, readout-, and service-components:

Component	PXD1	PXD2
L1 ladders	8	8
L2 ladders	2	12
DHH	4	8
ONSEN	16	32
PXD DAQ	1	1
PS	19	40

The upgrade from PXD1 to PXD2 provides significant advantages, even though the reconstruction of track impact parameters is primarily influenced by the inner layer. Simulations [70] have shown that the inclusion of the second layer in PXD2 leads to substantial improvements in PXD hit efficiency⁶ and purity⁷, especially for low transverse momentum tracks ($<0.6 \text{ GeV } c^{-1}$) under increased background conditions.

For charged particles with transverse momenta of $0.2 \text{ GeV } c^{-1}$ at a background occupancy of 2 %, the expected gains in hit efficiency and purity are approximately 20 %. A higher background occupancy is expected with increasing instantaneous luminosity after LS1. However, the most critical improvement introduced by PXD2 is its redundancy: in the event of damage to specific regions of the L1 sensors⁸, the L2 sensors can compensate.

⁶The fraction of true hits found in reconstructed tracks compared to all simulated true hits from a particle.

⁷The fraction of true hits in reconstructed tracks, estimating how much background was rejected.

⁸In Run 1, several sudden beam loss events in SuperKEKB brought damage to the switcher ASICs causing dead sensor regions.

5. The Pixel Vertex Detector

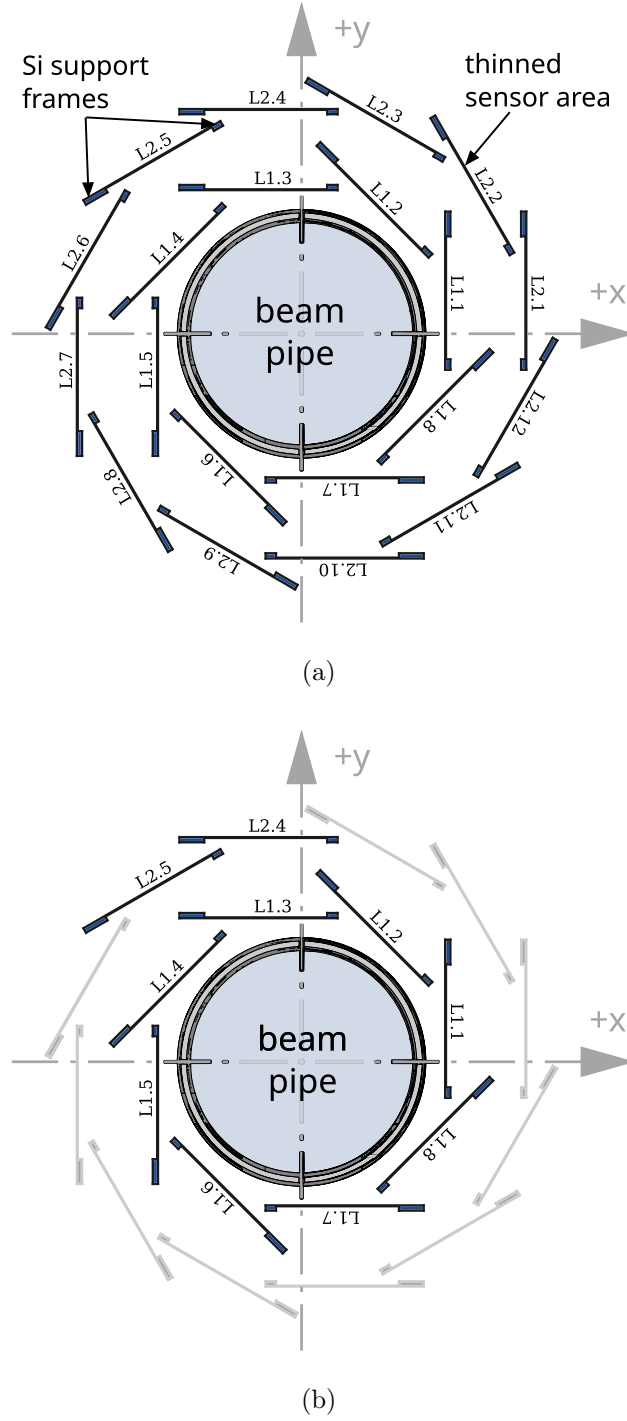


Figure 5.11.: (a) Schematic cross-section of the mounted PXD. The ten ladders above the x -axis belong to the upper half-shell, and the remaining ten belong to the lower half-shell. Inner layer ladders are labeled L1.x, and outer layer ladders are labeled L2.x. (b) Configuration of PXD1. L1.3 contains a non-functional module, with the area covered by two L2 ladders (L2.4 and L2.5).

6. τ -Lepton Lifetime Measurement Using Template Fits

In this chapter, a new method for the τ -lepton lifetime measurement is developed employing a template fit. The measurement method is discussed in detail and an estimation of the expected precision is presented.

6.1. Simulated and Experimental Data Samples

In this analysis, two types of datasets are distinguished: the first is the dataset recorded by the Belle II experiment, referred to as the *experimental dataset*; the second is a *simulated dataset* that is designed to closely approximate the expected observations in the experimental data. The simulations rely on current theoretical knowledge and understanding of the detector. To enhance simulation precision, the accelerator and detector conditions of specific data-taking periods are incorporated, referred to as *run-dependent simulation*. Simulations that do not include these conditions are referred to as *run-independent simulation*.

The simulated dataset is essential for interpreting the composition of the experimental data, assessing the impact of minor variations in the models, analyzing detector influence and performance, and evaluating the impact of new models. This section discusses the two different datasets used and their respective compositions.

6.1.1. τ -Lepton Pair Production

At Belle II, τ -leptons can be produced via e^+e^- annihilation and subsequent pair production, $e^+e^- \rightarrow \tau^+\tau^-$, through electroweak neutral currents, which involves a γ and the interference between γ and the Z boson. To produce a τ -lepton pair, a minimum \sqrt{s} of twice m_τ is required. The radiation-corrected Born-level cross-section $\sigma_{\tau\tau}$ for the $\tau^+\tau^-$ production is shown in Figure 6.1.

6.1.2. Simulated Data

A statistical approach, known as the *Monte Carlo (MC)* method, is used to produce the simulated dataset. Pseudo-random numbers are generated to replicate the statistical randomness inherent in quantum physics and the behavior of elementary particles.

The particles are generated using various generators, and the response of the Belle II detector is simulated with GEANT4[72]. The generators used, along with the simulated processes studied in this analysis, are detailed below.

The simulated dataset includes the modeling of several dominant processes occurring during e^+e^- collisions at SuperKEKB. The simulated samples used in this analysis can be categorized into two main groups: *signal (sig)* and *background (bkg)*. The signal process includes only

6. τ -Lepton Lifetime Measurement Using Template Fits

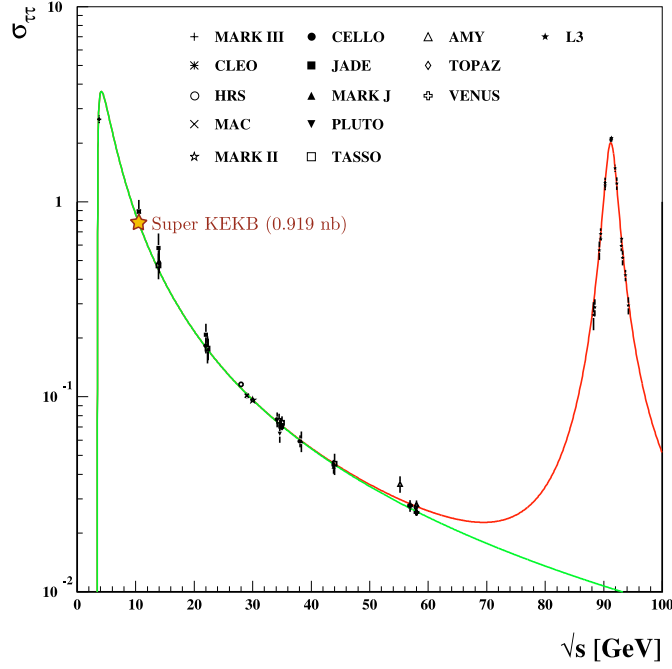


Figure 6.1.: τ -lepton production Born cross-sections from threshold to Z -Pole CM energy. Also shown are the experimental cross-section measurement results from various experiments. At low energies ($\sqrt{s} \ll M_Z$), production cross-sections of 3 nb to 4 nb are achievable. The production cross-section achievable at SuperKEKB is indicated. Green shows the production process via a virtual γ , red shows the resonant production process via a Z boson. (Figure adapted from [71])

the $e^+e^- \rightarrow \tau^+\tau^-$ channel, while the background includes all other processes relevant to the τ -lepton decay signature studied in this analysis (see Section 6.4.3).

The background processes are further divided into three subgroups: continuum ($e^+e^- \rightarrow q\bar{q}$) background, radiative di-lepton background, and two-photon and other low-multiplicity backgrounds. Below is an overview of each category and the channels grouped within each subgroup, detailing the processes considered and their generation.

Signal sample:

- $e^+e^- \rightarrow \tau^+\tau^-$: The τ -lepton pairs, including ISR, are generated with KKMC[73] and interfaced with TauolaBelle2 [74], [75] for their decays, including FSR, with a mean τ -lepton lifetime $\tau_0 = 290.57$ fs.

Continuum background samples:

- $e^+e^- \rightarrow q\bar{q}$: For quark flavors $q = \{u, d, s, c\}$, pairs are generated with KKMC, with their fragmentation simulated using PYTHIA[76].
- $e^+e^- \rightarrow b\bar{b}$: This includes $b\bar{b}$ -quark pairs decays into either mixed $B^0\bar{B}^0$ or charged B^+B^- meson pairs, generated with EvtGen [77], and interfaced with PYTHIA.

Radiative di-lepton background samples:

- $e^+e^- \rightarrow e^+e^-(\gamma)$: The Bhabha process, including ISR and FSR photons (γ), is generated using the **BabaYaga@NLO** [78]–[82].
- $e^+e^- \rightarrow \mu^+\mu^-(\gamma)$: The di-muon process, including corrections for ISR and FSR, is simulated using **KKMC**.

Two photon and other low-multiplicity background samples:

- $e^+e^- \rightarrow e^+e^-\ell^+\ell^-$: The channels $e^+e^-e^+e^-$, and $e^+e^-\mu^+\mu^-$ are simulated with the **AAFH** [83]–[85] generator.
- $e^+e^- \rightarrow \ell^+\ell^-X^+X^-$: This includes the channels $e^+e^-K^+K^-$, $e^+e^-\pi^+\pi^-$, and $e^+e^-p\bar{p}$ are simulated using **TREPS** [86], and $\mu^+\mu^-\tau^+\tau^-$, $\mu^+\mu^-\mu^+\mu^-$, and $e^+e^-\tau^+\tau^-$ are simulated using the **AAFH** generator.
- $e^+e^- \rightarrow h^+h^-(h)\gamma$: Including the channels $K^+K^-\gamma$, $K^0\bar{K}^0\gamma$, $\pi^+\pi^-\gamma$ and $\pi^+\pi^-\pi^0\gamma$, are generated using **PHOKHARA9.1** [87].

Currently, there is no generator available to simulate the $e^+e^- \rightarrow e^+e^-nh$, and $e^+e^- \rightarrow e^+e^-h^+h^-h^+h^-$ processes.

The majority of the simulated data used in this work is produced by the 15th Belle II official run-dependent MC campaign (**MC15rd**), which incorporates time-dependent beam positions and beam background conditions. Details on the cross-sections used and the sizes of the simulated samples are provided in Table 6.1. To reduce statistical uncertainty in the simulated dataset, up to four times the experimental data statistics are generated, particularly for the signal sample and the dominant $q\bar{q}$ background samples.

To conserve computing resources, several other background samples are pre-scaled. The largest pre-scale factor, 1/400, is applied to the e^+e^- sample due to its cross-section being nearly 300 times larger than that of $\tau^+\tau^-$.

To validate the analysis method (see Section 6.6.1), additional **MC15rd** $\tau^+\tau^-$ signal samples with shifted τ -lepton lifetimes of ± 0.5 fs and ± 1 fs are produced.

To study the impact of misaligned detector components (see Section 6.8.5) and variations in detector material density (see Section 6.8.6), additional samples are generated using run-independent MC (**MC15ri**). Run-independent simulations were necessary due to technical limitations. All additional samples are listed in Table 6.2.

To compare the simulated dataset with the experimental dataset, the simulated samples need to be scaled to the corresponding luminosity of experimental dataset (see Appendix A.2).

6.1.3. Experimental Data

The collected Run 1 dataset is shown in Figure 6.2 (online dataset). The calibrated, reconstructed and reprocessed data of good runs is called the offline dataset.

For this analysis, offline data from Experiments 10 to 26 within Run 1 is used, corresponding to periods when SuperKEKB operated at the $\Upsilon(4S)$ energy (on-resonance). Datasets recorded at energies deviating from this resonance (off-resonance) are excluded. This choice avoids potential complications that arise from combining datasets collected at different \sqrt{s} values, such as mismatched correction factors and calibration issues. In any case, the statistical precision in the dataset is already high enough (see Section 6.8).

6. τ -Lepton Lifetime Measurement Using Template Fits

	Process	σ [nb]	$\int \mathcal{L} dt$ [fb $^{-1}$]	N [10 6]
$\tau^+\tau^-$	$e^+e^- \rightarrow \tau^+\tau^-$	0.919	1455.052	1.34×10^3
	$e^+e^- \rightarrow c\bar{c}$	1.329	1455.052	1933.76
$q\bar{q}$	$e^+e^- \rightarrow d\bar{d}$	0.401	1455.052	583.48
	$e^+e^- \rightarrow s\bar{s}$	0.383	1455.052	557.28
	$e^+e^- \rightarrow u\bar{u}$	1.605	1455.052	2335.36
	$e^+e^- \rightarrow B^+B^-$	0.54	1455.052	785.73
$b\bar{b}$	$e^+e^- \rightarrow B^0\bar{B}^0$	0.51	1455.052	742.08
	$e^+e^- \rightarrow e^+e^-(\gamma)$	295.8	36.3731	10 759.16
$\ell\ell(\gamma)$	$e^+e^- \rightarrow \mu^+\mu^-(\gamma)$	1.148	1455.052	1670.40
	$e^+e^- \rightarrow e^+e^-e^+e^-$	39.55	363.767	14 386.98
$e^+e^-e^-$	$e^+e^- \rightarrow e^+e^-\mu^+\mu^-$	18.83	363.767	6849.73
	$e^+e^- \rightarrow e^+e^-\pi^+\pi^-$	1.895	363.767	689.34
$\ell\ell XX$	$e^+e^- \rightarrow e^+e^-K^+K^-$	0.0798	363.767	29.03
	$e^+e^- \rightarrow e^+e^-p\bar{p}$	0.0117	363.767	4.26
	$e^+e^- \rightarrow e^+e^-\tau^+\tau^-$	0.01836	363.767	6.68
	$e^+e^- \rightarrow \mu^+\mu^-\tau^+\tau^-$	1.441×10^{-4}	363.767	5.24×10^{-2}
	$e^+e^- \rightarrow \tau^+\tau^-\tau^+\tau^-$	2.114×10^{-7}	363.767	7.69×10^{-5}
	$e^+e^- \rightarrow K^+K^-\gamma$	0.0163	363.767	5.93
$hh(h^0)\gamma$	$e^+e^- \rightarrow K^0\bar{K}^0\gamma$	0.008864	363.767	3.22
	$e^+e^- \rightarrow \pi^+\pi^-\gamma$	0.1667	363.767	60.64
	$e^+e^- \rightarrow \pi^+\pi^-\pi^0\gamma$	0.02378	363.767	8.65

Table 6.1.: The simulated processes with their cross-sections σ , their integrated luminosity $\int \mathcal{L} dt$ and the number of events N .

6.1. Simulated and Experimental Data Samples

Sample	Scenario	$\int \mathcal{L} \, dt \, [\text{fb}^{-1}]$	$N \, [10^6]$
Shifted Lifetime (MC15rd)	−1 fs	364.436	364.44
	−0.5 fs		
	0.5 fs		
	1 fs		
Misalignment (MC15ri)	Nominal	50	45.95
	Prompt to proc		
	Intrinsic systematics 1		
	Intrinsic systematics 2		
Material Budget (MC15ri)	Day-to-day	500	459.50
	Nominal		
	Beam pipe density +5 %		
	Beam pipe density −5 %		

Table 6.2.: Simulated $e^+e^- \rightarrow \tau^+\tau^-$ processes with altered simulation parameters to model deviations from nominal simulation parameters. The scenarios with shifted τ -lepton lifetimes are statistically independent, whereas the scenarios for misalignment and material budget use exactly the same events among themselves, respectively.

Experiments 7 and 8 are excluded from the analysis due to suboptimal PXD configurations, reducing the dataset by only 0.6 % and thus having no significant impact on statistical precision. This results in an on-resonance dataset with a total integrated luminosity of

$$\mathcal{L}_{\text{int}}^{\text{data}} = (361.924 \pm 0.02 \pm 1.64) \, \text{fb}^{-1}, \quad (6.1)$$

where the first uncertainty is statistical and the second is systematic. The detailed composition of the data-taking periods included in the experimental dataset is shown in Table 6.3.

6. τ -Lepton Lifetime Measurement Using Template Fits

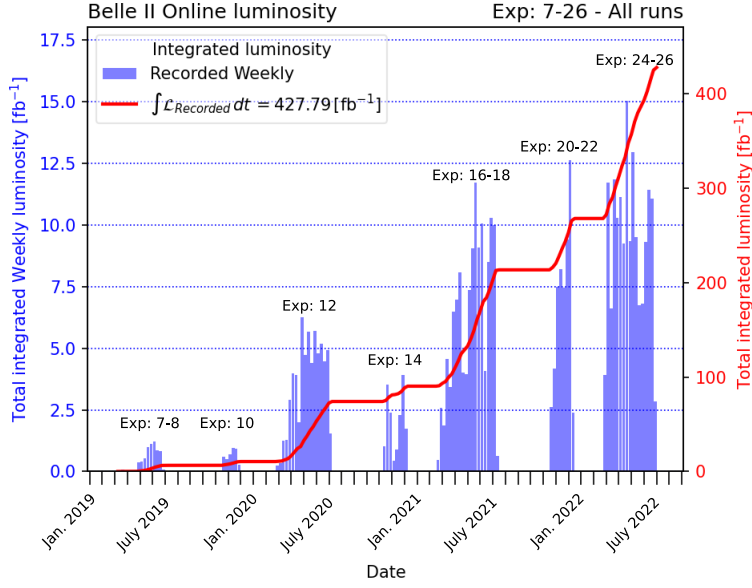


Figure 6.2.: Recorded integrated luminosity with the Belle II detector during Run 1. This includes all runs. The experimental data used in this work is aggregated in experiments. The respective experiments were recorded within the indicated data taking period. (Figure adapted from [88])

Sample	Exp.	Buckets	$\int \mathcal{L} dt \text{ [fb}^{-1}\text{]}$		
			Value [89]	stat. [89]	syst. [90]
Chunk 1	7	-	0.506	0.002	
	8	-	1.663	0.003	
	10	-	3.655	0.001	
Chunk 2	12	-	54.573	0.004	
Chunk 3	14	16, 16b	16.500	0.006	
Chunk 4	16	17	10.294	0.004	
	17	18	10.715	0.004	
Chunk 5	18	19a, 20, 21, 22, 23, 24, 25	89.900	0.011	
Prompt	20	26	3.788	0.002	
	22	28, 29	32.060	0.006	
	24	30, 31, 32, 33	85.642	0.010	
	26	35, 36	54.795	0.008	
Total			364.093	± 0.02	± 1.64
Exp. 7+8 excluded			361.924	± 0.02	± 1.64

Table 6.3.: The Belle II Run 1 on-resonant experimental dataset. The dataset is divided in Chunk 1-5 and Prompt. Chunk 1-5 were reprocessed in the official data processing campaign (**Proc13**). The **Prompt** sample was recorded after the processing of **Proc13** was initiated. Experiment 7+8 are excluded from the analysis.

6.2. Measurement Method

This analysis is based on the vertex method described in Section 3.3.1 and focuses on the 3x1 decay topology. This section introduces the novel approach developed in this work, which employs a template fit method to address limitations of the previous approach [91]. Validation of the template fit method is discussed in Section 6.6.1.

6.2.1. 3x1 Vertex Method

The 3x1 decay topology and the reconstructed decay vertex V from the three charged daughter particles are shown in Figure 6.3a. To separate the events on the 1-prong and 3-prong sides, the daughter particles must be associated with their respective τ decay. Figure 6.3b illustrates the separation of the 1-prong and 3-prong hemispheres through \hat{n}_{thrust} (see Section 3.3).

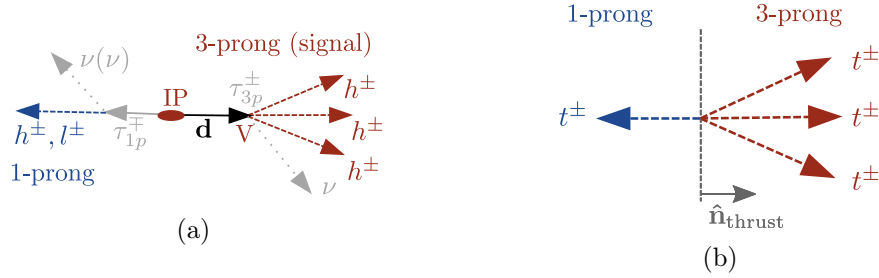


Figure 6.3.: (a) Illustration of the 3x1 topology using the vertex method to determine the τ_{3p} decay vertex from its daughter particles. (b) Separation of the 1-prong and 3-prong hemispheres through the thrust axis \hat{n}_{thrust} . Only the four tracks t^\pm of the event are shown here.

The decay length d is measured in the lab frame by:

$$d = (V - IP). \quad (6.2)$$

Figure 6.4a shows the decay length $|V - IP|$ distribution. The distribution has a minimum at zero, as the resolution effects from Equation (2.15) are convoluted with the “true” exponential decay length distribution in the positive range. To address the resolution smearing and partly disentangle it from the “true” exponential decay length distribution, d is projected onto the reconstructed τ -lepton flight direction:

$$d = (V - IP) \cdot \hat{e}_{3p}, \quad (6.3)$$

where $\hat{e}_{3p} = \mathbf{p}_{3p} / |\mathbf{p}_{3p}|$ is the unit vector of the three-hadron total momentum.

The nano-beam scheme of SuperKEKB (see Section 4.1) provides an IP with small median beam diameter in x of $12.7 \mu\text{m}$ and a narrow median diameter in y of $1.6 \mu\text{m}$, both of them are small compared to the median beam diameter in z of $309.3 \mu\text{m}$. Therefore, the measurement is performed in the x - y -plane, and only the transversal components are considered:

$$d_{xy} = (V - IP) \cdot \hat{e}_{3p_{xy}}. \quad (6.4)$$

6. τ -Lepton Lifetime Measurement Using Template Fits

Figure 6.4b shows the reconstructed decay length distribution of Equation (6.4). Clearly visible, the resolution effects result in a negative tail. For the remainder of this work, the term *decay length* will always refer to Equation (6.4) unless otherwise specified.

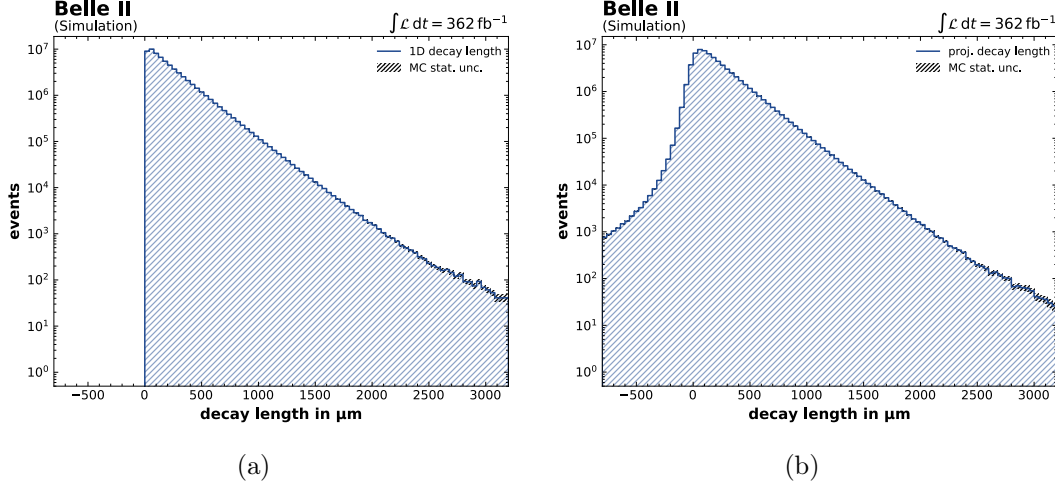


Figure 6.4.: Comparison of different decay length reconstruction methods studied on the $\tau^+\tau^-$ sample. (a): Reconstructed decay length distribution using only the absolute distance between IP and vertex, $|\mathbf{d}|$. (b): Reconstructed decay length distribution, projecting \mathbf{d} onto $\hat{\mathbf{e}}_{3p_{xy}}$.

Effects such as invisible neutrinos, detector inefficiencies (e.g. undetected photons), and resolution impede precise momentum reconstruction of the τ_{3p} . However, in the previous analysis strategies (see Section 3.3.2) a precise reconstruction was necessary since it was crucial to boost back from the lab frame into the τ -lepton rest frame. The novel approach presented in this work overcomes these challenges. Instead of reconstructing the full τ_{3p} momentum, including the neutrino(s) by using energy and momentum conservation in combination with the precisely known beam energy, the τ_{3p} momentum is reconstructed solely from the charged daughter particles. This “reduced” τ_{3p} momentum is calculated for both the experimental and simulated data.

A variation of the τ -lepton lifetime τ_τ results in a shift of the decay length distribution, as shown in Figure 6.5. In general, particles with a shorter lifetime decay, on average, faster, and vice versa. Thus, lower τ_τ values increase the number of events for smaller measured decay lengths and decrease the number of observed events for larger decay lengths. For larger τ_τ values, the opposite is true.

For the lifetime measurement, several decay length distributions with different τ -lepton lifetimes are simulated and compared with the experimentally measured decay length distribution. The comparison is achieved through a *template fit*, explained in the next section.

All studies in this work use blinded experimental data for decay length to prevent analysis bias by optimizing e.g. decay length distributions or fits subconsciously toward certain results. This means that the decay length distribution or any other lifetime-related distribution is never plotted or used in a lifetime fit in this work.

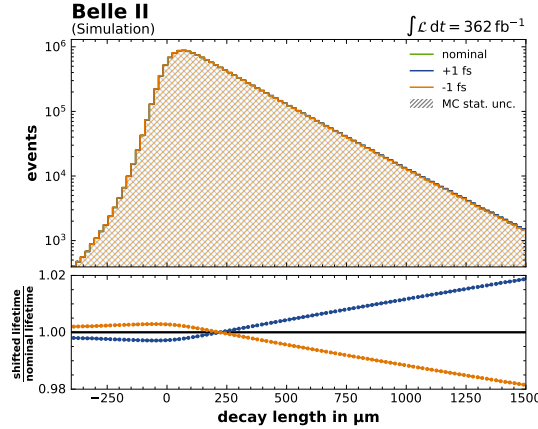


Figure 6.5.: Shift of the decay length distribution induced by different τ -lepton lifetimes on a simulated $\tau^+\tau^-$ sample. The statistical uncertainty is not visible.

6.2.2. Template Fit

This section bases on the works of [92]–[94], where the topic is discussed in greater detail.

To test the significance of the experimental data described by the simulated model, the technique of hypothesis testing is applied. The central element of this technique is the *likelihood function*, which expresses the probability to measure a distribution like the observed one given the model parameters for which it is evaluated. The hypothesis is represented in the form of a *template*.

Due to the limited accuracy of the templates, a set of parameters is defined, allowing for adjustments to the templates. This transforms the hypothesis test into an optimization problem known as the *template fit*. The parameter phase space is estimated a priori through auxiliary measurements.

The template fit method can be extended to test various hypotheses, favoring the one with the highest significance. This procedure is referred to as a *likelihood scan*.

The templates are created from the expected observable distributions of the simulated data. Each template can be generated for a specific hypothesis applied in the simulation, such as different assumptions about particle lifetime. Since in this analysis, the statistical distributions of observables are binned into *histograms*, the hypothesis testing is performed via *binned likelihoods*.

Based on the likelihood function, a fit function that includes the aforementioned parameters is defined. This function is then input into a minimization algorithm to adjust the parameters, minimizing the discrepancy between the template and the experimentally measured data.

For the template fit, `pyhf` [94] is used, which is a `Python` implementation of the `HistFactory` library [93]. Additionally, the `Python` library `cabinetry` [95] is employed to steer the fitting process for different τ -lepton lifetime templates.

The binned likelihood function \mathcal{L} used for the lifetime fit (referred to as “the fit”) is defined as:

6. τ -Lepton Lifetime Measurement Using Template Fits

$$\mathcal{L}(\mathbf{n}^{\text{data}} | \mathbf{n}^{\text{pred}}(\boldsymbol{\mu}, \boldsymbol{\chi})) = \prod_{i \in \text{bins}} \text{Pois} \left(n_i^{\text{data}} | n_i^{\text{pred}}(\boldsymbol{\mu}, \boldsymbol{\chi}) \right) \prod_{\chi \in \boldsymbol{\chi}} c_{\chi}(a_{\chi} | \chi), \quad (6.5)$$

where the first term represents the Poisson probability P_{Pois} of observing n_i^{data} events in the i -th bin, given a model n_i^{pred} and a set of parameters $(\boldsymbol{\mu}, \boldsymbol{\chi})$ that are optimized to maximize \mathcal{L} . Here, $\boldsymbol{\mu}$ consists of free normalization parameters, while $\boldsymbol{\chi}$ contains constrained parameters, referred to as nuisance parameters (NPs). The second term represents the constraints on the NPs, $c_{\chi}(a_{\chi} | \chi)$, defined through auxiliary measurements \mathbf{a} . The parameters $\boldsymbol{\mu}$, $\boldsymbol{\chi}$, and their constraints are described in detail in Section 6.2.3.

The events can be divided into separate sets, referred to as *channels* c , where the likelihoods are optimized independently. This enables additional constraints on the parameters using measurements from well-modeled phase space regions (*side regions*), which lie outside the signal phase space (*signal region*).

In the *sequential optimization*, a set of the parameters for a group of channels is optimized in one step, which are then fixed to their post-fit values in the next optimization step where the remaining parameters are fitted. This approach is not limited to two steps, the number of steps can be increased up to the number of parameters if each parameter should be fitted in a separate step. In the *simultaneous optimization*, parameters can be cross-correlated between channels or kept independently.

Each channel consists of a model for $n_{ci}^{\text{pred}}(\boldsymbol{\mu}, \boldsymbol{\chi})$, which predicts the number of expected events in each histogram bin and is defined as:

$$n_{ci}^{\text{pred}}(\boldsymbol{\mu}, \boldsymbol{\chi}) = \mu_{\text{sig}} \cdot n_{ci}^{\text{sig}, \tau_x}(\boldsymbol{\chi}_{ci}^{\text{sig}}) + \mu_{\text{bkg}} \cdot \sum_{k \in \text{bkg}} n_{cki}^{\text{bkg}}(\boldsymbol{\chi}_{ci}^{\text{bkg}}). \quad (6.6)$$

The prediction comprises all relevant physics processes, grouped in signal and background samples as discussed in Section 6.1. Each group includes a free normalization parameter, μ_{sig} for the signal and μ_{bkg} for the background, to adjust their overall contributions. The n_i^{sig, τ_x} denotes the number of events in the i -th bin of the $\tau^+ \tau^-$ sample, associated with the specific template of τ -lepton lifetime τ_x . Similarly, n_{ki}^{bkg} represents the number of events in the i -th bin for the respective background sample k .

In this analysis, two consecutive likelihood scans are performed: first, a normalization likelihood fit (referred to as the *normalization fit*), followed by the actual lifetime likelihood fit (referred to as the *lifetime fit*). The normalization fit is based on two channels: a signal region and a side region, while the lifetime fit is based on a single channel, which includes only the signal region. The detailed fit setup is discussed in Section 6.6.2.

In the likelihood scan, all optimized template likelihood values are compared, and the likelihood with the highest value is selected as the best fit result. Complementarily, this procedure is equivalent to selecting the minimum of the negative logarithm of the likelihood (NLL):

$$\text{NLL} = -\log(\mathcal{L}). \quad (6.7)$$

This reduces in the maximization process the potentially complex and computationally intensive calculation of the products to the calculation of sums. Multiplying eq. (6.7) by a factor of two

and subtracting the minimum NLL yields the likelihood scan expressed as:

$$2\Delta\text{NLL} = 2(\text{NLL} - \min(\text{NLL}(\tau_x))). \quad (6.8)$$

The factor two is added, since in the asymptotic case, the Poisson terms in the \mathcal{L} become Gaussian normal distributions and the $2\Delta\text{NLL}$ follows a χ^2 distribution.

Visualizing the $2\Delta\text{NLL}$ values of the likelihood scan, the distribution exhibits a parabolic shape, with the best-fitting value occurring at $2\Delta\text{NLL} = 0$, which represents the best-fitting template, and consequently, the best-fitting hypothesis. The width of the parabola reflects the uncertainty of the fit. A $2\Delta\text{NLL} = \pm 1$ corresponds to the 68 % confidence level (CL), while $2\Delta\text{NLL} = \pm 4$ corresponds to the 95 % CL. Figure 6.6 illustrates an example of the $2\Delta\text{NLL}$ distribution resulting from such a likelihood scan, including different lifetime templates.

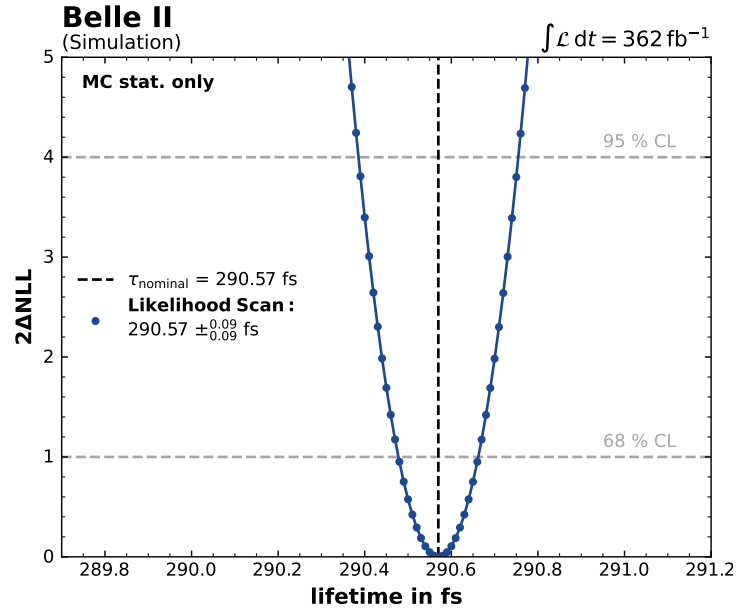


Figure 6.6.: $2\Delta\text{NLL}$ distribution of a lifetime template fit. The nominal template was provided to the fit as pseudo data. In this example, only the statistical precision of the simulated data sample was included as NPs. The best fit template is at $2\Delta\text{NLL} = 0$, which was generated with $\tau_\tau = 290.57$ fs. The fit uncertainty is estimated from the opening of the parabolic curve at $2\Delta\text{NLL} = 1$.

6.2.3. Model Parameters

The unconstrained normalization parameter μ scales the event rates across all bins and can be adjusted by the fit without constraints to correct any normalization discrepancy between \mathbf{n}^{data} and \mathbf{n}^{pred} . In contrast, the NPs χ can also modify the event rates but incur a penalty in the likelihood value the further they deviate from their prior value χ_0 . In this analysis, NPs can either modify all bins simultaneously or affect the bins individually.

6. τ -Lepton Lifetime Measurement Using Template Fits

In `pyhf`, event rate modifications are implemented as `modifiers`. The `modifiers` used in the fit setup of this work are listed and are explained in Table 6.4. They are categorized into multiplicative rate modifiers $\kappa(\phi)$ and additive rate modifiers $\Delta(\phi)$, where $\phi \in \mu, \chi$.

In the likelihood function, each χ is constrained by a Gaussian probability density function (p.d.f.) $P_{\text{Gauss}}(\chi | \chi_0, \sigma_\chi)$ with mean value of χ_0 and a width of σ_χ , which applies the penalty to the P_{Pois} term when the fit pulls χ away from χ_0 . The penalty increases the further χ deviates from χ_0 due to the decreasing probability. Although the fit incurs a penalty when χ deviates from χ_0 , the likelihood may still increase if the experimental data is better modeled with the adjusted parameter.

The NPs are further distinguished with $\chi \in \gamma, \alpha$, where γ represents bin-wise parameters, and α represents interpolation and extrapolation parameters, which interpolate the shape between χ_0 and the envelope defined by σ_χ or extrapolate beyond σ_χ .

Description	Modification	Constraint Term c_χ	Input
Corr. Shape	$\Delta_{sci}(\alpha) = f_p(\alpha \Delta_{\alpha=\pm 1})$	$P_{\text{Gauss}}(\alpha \bar{\alpha}, \sigma_{\bar{\alpha}})$	$\Delta_{\alpha=\pm 1}$
Norm. Uncert.	$\kappa_{sci}(\alpha) = g_p(\alpha \kappa_{\alpha=\pm 1})$	$P_{\text{Gauss}}(\alpha \bar{\alpha}, \sigma_{\bar{\alpha}})$	$\kappa_{\alpha=\pm 1}$
MC Stat. Uncert.	$\kappa_{sci}(\gamma_i) = \gamma_i$	$\prod_i P_{\text{Gauss}}(\gamma_i \bar{\gamma}_i, \sigma_{\bar{\gamma}_i})$	$\sigma_{\bar{\gamma}_i}^2 = \sum_s \delta_{si}^2$
Normalization	$\kappa_{sci}(\mu_i) = \mu_i$	-	-

Table 6.4.: Table of the modifiers constraint terms, and inputs. The indices correspond to sample (s), channel (c), and related bin (i). Here, $\Delta_{\alpha=\pm 1} \equiv \Delta_{sci, \alpha=\pm 1}$ and $\kappa_{\alpha=\pm 1} \equiv \kappa_{sci, \alpha=\pm 1}$. [94]

The *Correlated Shape modifiers* $\Delta_{sci}(\alpha)$ address the up and down shape variations induced by a systematic uncertainty. These variations are measured in an auxiliary measurement and define the envelope for $\Delta_{sci}(\alpha)$ at $\alpha = \pm 1$, denoted as $\Delta_{sci, \alpha=\pm 1}$. This defines the constraint term $P_{\text{Gauss}}(\alpha | \bar{\alpha}, \sigma_{\bar{\alpha}})$, where $\bar{\alpha}$ is the nominal parameter value before the optimization and $\sigma_{\bar{\alpha}}$ is the width defined by the envelope at $\alpha = \pm 1$. The rate modification is applied to all bins using an interpolation/extrapolation function $f_p(\alpha | \Delta_{sci, \alpha=\pm 1})$. For $\alpha = 0$ the modifier returns the prior value, $\chi = \chi_0$.

The *Normalization Uncertainty modifiers* $\kappa_{sci}(\alpha)$ address the up and down variation of the normalization-induced uncertainty. These are also measured in an auxiliary measurement to define $\kappa_{sci}(\alpha)$ at $\alpha = \pm 1$, denoted as $\kappa_{sci, \alpha=\pm 1}$. An overall factor α is applied to all bins to interpolate and extrapolate between the nominal rate and the up and down variations using an interpolation/extrapolation function $g_p(\alpha | \kappa_{sci, \alpha=\pm 1})$. The normalization uncertainty parameters are also Gaussian-constrained, similar to the parameters of the correlated shape `modifiers`. For $\alpha = 0$ the modifier returns the prior value, $\chi = \chi_0$.

The *MC Statistical Uncertainties modifiers* account for statistical fluctuations independently in each bin and are constrained by a Gaussian distribution with a width defined as $\sigma_{\gamma_i} = \sqrt{\sum_s \delta_{si}^2 / n_i^{\text{pred}, 0}}$, where δ_{si} is the absolute statistical yield uncertainty derived from the simulated dataset size for each sample in the respective bin.

6.2.4. Decay Length Models from Re-Weighting

For each model $n_{ci}^{\text{pred}}(\mu, \chi, \tau)$ in Equation (6.6), a dedicated simulated dataset is required for each lifetime hypothesis. A likelihood scan with sufficient resolution typically necessitates $\mathcal{O}(10)$

templates. Producing a separate simulation for each of these templates would take days to weeks and would also require thousands of CPU cores.

To avoid this extensive computational demand, only one lifetime hypothesis is fully simulated, referred to as the nominal lifetime τ_0 . Simulations for all other lifetime hypotheses, characterized by slightly shifted τ -lepton lifetimes, are obtained by re-weighting the τ_{3p} generator decay lengths d_{xy}^{MC} from the nominal $\tau^+\tau^-$ sample, based on the method of [96].

The p.d.f of d_{xy}^{MC} for the nominal $\tau^+\tau^-$ sample, $f(d_{xy}^{\text{MC}}|\tau_0)$ is proportional to the decay length distribution described in Equation (2.13).

To transform the p.d.f $f(d_{xy}^{\text{MC}}|\tau_0)$ into a p.d.f $f(d_{xy}^{\text{MC}}|\tau)$ corresponding to a lifetime τ , a weight factor $w(d_{xy}^{\text{MC}}, \tau)$ is calculated. The weight factor is applied event-by-event with respect to d_{xy}^{MC} .

The weights are derived from the ratio of the two p.d.f.s:

$$w(d_{xy}^{\text{MC}}, \tau) = \frac{f(d_{xy}^{\text{MC}}|\tau)}{f(d_{xy}^{\text{MC}}|\tau_0)} \quad (6.9)$$

$$= \frac{\tau_0}{\tau} e^{\frac{d_{xy}^{\text{MC}}}{c\beta\gamma\tau_0} - \frac{d_{xy}^{\text{MC}}}{c\beta\gamma\tau}}. \quad (6.10)$$

By applying a weight $w_{ij}(d_{xy}^{\text{MC}}, \tau)$ to each event j in bin i of the d_{xy}^{MC} histogram from the τ_0 simulation, the re-weighted histogram reflects the distribution that would be obtained if the events followed the p.d.f $f(d_{xy}^{\text{MC}}|\tau)$. The number of events in each bin i for d_{xy}^{MC} , denoted as n_i , is defined by

$$n_i(\tau) = \sum_j w_{ij}(\tau). \quad (6.11)$$

Figure 6.7a shows the d_{xy}^{MC} shifts obtained from Equation (6.11) for different τ . Once the event weights are computed and applied, the impact of the lifetime variation is transferred to the distribution of any other observable. For fully uncorrelated observables, the event-by-event re-weighting leads only to random, uniformly distributed fluctuations, resulting in no significant overall change to the distribution.

As a result, the corresponding reconstructed decay length distribution d_{xy}^τ is obtained by applying the event weights from Equation (6.11). The resulting distribution retains the full detector response, including finite resolution and inefficiencies from the full detector simulation. Figure 6.7b displays the reconstructed decay length distributions obtained from Equation (6.11).

However, this re-weighting method is valid only if the changes in the particle observables are small relative to the sub-detector scales. For instance, the Belle II detector is composed of millions of subcomponents made from various materials, rather than being a homogeneous structure. If the “true” statistical distribution of particle trajectories deviates significantly from the nominal simulated distribution, such that the detector response is affected by its substructure, a new detector simulation would be necessary. In the case of τ -lepton decays, a mean decay length shift on the order of 1 μm is expected. This shift is small compared to the distance of the BP, approximately 1 cm, the radius of the first PXD layer at 1.4 cm, or even the PXD pixel size of about 50 μm .

The validation of the re-weighting method is presented in Section 6.6.1.

6. τ -Lepton Lifetime Measurement Using Template Fits

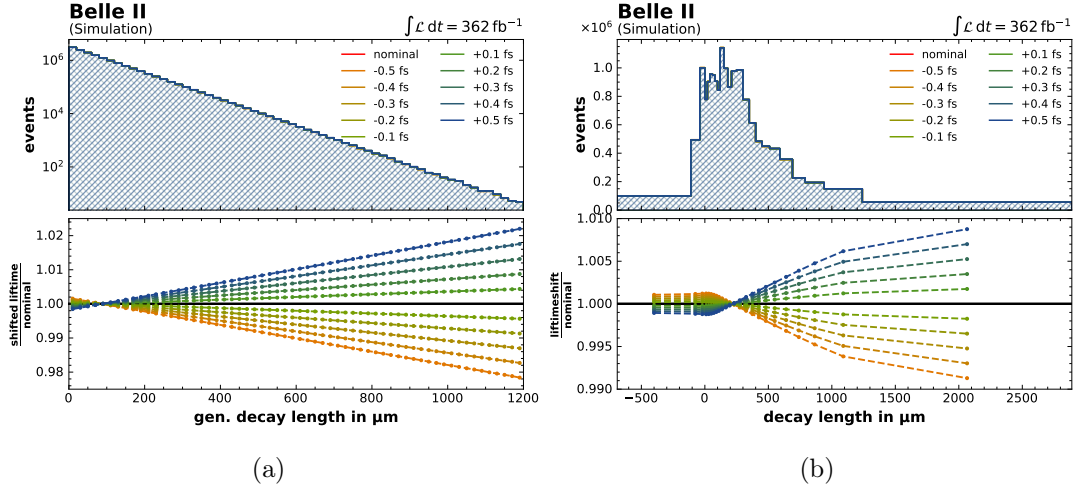


Figure 6.7.: (a) Re-weighted τ_{3p} generator decay length distribution d_{xy}^{MC} up to ± 1 fs difference from τ_0 . (b): Reconstructed decay length distribution d_{xy}^{τ} shifts induced by different τ -lepton lifetimes with respect to τ_0 . Custom binning applied to optimize the statistics per bin.

6.2.5. Properties of the Generator Decay Length Weights

The p.d.f Equation (6.10), used for the weight calculations, is examined for its symmetry in the up and down variations of the decay time, characterized by an absolute offset of Δ , where $\tau = \tau_0 \pm \Delta$.

At a crossing point, where the generator decay length distributions of symmetric up and down lifetime shifts intersect, denoted x , the respective generator decay length distribution functions must be equal. This can be calculated using the ratio

$$1 = \frac{w_{+\Delta}}{w_{-\Delta}} = \frac{\tau_0 - \Delta}{\tau_0 + \Delta} e^{\frac{x}{c\beta\gamma} \left(\frac{1}{\tau_0 - \Delta} - \frac{1}{\tau_0 + \Delta} \right)}. \quad (6.12)$$

Rearranging the equation to solve it for x results in

$$x = c\beta\gamma \cdot \frac{\ln \left[\frac{\tau_0 - \Delta}{\tau_0 + \Delta} \right]}{\frac{1}{\tau_0 + \Delta} - \frac{1}{\tau_0 - \Delta}}. \quad (6.13)$$

Equation (6.13) demonstrates that the intersection is not constant and depends on the $\pm \Delta$ shifts.

On the other hand, the intersection of the symmetric up and down shifted generator decay

lengths with the nominal generator decay length is defined by:

$$x = c\beta\gamma \cdot \frac{\ln \left[\frac{\tau_0 \pm \Delta}{\tau_0} \right]}{\frac{1}{\tau_0} - \frac{1}{\tau_0 \pm \Delta}} \quad (6.14)$$

$$\approx c\beta\gamma \cdot \left[\tau_0 \pm \frac{1}{2}\Delta \mp \frac{1}{6\tau_0}\Delta^2 + \mathcal{O}\left(\frac{\Delta^3}{\tau_0}\right) \right]. \quad (6.15)$$

Equation (6.15) indicates that the intersection is not symmetric with respect to symmetric up and down variations. The intersections, in the zeroth order, occur at $x \approx c\beta\gamma\tau_0$. However, this relationship diverges for higher-order terms in Δ .

This property can be observed when in Figure 6.5 the intersection of the shifted generator decay lengths is magnified, as shown in Figure 6.8.

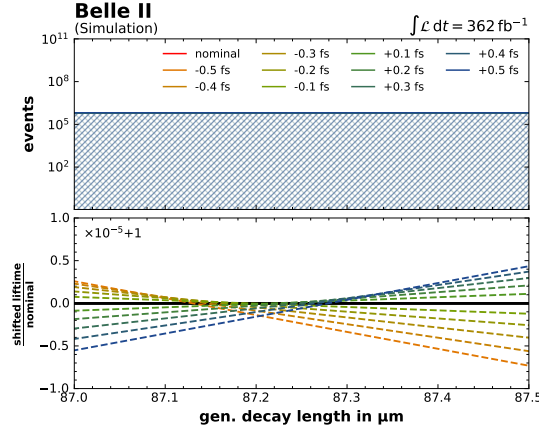


Figure 6.8.: Magnified intersection region of the generator decay length distributions.

For $\Delta \pm 1$ fs, Equation (6.15) results in $|x| \sim 0.15 \mu\text{m}$ for the respective shift, which is two orders of magnitude smaller than the τ_{3p} decay vertex resolution measured in Section 6.5.1.

6.3. Low Level Selections

The datasets used in this analysis undergo low-level selection criteria to reduce their size by removing a large fraction of background events. *Trigger selections* are applied to the experimental data during data-taking. To manage the heavy demand on computing resources, loosely processed selections, known as *skims*, are created for various event signatures. These selections are designed to achieve a high yield of signal events.

This section discusses these two low-level selections and their impact.

6.3.1. L1 Trigger Selection

For this analysis, only L1 ECL trigger bits, which are based on energy deposition in the ECL crystals, are used (see Appendix A.3). The requirements are the same for both the experimental and simulated datasets. In the simulated dataset, the L1 decision is simulated using the TSIM basf2 module. At least one of the following trigger bits must be enabled:

- **hie**, **lml0**, **lml1**, **lml2**, **lml4**, **lml6**, **lml7**, **lml8**, **lml9**, **lml10**, **lml12**, **lml13**

The **hie** trigger bit is enabled when an energy deposit greater than 1 GeV in the event is detected in the ECL. The **lml** trigger bits require additional criteria to be met for individual ECL clusters. Furthermore, all trigger bits require that the trigger bit for Bhabha events (Bhabha veto) is not enabled.

Since the data readout is triggered by the L1 trigger, the trigger selections are already applied to the experimental dataset. Therefore, these selections must also be incorporated into the simulation. Any discrepancies in the decay length distribution between the experimental and simulated data, caused by an inaccurate trigger simulation, could introduce a bias in the lifetime fit. To assess the agreement between the L1 trigger bits of interest and the simulated trigger bits of interest, the trigger efficiency is defined using orthogonal trigger bits based on a different sub-detector, in this case, the CDC.

The trigger efficiency, ε_{trg} , is measured on both the experimental and simulated datasets as

$$\varepsilon_{\text{trg}} = \frac{N_{\text{trg} \wedge \text{ref}}}{N_{\text{ref}}}, \quad (6.16)$$

where $N_{\text{trg} \wedge \text{ref}}$ is the number of events triggered by both the trigger of interest (**trg**) and orthogonal reference trigger bits (**ref**), and N_{ref} is the number of events triggered only by the reference bits.

For the CDC trigger bits used as orthogonal triggers, at least one of the following bits must be enabled:

- **ffo**, **fff**, **ffv**, **fyo**, (**stt**, only active in Exp 16)

The trigger efficiency is shown in Figure 6.9 for the signal region and in Figure 6.10 for the side region¹. Although the experimental data distributions are blinded, relative shifts are shown. For the signal region, a trigger efficiency of $\varepsilon_{\text{trig}} = 94.4\%$ is measured in simulation, while $\varepsilon_{\text{trig}} = 94.5\%$ is observed in the experimental data. In the side region, $\varepsilon_{\text{trig}} \sim 98.2\%$ is

¹The event selection discussed in Section 6.4 is applied apart from the $d_{2 \times 1}$ and d_{xy} selection criteria.

The definition of the signal and side region is discussed in Section 6.6.2.

observed for the simulation, and $\varepsilon_{\text{trig}} \sim 98.3\%$ for the experimental data. For both fit regions, $\varepsilon_{\text{trig}}$ is observed to be close to flat. This means no bias from the simulated trigger bits of interest is expected.

Table 6.5 shows $\varepsilon_{\text{trig}}$ for each ECL trigger bit. **lm12**, **lm114**, and **lm117** have an $\varepsilon_{\text{trig}} < 10\%$ in both the signal and side regions. The most effective trigger bits are **hie** and **lm112**, with $\varepsilon_{\text{trig}} \gtrsim 80\%$ in the signal region, increasing to $\varepsilon_{\text{trig}} \sim 95\%$ in the side region.

The impact of the trigger efficiency and the resulting uncertainty on the lifetime measurement are discussed in Section 6.8.8.

Trigger Bit	$\varepsilon_{\text{trg}}^{\text{signalregion}}$		$\varepsilon_{\text{trg}}^{\text{sideregion}}$	
	Exp. Data	Sim. Data	Exp. Data	Sim. Data
hie	0.856	0.853	0.942	0.947
lm10	0.513	0.512	0.550	0.547
lm11	0.123	0.125	0.144	0.152
lm12	0.011	0.011	0.038	0.027
lm14	0.000	0.000	0.003	0.001
lm16	0.088	0.082	0.056	0.053
lm17	0.005	0.004	0.006	0.005
lm18	0.151	0.149	0.213	0.220
lm19	0.215	0.216	0.292	0.288
lm110	0.439	0.435	0.537	0.531
lm112	0.792	0.792	0.882	0.889
lm113	0.058	0.055	0.030	0.029
Total	0.949	0.944	0.983	0.982

Table 6.5.: Trigger efficiency of the individual ECL trigger bits and the **or** combination to the total ECL trigger efficiency.

6.3.2. TauThrust Skim

The **tauThrust** skim is specifically designed to pre-select $\tau^+\tau^-$ events based on thrust observable V_{thrust} (see Section 6.2.1). Consequently, the analysis is performed on **tauThrust**-skimmed samples.

The loose selection criteria for the **tauThrust** skim partially overlap with the final event selection described in Section 6.4. At the skim processing stage, no corrections are applied. The **tauThrust** skim requirements are listed in Table 6.6. The selections are described in the following two subsections.

Track Selection

Owing to the small τ -lepton lifetime, the tracks of the charged τ -lepton decay products originate from a region close to the IP. Therefore, a loose requirement on the origin of the tracks with d_r and d_z is applied. Depending on the decay topology, a certain number of tracks, n_{track} , in the respective hemispheres are required, with zero net charge Σ_{charge} .

6. τ -Lepton Lifetime Measurement Using Template Fits

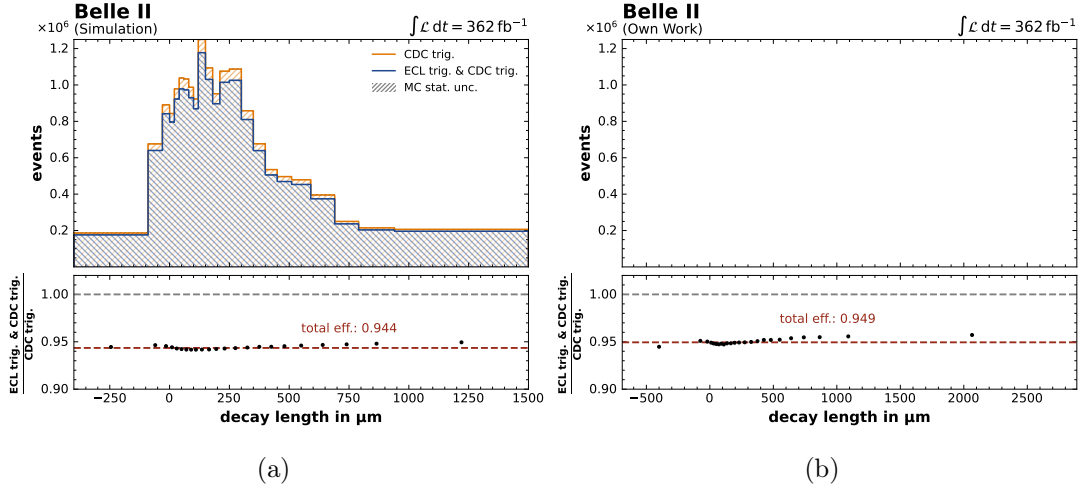


Figure 6.9.: Signal region decay length distribution. (a) ECL trigger efficiency of the simulated data. (b) ECL trigger efficiency of the experimental data. Decay length distribution is blinded. The statistical uncertainty is not visible.

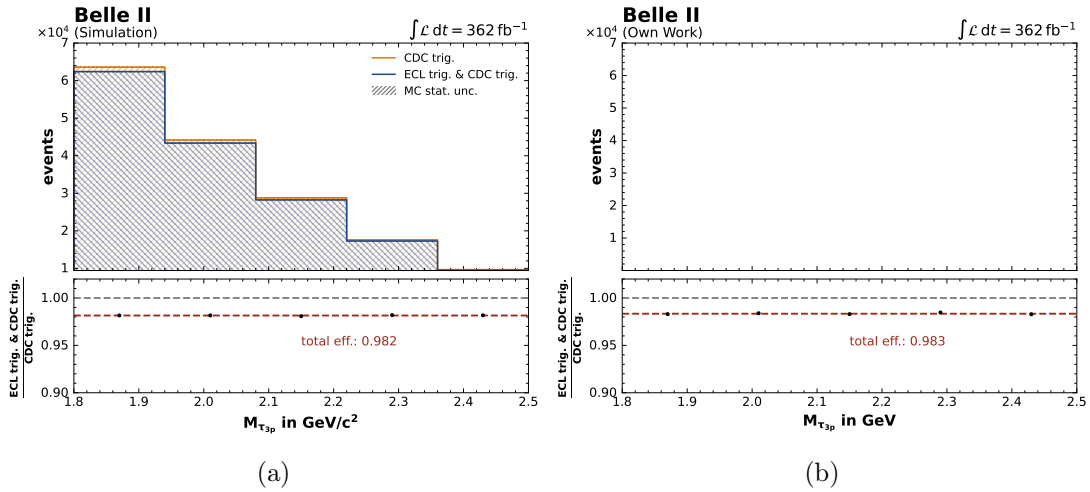


Figure 6.10.: Side region $M_{\tau_{3p}}$ distribution. (a) ECL trigger efficiency of the simulated data. (b) ECL trigger efficiency of the experimental data (distribution is blinded). The statistical uncertainty is not visible.

Photon and π^0 Selection

The beam-induced photon background is dominated by low-energy photons. To mitigate this background, a photon energy threshold is applied. However, increasing the threshold reduces the efficiency of signal reconstruction, necessitating a careful optimization. Two types of photons are distinguished: those originating from π^0 decays (π^0 -photons) and all other photons (non- π^0 -photons).

	Observable	Symbol	Value/Range
event	sum charge	Σ_{charge}	0
	thrust	V_{thrust}	> 0.8
	number of tracks	n_{tracks}	< 0.99 (for 1x1 topology)
	n_{tracks} per hemisphere	$n_{\text{tracks}}^{(1)}, n_{\text{tracks}}^{(2)}$	4
	visible event energy (CMS)	$E_{\text{evt}}^{\text{vis},*}$	1&1, 1&3, 1&5, 3&3 $< 10.4 \text{ GeV}$ $> 1.5 \text{ GeV}$ (for 1x1 topology)
track	distance of the track to IP in z	d_z	$< 3 \text{ cm}$
	POCA in r - ϕ plane	d_r	$< 1 \text{ cm}$
all photons	absolute cluster timing	$ \Delta t_{\text{cluster}} $	$< 200 \text{ ns}$
	cos of polar angle	$\cos \theta_\gamma$	$-0.8660 < \cos \theta_\gamma < 0.9563$
	number of cluster hist	$n_{\text{hits}}^{\text{cluster}}$	> 1.5
	min. cluster to track dist. or energy	$d_{\text{C2T}}^{\text{min}}, E_\gamma$	$d_{\text{C2T}}^{\text{min}} > 40 \text{ cm}$ or $E_\gamma > 0.4 \text{ GeV}$
π^0 -photons	leading cluster energy	E_{lead}	selection criteria depending on detector region, detailed in Table 6.7
	sub-leading cluster energy	E_{sublead}	
	cos angle between two photons	$\cos_{\gamma\gamma}$	
	π^0 momentum	p_{π^0}	
	two photon energy	$E_{\gamma\gamma}$	$0.115 \text{ GeV} < E_{\gamma\gamma} < 0.152 \text{ GeV}$
non- π^0 -photons	photon energy	E_γ	$> 0.2 \text{ GeV}$

Table 6.6.: tauThrust skim selection criteria, explanation in the text.

Regions		Cluster Energy in GeV		$\cos_{\gamma\gamma}$	p_{π^0} in GeV
γ_1	γ_2	E_{lead}	E_{sublead}		
FWD	FWD	> 0.5625	> 0.1625	> 0.9458	> 0.9444
BRL	BRL	> 0.4125	> 0.0625	> 0.8875	> 0.6333
BWD	BWD	> 0.4125	> 0.1125	> 0.8708	> 0.6111
BRL	FWD	> 0.3625	> 0.0875	> 0.8875	> 0.5889
BRL	BWD	> 0.3625	> 0.0875	> 0.8875	> 0.5889

Table 6.7.: π^0 -photon selection parameters in the individual detector regions. The detector regions are named: FWD = forward, BWD = backward, and BRL = barrel.

Requirements applied to *all photons* include the absolute time difference $|\Delta t_{\text{cluster}}|$ between the highest energy cluster signal in the ECL and the bunch collision time, ensuring it is narrow, the polar angle $\cos \theta_\gamma$ within the ECL acceptance region, and a minimum number of crystals in the ECL cluster, $n_{\text{hits}}^{\text{cluster}}$.

Two photons that meet the π^0 -photon requirements are selected to reconstruct a π^0 candidate. The π^0 -photon requirements are based on studies in [97]. Requirements on the leading cluster

6. τ -Lepton Lifetime Measurement Using Template Fits

energy E_{lead} , the sub-leading cluster energy E_{sublead} , the cosine of the angle between the two π^0 -photons $\cos_{\gamma\gamma}$, and the reconstructed π^0 momentum p_{π^0} vary depending on the detector region where the π^0 -photons are detected (see Table 6.7). Additionally, the combined energy of the two π^0 -photons, $E_{\gamma\gamma} = E_{\gamma_1} + E_{\gamma_2}$, must be close to the π^0 mass (135 MeV).

Photons that do not pass the π^0 -photon selection but have energy $E_\gamma > 200$ MeV are selected as non- π^0 -photons. Low-energy photons that do not meet these criteria are discarded but are still included in the calculation of the event's visible CM energy, $E_{\text{evt}}^{\text{vis},*}$, observable.

The **tauThrust** skim applies a “box cut” based on the minimum distance between each ECL cluster and the closest track $d_{\text{C2T}}^{\text{min}}$, as well as the photon energy E_γ . It requires that either $d_{\text{C2T}}^{\text{min}} > 40$ cm or $E_\gamma > 0.4$ GeV for both π^0 and non- π^0 -photons. Notably, this box cut was initially implemented in previous τ -lepton analyses to address inadequately simulated data, particularly issues with hadronic split-offs² and tracks with multiple ECL clusters mimicking low-energy photons. These discrepancies between simulation and experimental data are no longer observed with the current MC15rd simulations.

Skim Efficiency Study

Since the selection criteria are so loose, no events should be discarded in this stage that would otherwise end up in the final event selection if the skim was not applied. To verify that the **tauThrust** skim is not influencing the decay length distribution and that the box-cut in the skim is not introducing any bias, an efficiency study is conducted. The shape of the reconstructed decay length is examined for both simulated and experimental data samples. The skim efficiency, $\varepsilon_{\text{skim}}$, is defined as:

$$\varepsilon_{\text{skim}} = \frac{n_{\text{skim}}}{n_{\text{all}}}, \quad (6.17)$$

where n_{all} is the number of events before the skim is applied, and n_{skim} is the number of events after the skim is applied. In both cases, the event selection and corrections discussed in Section 6.4 are applied³. The study is conducted on **bucket26**, a 4 fb^{-1} sub-sample of the dataset described in Section 6.1.

Figure 6.24 presents the study results. The τ_{3p} decay length is compared with and without the **tauThrust** skim applied. The total skim efficiency is measured to be approximately 100 % for both simulated and experimental data. This indicates no significant impact on the τ -lepton lifetime measurement, and it is therefore neglected in this analysis.

²High momentum charged hadrons can shower in the ECL, producing a secondary neutral particle that creates a displaced cluster not associated with the original track.

³Apart from the $d_{2\times 1}$ and d_{xy} selection criteria.

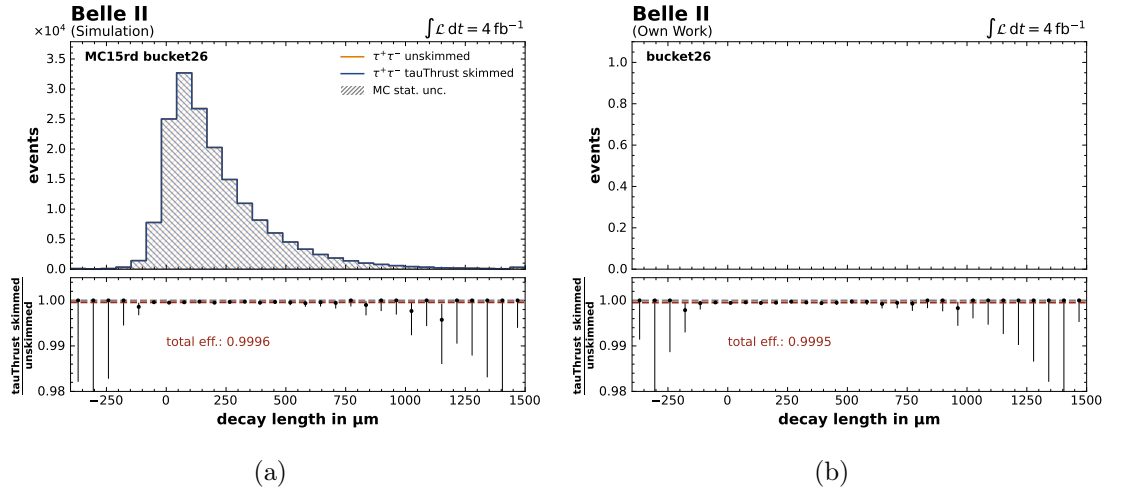


Figure 6.11.: (a): **tauThrust** skim efficiency for simulated data. The statistical uncertainty of the histogram is not visible. (b): **tauThrust** skim efficiency for experimental data (decay length distribution is blinded).

6.4. Particle Reconstruction and Event Selection

Various selection criteria are imposed on observables to enhance the signal-to-background ratio of the $e^+e^- \rightarrow \tau^+\tau^-$ sample. The carefully adjusted selection criteria ensure additionally a good modelling of the experimental data by simulated data (data/MC agreement).

6.4.1. Track Selection and Kinematic Correction

The track requirements are the same as in the `tauThrust` skim in Table 6.6. It is required that the number of tracks n_{track} in the event is exactly four, with zero net charge Σ_{charge} , to reject background events.

The track momenta p and their energy loss E_{loss} are corrected in bins of polar angle $\cos(\theta)$ and p for both experimental and simulated data, using the corrections from [98].

6.4.2. Photon and π^0 Selection and Correction

The photon and π^0 requirements (all photons, π^0 -photons, and non- π^0 -photons) are identical to those used in the `tauThrust` skim in Table 6.6 apart from the box cut from $d_{\text{C2T}}^{\text{min}}$ and E_γ . This box cut is not reapplied during event reconstruction due to the improved simulation.

For the experimental dataset, the E_γ bias is corrected using correction factors estimated after [99].

The photon detection efficiency ε_γ is corrected in simulated data for both π^0 -photons⁴ and non- π^0 photons. The ε_γ correction factors in bins of E_γ are studied in [100]. These correction factors are represented as weights to compensate for overestimated photon detection efficiency in the simulated dataset. For this compensation, photons are randomly discarded in the simulated dataset according to their correction factor weights.

6.4.3. Selection of 3x1-Topology

In the τ -lepton pair reconstruction, all tracks are associated with the π^\pm mass hypothesis. The angle between the tracks and the \hat{n}_{thrust} vector (see Section 6.2.1) is used to separate the tracks into two hemispheres and assign them to either the τ_{3p} or τ_{1p} . It is required that the cosine of the angle between the 1-prong track and \hat{n}_{thrust} has the opposite sign compared to the cosine of the angles between the 3-prong tracks and \hat{n}_{thrust} . The four-vectors of the τ_{3p} and τ_{1p} are reconstructed by summing the four-vectors of their associated reconstructed charged daughter particles.

Additionally, the π^0 s and non- π^0 photons are assigned to the respective hemispheres⁵.

6.4.4. Background and Mismodeling Suppression

The most challenging backgrounds for this analysis are the $c\bar{c}$ and $\ell^+\ell^-X^+X^-$ contributions.

The $c\bar{c}$ sample includes decay processes of mesons with their own lifetimes, featuring dominant

⁴An attempt to directly correct for the π^0 efficiency is studied in Appendix A.4 but was not finalized due to observed drawbacks.

⁵This assignment is based on the sign of the cosine of the angle between their flight directions and \hat{n}_{thrust} , as well as whether the 3-prong (1-prong) side aligns in the positive (negative) or negative (positive) \hat{n}_{thrust} direction.

decays such as D^\pm (~ 1040 fs), D^0 (~ 400 fs), D_s^\pm (~ 500 fs), as well as less frequent decays such as K^0 , K_s^0 , Σ_c^\pm , Ξ_c^0 , or Λ_c^\pm . Furthermore, a mixture of these decays is also possible when a specific combination of the decay chain is reconstructed mistakenly as a τ -lepton.

A key concern is that PYTHIA does not accurately model the *fragmentation* in terms of multiplicity (rate) and momentum distribution. To study this, the $c\bar{c}$ sample must be decomposed into its decay processes (sub-processes). However, separating these sub-processes and their decay chains is rather complex. At this stage of the analysis, a complete decomposition of the fragmentation and its impact on the decay length distribution is not available. A preliminary approximation of this impact is studied in Section 6.8.7.

The $\ell^+\ell^-X^+X^-$ contains $e^+e^-\tau^+\tau^-$ which is also sensitive to the τ -lepton lifetime and might also affect the reconstructed decay length. The cross-section of the $e^+e^-\tau^+\tau^-$ is known to an accuracy of 2 %.

Since the $c\bar{c}$ and $\ell^+\ell^-X^+X^-$ contributions can significantly affect the lifetime fit if not accurately modeled, they must be suppressed as much as possible. Additionally, any other poorly modeled processes or backgrounds must also be eliminated. To achieve this, additional selection criteria are applied, as discussed below.

To evaluate the quality of the modeling and to fine-tune the selection criteria, the agreement of the simulation with the experimental data is evaluated based on the transversal momentum $p_{T,\tau_{3p}}$ and the polar angle $\theta_{\tau_{3p}}$ of the τ_{3p} . These observables show a significant sensitivity to mismodeling with impact on the decay length shape shift (see Section 6.6.4). The remaining effects will be covered by systematic uncertainties (see Section 6.8).

The optimized selection criteria for this analysis are summarized in Table 6.8. The selections applied in the τ -lepton mass measurement [19] served as a reference.

The following distributions display the simulated and experimental datasets after the low-level selections discussed in Section 6.3, but before the final event selection is applied. The corrections mentioned earlier have been applied. The selection windows in the figures below will be indicated by black dashed lines. Distributions with all selections applied are presented in Appendix A.5.1.

The V_{thrust} distribution is shown in Figure 6.12a. The lower range primarily contains $e^+e^- \rightarrow q\bar{q}$ events, while the upper range contains peaking $e^+e^- \rightarrow e^+e^-$ events. To remove these regions, V_{thrust} is required to be between 0.9 and 0.99 (the upper selection is already applied in the reconstruction step to reduce the data size).

The total energy, $E_{\text{evt}}^{\text{vis},*}$, of all particles reconstructed in the event in the CMS frame, shown in Figure 6.12b, is used to eliminate the unmodeled $e^+e^- \rightarrow e^+e^-h^+h^-h^+h^-$ fraction below 3.5 GeV. Due to the missing neutrino(s), $E_{\text{evt}}^{\text{vis},*}$ is expected to be less than \sqrt{s} , so the upper range of $E_{\text{evt}}^{\text{vis},*}$ is set at 9 GeV. In contrast, background processes without neutrinos peak at 10.58 GeV.

The missing neutrino(s) affect momentum conservation in the CMS frame. By summing all reconstructed CMS particle momenta, a missing CMS momentum component, $p_{\text{evt}}^{\text{miss},*}$, is observed. For the event selection, $p_{\text{evt}}^{\text{miss},*}$ is required to be at least $0.3 \text{ GeV } c^{-1}$. Figure 6.13a illustrates that the region $< 0.3 \text{ GeV } c^{-1}$ is dominated by background processes. The polar angle distribution of the missing momentum, $\theta_{p,\text{evt}}^{\text{miss},*}$, shown in Figure 6.13b, shows that the very forward and backward regions exhibit peaking contributions from $e^+e^- \rightarrow e^+e^-$. To reduce these contributions, $\theta_{p,\text{evt}}^{\text{miss},*}$ is required to be between 0.4 rad and 2.6 rad.

The three reconstructed π^\pm tracks on the 3-prong side are ordered by their p_T value into

6. τ -Lepton Lifetime Measurement Using Template Fits

	Observable	Symbol	Value/Range
event	thrust	V_{thrust}	[0.9, 0.99]
	visible event energy (CMS)	$E_{\text{evt}}^{\text{vis},*}$	[3.5, 9] GeV
	missing event momentum (CMS)	$p_{\text{evt}}^{\text{miss},*}$	$\geq 0.3 \text{ GeV } c^{-1}$
	polar angle of missing event mom. (CMS)	$\theta_{p,\text{evt}}^{\text{miss},*}$	[0.45, 2.8] rad
	number of photons 3-prong side	$n_{\gamma 3p}$	≤ 1
	number of π^0 s 3-prong side	$n_{\pi 3p}^0$	$= 0$
	number of photons 1-prong side	$n_{\gamma 1p}$	≤ 1
	number of π^0 1-prong side	$n_{\pi 1p}^0$	≤ 1
π_{3p}^\pm	transverse momentum of $\pi_{3p,1}^\pm$	$p_{T\pi_{3p,1}}$	[0.3, 5] $\text{GeV } c^{-1}$
	transverse momentum of $\pi_{3p,2}^\pm$	$p_{T\pi_{3p,2}}$	$\geq 0.3 \text{ GeV } c^{-1}$
	transverse momentum of $\pi_{3p,3}^\pm$	$p_{T\pi_{3p,3}}$	$\geq 0.1 \text{ GeV } c^{-1}$
	polar angle of π_{3p}^\pm directions	$\theta_{\pi_{3p,1}}, \theta_{\pi_{3p,2}}, \theta_{\pi_{3p,3}}$	[0.45, 2.6] rad
τ_{3p}^\pm	polar angle of reconstructed τ_{3p}^\pm	$\theta_{\tau_{3p}}$	[0.4, 2.6] rad
	transverse momentum of reconstructed τ_{3p}^\pm	$p_{T\tau_{3p}}$	$\geq 1 \text{ GeV } c^{-1}$
	significance of vertex fit	$p\text{-value or } \chi_{\text{prob}}^2$	> 0.001
	vertex residual	$d_{2\times 1}$	[-100, 100] μm
	reconstructed decay length	d_{xy}	[-400, 1500] μm
	reconstructed τ_{3p}^\pm mass (signal region)	$M_{\tau_{3p}}$	[0.75, 1.5] $\text{GeV } c^{-2}$
	reconstructed τ_{3p}^\pm mass (side region)	$M_{\tau_{3p}}$	[1.8, 2.5] $\text{GeV } c^{-2}$

Table 6.8.: Fine-tuned event selection criteria for the background and mismodeling suppression.

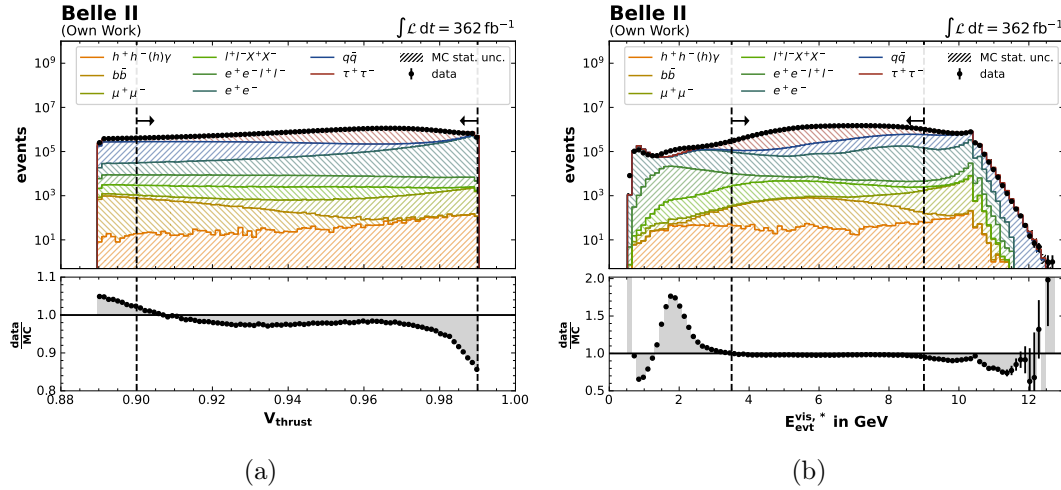


Figure 6.12.: Distribution after the low level selection before final event selection of (a) V_{thrust} and (b) $E_{\text{evt}}^{\text{vis},*}$. The statistical uncertainties of the histograms are not visible.

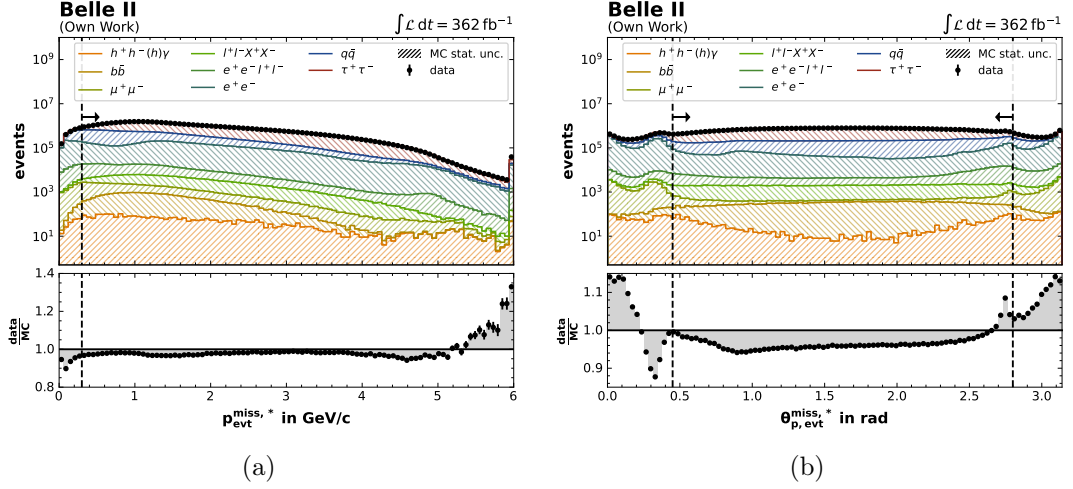


Figure 6.13.: Distribution after the low level selection before final event selection of (a) $p_{\text{evt}}^{\text{miss},*}$ and (b) $\theta_{p,\text{evt}}^{\text{miss},*}$. The statistical uncertainties of the histograms are not visible.

leading p_T ($p_{T,\pi_{3p,1}}$), sub-leading p_T ($p_{T,\pi_{3p,2}}$), and low p_T ($p_{T,\pi_{3p,3}}$). As shown in Figure 6.14a, Figure 6.14b, and Figure 6.14c, the low p_T regions for all three tracks are dominated by background processes. In these regions, the experimental data do not match well with the simulation. Unmodeled processes, such as $e^+e^- \rightarrow e^+e^-h^+h^-h^+h^-$ or radiative Bhabha scattering, also contribute to the low p_T spectrum. In the case of $e^+e^- \rightarrow e^+e^-h^+h^-h^+h^-$, most often, the hadrons are detected and the e^+e^- are lost as they are almost collinear with the beam. Due to the e^+e^- , the h^\pm have low momentum [101]. The lower selection threshold for p_T depends on the ranked p_T position, which is lower for the lower ranked π_{3p}^\pm . The lower selection threshold for p_T depends on the ranked p_T position, which is lower for the lower ranked π_{3p}^\pm . The $p_{T,\pi_{3p,1}}$ distribution also shows significant mismodeled phase space for $p_T \geq 5 \text{ GeV } c^{-1}$, which is removed with this selection.

The polar angles of the tracks, $\theta_{\pi_{3p,1}}$, $\theta_{\pi_{3p,2}}$, and $\theta_{\pi_{3p,3}}$, ordered by the π^\pm p_T , help separate background-dominated regions from the signal region. The respective distributions are shown in Figure 6.15a, Figure 6.15b, and Figure 6.15c. Notably, $e^+e^- \rightarrow e^+e^-$ peaks in the very forward direction (small θ). A smaller, poorly modeled peak is also visible in the very backward direction. The selection window for all three $\theta_{\pi_{3p}}$ is set between 0.45 rad and 2.8 rad.

The $p_{T,\tau_{3p}}$ and $\theta_{\tau_{3p}}$ distributions in Figure 6.16a and Figure 6.16b show similar characteristics to those observed for π_{3p}^\pm . Consequently, $p_{T,\tau_{3p}}$ is required to be at least $1 \text{ GeV } c^{-1}$, and $\theta_{\tau_{3p}}$ is required to be between 0.4 rad and 2.6 rad.

Limiting the number of non- π^0 photons on the 1-prong side, $n_{\gamma_{1p}}$, also aids in background suppression. Figure 6.17a shows that requiring $n_{\gamma_{1p}}$ to be fewer than 2 retains most of the statistics while significantly reducing $e^+e^- \rightarrow q\bar{q}$ events. The distribution of the number of π^0 s on the 1-prong side, $n_{\pi_{1p}^0}$, is shown in Figure 6.17b. To avoid double-counting π^0 photons in the π^0 reconstruction step⁶, $n_{\pi_{1p}^0}$ is required to be less than 2. Additionally, the $\tau^+\tau^-$ statistics

⁶If more than two π^0 photons are present, several possible photon pairings are available for π^0 reconstruction.

6. τ -Lepton Lifetime Measurement Using Template Fits

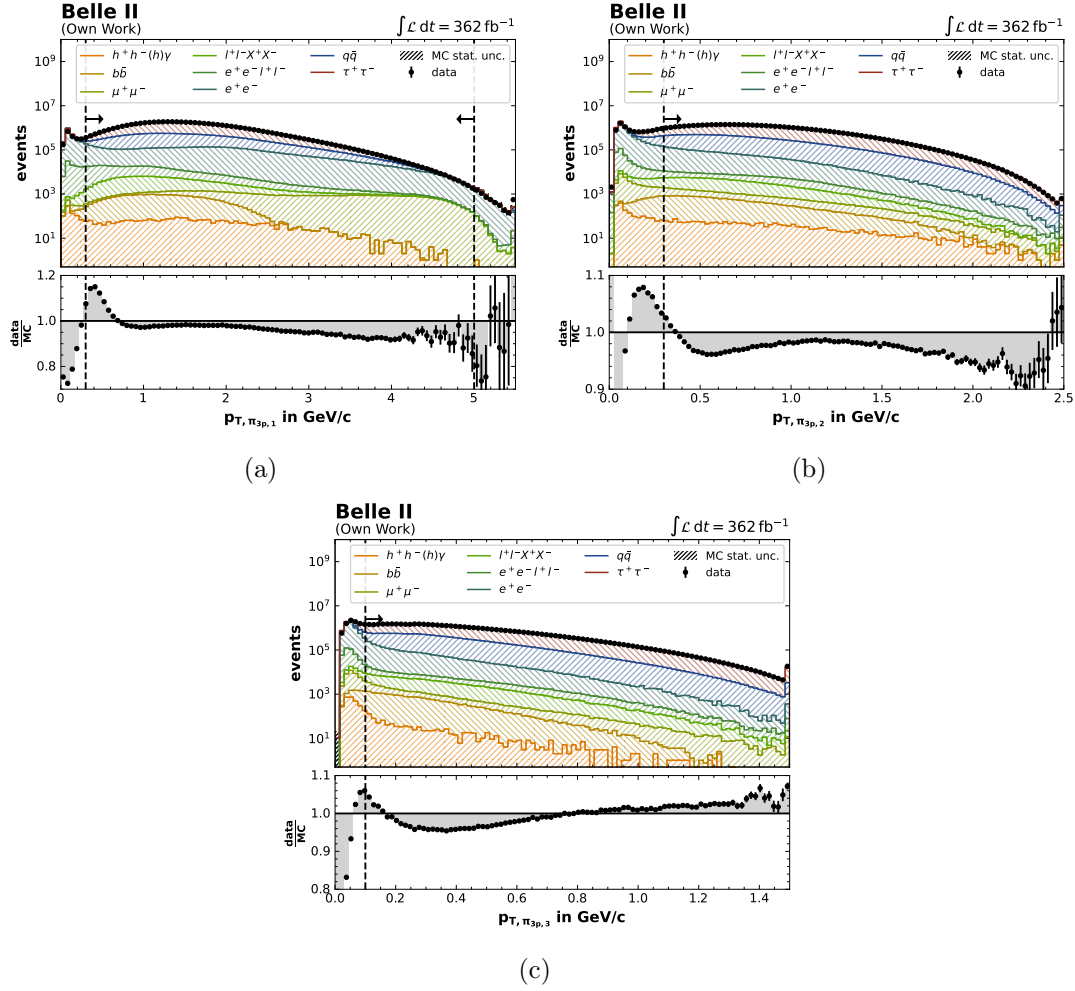


Figure 6.14.: Distribution after the low level selection before final event selection of (a) $p_{T,\pi_{3p,1}}$, (b) $p_{T,\pi_{3p,2}}$, and (c) $p_{T,\pi_{3p,3}}$. The statistical uncertainties of the histograms are not visible.

are low for cases where $n_{\pi_{1p}^0} > 1$.

The distribution of the number of non- π^0 photons on the 3-prong side, $n_{\gamma_{3p}}$, is shown in Figure 6.18a. Requiring $n_{\gamma_{3p}}$ to be fewer than 2 retains most of the signal statistics while significantly removing $e^+e^- \rightarrow q\bar{q}$ events. The distribution of the number of π^0 's on the 3-prong side, $n_{\pi_{3p}^0}$, is shown in Figure 6.18b. $n_{\pi_{3p}^0}$ is required to be zero. Although this requirement also removes a significant fraction of the signal, along with $e^+e^- \rightarrow q\bar{q}$, it is accepted to achieve a higher signal purity.

The χ^2_{prob} of the vertex fit is required to be >0.001 . The requirement of the vertex residual, $d_{2\times 1}$, is discussed in Section 6.5. The d_{xy} selection window spans from $-400 \mu\text{m}$ to $1500 \mu\text{m}$. The

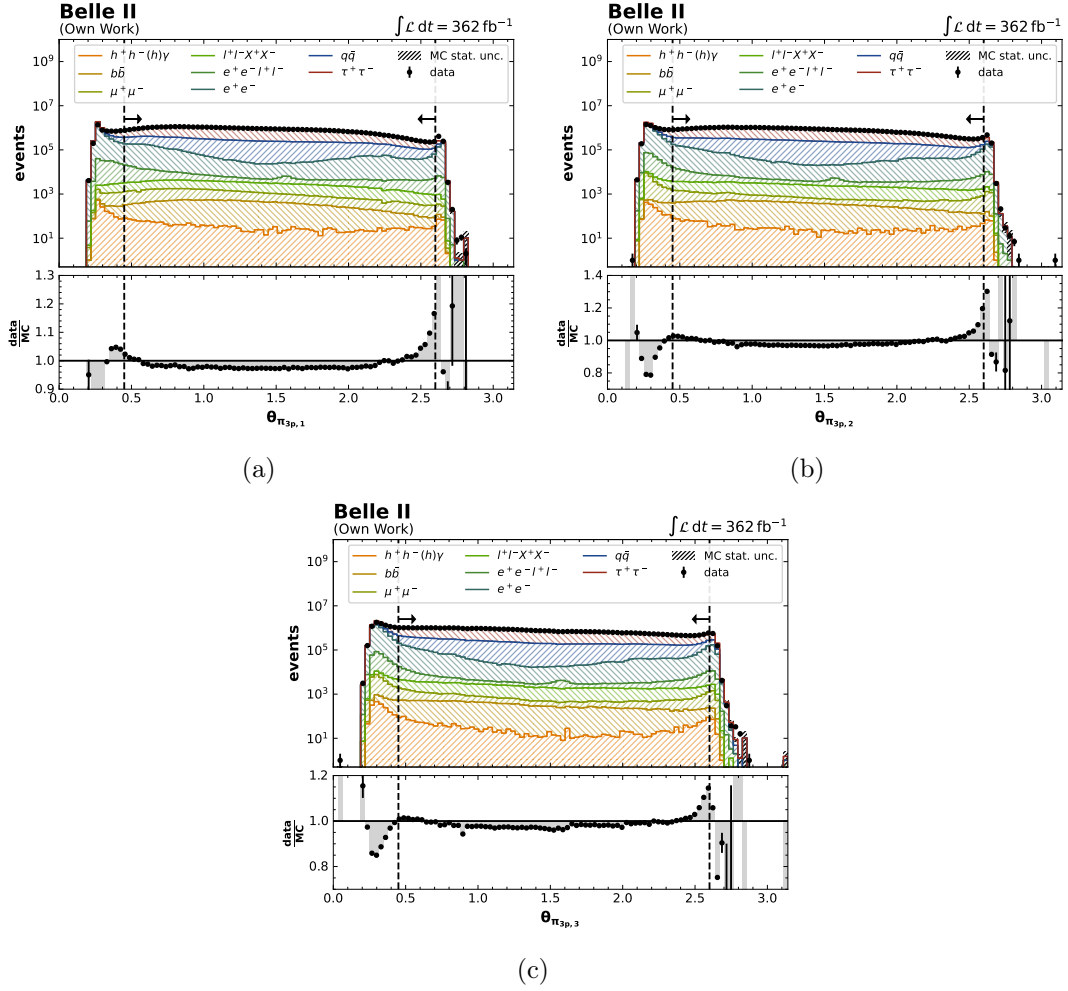


Figure 6.15.: Distribution after the low level selection before final event selection of (a) $\theta_{\pi_{3p,1}}$, (b) $\theta_{\pi_{3p,2}}$, and (c) $\theta_{\pi_{3p,3}}$. The statistical uncertainties of the histograms are not visible within the selection window.

upper limit corresponds to approximately seven times the reconstructed mean decay length⁷, \bar{d}_{xy} , which is approximately 219 μm . The lower limit removes improper reconstructed decay vertices with bad resolution.

For the normalization fit (Section 6.2.2) two fit regions must be defined. A high $\tau^+\tau^-$ purity is required in the signal region and the side region must be dominated by $q\bar{q}$ background. The τ_{3p} mass distribution, $M_{\tau_{3p}}$, is used to select these two fit regions.

If selecting a specific spectrum of an observable A significantly reduces the background, this reduction will also suppress the background in other observable distributions. As a result, this may allow for looser selection requirements on other observables than would be possible without

⁷Only positive d_{xy} values are considered.

6. τ -Lepton Lifetime Measurement Using Template Fits

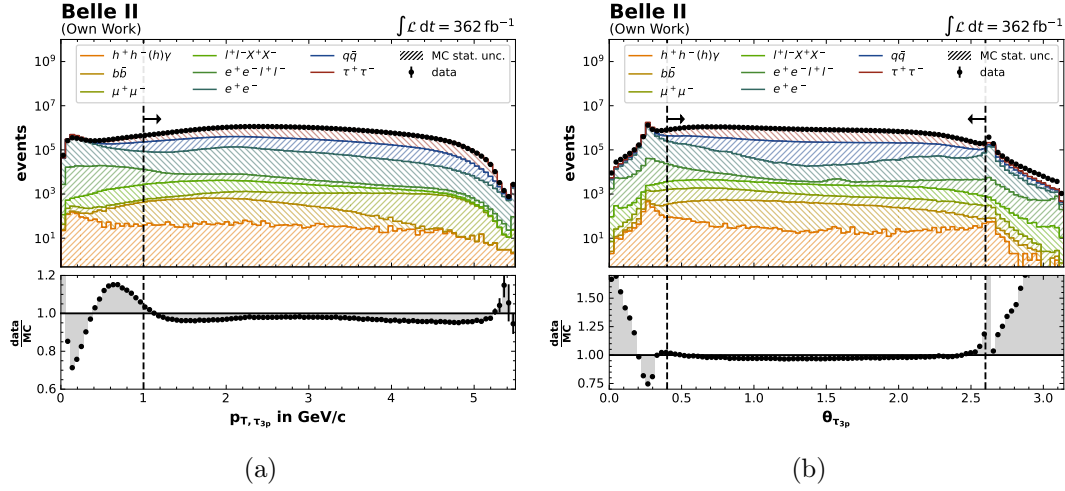


Figure 6.16.: Distribution after the low level selection before final event selection of (a) $p_{T, \tau_{3p}}$ and (b) $\theta_{\tau_{3p}}$. The statistical uncertainties of the histograms are not visible.

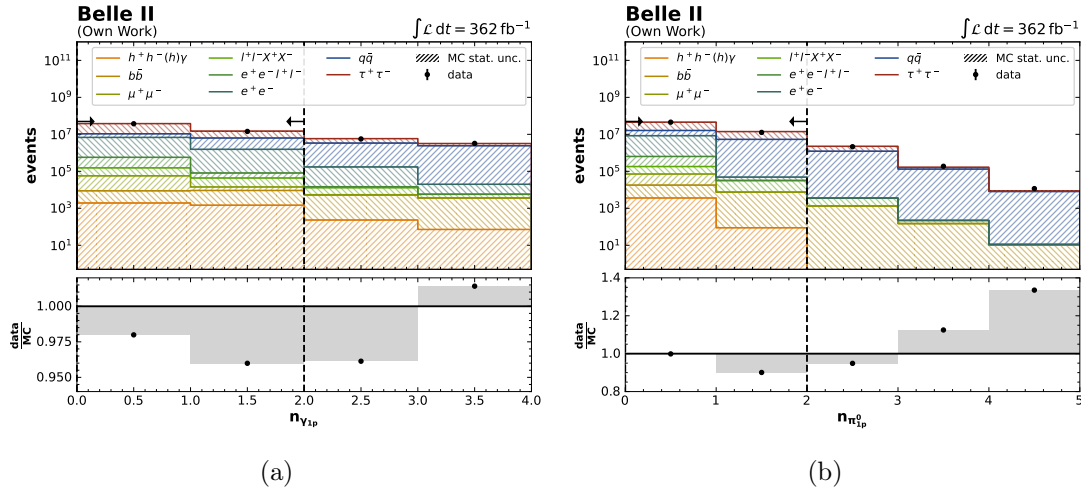


Figure 6.17.: Distribution after the low level selection before final event selection of (a) $n_{\gamma_{1p}}$ and (b) $n_{\pi_{1p}^0}$. The statistical uncertainties of the histograms are not visible.

first applying the selection on observable A .

This can be observed by comparing Figure 6.12 to Figure 6.18 with Figure A.4 to Figure A.10. In Figure 6.12 through Figure 6.18, the indicated selection windows do not always seem to select the optimal region. In contrast, Figure A.4 to Figure A.10, which have all final selections from Table 6.8 applied (except for the observable shown), display optimal selection windows as the majority of the background has already been removed by the previously applied selections.

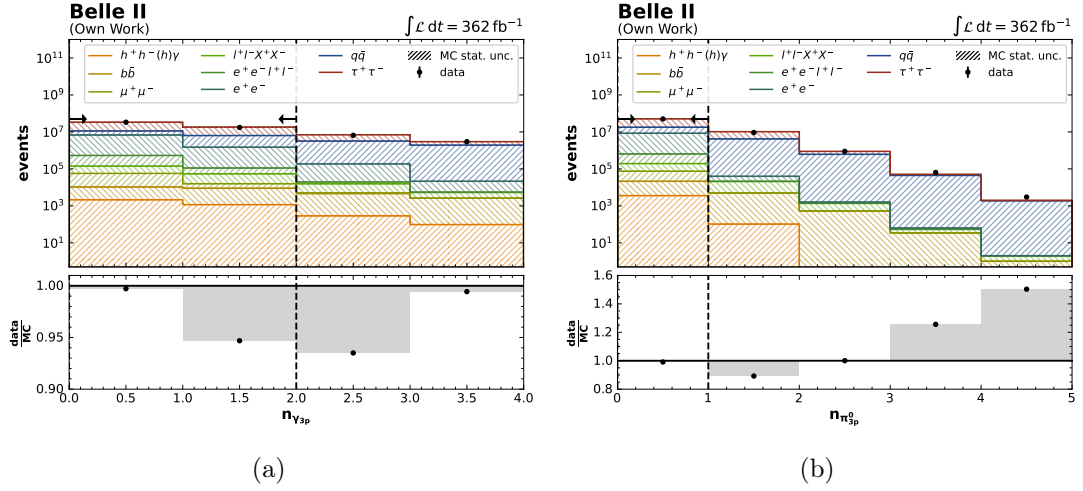


Figure 6.18.: Distribution after the low level selection before final event selection of (a) $n_{\gamma_{3p}}$ and (b) $n_{\pi_{3p}^0}$. The statistical uncertainties of the histograms are not visible.

6.4.5. Expected $\tau^+\tau^-$ Background

The composition of the $\tau^+\tau^-$ sample after applying all selections discussed in Section 6.4.4 is shown in Table 6.9 for the 20 decay modes with the largest contributions. The relations between the six most dominant decay modes are also visualized in Figure 6.19. The primary decay channel is $\tau^- \rightarrow 2\pi^-\pi^+\nu_\tau$ with a fraction of 78.8 %, followed by $\tau^- \rightarrow \pi^-\omega(\rightarrow \pi^+\pi^-\pi^0)\nu_\tau$ with a fraction of 14.6 %. Together, these two decay modes make up 93.4 % of the sample.

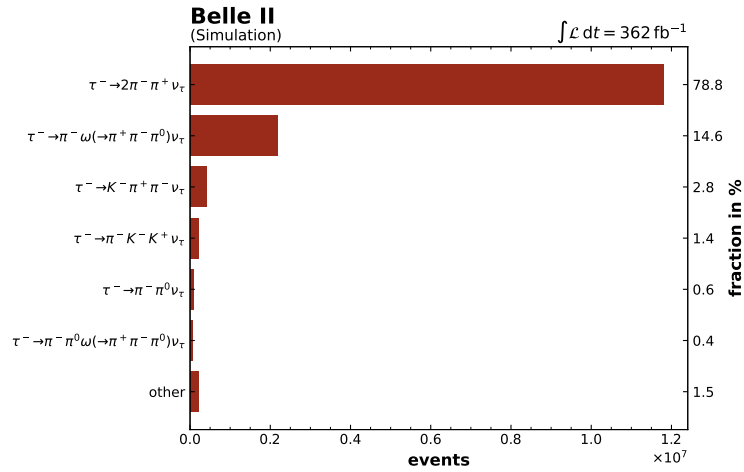


Figure 6.19.: Decay mode composition of the $\tau^+\tau^-$ sample (before yield and template correction, but this has no impact on the showed fractions).

Since all tracks are assumed to be π^\pm without applying additional PID selection criteria,

6. τ -Lepton Lifetime Measurement Using Template Fits

Decay Mode	Events	Fraction in %
$\tau^- \rightarrow 2\pi^- \pi^+ \nu_\tau$	11,814,900	78.75
$\tau^- \rightarrow \pi^- \omega (\rightarrow \pi^+ \pi^- \pi^0) \nu_\tau$	2,192,034	14.61
$\tau^- \rightarrow K^- \pi^+ \pi^- \nu_\tau$	416,384	2.78
$\tau^- \rightarrow \pi^- K^- K^+ \nu_\tau$	208,072	1.39
$\tau^- \rightarrow \pi^- \pi^0 \nu_\tau$	92,081	0.61
$\tau^- \rightarrow \pi^- \pi^0 \omega (\rightarrow \pi^+ \pi^- \pi^0) \nu_\tau$	60,784	0.41
$\tau^- \rightarrow e^- \bar{\nu}_e \nu_\tau$	36,664	0.24
$\tau^- \rightarrow \pi^- \omega (\rightarrow \pi^+ \pi^-) \nu_\tau$	32,298	0.22
$\tau^- \rightarrow \mu^- \bar{\nu}_\mu \nu_\tau$	31,560	0.21
$\tau^- \rightarrow K^- \pi^+ \pi^- \pi^0 \nu_\tau$	22,526	0.15
$\tau^- \rightarrow K^- \omega (\rightarrow \pi^+ \pi^- \pi^0) \nu_\tau$	21,792	0.15
$\tau^- \rightarrow \pi^- \nu_\tau$	18,848	0.13
$\tau^- \rightarrow \pi^- 2\pi^0 \nu_\tau$	14,320	0.1
$\tau^- \rightarrow 2\pi^- \pi^+ K_L^0 \nu_\tau$	9,138	0.06
$\tau^- \rightarrow \pi^- \pi^0 \omega (\rightarrow \pi^+ \pi^-) \nu_\tau$	3,849	0.03
$\tau^- \rightarrow \pi^- K^- K^+ \nu_\tau$	3,267	0.02
$\tau^- \rightarrow 2\pi^- \pi^+ K_S^0 \nu_\tau$	2,502	0.02
$\tau^- \rightarrow \pi^- \pi^0 \eta (\rightarrow \pi^+ \pi^- \pi^0) \nu_\tau$	2,224	0.01
$\tau^- \rightarrow \pi^- K_S^0 \nu_\tau$	2,144	0.01
$\tau^- \rightarrow K^- \eta (\rightarrow \pi^+ \pi^- \pi^0) \nu_\tau$	1,645	0.01
Other	15,202	0.1

Table 6.9.: Table with 20 most dominant contributing τ -lepton decay modes (before yield and template correction, this has only minor impact on the second decimal place in the percentage value). Blue are 3-prong decay channels with misidentified particles as π^\pm . Red are the 1-prong decay channels identified as 3-prong channel.

misidentified particles such as K^\pm , μ^\pm , or e^\pm are incorrectly assigned as π^\pm , resulting in an incorrect mass assumption. The wrong mass hypothesis then enters both the track fit and the vertex fit. For the template creations, the generator level momentum and mass from the τ -leptons are used in Equation (6.10), where the relation $c\beta\gamma = p/m$ enters the weight calculation. Consequently, any incorrect daughter particle assignment has no effect for the different lifetime templates.

Incorrect particle reconstruction does not affect the 1-prong side because the π_{1p}^\pm is only used to identify the 3x1 topology.

The 3-prong decay modes with falsely assumed K^\pm to be π^\pm such as $\tau^- \rightarrow K^- \pi^+ \pi^- \nu_\tau$ or $\tau^- \rightarrow \pi^- K^- K^+ \nu_\tau$ are selected with a total fraction of 4.39%.

Figure 6.20a and Figure 6.20b show the impact of incorrectly reconstructed K^\pm events (referred to as misidentified K^\pm modes) on the distributions of decay length and vertex residual (see Section 6.5.1). It is observed that the fraction of misidentified K^\pm modes in Figure 6.20a exhibits an improved decay length resolution compared to other decay modes (referred to as no K^\pm modes). No shape distortion is observed in the exponential tail, indicating that no general

lifetime shift is expected from the incorrectly reconstructed K^\pm events.

The improved decay length resolution for the K^\pm modes is further supported by Figure 6.20b, which shows enhanced precision in the vertex reconstruction for these modes. This improvement can be explained by the fact that the K^\pm modes originate exclusively from a τ_{3p} 3-prong decay. In contrast, the non- K^\pm modes include decays where the 3-prong vertices are reconstructed incorrectly from e.g. 1-prong decays, as discussed below.

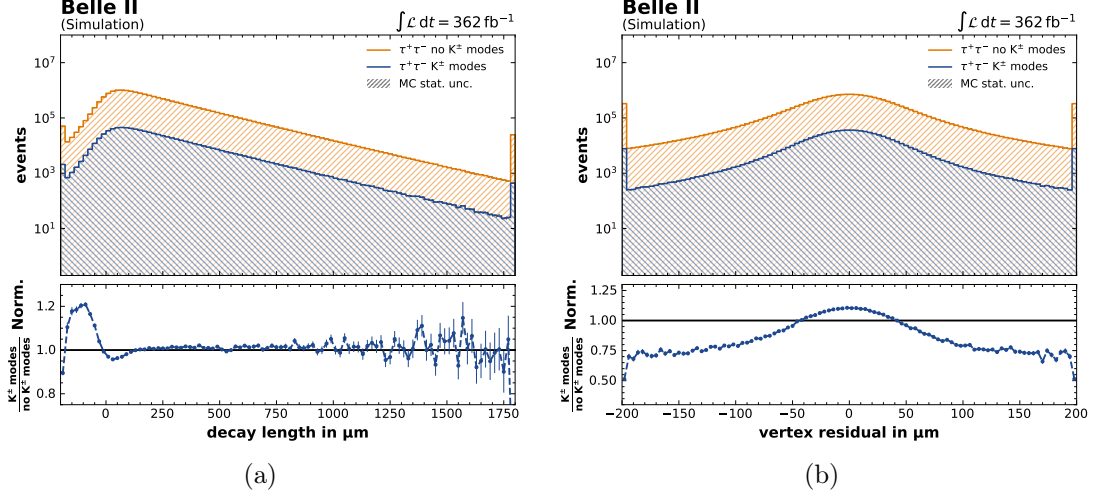


Figure 6.20.: Study with final corrections and selections applied. (a): Fraction of the K^\pm modes in the decay length distribution. (b): Fraction of the K^\pm modes in the vertex residual distribution. The statistical uncertainties of the histograms are not visible.

Another type of incorrect reconstruction occurs in decays such as $\tau^- \rightarrow \pi^- K_S^0 \nu_\tau$, where the K_S^0 decays into $\pi^+ \pi^-$ (referred to as K_S^0 modes). In this case, the K_S^0 has a displaced vertex relative to the actual τ -lepton decay vertex. The total fraction of K_S^0 events in the $\tau^+ \tau^-$ sample is expected to be 0.06 %. This relatively low contribution arises from the small branching ratios of these decay modes.

Figure 6.21a and Figure 6.21b show the contribution of K_S^0 modes to the distributions of the decay length and the vertex residual. It is observed that the resolution in the decay length is degraded for the K_S^0 modes, and the precision of the vertex reconstruction is reduced. Additionally, a significant shape distortion is observed in the exponential tail of the decay length distribution. This could pose challenges if these modes are not accurately modeled in the simulation.

In Section 6.8.9, systematic uncertainties are derived from the impact of incorrectly reconstructed K^\pm and K_S^0 particles on the lifetime fit.

A third background in the $\tau^+ \tau^-$ sample arises from 1-prong decay modes that can mimic signatures similar to 3-prong decays. For example, decay channels such as $\tau^- \rightarrow \pi^- \pi^0 \nu_\tau$ and $\tau^- \rightarrow e^- \bar{\nu}_e \nu_\tau$ have branching fractions of 0.61 % and 0.24 %, respectively. In the case of $\tau^- \rightarrow e^- \bar{\nu}_e \nu_\tau$, if a photon is radiated, it can convert into an additional $e^+ e^-$ pair, resulting in a total of three charged tracks and thus creating a false 3-prong signature. Similarly, for $\tau^- \rightarrow \pi^- \pi^0 \nu_\tau$, one of the photons from the π^0 decay can convert into an $e^+ e^-$ pair, also leading

6. τ -Lepton Lifetime Measurement Using Template Fits

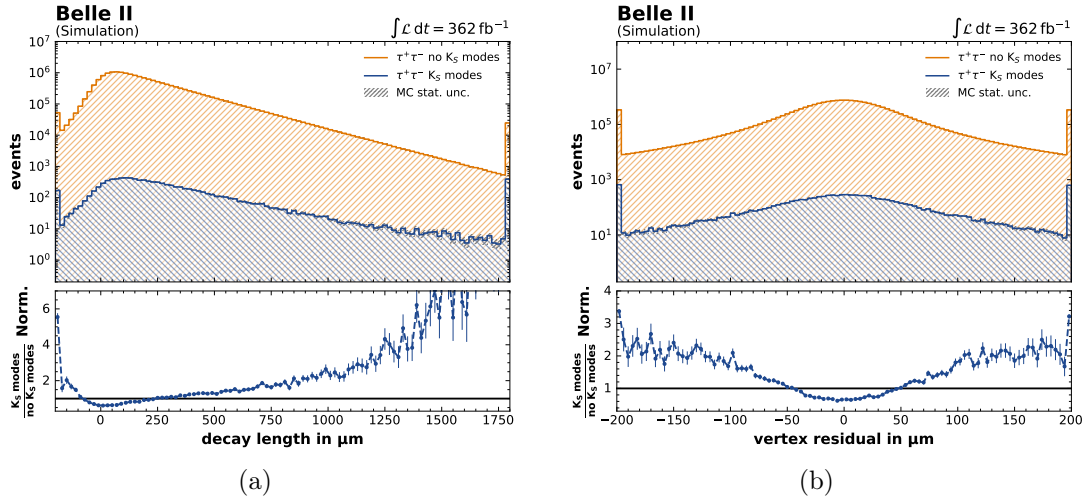


Figure 6.21.: Study with final corrections and selections applied. (a): Fraction of the K_S^0 modes in the decay length distribution. (b): Fraction of the K_S^0 modes in the vertex residual distribution. The statistical uncertainties of the histograms are not visible.

to a 3-prong-like topology.

The decay length shift between the 3-prong decay channels and the misidentified 1-prong decay channels is shown in Figure 6.22a. It is apparent that the misidentified 1-prong decay channels have a lower resolution compared to the 3-prong decay channels. Additionally, the $\tau^- \rightarrow \pi^- \pi^0 \nu_\tau$ channel shows slightly worse resolution than the channels without the π^0 . All the *other* combined misidentified 1-prong decay channels display even more pronounced resolution degradation.

Displaced vertices, as from photon conversion, lead to lower χ_{prob}^2 values in the vertex fit (see Section 6.5). This is illustrated in the ratio plot in Figure 6.22b, where the χ_{prob}^2 values for the misidentified 1-prong decay channels are compared to those for the 3-prong decay channels. A tighter selection in terms of the χ_{prob}^2 might be beneficial to reduce further the fraction of the 1-prong modes.

6.4.6. Selection Summary

The discussed selections result in a simulated dataset containing 15,002,235 signal events and 613,493 background events in the signal region, leading to a signal purity of 96.07%. For the background-dominated side region, the simulated dataset consists of 565 signal events and 151,701 background events, corresponding to a background contribution of 99.63%. The composition of the simulated dataset is listed in Table 6.10.

In the signal region, the $c\bar{c}$ contribution is found to be 0.56%, and the $\ell^+\ell^- X^+ X^-$ contribution is found to be 0.2%.

Figure 6.23a shows the composition of the decay length distribution for the signal region and Figure 6.23b shows the composition of the $M_{\tau_{3p}}$ distribution of the side region. In the decay length distribution, the exponential tails caused by own lifetimes is visible for the challenging $c\bar{c}$ and $\ell^+\ell^- X^+ X^-$ samples.

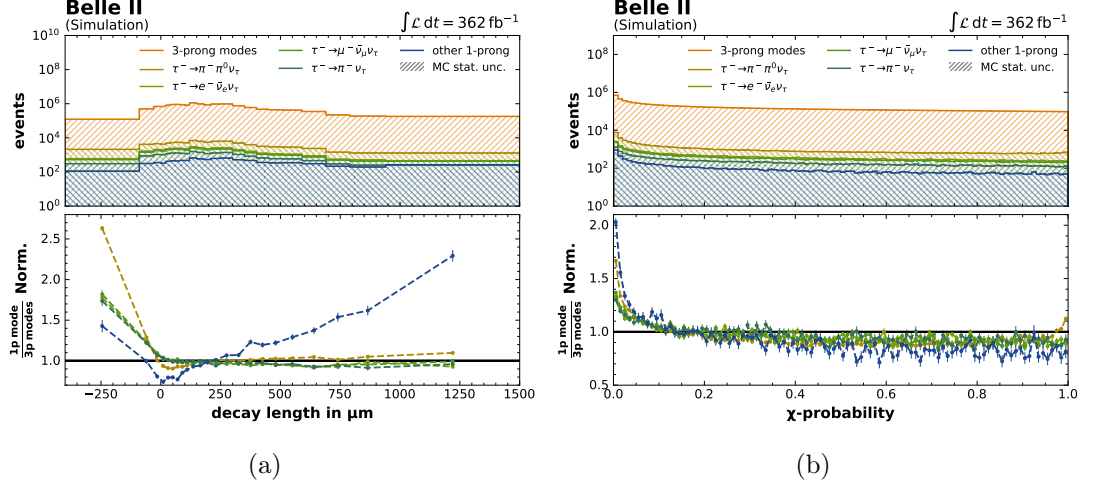


Figure 6.22.: (a) Introduced decay length shift by the 1-prong decay mode contribution of the $\tau^+\tau^-$ sample. (b) χ -probabilities of the τ_{3p} vertex fit of the 1-prong decay mode contribution compared to the 3-prong modes. The statistical uncertainties of the histograms are not visible. (Both figures after yield and template correction, see Section 6.6.2 and Section 6.6.4)

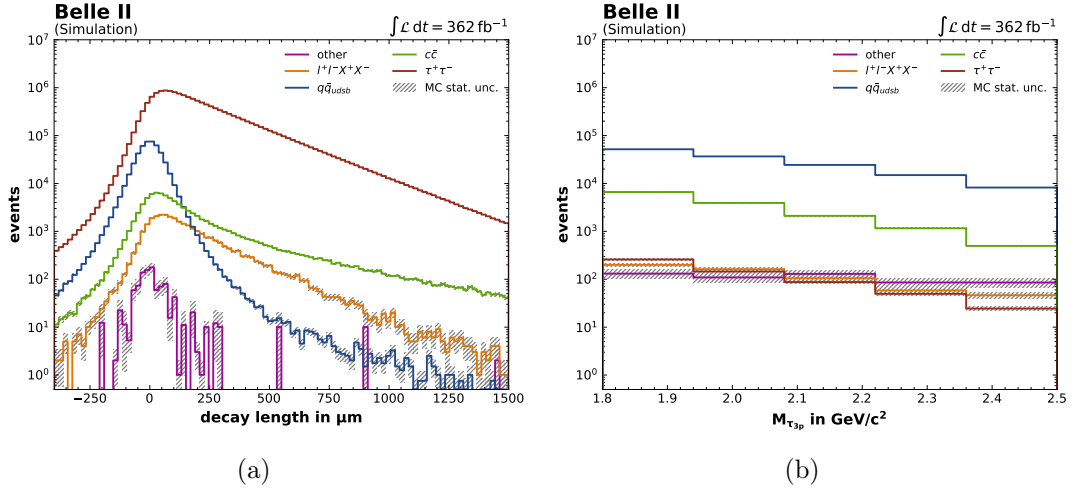


Figure 6.23.: Simulated data set with applied event selection: (a) Signal region decay length composition. (b) Side region $M_{\tau_{3p}}$ composition.

The experimental data sample includes 15,759,197 events after all selections, resulting in a residual yield difference of 0.91 % between the experimental data and simulated data in the signal region. In the side region, the experimental data includes 98,087 events, leading to a residual yield difference of 35.58 %. This is caused by the mismodeling of the $q\bar{q}$ sample due to probably incorrect cross-sections in the $q\bar{q}$ generation. This effect was already observed in [19].

To address the yield discrepancies and improve the modeling accuracy, correction studies are

6. τ -Lepton Lifetime Measurement Using Template Fits

Sample	Signal region		Side region	
	Events	Fraction in %	Events	Fraction in %
Signal	15,002,235	96.07	565	0.37
Background	613,493	3.93	151,701	99.63
$u\bar{u}$	329,959	2.11	92,721	60.89
$s\bar{s}$	6974,778	0.62	26,608	17.47
$c\bar{c}$	87,218	0.56	14,324	9.41
$d\bar{d}$	64,724	0.41	16,816	11.04
$\ell^+\ell^-X^+X^-$	31520	0.20	572	0.38
$b\bar{b}$	1,577	0.01	119	0.08
e^+e^-	847	0.01	222	0.15
$e^+e^-\ell^+\ell^-$	155	<0.01	316	0.21
$\mu^+\mu^-$	10	<0.01	3	<0.01
$hh(h^0)\gamma$	5	<0.01	1	<0.01
Experimental data	15,759,197		98,087	

Table 6.10.: Number of events in the simulated and experimental datasets. Additionally, the simulated dataset is split by sample.

presented in Section 6.6.4.

6.5. Vertex Fit

The key element of the τ -lepton lifetime measurement is the reconstruction of the τ_{3p} decay vertex from the tracks of the charged daughter particles, as discussed in Section 6.2. With infinite detector resolution and no material interaction, the three tracks would meet exactly at the point where the τ_{3p} decays⁸. Due to the finite precision of trajectory measurements, the three tracks do not intersect at a single point. In a process called *vertex fitting*, the track parameters are adjusted so that they converge at the most probable vertex. In this analysis, the vertex fit is performed using **TreeFitter** (see Section 4.4.4).

In this section, the precision of the vertex fit is evaluated using both simulated and experimental datasets. The impact of the PXD hits (see Chapter 5) on the vertex reconstruction is analyzed, and a corresponding selection criterion is derived.

6.5.1. Measuring the Vertex Resolution

To study the agreement of the vertex fit between simulated and experimental data, a method that is not sensitive to the lifetime is needed. Using observables such as the vertex position or the decay length would “unblind” the measurement. This challenge is addressed by reconstructing the π_{3p}^\pm tracks into a two-track vertex and measuring the DOCA $\mathbf{d}_{2\times 1}$ from that two-track vertex to the remaining track, as shown in Figure 6.24a. This approach enables measurement of the vertex residual, a quantity that is unaffected by the lifetime.

The two-track vertex fit is performed on the sub-leading p_T and low p_T track, with the remaining single track being the leading p_T track. The DOCA vector $\mathbf{d}_{2\times 1}$ is calculated by

$$\mathbf{d}_{2\times 1} = \mathbf{r}_p - \mathbf{r}. \quad (6.18)$$

Here, \mathbf{r} is the vector from the leading p_T track at the POCA \mathbf{t} to the reconstructed two-track vertex \mathbf{v} with $\mathbf{r} = (\mathbf{v} - \mathbf{t})$, and $\mathbf{r}_p = (\mathbf{r} \cdot \hat{\mathbf{e}}_p) \cdot \hat{\mathbf{e}}_p$ is the projection of \mathbf{r} onto the direction $\hat{\mathbf{e}}_p = \frac{\mathbf{p}}{|\mathbf{p}|}$ of the leading p_T track.

Since the measurement of the decay length is performed in the xy -plane, the distance vector $\mathbf{d}_{2\times 1, xy}$ is also treated in the xy -plane. It is accounted for, whether the track passes “left” or “right” the two track vertex. The so-called *vertex residual* $d_{2\times 1}$ in the xy -plane is the z -component of the cross-product

$$d_{2\times 1} = (\hat{\mathbf{e}}_p \times \mathbf{d}_{2\times 1})_z \quad (6.19)$$

$$= \cos \varphi \cdot d_{2\times 1, y} - \sin \varphi \cdot d_{2\times 1, x}, \quad (6.20)$$

with φ as the azimuthal angle of the leading p_T track. Figure 6.24b shows the measured vertex residual distribution for the simulated and experimental datasets.

The distribution shows increasing mismodeling in the tails $|d_{2\times 1}| > 100 \mu\text{m}$, while in the central region $|d_{2\times 1}| < 100 \mu\text{m}$ the experimental data is described well by the simulation. Therefore, the $|d_{2\times 1}| < 100 \mu\text{m}$ selection criteria is required in Table 6.8.

The *vertex resolution* is estimated via the width of the vertex residual distribution, extracted

⁸Assuming intermediate states have no lifetime.

6. τ -Lepton Lifetime Measurement Using Template Fits

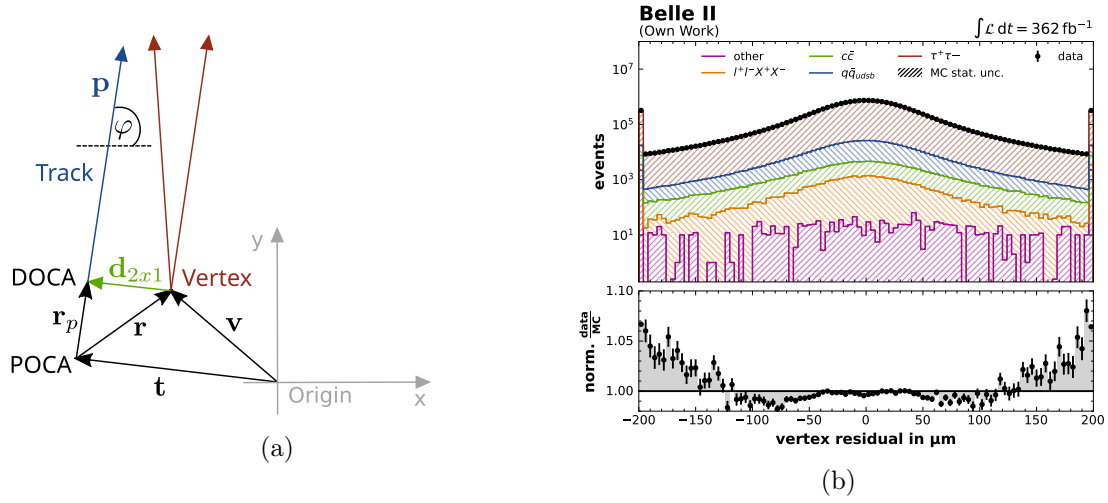


Figure 6.24.: (a): Definition of the closest distance $d_{2 \times 1}$ between a track and a two-track vertex \mathbf{v} . (b): Measured vertex residual of the simulation and experimental data. The statistical uncertainty of the histogram is not visible.

from a *Student's t* fit, defined by

$$f(t|\nu) = A \frac{\Gamma\left(\frac{\nu+1}{2}\right)}{\sqrt{\nu\pi} \Gamma\left(\frac{\nu}{2}\right)} \left(1 + \frac{t^2}{\nu}\right)^{-\frac{\nu+1}{2}}, \quad (6.21)$$

where $t = (x - \mu)/\sigma$, μ is the location of the maximum, σ is the distribution width (vertex resolution), A is the normalization factor, Γ is the Gamma distribution, and the parameter ν describes the tail contributions, shifting the distribution away from a Gaussian shape. For $\lim_{\nu \rightarrow \infty}$, the Student's t-distribution approaches a Gaussian distribution.

Figure 6.25 shows the results for simulated and experimental data, respectively. For both datasets, a vertex resolution of approximately $33 \mu\text{m}$ is measured.

6.5.2. Impact of PXD Hit Requirements

To understand how the vertex resolution is influenced by the number of PXD hits, a study is conducted with different configurations of PXD hit requirements for the π_{3p}^\pm tracks:

- **No PXD requirement:** The π_{3p}^\pm tracks may have PXD hits or lack them (this configuration is shown in Figure 6.25).
- **≥ 1 PXD hit:** Each of the π_{3p}^\pm tracks must have at least one PXD hit.
- **1 w/o PXD hit:** One of the π_{3p}^\pm tracks has no PXD hit, while the others have at least one PXD hit.
- **No PXD hit:** None of the π_{3p}^\pm tracks has a PXD hit.

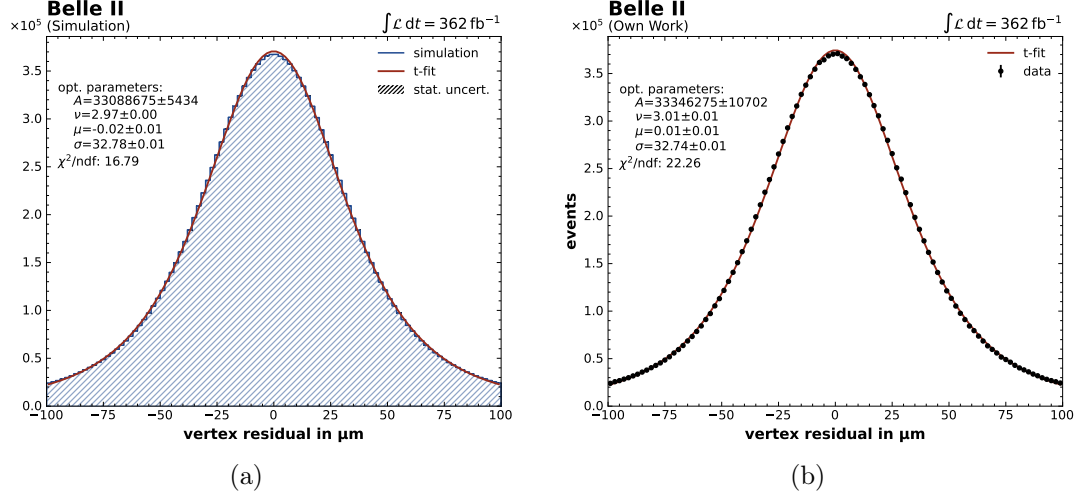


Figure 6.25.: (a): Student's t fit of simulated vertex resolution. (b): Student's t fit of experimental vertex resolution.

For each configuration, the vertex resolution is measured as explained in Section 6.5.1. The fit results are listed in Table 6.11. The ≥ 1 *PXD hit* configuration shows a $1 \mu\text{m}$ improvement in vertex resolution compared to the *no PXD requirement* configuration, due to the overall high PXD hit efficiency. When one of the π_{3p}^\pm tracks lacks a PXD hit, the vertex resolution is approximately 30% poorer compared to the ≥ 1 *PXD hit* configuration. The *no PXD hit* configuration exhibits roughly twice the degradation in vertex resolution relative to the *no PXD requirement* or ≥ 1 *PXD hit* configurations⁹.

The results show that requiring a PXD hit is beneficial. However, the PXD inefficiency is not well-modeled in the simulation which can introduce systematic uncertainties into the lifetime fit. Figure 6.26 shows the PXD inefficiency for π_{3p}^\pm tracks missing a PXD hit in both simulated and experimental data. It is visible, that the *dead and inefficient gates* are more prominent in the experimental data than in the simulation. Additionally, the detector exhibits a gap between the two half-shells at $\phi \approx -0.1$ rad and $\phi \approx 2.95$ rad, which is not modeled in the simulation.

The discrepancy between simulation and experimental data is also reflected in the normalization factor A in Table 6.11. For example, the *no PXD hit* configuration shows a normalization factor for experimental data that is ten times larger than for the simulation.

Requiring a PXD hit for each π_{3p}^\pm track increases mismodeling for $\theta_{\tau_{3p}}$ and $p_{T,\tau_{3p}}$, which significantly impacts the decay length shape distribution. Figure 6.27a shows the decay length shape-shifts for the simulation and the experimental data¹⁰ when additionally, a PXD hit requirement is applied. The relative shift between these two shape-shifts is shown in Figure 6.27b.

⁹Since the number of events with the *no PXD hit* configuration is rather small, and this study does not account for the track arrangement forming the decay vertex, it is possible that a disadvantageous track arrangement not only leads to a reduced number of PXD hits but also directly causes a reduced vertex resolution. Consequently, the *no PXD hit* configuration should not be interpreted as the resolution obtainable in the absence of a PXD.

¹⁰Only the relative shape-shift is studied with and without PXD requirements. This analysis contains no lifetime information.

6. τ -Lepton Lifetime Measurement Using Template Fits

Track Req.	Dataset	Fit Parameters				χ^2/ndf
		A	ν	μ	σ	
no PXD req.	simulation	$3.31 \times 10^7 \pm 5 \times 10^3$	2.97 ± 0	-0.02 ± 0.01	32.78 ± 0.01	16.8
	experiment	$3.33 \times 10^7 \pm 1 \times 10^4$	3.01 ± 0.01	0.01 ± 0.01	32.74 ± 0.01	22.3
≥ 1 PXD hit	simulation	$2.96 \times 10^7 \pm 5 \times 10^3$	3.26 ± 0.01	-0.01 ± 0.01	31.91 ± 0.01	16.3
	experiment	$2.81 \times 10^7 \pm 9 \times 10^3$	3.58 ± 0.01	0.01 ± 0.01	31.43 ± 0.01	19.9
1 w/o PXD hit	simulation	$3.34 \times 10^6 \pm 4 \times 10^3$	2.07 ± 0.02	0.07 ± 0.02	45.06 ± 0.03	0.4
	experiment	$5 \times 10^6 \pm 1 \times 10^4$	1.93 ± 0.03	0.01 ± 0.04	44.79 ± 0.05	1.5
no PXD hit	simulation	$2 \times 10^4 \pm 1 \times 10^3$	4 ± 1.9	0.3 ± 0.56	69 ± 1.3	0.3
	experiment	$2 \times 10^5 \pm 1 \times 10^4$	1.6 ± 0.3	0.1 ± 0.35	72 ± 1.4	0.9

Table 6.11.: Student's t fit results of the vertex resolution with different PXD hit requirements for the π_{3p}^\pm tracks. The fit parameter A corresponds to the number of events, and the fit parameter σ corresponds to the vertex resolution.

It is clearly visible that imposing a PXD hit requirement introduces a decay-length shape-shift between simulation and experimental data.

This study shows that requiring a PXD hit would introduce a new source of systematic uncertainty, while the observed improvement in the vertex resolution remains small. For that reason, an alternative approach is chosen by imposing a selection criterion on the vertex residual, as discussed in Section 6.5.4.

6.5.3. Mismodeling of the Vertex Residual

In Section 6.5.1, it was shown that vertex residual (Figure 6.24b) is not well represented by the simulation in the tail regions. The origin of these vertex residual tails can be attributed to multiple scattering.

Figure 6.28 (a), (c), and (e) show the ϕ distribution for each of the π_{3p}^\pm in the vertex residual tail region ($|d_{2 \times 1}| > 100 \mu\text{m}$), while Figure 6.28 (b), (d), and (f) show the ϕ distribution in the vertex residual central region ($|d_{2 \times 1}| < 100 \mu\text{m}$). It can be clearly seen that events with large vertex residual (Figure 6.28 (a), (c), and (e)) predominantly occur in the PXD overlap regions, visible as peaking structures. These PXD overlap regions contain switcher ASICs and capacitors which exhibit significantly more material budget than the active sensor region. The structures become more prominent for lower $\pi_{3p}^\pm p_T$ tracks, with the most pronounced effect observed in Figure 6.28e. This is caused by the lower $p_T \pi_{3p}^\pm$, which on average also have a lower momentum compared to the higher $p_T \pi_{3p}^\pm$ (see Figure A.11) and are, therefore, more affected by multiple scattering (see Section 2.3). In the ϕ distributions, small dips appear for events with low vertex residual ($|d_{2 \times 1}| < 100 \mu\text{m}$) in Figure 6.28 (b), (d), and (f). The high-momentum track in Figure 6.28 ((a) and (b)) is the least affected. The dips in the $|d_{2 \times 1}| < 100 \mu\text{m}$ distribution are caused by the fact that more events appear at the spikes in the $|d_{2 \times 1}| > 100 \mu\text{m}$ distribution.

Figure 6.28a shows that the vertex residual in the experimental data is worse modeled for $\phi \leq -2 \text{ rad}$ and $\phi \geq 1 \text{ rad}$. This trend is also observable in Figure 6.28 (c) and (e), although additional mismodeling of the overlap regions distorts it further, particularly for lower p_T tracks.

The $\phi_{\pi_{3p}^\pm}$ distributions in the central region of the vertex residual distribution have a small but still sizable deviation between experimental data and simulation. The deviation is more

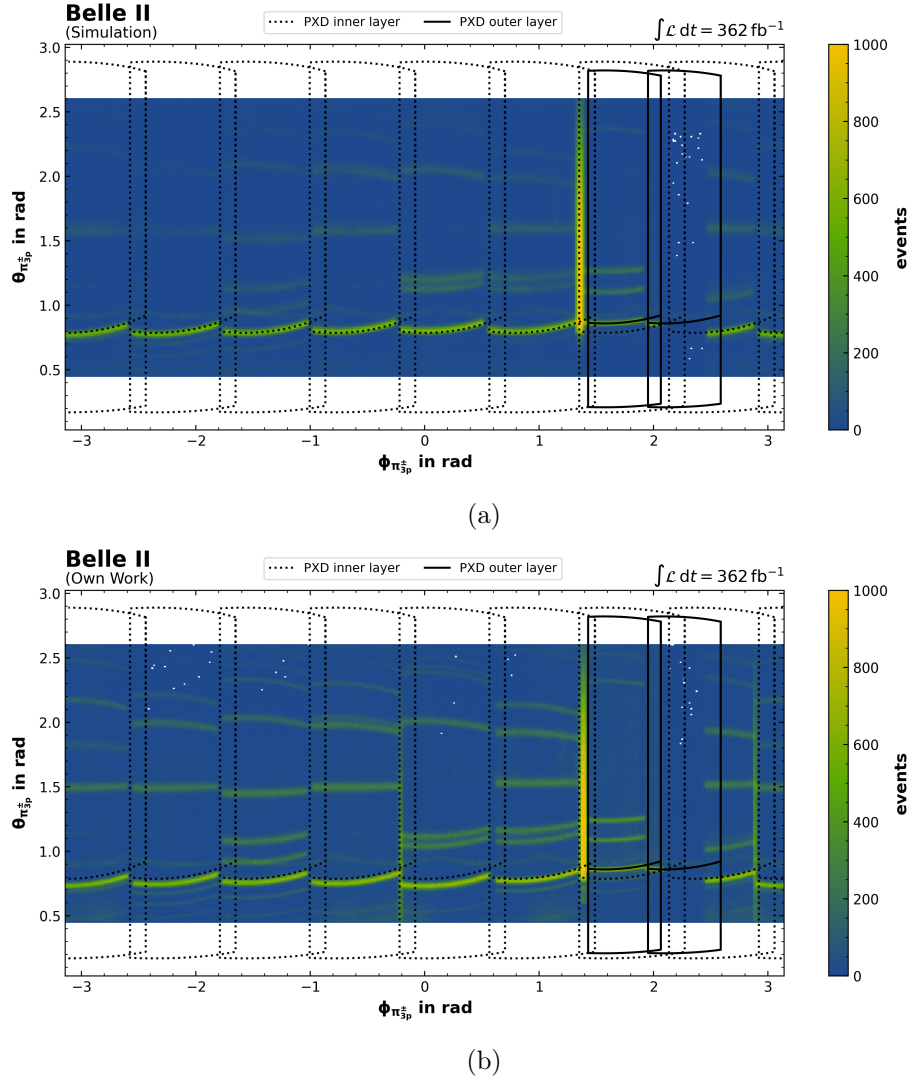


Figure 6.26.: π_{3p}^{\pm} tracks without PXD hit, no vertex residual requirement applied. For orientation, the contours of the 8 inner layer ladders and 2 outer layer ladders are indicated. The green to orange colored areas highlight the inefficient PXD regions. The stripes at $0.7 \text{ rad} \geq \theta \leq 0.9 \text{ rad}$ correspond to glue gaps between PXD modules, and the region at $\phi \approx 1.2 \text{ rad}$ indicates a small gap due to a “dead” module, not fully covered by the outer layer ladders. (a) shows the simulated data and (b) shows the experimental data.

pronounced for π_{3p}^{\pm} with lower p_T (compare Figure 6.28b and Figure 6.28f).

The $\theta_{\pi_{3p}^{\pm}}$ distributions are shown in Figure 6.29. For the low p_T track in Figure 6.29 (e) and the sub-leading p_T track in Figure 6.29 (c), it is apparent that the PXD ladder glue gaps between 0.7 rad and 0.85 rad , as well as the SVD glue gap between 0.85 rad and 0.95 rad , are shifted between the experimentally measured tracks angles and the simulation. This shift is caused by

6. τ -Lepton Lifetime Measurement Using Template Fits

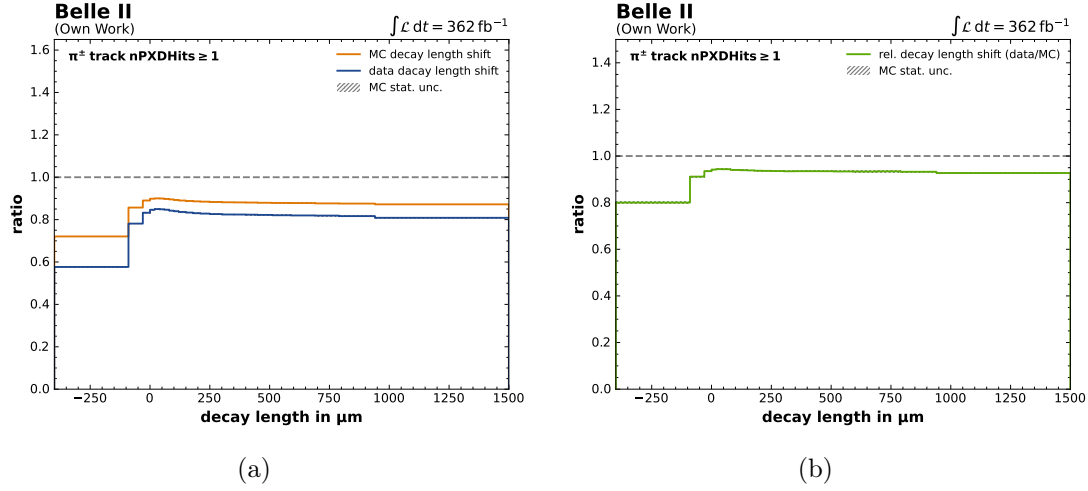


Figure 6.27.: (a): Decay length shape-shifts of ≥ 1 *PXD hit* requirement and *no PXD hit* requirement for experimental data and simulated data. (b): Ratio between the two decay length shape-shifts in (a).

detector misalignment (see Section 6.5.5) which is not accounted for in the simulation. This shift is also visible in Figure 6.26, when comparing the inefficiencies in the simulation (a) with the experimental data (b).

In Figure 6.29 (c) and (e) in $1\text{rad} \leq \theta \leq 1.15\text{rad}$, $1.35\text{rad} \leq \theta \leq 1.6\text{rad}$, and $1.9\text{rad} \leq \theta \leq 2.1\text{rad}$ the not well modeled dead and inefficient gates are visible (see Section 6.5.2). Figure 6.29e shows that the mismodeling increases for small and large θ values. For the leading p_T track in Figure 6.29a, this effect is smeared out because lower p_T tracks are more affected by a missing PXD hit, which thus drives vertex residual.

It is observed that events with large vertex residual values also exhibit the largest mismodeling in the $\phi_{\pi_{3p}^\pm}$ and $\theta_{\pi_{3p}^\pm}$ distributions. The mismodeling is attributed to the PXD efficiency in regions with inefficient and dead gates, as well as in the very forward and backward regions of the π_{3p}^\pm tracks, particularly for low- p_T tracks.

6.5.4. Vertex Requirements

For a precise decay length measurement, which is essential for the τ -lepton lifetime measurement, an accurately reconstructed decay vertex is crucial. As discussed in Section 6.5.2, PXD hit requirements cannot be used to ensure a precise vertex reconstruction. Instead, the vertex residual, discussed in Section 6.5.3, offers an alternative approach to achieve an accurate reconstructed decay vertex. A vertex residual requirement of $|d_{2 \times 1}| \leq 100 \mu\text{m}$ is chosen, which is approximately half of the mean tau decay length ($\sim 219 \mu\text{m}$).

Figure 6.30a shows this requirement has no significant impact on the shape-shift of the decay length distributions of both the experimental data and the simulation. Only the negative region and the far away positive region indicate a small resulting shape-shift relative to each other. This is depicted in the ratio in Figure 6.30b. In the relevant high statistic region $0 \mu\text{m} - 500 \mu\text{m}$ no significant deviation is observed.

The template correction discussed in Section 6.6.4 will mitigate the mismodeling in the central region of the vertex residual distribution. In Section 6.8.4, the impact of the remaining mismodeling after applying the template correction is evaluated.

6.5.5. Alignment

In the simulation, each detector and component is assumed to be exactly positioned and shaped as designed. However, mechanical inaccuracies, movements, and deformations distort the measured trajectories, leading to degradation in detector performance. Mechanical inaccuracies on the order of a few 100 μm to a few mm (as observed in Figure 6.26) can significantly impact the physics performance of the VXD, which has a vertex resolution of approximately 30 μm . Calibration measurements are conducted to determine alignment constants, which are then used to correct for shifts and distortions.

At Belle II, a track-based alignment is performed, wherein the positions of numerous reconstructed tracks are compared to the actual locations of the hits they produce in the detectors. The distances between the reconstructed tracks and their corresponding hits are termed residuals, and the alignment procedure is based on minimizing these residuals. However, certain detector movements or deformations, known as weak modes, do not affect the residuals when the tracks originate from the IP. To reduce these weak modes, different track topologies are used in the alignment procedure, such as cosmic tracks, single tracks from the IP or off-IP, and IP-constrained decays. The alignment procedure at Belle II is described in detail in [102][42].

The alignment procedure and the resulting parameters are also subject to uncertainties. These uncertainties may arise from detector vibrations, movements between alignment survey measurements, and other systematic or statistical uncertainties in these measurements. This results in a residual misalignment despite the applied alignment corrections, referred to as *misalignment*. Misalignment impacts tracking accuracy and therefore affects the vertex position. This is addressed and studied in Section 6.8.5.

6. τ -Lepton Lifetime Measurement Using Template Fits

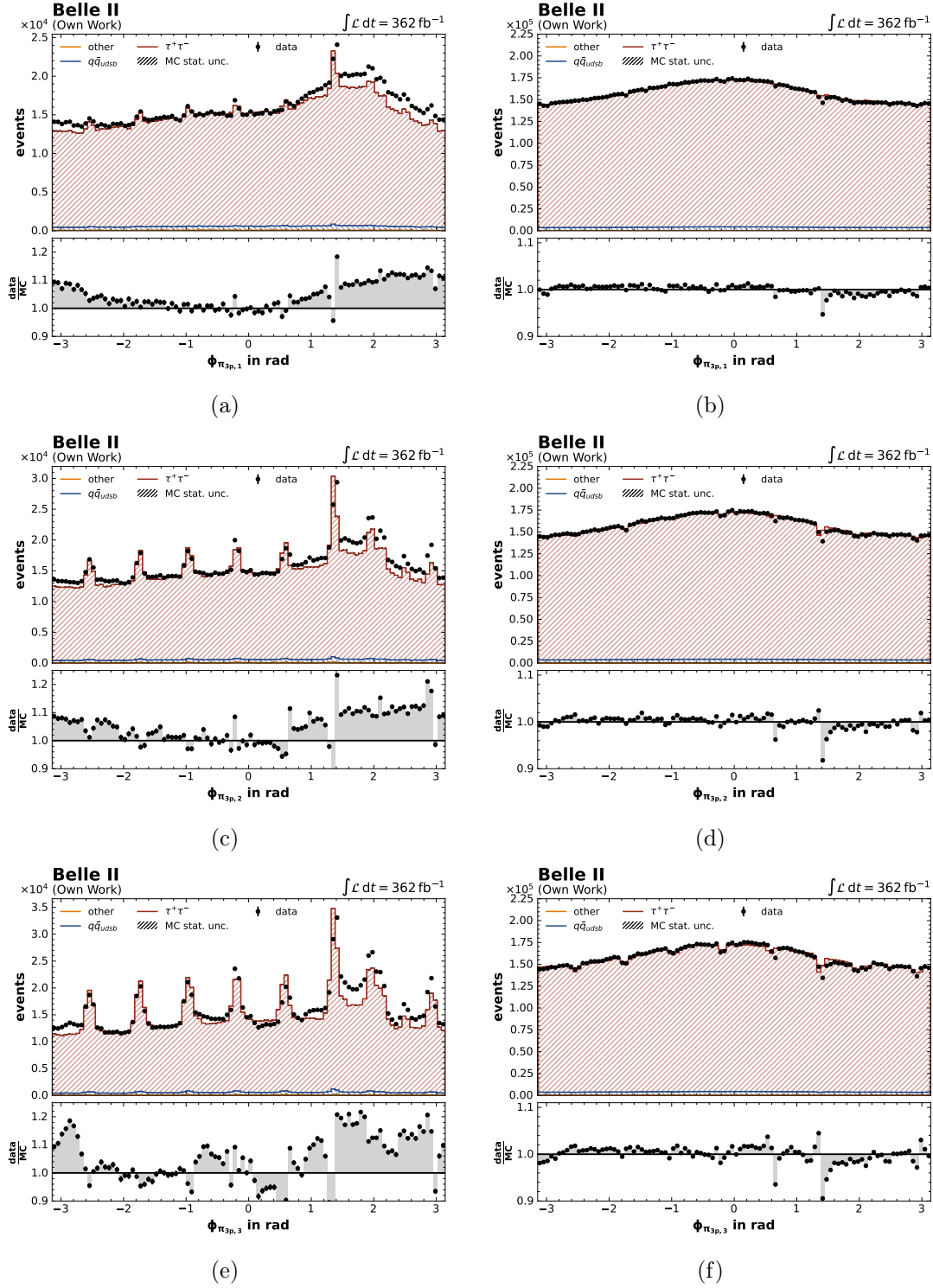


Figure 6.28.: The left column shows the $\phi_{\pi_{3p}^\pm}$ distributions for events with large vertex residual $|d_{2 \times 1}| > 100 \mu\text{m}$, while the right column shows events with $|d_{2 \times 1}| < 100 \mu\text{m}$. From top to bottom: (a) and (b) correspond to the leading $p_T \pi_{3p}^\pm$, (c) and (d) to the sub-leading $p_T \pi_{3p}^\pm$, and (e) and (f) to the low $p_T \pi_{3p}^\pm$. The statistical uncertainties of the histograms are not visible.

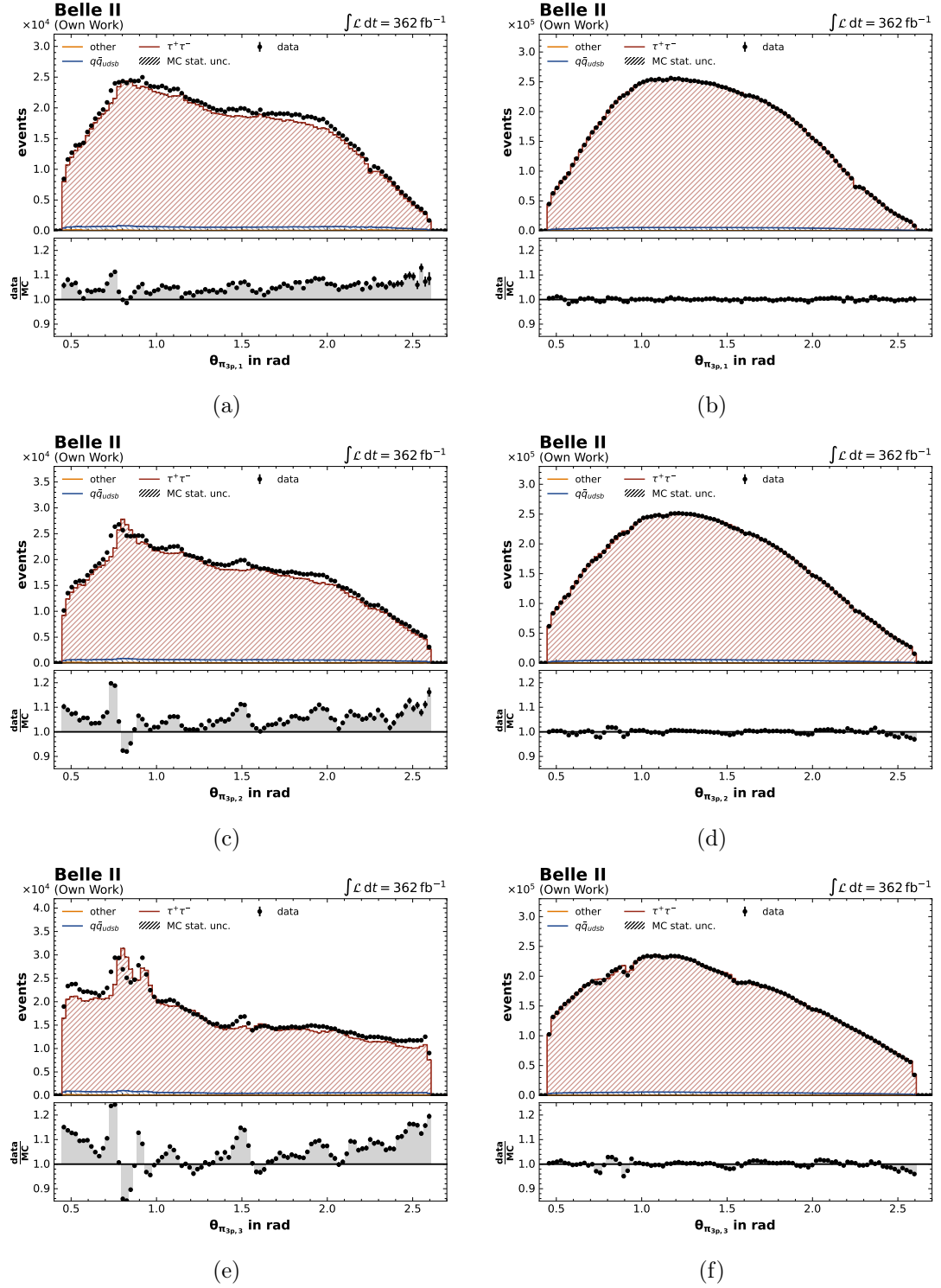


Figure 6.29.: The left column shows the $\theta_{\pi_{3p}^{\pm}}$ distributions for events with large vertex residual $|d_{2 \times 1}| > 100 \mu\text{m}$, while the right column shows events with $|d_{2 \times 1}| < 100 \mu\text{m}$. From top to bottom: (a) and (b) correspond to the leading $p_T \pi_{3p}^{\pm}$, (c) and (d) to the sub-leading $p_T \pi_{3p}^{\pm}$, and (e) and (f) to the low $p_T \pi_{3p}^{\pm}$. The statistical uncertainties of the histograms are not visible.

6. τ -Lepton Lifetime Measurement Using Template Fits

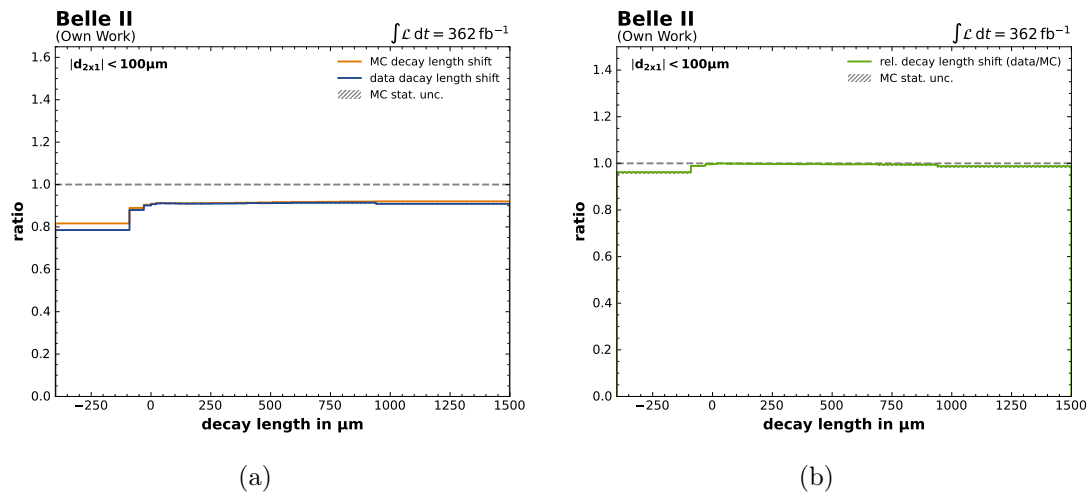


Figure 6.30.: (a): Decay length shape-shift between experimental data and simulation after applying the vertex residual requirement. (b): Relative decay length shape-shift between experimental data and simulation after applying the vertex residual requirement.

6.6. Template Configuration and Fit Setup

The base decay length template (referred to as the *nominal template*) is created from the samples discussed in Section 6.1.2. The nominal template corresponds to a τ -lepton lifetime of 290.57 fs. Templates with shifted lifetime hypotheses for the likelihood scan are generated from the nominal template using the re-weighting method discussed in Section 6.2.4. A step size of 0.01 fs is used within the range of 290.07 fs to 291.07 fs, and a step size of 0.05 fs is applied in the extended range from 289.07 fs to 292.07 fs.

This section begins with the validation of the re-weighting method. Next, the fit regions are introduced, followed by a discussion on the normalization of the simulated samples. Then the mismodeling of the observables is addressed, and a template correction is derived. Finally, the overall fit stability is evaluated.

6.6.1. Validation of the Template Re-Weighting Method

The re-weighting method is validated using four additional MC-generated $\tau^+\tau^-$ samples with different generator τ -lepton lifetimes (see Table 6.2). The validation study is performed exclusively on $\tau^+\tau^-$ samples.

For this study, two sets of templates are generated via re-weighting, each originating from a different base template. The first set is created using the nominal $\tau^+\tau^-$ sample, while the second set is generated from the separately generated and simulated -1 fs shifted lifetime $\tau^+\tau^-$ sample.

Figure 6.31a shows the decay length shifts relative to the -1 fs MC-generated template. The agreement of the observed decay length shifts between the MC-generated samples and the re-weighted templates demonstrates that the re-weighted templates closely match the shifts seen with the MC-generated shifted lifetime samples.

To validate that the template fit can distinguish between shifted lifetime samples, the two sets of templates are used in two separate fit setups. Since all the MC-generated $\tau^+\tau^-$ samples have the same size and result from the same production process with the same production cross-section, a normalization step is not necessary for this study.

Each fit setup is tested using the four MC-generated shifted lifetime samples as pseudo-data in a likelihood scan. Figure 6.31b shows the fit results for each of the two fit setups separately. The fit study covers a 2 fs range. The nominal fit setup is effectively fed with pseudo-data up to ± 1 fs symmetric around the nominal base template. The -1 fs shifted lifetime fit setup is effectively fed with pseudo-data up to $+2$ fs shifted lifetimes relative to the central base template.

For both fit setups, the fit results show no significant disagreement between the best-fit lifetime values and the expected lifetime values. All fit values lie within $\sim \pm 0.1$ fs with a fit uncertainty of approx 0.1 fs.

Given the previous τ -lepton lifetime measurements (see Section 3.3.2), it is expected that the measured lifetime value will be covered by the ± 2 fs range relative to the nominal template. The lifetime value of the -2 fs template is 3.46σ away from the current PDG τ -lepton lifetime value¹¹.

¹¹For the $+2$ fs template this is a bit less since the PDG τ -lepton lifetime is not exactly the lifetime value of the nominal template.

6. τ -Lepton Lifetime Measurement Using Template Fits

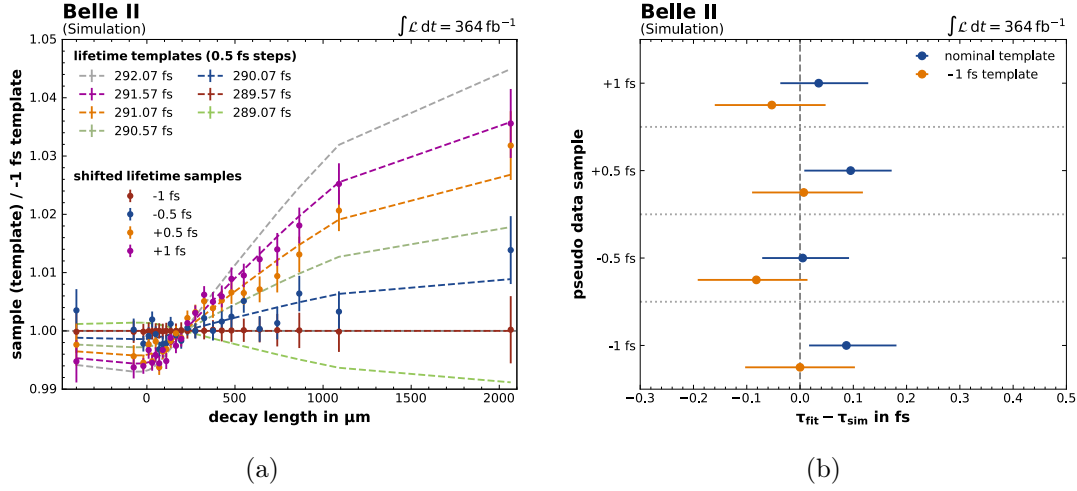


Figure 6.31.: (a): Comparison between templates created using the re-weighting method and MC-generated templates with different generator lifetimes. Shown are the relative decay length shifts with respect to the -1 fs sample. The dashed lines represent the expected decay length shifts from templates created with the re-weighting method using the -1 fs base template. The data points with error bars indicate the observed decay length shifts of the respective MC-generated samples, relative to the -1 fs base template. Since the base template corresponds to the MC-generated -1 fs sample, the data points for this sample lie exactly on the horizontal line at 1.0. (b): Lifetime fit results using two different sets of templates, one based on the nominal sample and the other on the -1 fs sample. Shown are the difference between the best-fit lifetime values, τ_{fit} , obtained from the best-fitting template, and the lifetime values of the MC-generated pseudo-data samples, τ_{sim} , used in the fit.

6.6.2. Fit Regions and Normalization

The two free normalization parameters, μ_{sig} and μ_{bkg} , included in Equation (6.6), allow for independent scaling of the signal and background components. Since the signal and background decay length distributions in the templates have different shapes, an incorrect predicted ratio between these components can introduce an artificial lifetime shift. Therefore, it is essential to determine the correct signal-to-background ratio. A prior *normalization likelihood fit* (referred to as the normalization fit) is performed before the lifetime fit to determine the signal-to-background normalization parameters.

To improve the background normalization capabilities, in addition to the *signal region*, a background-dominated *side region* is included in the normalization fit. The fit regions are described in detail below.

The normalization fit is set up with two single-bin fit channels. Each channel corresponds to a fit region and uses the two normalization parameters, μ_{sig} and μ_{bkg} . The normalization parameters are fully correlated between the two channels in the fit:

$$\mu_{\text{sig},1} = \mu_{\text{sig},2} \quad \text{and} \quad \mu_{\text{bkg},1} = \mu_{\text{bkg},2}.$$

The first channel contains the event yield from the signal region, while the second channel contains the event yield from the side region (see Table 6.10). The simulated data is fitted to the experimental data. Using the event selection discussed in Section 6.4, the normalization fit results in normalization factors of

$$\mu_{\text{sig}} = 1.024 \pm 0.011 \quad \text{and} \quad \mu_{\text{bkg}} = 0.645 \pm 0.007.$$

The two fit regions, with all other selection criteria applied (see Table 6.8), are illustrated in Figure 6.32. For the signal region, a mass window around the $M_{\tau_{3p}}$ peak is selected. This peak

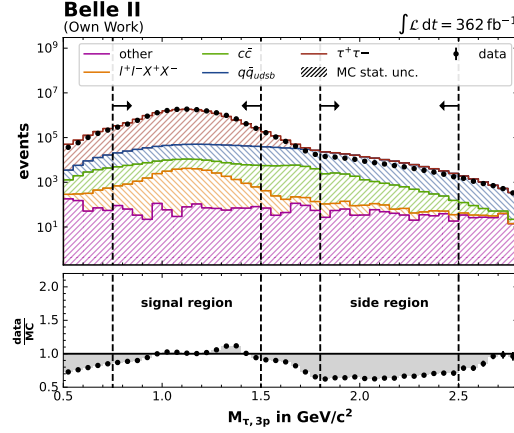


Figure 6.32.: Definition of the signal region and the background-dominated side region via the reconstructed τ_{3p} mass. The statistical uncertainty of the histogram is not visible.

appears approximately $500 \text{ MeV } c^{-2}$ below the actual τ -lepton mass value ($1.777 \text{ GeV } c^{-2}$) due to the missing energy described in Section 6.4.4. Consequently, the τ -lepton mass peak shifts to around $1.1 \text{ GeV } c^{-2}$. The $\tau^+ \tau^-$ purity in the low $M_{\tau_{3p}}$ region decreases significantly; therefore, $M_{\tau_{3p}}$ is required to be between $0.75 \text{ GeV } c^{-2}$ and $1.5 \text{ GeV } c^{-2}$.

In contrast, the high mass region is dominated by $e^+ e^- \rightarrow q\bar{q}$, leading to the selection of the side region where $M_{\tau_{3p}}$ is between $1.8 \text{ GeV } c^{-2}$ and $2.5 \text{ GeV } c^{-2}$. In this region, it is evident that the simulated $q\bar{q}$ contribution is overestimated by approximately 60%. However, due to the small background contribution in the signal region, this significant overestimation is not directly visible there.

Two sources of $M_{\tau_{3p}}$ mismodeling have been identified. The first arises in the $\tau^+ \tau^-$ sample and is caused by the **TauolaBelle2** generator. The second is related to the $q\bar{q}$ sample and is due to incorrect cross-sections (see Section 6.4.6).

For the actual lifetime fit, only the signal region is used. The templates are scaled using the normalization parameters obtained from the normalization fit. Since the lifetime fit is performed exclusively on the signal region, while the normalization fit was conducted on both the signal and side regions, the overall normalization between simulated and experimental data may still not be optimal when considering only the signal region.

To address this, the likelihood model of the lifetime fit is configured such that its two nor-

6. τ -Lepton Lifetime Measurement Using Template Fits

malization parameters are fully correlated: $\mu_{\text{glob}} = \mu_{\text{sig}} = \mu_{\text{bkg}}$. This approach allows for an overall normalization adjustment within the lifetime fit and ensures that the lifetime measurement is influenced only by decay length shape-shifts. Any effects related to normalization are absorbed. Systematic uncertainties introduced by normalization in the lifetime fit are discussed in Section 6.8.11.

6.6.3. Template Variations to Address Systematic Uncertainties

The likelihood model (Equation (6.6)) of the lifetime fit incorporates a global normalization (see Section 6.6.2) and NPs to account for systematic uncertainties. Since different lifetimes manifest only as decay length shape-shifts, systematic uncertainties are implemented as *template variations* with relative shape-shifts. These relative shape variations are calculated using the normalized ratio s :

$$s_i = \frac{n_i^{\text{var}}}{n_i^{\text{nom}}} \cdot \frac{n_{\text{tot}}^{\text{nom}}}{n_{\text{tot}}^{\text{var}}}, \quad (6.22)$$

where i is the decay length bin, n_i^{nom} is the yield in the nominal histogram, and n_i^{var} is the yield in the variation histogram. The last term is the normalization factor, where $n_{\text{tot}}^{\text{nom}}$ and $n_{\text{tot}}^{\text{var}}$ represent the total yield in the respective histograms. These relative shape variations are included as 1σ *envelopes* to constrain the correlated shape NPs (see Section 6.2.3). Parametrized is s associated with $\sigma_{\bar{\alpha}}$ of the correlated shape modifiers.

To generate a template variation caused by correcting discrepancies between simulated and experimentally measured data in a specific observable distribution, the simulated data are corrected through re-weighting. The derived event weights are applied during the binning process of template observable, resulting in the variation histogram.

If only one direction of variation (up or down) is available, the variation is mirrored (referred to as *symmetrized*). This process creates symmetric up and down variations of the templates. While this approach is conservative and may increase the fit uncertainty – since the fit can adjust the NPs in the opposite direction of the expected variation – it is necessary because the fit algorithm requires both up and down variations to constrain the NPs.

Significant asymmetric up and down variations are also symmetrized by mirroring the respective maximal up or down variation per bin (referred to as *maximal symmetrized*).

Depending on the statistical precision of the simulated dataset, varied decay length distributions are *smoothed* to remove statistical fluctuations. For instance, strong oscillations in the variations may reduce the impact of the fit uncertainty, leading to underestimation. To smooth the distribution, individual bins are averaged with adjacent bins; if needed, one or two neighboring bins are combined.

6.6.4. Mismodeling and Template Correction

After applying all selections from Table 6.8, the observable distributions in Figure A.4 to Figure A.10 still exhibit mismodeling in various regions. In this section, the mismodeling with the largest impact is identified, and a correction method is proposed.

NPs are derived from the deviations between the simulated and experimental data distribu-

tions¹². Event weights are calculated based on their ratios, and variation histograms are created to constrain the NPs, as discussed in Section 6.6.3.

The mismodeling and its impact is examined with pseudo-data lifetime fits. The nominal template is fed as pseudo-data into the various fit setups explained below. The respective fit uncertainties obtained from the fits are used to evaluate the results.

As a reference, a *baseline* lifetime fit is set up, including only data and MC statistical uncertainty NPs. This baseline result is compared to fit setups where additional mismodeling NPs are included. In this way, the mismodeling with the largest impact is determined. In the next step, the templates are corrected for the mismodeling of observables with large impact, by re-weighting.

Two re-weighting methods are applied, *1D re-weighting* and *2D re-weighting*, to correct the simulated distributions so that they more accurately describe the experimental data distribution. In the 1D re-weighting method, the simulated data is corrected only in a single observable distribution using event weights obtained from the shape differences of the distributions. In the 2D re-weighting method, the event weights are derived from the shape differences in 2D histograms of two observable distributions, allowing both distributions to be corrected simultaneously. The event weights from the 1D or 2D re-weighting are then applied to all signal region templates and all correlated shape uncertainty NP constraint envelopes (referred to as *template correction*). The technical implementation is discussed in Section 6.7.4 and Appendix A.7.1.

The residual mismodeling after the template correction is also incorporated into NPs to evaluate the impact of the corrections. Lifetime fits with the individual NPs included are evaluated both with and without the corrections. The results of this study are presented in Table 6.12 and are explained in detail below.

The baseline fit exhibits a fit uncertainty of 0.09 fs, corresponding to the statistical and systematic uncertainties arising from limited statistical precision in the simulation. For the original *uncorrected templates*, dominant fit uncertainties are observed due to mismodeling, particularly for $p_{T,\tau_{3p}}$ and $\theta_{\tau_{3p}}$. The fit setups including the $p_{T,\tau_{3p}}$ and $\theta_{\tau_{3p}}$ NPs increase the uncertainty from 0.09 fs to 0.23 fs and 0.24 fs, respectively. The individual $p_{T,\pi_{3p}}$ and $\theta_{\pi_{3p}}$ distributions also contribute considerably to this uncertainty. Including all listed mismodeling NPs in Table 6.12 results in a fit uncertainty of 0.36 fs.

In general, if a decay length shape-shift due to mismodeling uncertainties resembles the lifetime-induced decay length shape-shift, a significant increase in fit uncertainty is expected. The fit can adjust these NPs without a large penalty to improve the likelihood of several lifetime templates fitting the observed data. Figure 6.33 shows the associated 1σ envelopes of the symmetrized decay length shape-shifts caused by the mismodeling of (a) $M_{\tau_{3p}}$ and (b) $\theta_{\tau_{3p}}$. For the $M_{\tau_{3p}}$ mismodeling, the symmetrized shape-shift envelopes do not follow the lifetime-dependent decay length shape-shifts, which keeps the fit uncertainty for this NP included at a level comparable to the observed baseline fit uncertainty. In contrast, the $\theta_{\tau_{3p}}$ mismodeling-induced decay length shape-shift closely aligns with the lifetime-dependent decay length shape-shift from 0 μm to 1250 μm , with a crossing point around 200 μm . This alignment increases the fit uncertainty from 0.09 fs to 0.24 fs when this NP is included.

Figure 6.34a and Figure 6.34c show the mismodeling in the $p_{T,\tau_{3p}}$ and $\theta_{\tau_{3p}}$ distributions. The $p_{T,\tau_{3p}}$ distribution shows a $\sim 5\%$ overestimation in the low- p_T region, transitioning to a $\sim 4\%$ underestimation in the high- p_T region. The $\theta_{\tau_{3p}}$ distribution shows a $\sim 5\%$ underestimation in

¹²After normalization discussed in Section 6.6.2.

6. τ -Lepton Lifetime Measurement Using Template Fits

Included Systematic	Best Fit in fs	68 % CL in fs		
		no correct.	$p_{T,\tau_{3p}}$	$p_{T,\tau_{3p}} \otimes \theta_{\tau_{3p}}$
data + mc stat.	290.57	± 0.09	± 0.09	± 0.09
+ $p_{T,\tau_{3p}}$	290.57	± 0.23	± 0.09	± 0.09
+ $p_{\tau_{3p}}$	290.57	± 0.15	± 0.09	± 0.09
+ $M_{\tau_{3p}}$	290.57	± 0.09	± 0.09	± 0.09
+ $d_{2 \times 1}$	290.57	± 0.09	± 0.09	± 0.09
+ $\theta_{\tau_{3p}}$	290.57	± 0.24	± 0.12	± 0.09
+ $p_{T,\pi_{3p,1}}$	290.57	± 0.11	± 0.13	± 0.13
+ $p_{T,\pi_{3p,2}}$	290.57	± 0.16	± 0.12	± 0.12
+ $p_{T,\pi_{3p,3}}$	290.57	± 0.10	± 0.10	± 0.10
+ $\theta_{\pi_{3p,1}}$	290.57	± 0.21	± 0.11	± 0.09
+ $\theta_{\pi_{3p,2}}$	290.57	± 0.19	± 0.11	± 0.10
+ $\theta_{\pi_{3p,3}}$	290.57	± 0.14	± 0.10	± 0.10
+ V_{thrust}	290.57	± 0.09	± 0.09	± 0.09
+ $E_{\text{evt}}^{\text{vis},*}$	290.57	± 0.09	± 0.09	± 0.09
+ $\theta_{p,\text{evt}}^{\text{miss},*}$	290.57	± 0.10	± 0.09	± 0.10
+ $p_{\text{evt}}^{\text{miss},*}$	290.57	± 0.09	± 0.09	± 0.09
+ $M_{\text{evt}}^2 \text{ miss},*$	290.57	± 0.09	± 0.09	± 0.09
+ $n_{\pi_{0,1p}}$	290.57	± 0.09	± 0.09	± 0.09
+ $n_{\gamma_{1p}}$	290.57	± 0.10	± 0.09	± 0.09
+ $n_{\gamma_{3p}}$	290.57	± 0.10	± 0.09	± 0.09
all mismodeling	290.57	± 0.36	± 0.23	± 0.21

Table 6.12.: τ -lepton lifetime pseudo-data fit results for various observable mismodeling cases.

Three types of template corrections are compared in the 68 % CL (fit uncertainty) columns: the first has no template correction, the second includes a $p_{T,\tau_{3p}}$ template correction, and the third applies a combined $p_{T,\tau_{3p}} \otimes \theta_{\tau_{3p}}$ correction. The final row shows results for a fit setup incorporating all single observable mismodeling NPs.

the forward direction, an almost constant $\sim 2\%$ underestimation in the barrel region, and up to $\sim 4\%$ overestimation in the backward region.

Since $p_{T,\tau_{3p}}$ directly influences the decay length calculation (see Equation (6.4)) and its mismodeling significantly impacts the fit uncertainty, a $p_{T,\tau_{3p}}$ mismodeling correction (referred to as the $p_{T,\tau_{3p}}$ template correction) is derived and examined. As shown in Table 6.12, this correction reduces the fit uncertainties for the fits with the included $p_{T,\tau_{3p}}$ and $p_{\tau_{3p}}$ NPs to the baseline level. Additionally, the fit with the included $\theta_{\tau_{3p}}$ NP shows a significant reduction in fit uncertainty, improving from 0.24 fs to 0.12 fs. Similarly, the fit with the included $\theta_{\pi_{3p}}$ NP also improves, with the largest reduction observed for $\theta_{\pi_{3p,1}}$. The fit with the included $p_{T,\pi_{3p,2}}$ NP exhibits a reduced fit uncertainty, decreasing from 0.16 fs to 0.12 fs. However, the fit with the included $p_{T,\pi_{3p,1}}$ NP shows a slight increase in fit uncertainty, rising from 0.11 fs to 0.13 fs. When all mismodeling NPs are included, the fit uncertainty decreases from 0.36 fs to 0.23 fs with the $p_{T,\tau_{3p}}$ -corrected templates.

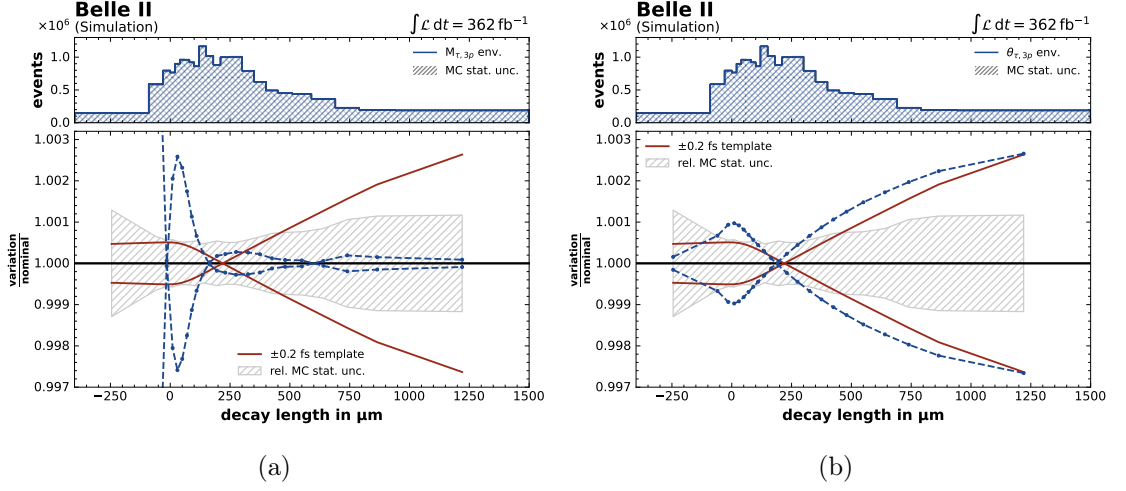


Figure 6.33.: Mismodeling induced symmetrized decay length shape-shifts. Also indicated as a reference, a ± 0.2 fs lifetime induced decay length shape-shifts and the relative MC stat. uncertainty of the templates. Mismodeling of (a) $M_{\tau_{3p}}$, and (b) $\theta_{\tau_{3p}}$ observables. The statistical uncertainties of the histograms are not visible.

Since the $p_{T,\tau_{3p}}$ correction does not entirely resolve the mismodeling of $\theta_{\tau_{3p}}$, a combined $p_{T,\tau_{3p}}$ and $\theta_{\tau_{3p}}$ correction is derived (referred to as the $p_{T,\tau_{3p}} \otimes \theta_{\tau_{3p}}$ template correction). The 2D weights obtained for this template correction are shown in Figure 6.35. It is evident that the yield of the simulated data is primarily reduced in the low p_T region ($< 1.7 \text{ GeV } c^{-1}$) and for $0.6 \text{ rad} \leq \theta_{\tau_{3p}} \leq 2 \text{ rad}$ with this correction. Figure 6.34b and Figure 6.34d show the $p_{T,\tau_{3p}}$ and $\theta_{\tau_{3p}}$ distributions after applying the $p_{T,\tau_{3p}} \otimes \theta_{\tau_{3p}}$ correction. The mismodeling for both observables is nearly eliminated.

The fit results for the $p_{T,\tau_{3p}} \otimes \theta_{\tau_{3p}}$ correction, as shown in Table 6.12, indicate that the fit uncertainty for the included $\theta_{\tau_{3p}}$ NP is now reduced to the baseline value of 0.09 fs. The fit uncertainties for the included $\theta_{\pi_{3p,1}}$ and $\theta_{\pi_{3p,2}}$ NPs slightly decrease. When all mismodeling NPs are included, the fit uncertainty is reduced by 0.02 fs compared to the $p_{T,\tau_{3p}}$ template correction, resulting in a fit uncertainty of 0.21 fs.

Based on the results discussed above, the $p_{T,\tau_{3p}} \otimes \theta_{\tau_{3p}}$ correction most effectively reduces the observable mismodeling and is therefore the primary choice. However, an alternative approach arises from the fact that the τ_{3p} is a reconstructed particle derived from the actual measured π_{3p}^\pm decay particles. Consequently, $p_{T,\tau_{3p}}$ and $\theta_{\tau_{3p}}$ are reconstructed quantities.

The π_{3p}^\pm particles contain all the relevant physics information, while the reconstructed τ_{3p} represents a composite of these objects. Therefore, a more accurate procedure would be to correct the $p_{T,\pi_{3p}}$ and $\theta_{\pi_{3p}}$ observable distributions, which would then propagate the corrections to the reconstructed τ_{3p} . This “bottom-up” approach requires simultaneous 6D re-weighting of the π_{3p}^\pm p_T and θ observables. The current dataset lacks sufficient statistics in the 6D bins, particularly in the tails. For this reason, the 2D re-weighting approach discussed above is applied (also referred to as “top-down” approach).

As a closure test and to address a systematic uncertainty of the $p_{T,\tau_{3p}} \otimes \theta_{\tau_{3p}}$ correction method, a “simplified bottom-up” template correction is derived based on a 3D re-weighting method to

6. τ -Lepton Lifetime Measurement Using Template Fits

Sample	Signal region	
	Events	Fraction in %
signal	15,363,868	97.49
background	394,122	2.51
$u\bar{u}$	212,095	1.35
$s\bar{s}$	62,657	0.40
$c\bar{c}$	55,953	0.36
$d\bar{d}$	41,558	0.26
$\ell^+\ell^-X^+X^-$	20,204	0.13
$b\bar{b}$	1,007	0.01
e^+e^-	539	<0.01
$e^+e^-\ell^+\ell^-$	99	<0.01
$\mu^+\mu^-$	6	<0.01
$hh(h^0)\gamma$	3	<0.01
experimental data	15,759,197	100

Table 6.13.: Number of events in the simulated and experimental dataset. The simulated dataset is split by sample. The normalization from Section 6.6.2 and the $p_{T,\tau_{3p}} \otimes \theta_{\tau_{3p}}$ correction is applied to the simulated dataset.

correct the mismodeling of the $p_{T,\pi_{3p}}$ and $\theta_{\pi_{3p}}$ observable distributions respectively. Similar to the 2D re-weighting, the 3D event weights for the simultaneous $p_{T,\pi_{3p,1}} \otimes p_{T,\pi_{3p,2}} \otimes p_{T,\pi_{3p,3}}$ correction are derived (referred to as the $p_{T,\pi_{3p}}$ correction). Similarly, the event weights for the simultaneous $\theta_{\pi_{3p,1}} \otimes \theta_{\pi_{3p,2}} \otimes \theta_{\pi_{3p,3}}$ correction are derived (referred to as the $\theta_{\pi_{3p}}$ correction). Using these event weights, the template variations of each of the two alternative corrected observable distributions are created. The derived systematic uncertainty for the $p_{T,\tau_{3p}} \otimes \theta_{\tau_{3p}}$ template correction is discussed in Section 6.8.3.

To ensure that the template correction does not compensate for a different τ -lepton lifetime in the experimental data, the $p_{T,\tau_{3p}} \otimes \theta_{\tau_{3p}}$ re-weighting was propagated to the generator-level decay length distribution of the simulated data sample. The re-weighting showed no impact on this distribution apart from statistical fluctuations. From this, it can be concluded that the template correction is not sensitive to the τ -lepton lifetime of the experimental data sample.

In the following analysis, all templates include the $p_{T,\tau_{3p}} \otimes \theta_{\tau_{3p}}$ correction. The updated composition of the sample, initially presented in Table 6.10, now incorporating normalization (see Section 6.6.2) and template correction, is shown in Table 6.13. In the signal region, the $\tau^+\tau^-$ purity increases from 96.07% to 97.49%, while the challenging $c\bar{c}$ background decreases from 0.56% to 0.36%, and the challenging $\ell^+\ell^-X^+X^-$ background decreases from 0.2% to 0.13%. The overall yield difference in the signal region is reduced to 8×10^{-3} %.

6.6.5. Lifetime Fit Stability

The fit stability is tested by repeating the lifetime fit procedure 5000 times using random template decay length distributions as pseudo-data. Gaussian statistical fluctuations are added to each distribution, along with a random scaling factor μ_{exp} . This test demonstrates that the

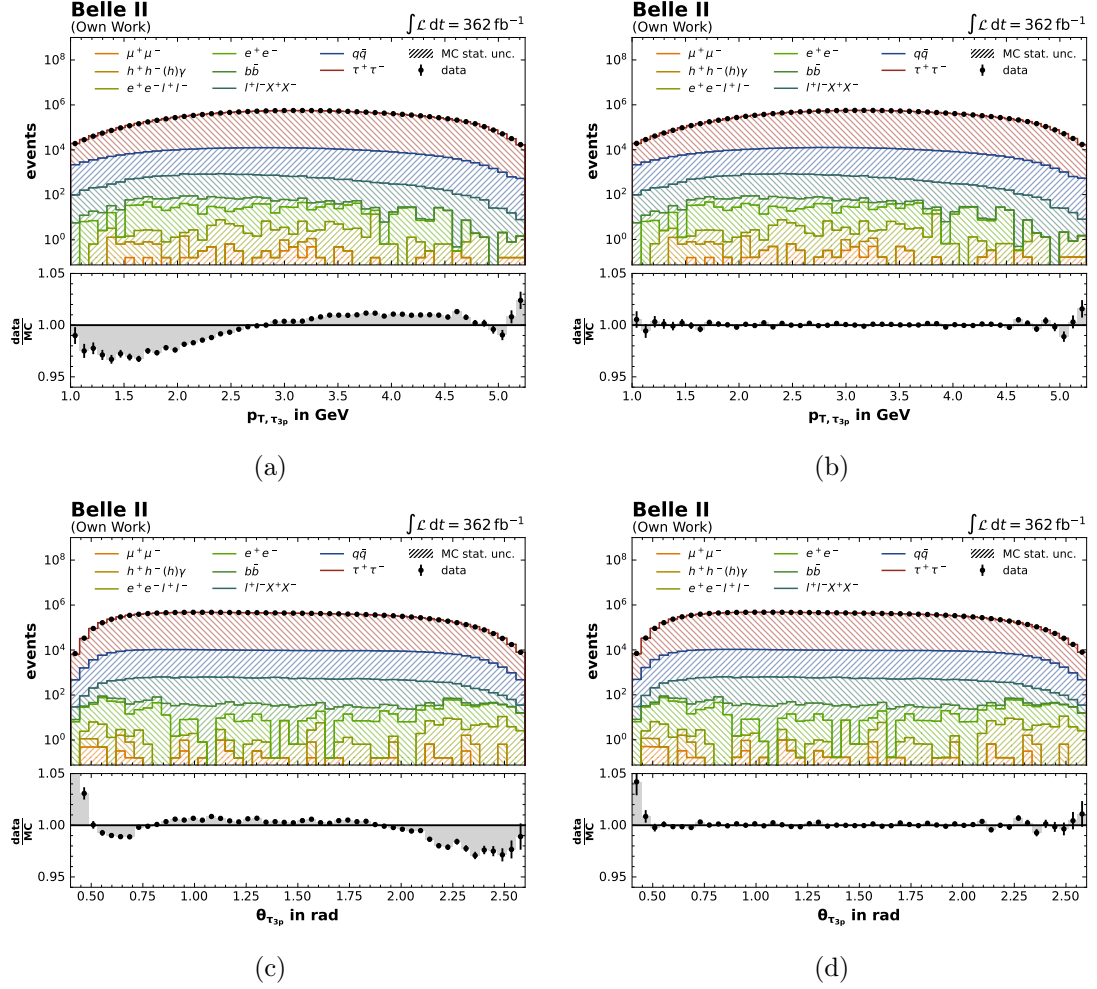


Figure 6.34.: Mismodeling of the simulation for (a) the $p_{T,\tau_{3p}}$ observable, (b) the $p_{T,\tau_{3p}}$ observable after the $p_{T,\tau_{3p}} \otimes \theta_{\tau_{3p}}$ template correction, (c) the $\theta_{\tau_{3p}}$ observable, and (d) the $\theta_{\tau_{3p}}$ observable after the $p_{T,\tau_{3p}} \otimes \theta_{\tau_{3p}}$ template correction. The statistical uncertainties of the histograms are not visible.

fit can accurately estimate the correct lifetime value, and scaling parameter. In this study, the best-fit μ_{glob} parameter is denoted μ_{obs} .

Figure 6.36a shows the μ_{obs} parameters from each fit relative to the applied μ_{exp} . A linear fit is performed to assess bias. The results are consistent with a straight line of slope 1 and y -intercept 0. The normality test on the residuals $\mu_{\text{obs}} - \mu_{\text{exp}}$ is presented in Figure 6.36b. The distribution of residuals, divided by their μ_{obs} fit uncertainty $\sigma_{\mu_{\text{glob}}}$, is compatible with a Gaussian p.d.f., within the 2σ parameter uncertainties of the central value μ and width σ of the fit.

Figure 6.37a shows the best-fit lifetime template, τ_{obs} , from each fit relative to the inserted template, τ_{exp} , used as pseudo-data. To reduce leverage, the distribution is evaluated around

6. τ -Lepton Lifetime Measurement Using Template Fits

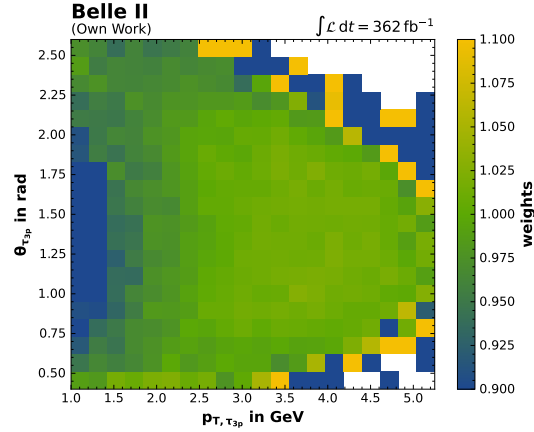


Figure 6.35.: 2D weights for the top-down template correction. The strong fluctuations in the bins at the curved edges is caused by low statistics in that phase space.

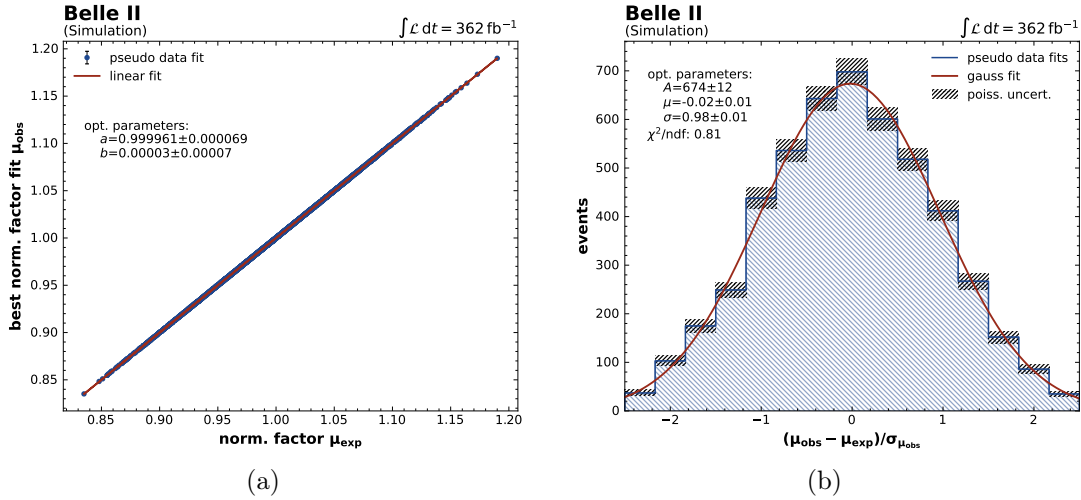


Figure 6.36.: Stability tests performed on 5000 randomly selected lifetime templates with statistical and normalization fluctuations as pseudo-data. (a) Comparison between input normalization scaling μ_{exp} and best-fit value μ_{obs} . (b) Distribution of the normalized residuals with a Gaussian fit.

the nominal lifetime, τ_0 . A linear fit is performed to assess bias, yielding a result consistent with a straight line of slope 1 and y -intercept 0.

The normality test on the residuals, $\tau_{\text{obs}} - \tau_{\text{exp}}$, is shown in Figure 6.37b. The residuals, divided by their lifetime fit uncertainty, $\sigma_{\tau_{\text{obs}}}$, form a distribution compatible with a Gaussian p.d.f., within the 1σ parameter uncertainties of the central value μ and width σ of the fit. Since the best-fit lifetime values correspond to the best-fitting template and are therefore discrete values, an overshoot in the mean value region is observed.

As an alternative, the best lifetime value can be estimated through interpolation with a

spline applied to the $2\Delta\text{NLL}$ values from the likelihood scan (see Figure 6.6), which resolves the overshoot. However, it was observed that the best lifetime value found via spline interpolation can deviate by more than the distance between two templates from the best-fitting template value. For this reason, and given that the template steps are chosen to be sufficiently narrow relative to the expected systematic uncertainty (see Section 6.8), the method of selecting the best-fitting template is preferred¹³.

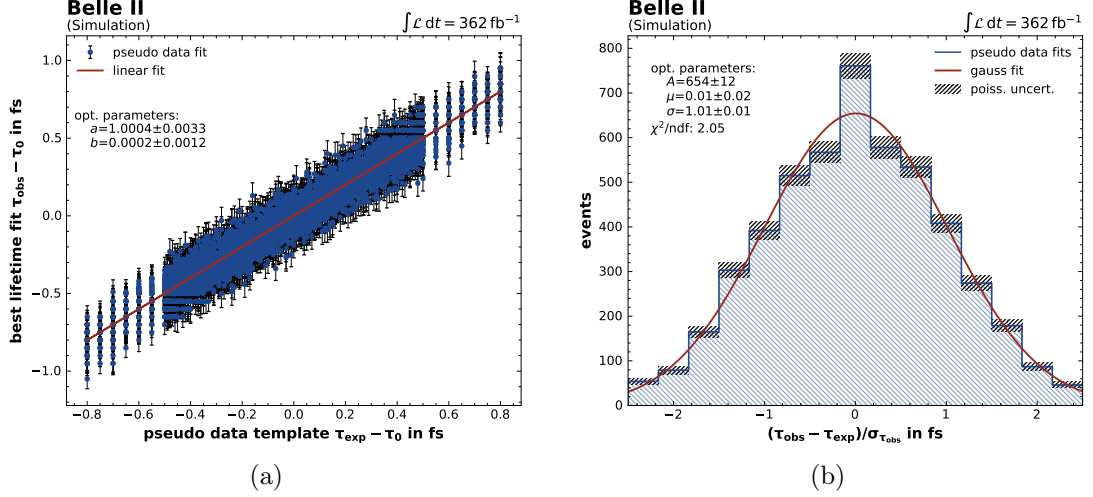


Figure 6.37.: Stability tests on 5000 randomly selected lifetime templates with statistical and normalization fluctuations used as pseudo-data. (a) Comparison between the input lifetime template, τ_{exp} , and the best-fit template, τ_{obs} . The transition from fine-grained to coarser templates is visible at approximately $\tau_{\text{exp}} - \tau_0 = \pm 0.5$ fs. (b) Distribution of the normalized residuals with a Gaussian fit, showing an overshoot at 0 due to discrete template steps.

A final study is performed to prove that no bias between the lifetime templates τ_{exp} and τ_{obs} , or in the best-fit scaling parameter μ_{obs} is observed. Again, τ_{exp} and τ_{obs} are evaluated around τ_0 to reduce the leverage.

Figure 6.38a shows the residuals, $\mu_{\text{obs}} - \mu_{\text{exp}}$, as a function of the inserted τ_{exp} , while Figure 6.38b shows the same distribution using the best-fit lifetime template, τ_{obs} . In both cases, linear fits yield slopes of 0 and y -intercepts of 0, within suitable precision, indicating no systematic deviation.

In summary, no bias is observed in the stability tests for the free normalization parameter or the best-fit lifetime template.

¹³If, during the unblinding procedure, the best-fit value appears to be in a coarse template step region, the fine-grained template region can be extended accordingly, and the fit can simply be repeated.

6. τ -Lepton Lifetime Measurement Using Template Fits

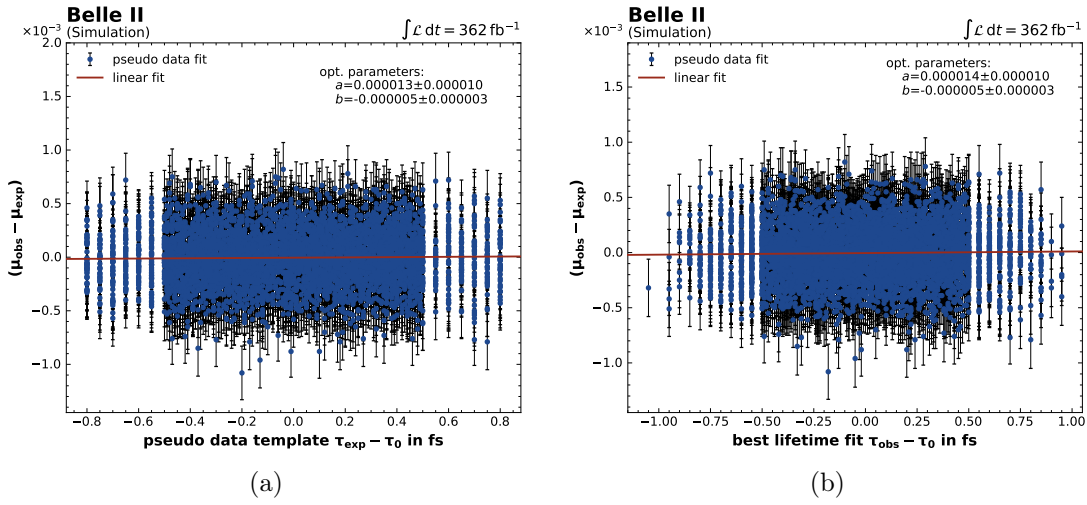


Figure 6.38.: Stability tests performed on 5000 randomly selected lifetime templates with statistical and normalization fluctuations used as pseudo-data. (a) Comparison between the input lifetime template, τ_{exp} , and the observed deviation in the normalization factor, $(\mu_{obs} - \mu_{exp})$. (b) Same as (a), but for the best-fit lifetime, τ_{obs} . The transition from fine-grained to coarser templates is visible at approximately $\tau_{exp} - \tau_0 = \pm 0.5$ fs or equivalently $\tau_{obs} - \tau_0 = \pm 0.5$ fs.

6.7. Lifetime Analysis Framework

A standalone *framework* was developed in this work to conduct all studies and perform the lifetime fit. The framework is written in Python [103] and utilizes various open-source software components, such as `basf2`, `b2luigi` [104], `parquet` [105], `pyhf` [94], and `cabinetry` [95].

Section 6.7.1 provides an overview of the framework’s structure, while Sections 6.7.2 through 6.7.5 describe its main components in detail. The performance, advantages, and limitations of the developed framework are discussed in Section 6.7.6.

6.7.1. General Overview

The framework is structured as a *pipeline*, as illustrated in Figure 6.39, to organize the workflow and streamline the analysis process. It begins with particle *reconstruction* (see Section 6.7.2), followed by the final *event selection* (see Section 6.7.3). These two stages are common to both simulated and experimental data, although specific corrections are applied differently for each.

At the third stage, the experimental data follows a separate pipeline branch from the simulated data. For experimental data, a *decay length histogram* is generated and used in the next stage as input for the lifetime fit, while for simulated data, the *template creation* process is performed. In combination with the template creation also the template variations are created to address the systematic uncertainties (see Section 6.7.4).

At the final stage of the pipeline the likelihood model is built and the *lifetime fit* is executed, where the templates are fitted to the experimental data (see Section 6.7.5). Additionally, the experimental data used in the fit can be replaced with pseudo-data for testing and validation purposes.

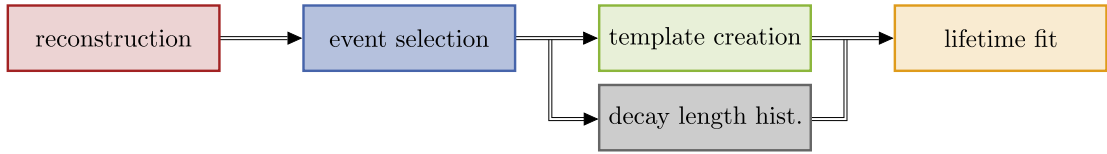


Figure 6.39.: Overview of the analysis pipeline organized in four components.

This modular pipeline architecture improves modularity, maintainability, and reproducibility. Well-defined output files at each stage facilitate a structured and collaborative workflow, ensuring clear analysis states. This design allows multiple configurations to be tested in parallel, enabling systematic comparisons of results at each stage.

6.7.2. Reconstruction

The analysis pipeline begins with particle and event reconstruction. Since the recorded experimental and simulated data are provided exclusively in Belle II-specific file formats, the reconstruction process can only be performed using `basf2` (see Section 4.4)¹⁴.

The reconstruction is implemented within a `basf2` steering file, defining a `basf2 Module Path`, as illustrated in Figure 6.40.

First, the *experimental and simulated particle data* are loaded from the storage system. The

¹⁴In this work, `basf2 release-2403-persian` is used.

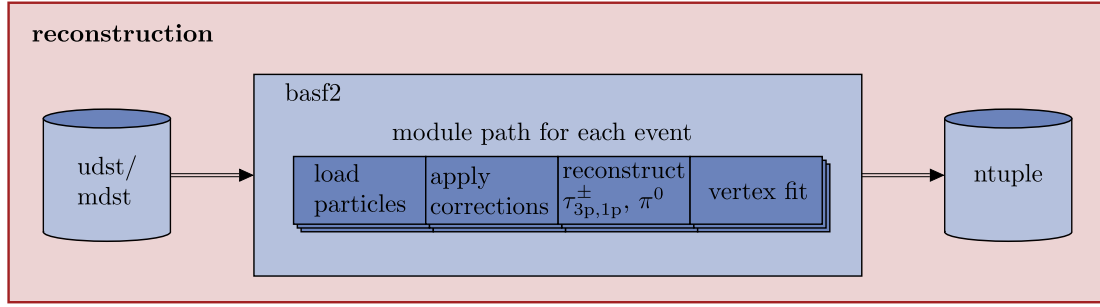


Figure 6.40.: Structure of the **basf2** reconstruction part in the steering file.

physics objects, such as tracks and photons (see Section 4.4), are processed on an *event-by-event* basis. Specific *corrections* are applied to these physics objects (see Section 6.4.1 and Section 6.4.2), followed by the *reconstruction* of π^0 s and $\tau^+\tau^-$ pairs. Event shape variables and kinematic properties are then computed, and the event topology is selected (see Section 6.4.3). Subsequently, a *vertex fit* is applied to the reconstructed τ_{3p} for the decay length measurement (see Section 4.4.4), followed by a second *vertex fit* to evaluate the vertex residual (see Section 6.5.1).

At the end of the **Path**, the reconstructed events are stored in **ntuple** files, a column- and row-based ROOT [106] data format. For the simulated data, generator-level information, such as the *generator decay length*, is appended to the reconstructed values in the **ntuple**. The **ntuple** columns contain observables, with each row representing values per candidate and event.

Event-by-event processing allows for parallelization across thousands of CPUs simultaneously. Splitting the processing into multiple jobs with individual output files results in thousands of **ntuple** files, which are partially concatenated in the event selection stage.¹⁵

6.7.3. Event Selection

The event selection and background suppression is implemented at this stage of the analysis pipeline. The schema for event selection is shown in Figure 6.41.

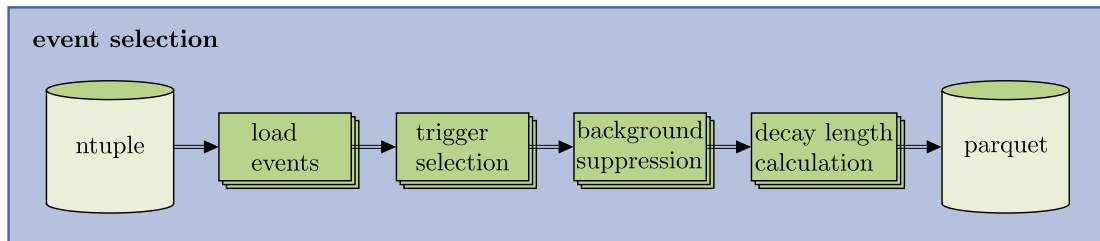


Figure 6.41.: Structure of the event selection stage in the framework.

In the first instance, *events* are loaded from the **ntuples** created at the reconstruction stage.

¹⁵Certain samples, such as experimental and simulated data, must remain separate due to differing corrections and analysis requirements. Simulated dataset subsamples are not mixed in reconstruction to facilitate signal and dedicated background type separation during analysis.

The dataset size after reconstruction is approximately ~ 2 TB, which exceeds the available memory resources. Therefore, only a subset of the `ntuples` is loaded into the memory using `uproot` [107] and `pandas DataFrames` [108], with an optimal concatenation of 30 files, keeping memory consumption below 60 GB.

The reconstructed particles are loaded into separate `DataFrames`, linked by a *unique event index* generated by hashing a string containing the *experiment number*, *production number*, *run number*, and *event number*. This index enables efficient filtering based on specific event selection criteria.

The selection process begins by applying *trigger bit selections* (see Section 6.3.1). Particles with the required trigger bits are filtered by the unique event index.

Next, *background and mismodeling suppression* is applied¹⁶ (see Section 6.4.4). For the selected events, the τ_{3p} *reconstructed decay length* (see Section 6.2.1) and *vertex residual* (see Section 6.5.1) are calculated. For the simulated $\tau^+\tau^-$ sample, also the *generated “true” decay length* is calculated.

At the end of event selection, the various particle `DataFrames` are *stored* as `parquet` files with a subset of observables essential for analysis.

The concatenated `ntuples` are converted to individual `parquet chunks`. These chunks can be sequentially loaded to generate histograms. When iterating over all chunks, histogram entries for each chunk are summed to create a histogram for the entire dataset.

The event selection step, combined with `parquet` conversion, reduces the overall data size from ~ 2 TB to approximately ~ 38 GB.

6.7.4. Template Creation

In the framework, the templates and template variations discussed in 6.6.3 are organized in the `Template` class. For each *fit region* (see Section 6.6.2), a dedicated `Template` object is instantiated. Each object contains the template histograms that are part of the likelihood model, as well as the 1σ envelope histograms that are needed to constrain the NPs for the correlated shape systematics. These envelopes are stored in dedicated instantiated `Systematic` objects.

The general schema of the `Template` object creation is shown in Figure 6.42.

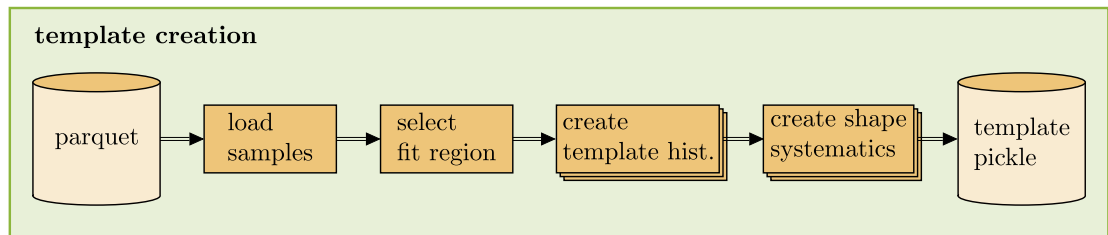


Figure 6.42.: Structure of the consecutive steps for the template creation.

The particle data from the *required samples* are loaded from the `parquet` files in chunks. First, the *fit region* is selected based on the specified $M_{\tau_{3p}}$ window. Next, the *template histograms* are created, where normalization factors (see Section 6.6.2) and correction weight factors (see Sec-

¹⁶The $M_{\tau_{3p}}$ requirement is not applied in this step. It is later applied during the template creation stage.

6. τ -Lepton Lifetime Measurement Using Template Fits

tion 6.6.4) are applied to the events. The template histogram for the entire dataset is obtained by aggregating individual chunk histograms through summation. The resulting histogram is stored within an instantiated **Template** object. If necessary, additional model hypotheses can be incorporated as supplementary template histograms (see Section 6.2.4).

Following the template histogram creation, **Systematic** objects are instantiated according to the procedures described in Section 6.2.3 and Section 6.6.3.

Finally, the attributes of the **Template** object are stored in a **pickle** file, enabling the object to be restored at any time by reloading its serialized attributes. This allows for further modifications or extensions as needed. The modular design of the template creation pipeline allows parallel workload distribution across individual **b2luigi** Tasks (see Appendix A.7.1).

6.7.5. Lifetime Fit

In the final stage of the analysis pipeline, the *template fits* are performed (see Section 6.2.2). The pipeline structure is identical for both normalization and lifetime fits, differing only in the configuration of the fit setups. A schematic overview of the fitting pipeline is shown in Figure 6.43.

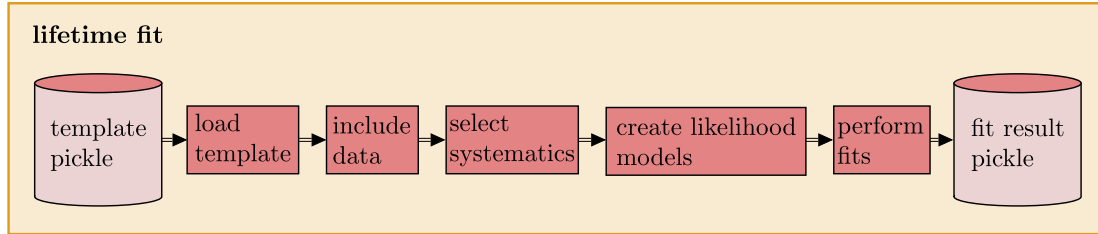


Figure 6.43.: Structure of the lifetime fit component in the framework.

For each fit region, the attributes of the instantiated **Template** object are loaded from the corresponding **pickle** file. The (experimental) data histograms to which the templates are fitted are included.¹⁷ Next, the NPs to be included in the fit are selected, and their corresponding **Systematic** objects are retrieved from the **Template** object.

With all necessary inputs loaded, the *likelihood models* are constructed, and the **pyhf Workspaces** are configured. In the final step, the $2\Delta\text{NLL}$ minimization *fits* of the likelihood scan are performed. The fit results, configuration, and input data are stored in a dedicated *fit result pickle* dictionary.

This implementation supports parallel execution of multiple fit configurations within a **b2luigi** Task pipeline. At the end, all fit results are aggregated (see Appendix A.7.2). The framework allows for various data samples – such as pseudo-data with different lifetimes – to be analyzed under different NP configurations.

6.7.6. Framework Summary

The framework developed in this work is tailored to the specific requirements of the τ -lepton lifetime analysis method and the resource constraints of the National Analysis Facility (NAF)

¹⁷If pseudo-data is used, any pseudo-data histogram – such as a template histogram – can optionally be included, with the possibility of additional statistical fluctuations.

at DESY [109]. It is optimized for processing experimental and simulated data samples on the DESY `JupyterHub`, which provides `Jupyter Notebooks` [110] with limited memory. During development, the memory of a `Jupyter Notebook kernel` was restricted to 10 GB. The framework enables event filtering (event selection), histogram creation, and full dataset plotting with a memory consumption of approximately 6 GB. More resource-intensive tasks, such as `parquet` conversion and 2D re-weighting, require additional memory but remain below 60 GB.

Heavy computations are deployed to dedicated *worker nodes* via the NAF `HTCondor` [111] system, which provides greater resources but operates under strict user priority rules, making interactive script optimization challenging. To facilitate development, computationally intensive jobs can first be tested on a single “test” chunk using a `Jupyter Notebook` before submitting them for full-scale processing.

One bottleneck of the framework is the `ntuple` to `parquet` conversion, which is relatively time- and memory-intensive compared to other analysis steps. Conversion, combined with event selection, can take up to 24 h¹⁸. An additional challenge arises in the creation and concatenation of large `pandas DataFrames` during event selection. Aside from this, the framework operates efficiently and is highly scalable. It is expected to handle datasets up to 10 times larger than the current $\sim 362 \text{ fb}^{-1}$ dataset.

¹⁸This duration also depends on the load of the `HTCondor` system and the `userprio`, a metric penalizing heavy computation and usage.

6.8. Estimated Precision

The uncertainties are categorized into two types: *statistical and systematic uncertainties*. Statistical uncertainties account solely for the statistical uncertainty of the experimental dataset, whereas all other uncertainties are classified as systematic uncertainties.

In this section, a sensitivity study is conducted to estimate the expected uncertainty on the τ -lepton lifetime, measured using the novel approach presented in this work. The normalized and $p_{T,\tau_{3p}} \otimes \theta_{\tau_{3p}}$ -corrected templates (see Section 6.6.2 and Section 6.6.4) serve as the model prediction in the likelihood model, while the experimental data is replaced by the nominal template as pseudo-data. Since the pseudo-dataset is in perfect agreement with the nominal template, the fit is expected to yield the corresponding lifetime value of the nominal template as the best-fit value. Due to this perfect agreement, no pulls of the normalization parameters or the NPs are expected.

The fit setups in this sensitivity study estimate the expected fit uncertainty at a 68 % CL (see Section 6.2.2), considering the included NPs. The following fits incorporate the NPs based on the template variations discussed in Section 6.6.3.

To assess the contribution of certain systematic uncertainties, the pseudo-data fit is first performed with the full set of the NPs included, resulting in a fit result with total uncertainty σ_{tot} . The fit is then repeated fixing the NPs of a specific systematic source i , resulting in a best-fit value with an uncertainty $\sigma_{\text{tot}-i}$. The uncertainty induced by the systematic source of interest, σ_i , is then calculated as

$$\sigma_i = \sqrt{\sigma_{\text{tot}}^2 - \sigma_{\text{tot}-i}^2}. \quad (6.23)$$

The NPs of the studied systematic sources are fixed to the values estimated in the fit with the full set of NPs. This approach is referred to as *breakdown*.

To increase the fit stability and reduce correlations among NPs, NPs without any measurable impact ($\sigma_i < 0.01$ fs) are successively excluded, a process referred to as *pruning*. A final breakdown fit, including the remaining NPs, is performed in Section 6.8.13 to estimate their expected contributions and the total expected uncertainty. The correlations and fit stability of the NPs are evaluated in Section 6.8.12. Table A.3 shows all NPs before pruning.

6.8.1. Statistical Uncertainty

The statistical uncertainty, is determined by the fit uncertainty of the likelihood scan when all NPs are fixed to their best-fit values. Since the fit is fed with the pseudo-dataset, its statistical precision is replaced by the statistical precision of the experimental dataset to estimate the correct sensitivity.

In the previous Belle τ -lepton lifetime measurement, precision was limited by the statistical uncertainty. Although the dataset collected with the Belle II detector for this analysis is about half the size of the Belle dataset, the higher branching fraction of the 3x1-prong decay topology and improved selection have increased the number of expected events by a factor of approximately 14.

The ~ 14 times larger dataset, compared to the Belle dataset, reduces the statistical uncertainty from 0.5 fs (Belle) to 0.08 fs in this analysis. Consequently, the total uncertainty is no longer dominated by statistics but by systematic uncertainty, which is discussed in more detail below.

6.8.2. Simulated Data Statistical Uncertainty

The statistical precision of the simulated data for the $\tau^+\tau^-$ sample and the dominant background samples is up to four times larger than in the experimental dataset (see Section 6.1). The corresponding uncertainty is included as NPs in into the likelihood model (see Section 6.2.3). By fitting with and without these NPs, an impact of ± 0.07 fs on the τ -lepton lifetime value is estimated.

6.8.3. Template Correction Uncertainty

The template correction uncertainty is derived from an alternative approach of re-weighting the $p_{T,\pi_{3p}}$ and $\theta_{\pi_{3p}}$ distributions, as explained in Section 6.6.4. The decay length shape-shift observed between the 2D $p_{T,\tau_{3p}} \otimes \theta_{\tau_{3p}}$ correction and the 3D $p_{T,\pi_{3p}}$ and $\theta_{\pi_{3p}}$ corrections are shown in Figure 6.44. For reference, the decay length shape-shifts for the ± 0.2 fs templates are indicated, and the statistical precision of the templates is shown as a gray hatch.

In particular, the 3D $p_{T,\pi_{3p}}$ correction induces a shape-shift towards larger decay lengths, which, in the high-statistics region, resembles the lifetime induced shape-shift with a crossing point near $\sim 200 \mu\text{m}$. A second crossing point is observed near $\sim 0 \mu\text{m}$, followed by a deviation of up to 0.4 % in the negative low-statistics decay length region.

The two crossing points of the 3D $\theta_{\pi_{3p}}$ correction are shifted towards smaller decay lengths, occurring at approximately $\sim -100 \mu\text{m}$ and $\sim 125 \mu\text{m}$. In general, the variations are smaller than those induced by the $p_{T,\pi_{3p}}$ corrections.

In the positive decay length region, both envelopes show similar behavior, with a variation of up to ~ 0.06 %.

In contrast to the studies in Section 6.6.4, all relevant NPs are included simultaneously into the likelihood model. Correlations between the NPs can result in unexpected impacts of individual NPs making a straight forward interpretation of the input distribution difficult.

Including several shape uncertainty NPs can affect the fit precision, even when the shape-shift no longer resembles the lifetime induced shape-shift. This is shown in more detail in Figure 6.44b with respect to the ± 0.2 fs template. This effect results from correlation with other NPs, as discussed in Section 6.8.12.

An impact of ± 0.02 fs on the τ -lepton lifetime value is estimated. Both NPs are included in the pruned pseudo-data fit for the total uncertainty estimation in Section 6.8.13.

6.8.4. Remaining Mismodeling of Observables

Despite the template correction and its associated systematic uncertainty, as discussed in Section 6.8.3, it remains unclear whether all underlying sources of mismodeling that affect the decay length distribution are fully accounted for. Due to the complex correlations among these sources, it is impossible to disentangle them completely. Therefore, the impact of several observables, which still exhibit significant mismodeling after the $p_{T,\tau_{3p}} \otimes \theta_{\tau_{3p}}$ -correction, is evaluated in terms of their influence on the fit result. To address this, relevant kinematic and event shape observables are incorporated as NPs in the fit (see Section 6.6.3).

Table 6.14 shows the expected impact of each observable on the best-fit τ -lepton lifetime value. The three observables listed at the top of the table have measurable contributions ranging from ± 0.02 fs to ± 0.08 fs. These NPs are retained in the pruned likelihood model for the total uncertainty estimation in Section 6.8.13. In contrast, the other NPs, whose contributions are

6. τ -Lepton Lifetime Measurement Using Template Fits

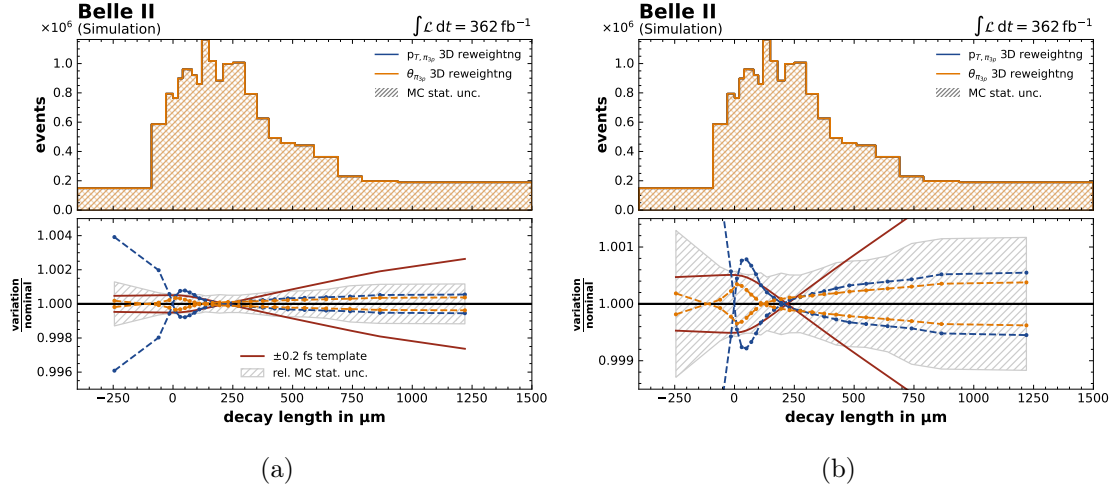


Figure 6.44.: (a): Alternative template correction induced decay length shape-shifts affecting fit uncertainty. (b): Zoom of (a) in the lower ratio plot. The statistical uncertainties of the histograms are not visible.

smaller than ± 0.01 fs, are expected to have a negligible impact on the fit result and are therefore excluded in Section 6.8.13.

Systematic	Uncertainty in fs
$M_{\tau_{3p}}$	0.08
$\theta_{p,\text{evt}}^{\text{miss},*}$	0.03
V_{thrust}	0.02
$d_{2 \times 1}$	< 0.01
$p_{\tau_{3p}}$	< 0.01
$E_{\text{evt}}^{\text{vis},*}$	< 0.01
$p_{\text{evt}}^{\text{miss},*}$	< 0.01
$M_{\text{evt}}^2 \text{ miss},*$	< 0.01
$n_{\pi_{0,1p}}$	< 0.01
$n_{\gamma_{1p}}$	< 0.01
$n_{\gamma_{3p}}$	< 0.01

Table 6.14.: τ -lepton lifetime fit results for several observable mismodeling corrections. The observables with uncertainties < 0.01 are expected to have a negligible impact on the fit.

Figure 6.45 shows the decay length shape-shifts induced by the three mismodeled observables with measurable impact. The shape-shifts exhibit a different crossing point with the nominal shape compared to the lifetime induced shape-shifts. For the $M_{\tau_{3p}}$ NP, which has the largest impact among the remaining mismodeling NPs, the envelope crossing points occur at $\sim -10 \mu\text{m}$, $\sim 175 \mu\text{m}$, and $\sim 600 \mu\text{m}$, with local maximum variations of $\sim \pm 0.24\%$ and $\sim \pm 0.03\%$ in the

high-statistics region.

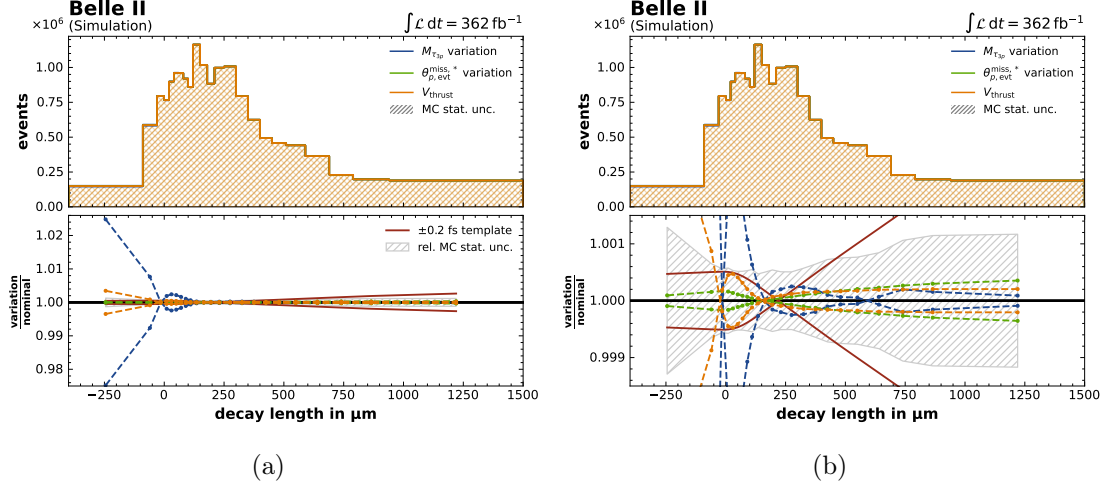


Figure 6.45.: (a): Mismodeling induced decay length shape-shifts with impact on the fit uncertainty. (b): Zoom of (a) in the lower ratio plot. The statistical uncertainties of the histograms are not visible.

6.8.5. Misalignment

The detector misalignment was the largest systematic uncertainty in the Belle τ -lepton lifetime measurement, as Belle had neither any alignment calibration nor a precise pixel detector. This is different at Belle II. The alignment and the PXD significantly improve the precision of the decay length measurement. The impact of remaining potential misalignment on the decay length distribution is examined and included as NPs in the likelihood model.

Following the recommendations of [42], four different misalignment scenarios are simulated in a dedicated run independent $\tau^+\tau^-$ sample production corresponding to 50 fb^{-1} . For that, the observed difference in derived alignment constants, and intrinsic alignment uncertainties are applied as alignment constants to the nominal (perfect alignment) scenario. The misalignment scenarios, are [112]:

- **Prompt to proc $\Delta x_{\text{PromptProc}}$:** This scenario captures the alignment differences between the major full data processing campaign (**proc12**) and a minor data reprocessing (**prompt**) for data from **bucket17** up to **bucket26**. It includes full VXD, CDC layer, and CDC wire alignment.
- **Intrinsic systematics 1 $\Delta x_{\text{IntrSyst},1}$:** This misalignment scenario is based on simulated data studies associating intrinsic alignment systematics from residual misalignment for VXD, CDC layer, and CDC wire alignment.
- **Intrinsic systematics 2 $\Delta x_{\text{IntrSyst},2}$:** This is based on simulated data studies associating intrinsic alignment systematics from residual misalignment for VXD, CDC layer alignment (excluding CDC wire alignment).

6. τ -Lepton Lifetime Measurement Using Template Fits

Misalignment Systematic	Uncertainty in fs
Prompt to proc	0.08
Intrinsic systematics 2	0.05
Intrinsic systematics 1	0.03
Day-to-day	< 0.01

Table 6.15.: Measured expected uncertainties for the misalignment scenarios. Observables with uncertainty < 0.01 are expected to have a negligible impact on the fit.

- **Day-to-day $\Delta x_{\text{Day2Day}}$:** This scenario addresses alignment differences, observed in the day-to-day alignment from experimental data, including VXD, and CDC layer alignment.

The same events are used across all alignment scenarios (misalignment + nominal), enabling a direct comparison between misaligned and nominal samples without statistical fluctuations. Consequently, any observed shifts in the decay length distribution are attributable to misalignment¹⁹. The variations between the samples are propagated to template variations to derive the 1σ envelopes, which are used to constrain dedicated NPs (see Section 6.6.3). However, statistical fluctuations appear between the variation histograms derived from the run-independent samples and the templates constructed from the run-dependent samples (see below).

Since the misalignment variation is measured in only one direction, it is symmetrized and additionally smoothed. The variations are incorporated as four NPs in the likelihood model. The respective impact on the τ -lepton lifetime fit results is shown in Table 6.15. The largest impact arises from the *Proc to prompt misalignment*, contributing ± 0.08 fs, while the *Day-to-day misalignment* exhibits no measurable effect and is therefore excluded from the fit.

Figure 6.46 shows the decay length shape-shifts induced by misalignment. The *Prompt to proc* scenario exhibits the most significant variations, with shape deviations reaching up to 5 % in the negative low-statistics region and approximately 1.5 % in the positive region. The shape-shift crossing point occurs around $75\mu\text{m}$.

The *Intrinsic systematics 1 and 2* scenarios exhibit significant fluctuations between the 50fb^{-1} run-independent sample and the run-dependent templates. Since these fluctuations impact the fit uncertainty, a larger run-independent misalignment sample is required to repeat the study.

6.8.6. Material Budget

A study [113] on nuclear interactions of 3-track hadron vertices from material interactions shows a 4 % cumulative discrepancy between simulated and experimental vertex counts. This discrepancy arises from incorrect modeling of the BP, the PXD Si, and inner SVD Si layer material densities.

To estimate the impact of material density variations on the decay length distribution, dedicated simulations are performed. A simplified model is employed to reduce the complexity of the technical implementation. Rather than varying all material components of the detector, only the density of the BP is varied by $\pm 5\%$. Dedicated studies to validate this approach are

¹⁹Minor fluctuations may arise from gamma efficiency corrections due to random photon loss combined with photon and π^0 selection cuts.

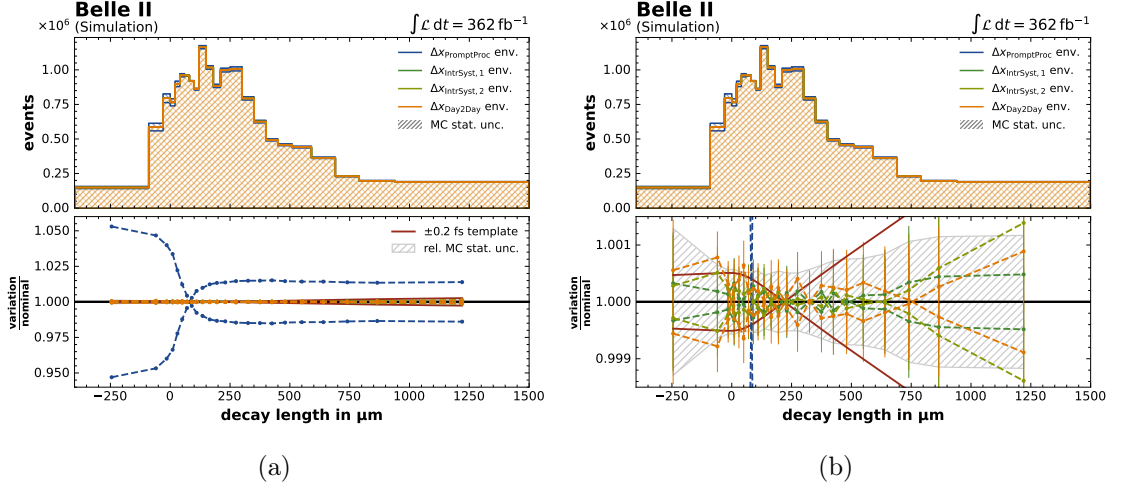


Figure 6.46.: (a): Misalignment induced decay length shape-shifts with impact on the fit result. (b): Zoom of (a) in the lower ratio plot. The statistical uncertainties of the histograms are not visible.

currently ongoing.

Similarly to the misalignment simulations in Section 6.8.5, a 500 fb^{-1} run-independent sample is created for the nominal and $\pm 5\%$ material density variations.

The resulting decay length shape-shifts are symmetrized and smoothed. The BP density variation is included as $\varrho_{\text{BP}, \pm 5\% \text{ NP}}$ in the likelihood model. A $\pm 0.1 \text{ fs}$ contribution to the τ -lepton lifetime value is observed.

Figure 6.47 shows the BP density induced decay length shape-shifts. The up and down variations cross over at $0 \mu\text{m}$ and $150 \mu\text{m}$. Maximum variations are observed in the negative decay length tail up to $\pm 0.9\%$, while the positive region has variations up to 0.3% .

6.8.7. Background Contribution

Despite the powerful background suppression discussed in Section 6.4.4 and template correction, a small $c\bar{c}$ fraction still remains (0.6%). The impact of wrong predictions in the $c\bar{c}$ process on the τ -lepton lifetime fit result is studied. The main source is expected to originate from *fragmentation mismodeling*.

The mismodeling of fragmentation has several consequences for the decay length measurement. Since multiple particles with finite lifetimes contribute to the sub-processes (see Section 6.4.4), an incorrect composition of particle fractions with different lifetimes leads to a shift in the measured decay length. Additionally, the reconstructed 3-prong vertex from $c\bar{c}$ processes include incorrectly reconstructed particles originating from cascade decays within the sub-processes. A misrepresentation of these cascade decays, particularly those involving intermediate decay vertices, also affects the decay length distribution. Within the scope of this work, it was not possible to separate the $c\bar{c}$ sample into its dozens of sub-processes due to missing decay information in the simulated samples²⁰.

²⁰The $c\bar{c}$ sample was regenerated with particle decay information. Currently, a study is underway to

6. τ -Lepton Lifetime Measurement Using Template Fits

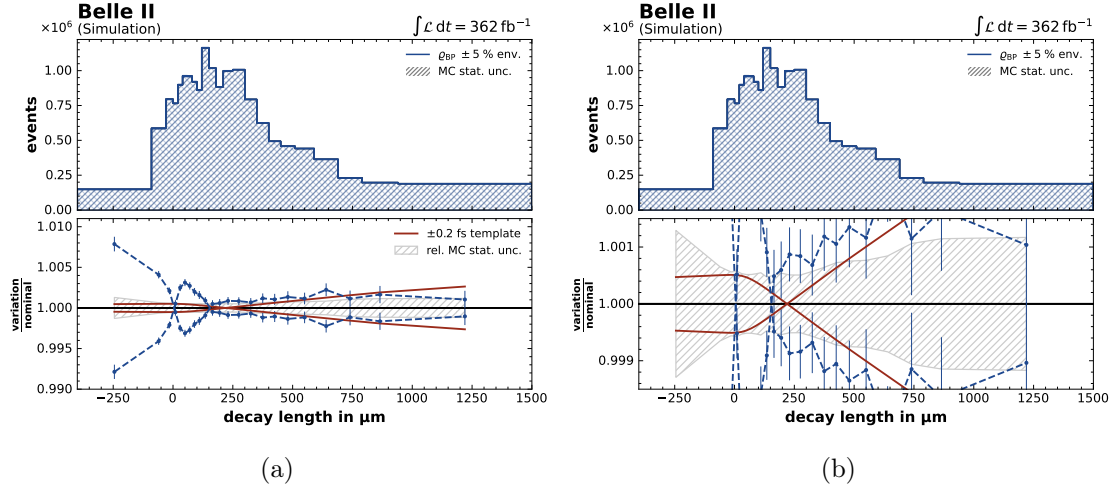


Figure 6.47.: (a): BP material density induced decay length shape-shifts. (b): Zoom of (a) in the lower ratio plot. The statistical uncertainties of the histograms are not visible.

To estimate the systematic uncertainty, the overall variation of the $c\bar{c}$ contribution within the total $q\bar{q}$ background is studied. As an alternative to directly varying the sub-process representation, the $c\bar{c}$ yield is scaled within the $q\bar{q}$ samples. The $c\bar{c}$ contribution is adjusted up and down while keeping the overall background yield constant. This scaling modifies the fraction of the decay length distribution originating from $c\bar{c}$ sub-processes with lifetime relative to sub-processes without lifetime. As a result, a decay length shape-shift occurs, similar to what would be expected from incorrectly simulated fragmentation.

In total, eight $c\bar{c}$ scaling scenarios are examined, with four upscaling and four downscaling factors chosen symmetrically: $\pm 30\%$, $\pm 50\%$, $\pm 70\%$, and $\pm 100\%$. Each scenario is included as NP in a separate likelihood model.

The expected impact of these NPs on the τ -lepton lifetime value is shown in Table 6.16. An uncertainty of ± 0.07 fs is observed for the smallest variation, while an uncertainty of ± 0.12 fs is observed when the $c\bar{c}$ contribution is either removed or doubled.

Figure 6.48 shows the decay length shape-shifts for the four scenarios. In the negative decay length region, a maximum variation from 0.5 % to 1.5 % is observed, depending on the scaling. In the positive range, a variation in the tail from 0.3 % up to 0.8 % is observed. The shape-shifts intersect at approximately $\sim 50 \mu\text{m}$.

The measured uncertainties in Table 6.16 provide valuable insights. Even if the $c\bar{c}$ contribution is entirely removed or doubled ($\pm 100\%$), the impact on the best-fit τ -lepton lifetime value does not exceed ± 0.12 fs. However, this scenario is highly conservative. For the likelihood model in Section 6.8.13, the $\pm 50\%$ scenario is adopted, which is expected to remain sufficient.

6.8.8. Trigger

The relative decay length shape-shift induced by differences in trigger efficiency between simulated data and experimentally measured data, as discussed in Section 6.3.1, is used as a template

decompose all sub-processes and examine their individual contributions in detail.

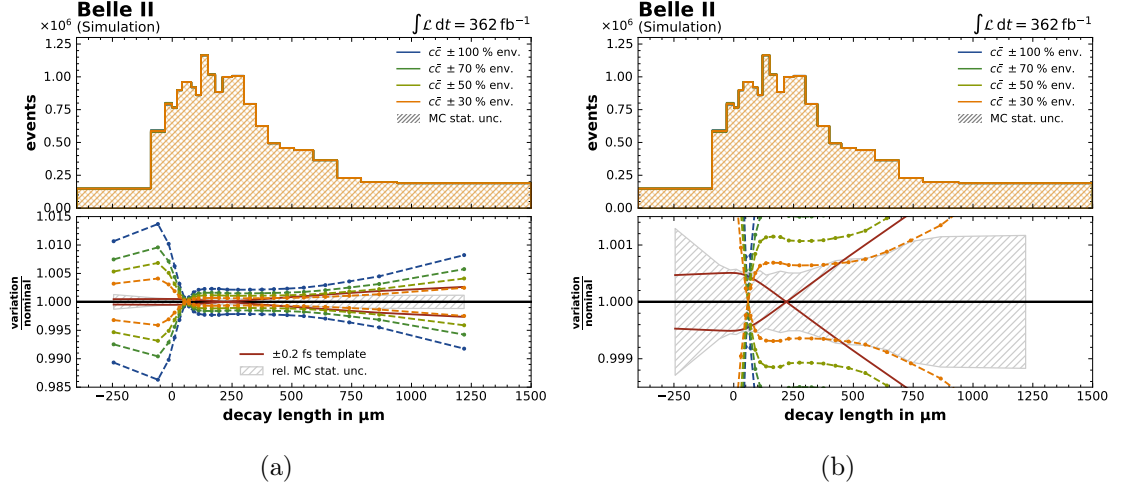


Figure 6.48.: (a): $c\bar{c}$ contribution variation induced decay length shape-shifts with impact on the fit uncertainty. (b): Zoom of (a) in the lower ratio plot. The statistical uncertainties of the histograms are not visible.

$c\bar{c}$ Variation	Uncertainty in fs
$\pm 100\%$	0.12
$\pm 70\%$	0.11
$\pm 50\%$	0.10
$\pm 30\%$	0.07

Table 6.16.: Expected contribution to the overall lifetime fit uncertainty

variation and included as the $\varepsilon_{\text{trig}}$ NP in the likelihood model. An expected impact of ± 0.04 fs on the total uncertainty is observed.

Figure 6.49 shows the decay length shape-shift induced by $\varepsilon_{\text{trig}}$. In the negative decay length region, a variation of up to 0.04% is observed, while in the positive decay length region, a variation of up to 0.08% is observed. The shape-shifts intersect at 0 μm , 100 μm , 225 μm , and 400 μm .

6.8.9. Kaon Contribution

In Section 6.4.5, the expected $\tau^+\tau^-$ backgrounds are discussed. One significant contribution arises from K^\pm being falsely assumed to be π^\pm . The decay length shape-shift in the $\tau^+\tau^-$ sample with variation of the K^\pm contribution, based on the branching fraction uncertainties provided in [75], is studied. The resulting decay-length shape-shift is included as NP in the likelihood model. No measurable impact on the total τ -lepton lifetime fit result is observed; thus, this NP is excluded.

Figure 6.50 shows the introduced decay length shape-shift. A decay length variation of less than $\mathcal{O}(1 \times 10^{-5} \%)$ is observed. Since the K_s^0 contribution is two magnitudes smaller, its

6. τ -Lepton Lifetime Measurement Using Template Fits

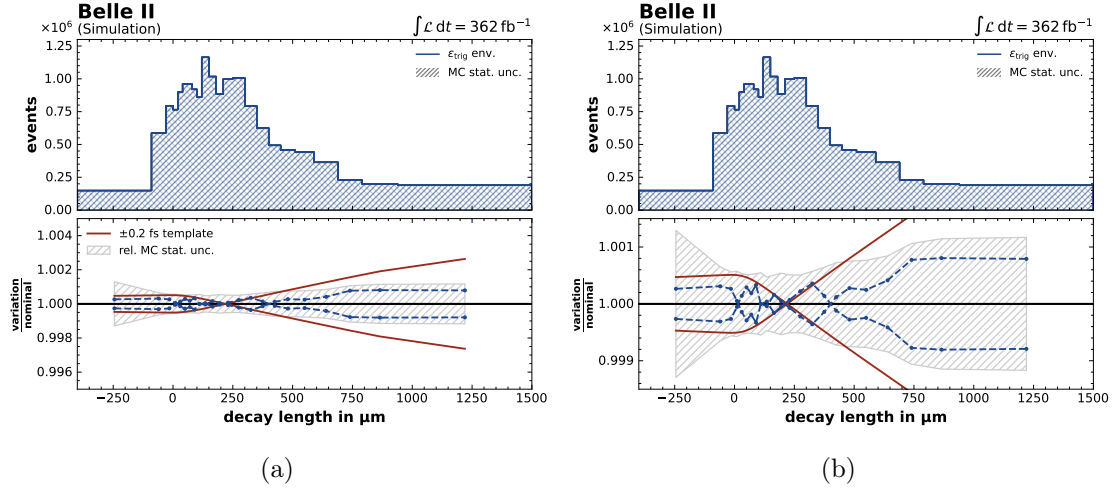


Figure 6.49.: (a): Trigger efficiency variation induced decay length shape-shifts. (b): Zoom of (a) in the lower ratio plot. The statistical uncertainties of the histograms are not visible.

variation of branching fraction is expected to have a negligible impact on the fit result, and is therefore not considered.

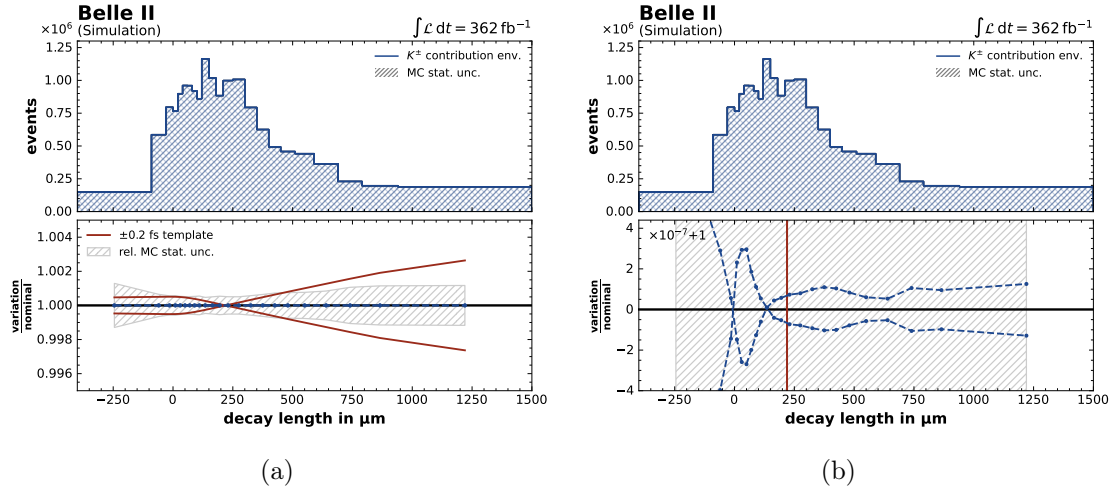


Figure 6.50.: (a): K^\pm contribution variation induced decay length shape-shifts. (b): Zoom of (a) in the lower ratio plot. The statistical uncertainties of the histograms are not visible.

6.8.10. Reconstruction Corrections

During the event reconstruction, several corrections are applied (see Section 6.4.1 and Section 6.4.2). For each correction, the reconstruction was processed with both the nominal cor-

rection and variations applied symmetrically up and down. Depending on the correction type, this was performed on either the experimental data, the simulated data, or both.

The uncertainties associated with these corrections are propagated as NPs into the likelihood model. The impact of these uncertainties on the decay length distribution is symmetrized and transferred to a template variation (see Section 6.6.3). The shift in the decay length distribution is measured by varying each correction relative to its nominal value. For corrections applied to the experimental data, the relative difference between the varied and nominal decay length distributions is computed and transferred to a template variation. Only relative shifts in the decay length distribution due to correction uncertainties are studied, ensuring that no lifetime information is “unblinded” from the experimental data.

For each correction, a NP is included in the likelihood model. The expected impacts on the τ -lepton lifetime fit result are shown in Table 6.17. Only the ε_γ shows a measurable contribution, while the remaining NPs are pruned from the likelihood model in Section 6.8.13.

Reco. Correction Systematic	Uncertainty in fs
ε_γ	0.03
E_γ	< 0.01
$E_{\text{loss,PDG}}^{\text{data}}$	< 0.01
$E_{\text{loss,bias}}^{\text{data}}$	< 0.01
$E_{\text{loss,bias}}^{\text{MC}}$	< 0.01
$E_{\text{loss,stat}}^{\text{data}}$	< 0.01
$E_{\text{loss,stat}}^{\text{MC}}$	< 0.01
$p_{\text{PDG}}^{\text{data}}$	< 0.01
$p_{\text{bias}}^{\text{data}}$	< 0.01
$p_{\text{bias}}^{\text{MC}}$	< 0.01

Table 6.17.: Observed contributions to the fit uncertainty from the pseudo-data fit, where “PDG” represents the uncertainty on the PDG average value, “stat” represents the statistical uncertainty, and “bias” represents the fit bias from the mass peak fit in [98].

The observed decay length shape-shift of ε_γ is shown in Figure 6.51. A relative variation of up to $\sim 0.4\%$ in the negative decay length region and up to $\sim 0.1\%$ in the positive region is observed. The intersection occurs at approximately $75\mu\text{m}$.

6.8.11. Normalization Uncertainties

Two sources of normalization uncertainties are identified for the overall normalization in the lifetime fit: the uncertainty in tracking efficiency and the uncertainty in the luminosity measurement. These sources are included as normalization uncertainties in the likelihood model with two NPs constrained by a 1σ envelope at 0.45% for the luminosity uncertainty (discussed in Section 6.1.3) and 0.96% for the tracking efficiency uncertainty, obtained by a 0.24% ²¹ uncertainty per track [115].

²¹In the meanwhile, the tracking efficiency and also its uncertainty got updated to 0.27% [114]. This is expected to have no impact on the fit result.

6. τ -Lepton Lifetime Measurement Using Template Fits

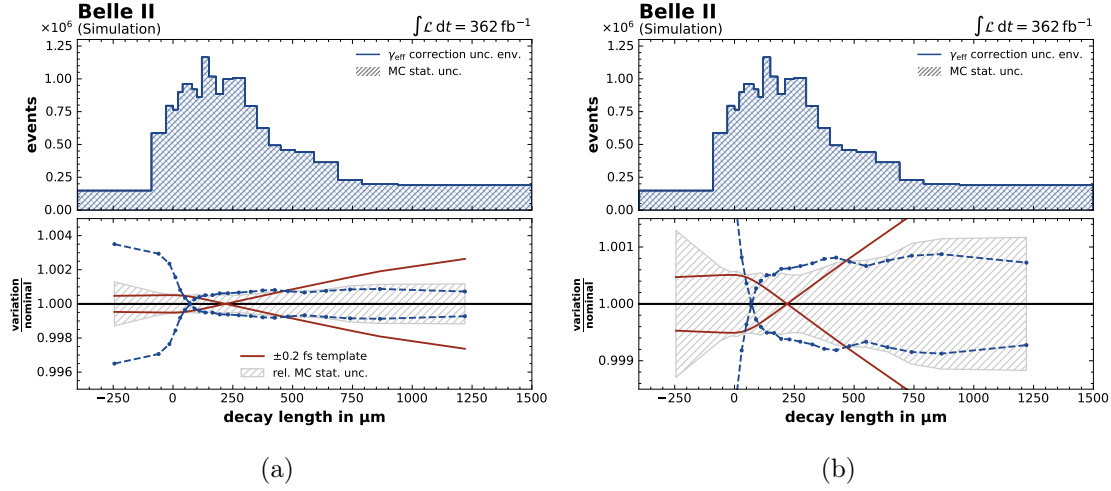


Figure 6.51.: (a): ε_γ correction precision induced decay length shape-shift with impact on the fit uncertainty. (b): Zoom of (a) in the lower ratio plot. The statistical uncertainties of the histograms are not visible.

Neither of the normalization NPs exhibits a measurable impact on the τ -lepton lifetime fit result. Consequently, the two normalization uncertainties are pruned from the likelihood model in Section 6.8.13.

6.8.12. NP Pulls and Correlations

A sanity check of the template fit involves examining the *post-fit* NP values, $\hat{\alpha}$, after fitting to the pseudo-data. In such a fit setup, the post-fit NP values are expected to be equal to their central values, which for the correlated shape modifiers corresponds to $\hat{\alpha} \equiv \bar{\alpha} = 0$.

The uncertainty of the NPs should not increase during the fit compared to the intrinsic uncertainties associated with the 1σ envelopes of the NP constraints. This is visualized in the so-called *pull plot*, shown for the nominal template in Figure 6.52a. This implies that the error bars of the post-fit NP values from the pseudo-data fit should lie within the green band (see Section 6.2.3). The pull itself should be centered at 0, as the nominal template is fed as pseudo-data into the fit. Consequently, the fit should identify the nominal template as the best-fit value without pulling the NPs.

As visible in Figure 6.52a for the nominal template, an increased post-fit uncertainty is present for the $c\bar{c} \pm 50\%$, $p_{T,\pi_{3p}}^{3D}$, and $\Delta x_{\text{IntrSyst},1}$ NPs. In contrast, the post-fit pull plot in Figure 6.52b shows the $+0.01 \text{ fs}$ template²². Here are no increased NP uncertainties observed. In this case, a slight variation in the pseudo-data distribution compared to the template distribution helped to *stabilize* the fit.

Due to the Gaussian constraint term in Equation (6.5), the likelihood fit tends to distribute the pull across multiple NPs rather than strongly pull a single NP. As a result, if, for example, two NPs can compensate for a decay length shape-shift, a correlation between these NPs is observed. Through this mechanism, the impact of an otherwise negligible NP can become significantly

²²This fit was also performed with the pseudo-data from the nominal template.

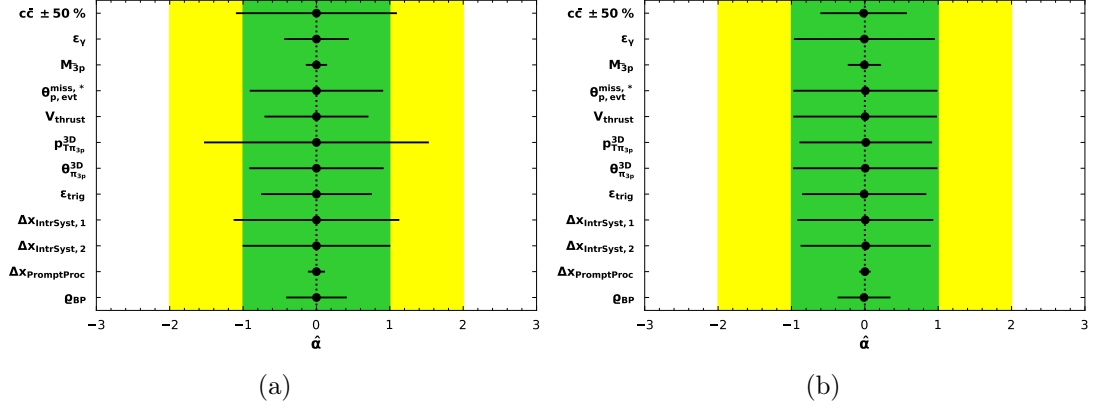


Figure 6.52.: Pull plot of the final pseudo-data fit, excluding the MC stat NPs. (a) For the nominal template (b) for the +0.01 fs template.

larger when additional NPs are included. Complex correlations can lead to increased post-fit NP uncertainties and may result in unstable fit results if not properly controlled.

Figure A.16 presents a scan of all post-fit shape NP uncertainty pulls for the entire likelihood scan. It is clearly visible that as the lifetime variation increases, the NPs are pulled further from their nominal values. Additionally, it can be observed that NP uncertainties increase only for specific templates, as seen in the nominal template fit. The vast majority of fits exhibit normal behavior. Individual fits that show unstable behavior can still be controlled by stable neighboring template fits. If necessary, since only single fits are affected and the parabolic $2\Delta\text{NLL}$ curvature (see Figure 6.6) remains stable, the overall minimum can be estimated using a parabolic fit.

To examine the origin of the increased post-fit NP uncertainties for the nominal template fit, the *correlation matrix* of the stable +0.01 fs template fit is compared with the correlation matrix of the unstable nominal template fit.

Figure 6.53 shows the correlation matrix for the +0.01 fs template fit. The following (anti-)correlation between the NPs are observed:

- **Remaining mismodeling NPs:** A moderate anti-correlation of -0.58 is observed between the NPs $M_{\tau_{3p}}$ and V_{thrust} , and a moderate anti-correlation of -0.4 between $M_{\tau_{3p}}$ and $p_{T, \pi_{3p}}^{3D}$.
- **Material budget:** Anti-correlations between $\varrho_{\text{BP}, \pm 5\%}$ and $\Delta x_{\text{PromptProc}}$, as well as ϵ_{trig} , with moderate values up to -0.53 are observed. Additionally, correlations between $\varrho_{\text{BP}, \pm 5\%}$ and $p_{T, \pi_{3p}}^{3D}$, $c\bar{c} \pm 50\%$, and $\Delta x_{\text{IntrSyst}, 1}$ with moderate values up to 0.53 are observed.
- **$c\bar{c}$ contribution:** An anti-correlation between $c\bar{c} \pm 50\%$ and $\Delta x_{\text{PromptProc}}$, as well as ϵ_{trig} , with a high value up to -0.76 is observed. Furthermore, correlations between $c\bar{c} \pm 50\%$ and $\varrho_{\text{BP}, \pm 5\%}$, $\Delta x_{\text{IntrSyst}, 2}$, and $M_{\tau_{3p}}$ with moderate values up to 0.53 are observed.

6. τ -Lepton Lifetime Measurement Using Template Fits

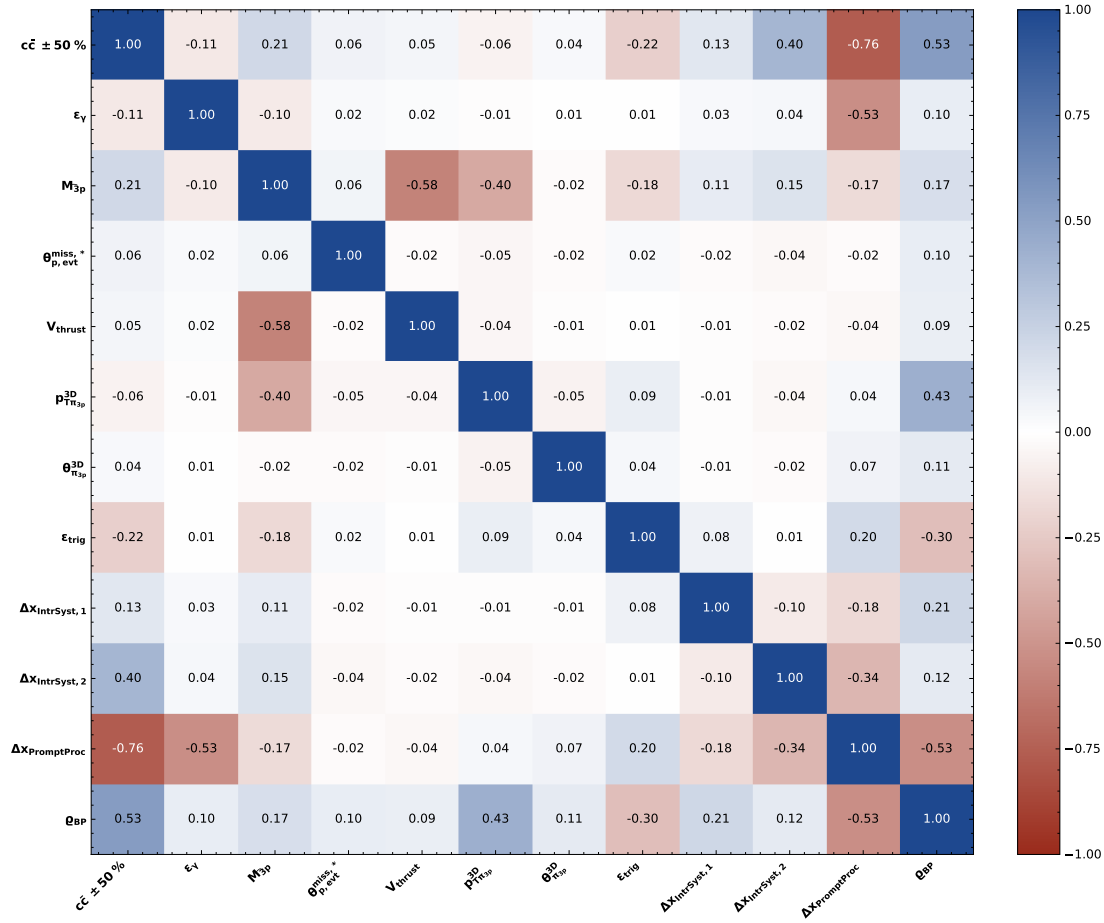


Figure 6.53.: Correlation matrix of the pruned pseudo-data fit of the +0.01 fs template. Shown are the shape NPs with blue indicating correlations and red indicating anti-correlations. Not shown are the MC stat. NPs.

- **Trigger efficiency:** Anti-correlations between ϵ_{trig} and $\varrho_{BP, \pm 5\%}$, as well as $c\bar{c} \pm 50\%$, with low values up to -0.3 , and a correlation between ϵ_{trig} and $\Delta x_{\text{PromptProc}}$ with a low value of 0.2 is observed.
- **Reconstruction correction NP:** The ϵ_γ NP shows a moderate anti-correlation of -0.53 with the $\Delta x_{\text{PromptProc}}$ NP.

All other absolute (anti-)correlations between the NPs are below $|\pm 0.2|$.

Even though some significant (anti-)correlation between the NPs of the +0.01 fs fit are observed, the fit remains stable. Figure 6.54 shows the correlation matrix for the nominal template fit. For this particular fit, the (anti-)correlation between the shape uncertainty NPs are significantly increased. The most prominent observations are summarized in the following:

- The already high $c\bar{c} \pm 50\%$ and $\Delta x_{\text{PromptProc}}$ anti-correlation increased further to a value

of -0.98 .

- The moderate $c\bar{c} \pm 50\%$ and $\varrho_{\text{BP}, \pm 5\%}$ correlation turned to a high anti-correlation with value of -0.87 .
- A new high ant-correlation between $c\bar{c} \pm 50\%$ and $p_{T, \pi_{3p}}^{3D}$ with value of -0.93 is observed.
- A new high correlation between $p_{T, \pi_{3p}}^{3D}$ and $\varrho_{\text{BP}, \pm 5\%}$, as well as $\Delta x_{\text{PromptProc}}$, with values up to 0.92 is observed.
- In general, more pronounced (anti-)correlations between the misalignment NPs is observed.

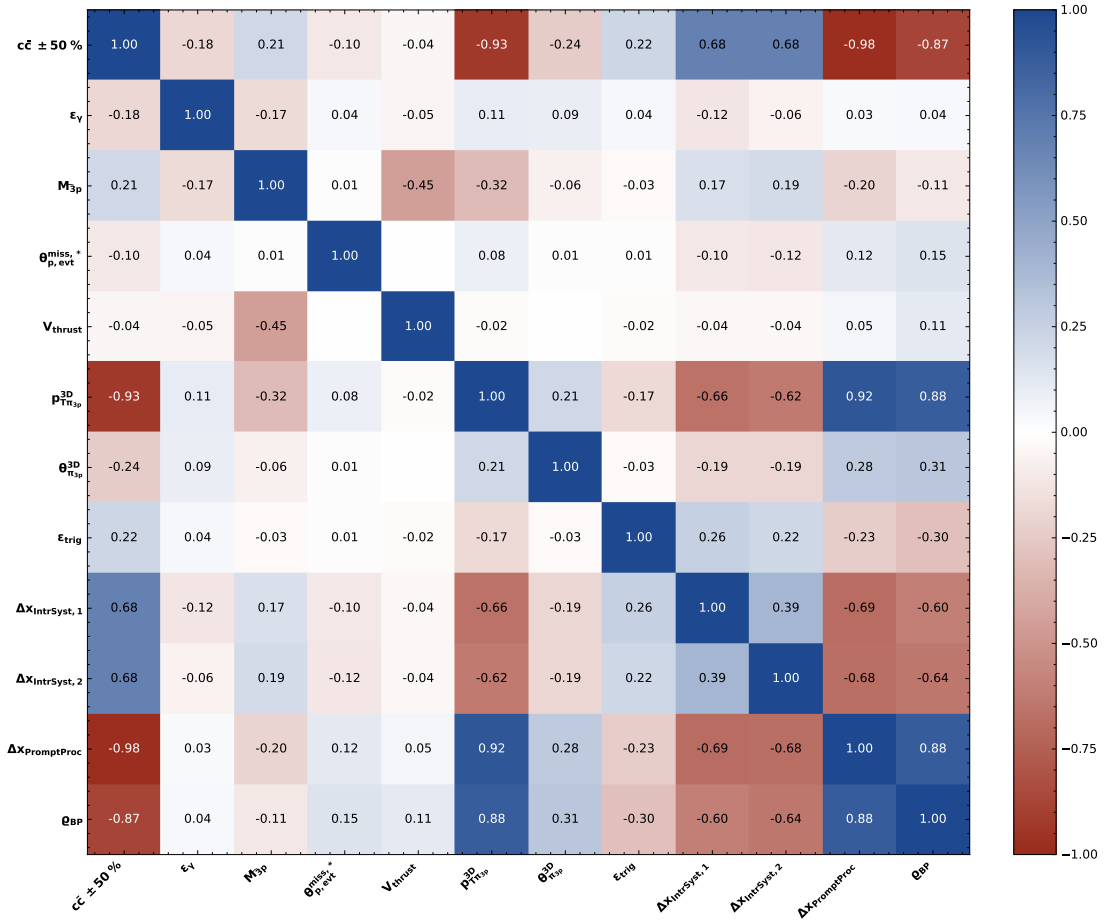


Figure 6.54.: Correlation matrix of the pruned pseudo-data fit with the nominal template. Shown are the shape NPs with blue indicating correlations and red indicating anti-correlations. Not shown the MC stat. NPs. Not shown are the MC stat. NPs.

6. τ -Lepton Lifetime Measurement Using Template Fits

Such an increase in the (anti-)correlations of the shape uncertainty NPs between the two likelihood fits is also observed among the MC stat. NPs in the decay length bin regions that include a *crossing point* of shape uncertainty NP envelopes or the lifetime-dependent crossing point. The correlations of the MC stat. NPs are shown in Figure A.14 for the nominal template fit and in Figure A.15 for the $+0.01$ fs template fit. In general, the (anti-)correlations are more pronounced in the nominal template (Figure A.14).

The study of decay length shape-shifts and correlations highlights the importance of considering all types of uncertainties and examining their interplay, as they may cancel or amplify each other. At the same time, it is crucial to remove unnecessary degrees of freedom from the likelihood fit to ensure stability. In particular, double-counting of systematic uncertainties or overly conservative estimations of NP constraints can introduce instability.

6.8.13. Total

The total uncertainty is obtained from the pseudo-data fit without the pruned NPs discussed in the previous subsections. The best-fit results of the pseudo-data likelihood scan for the lifetime templates are shown in Figure 6.55. A fit result of 290.57 ± 0.2 fs is obtained. The central value corresponds to the expected value associated with the nominal template used as pseudo-data.

Table 6.18 provides a summary overview of the breakdown of the remaining systematics, which are included as NPs in the pseudo-data fit. The overall systematic contribution to the total uncertainty is measured to be 0.18 fs. Four main systematic uncertainties can be identified: alignment, the $c\bar{c}$ contribution, remaining mismodeling, and the material budget, each with an expected contribution of 0.1 fs.

Source	σ in fs
Statistical	0.08
Systematic	0.18
MC stat. (12 NPs)	0.07
template correction (2 NPs)	0.06
remaining mismodeling (3 NPs)	0.10
misalignment (3 NPs)	0.10
material budget	0.10
trigger efficiency	0.04
$c\bar{c}$ contribution	0.10
ε_γ	0.03
Total	0.20

Table 6.18.: Table of total uncertainty without pruned NPs.

The expected precision of the τ -lepton lifetime measurement, compared to the PDG world average in conjunction with the LFU test discussed in Section 3.2, is shown in Figure 6.56. Although a significant improvement in the precision of the test is expected, the absolute shift in the τ_τ value remains blinded in this work.

The relative τ -lepton lifetime precision is expected to improve from 1.72×10^{-3} to 6.90×10^{-4} ,

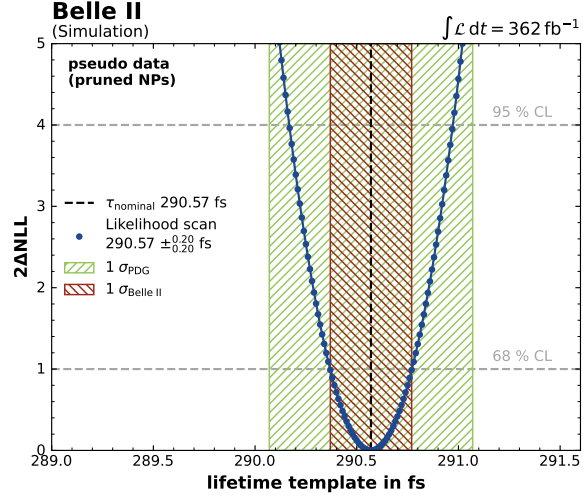


Figure 6.55.: Fit results of the pseudo-data likelihood scan without the pruned NPs to estimate the total expected uncertainty. Indicated is the precision of the world average τ -lepton lifetime value σ_{PDG} and the expected precision of this work $\sigma_{\text{Belle II}}$.

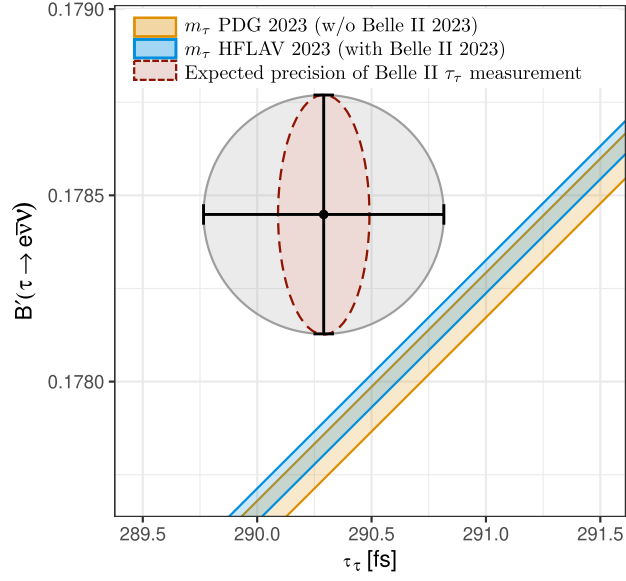


Figure 6.56.: The expected precision of the τ -lepton lifetime measurement, in conjunction with the measured $B'_{\tau e}$ value and the SM prediction (see Figure 3.2). (Figure adapted from [20])

which is still two orders of magnitude worse than the relative μ lifetime precision of 1.001×10^{-6} .

The expected precision of the novel measurement method presented in this work is approximately three times better than the Belle measurement and two-and-half times better than the world average [116].

7. PXD2 DEPFET Biasing Optimization

In 2022, the PXD2 half-shells were assembled at the *Max-Planck-Institut für Physik (MPP, Werner Heisenberg Institut) (Munich)* and transported to the *Deutsches Elektronen Synchrotron (DESY) (Hamburg)* for pre-commissioning before being shipped to KEK for commissioning and installation.

During the commissioning and operation of PXD1, it was observed that for several modules the optimal DEPFET working points were not identified during the series testing optimization procedure, discussed in Section 7.1. The main reason for this was the application of non-uniform measurement and evaluation criteria during the series testing phase. For PXD2, in the pre-commissioning phase, a revised and uniform evaluation and optimization of the DEPFET working points is addressed in this work.

Originally, it was planned that a detailed optimization and characterization of PXD2 would be performed during a long-term operation period as part of the pre-commissioning at DESY. A dedicated PXD half-shell test setup was designed and implemented for this purpose, as discussed in Section 7.4. During this first long-term operation, a multidimensional parameter space source scan (referred to as the *multi-parameter source scan*) was performed, as discussed in Section 7.5.1.

This first long-term operation on the fully populated two-layer PXD half-shell (*upper HS v1*) revealed general mechanical design flaws. Specifically, the SCB and ladder gliding mechanisms, intended to relax thermal tension, did not function as expected. Consequently, two L1 ladders developed a kink (see Figure A.17), leading to a halt in operations and measurements. As a result, both half-shells were reworked and mechanically improved. The time window for the pre-commissioning, source scan measurements, and the commissioning at KEK was significantly reduced due to constraints imposed by the global project schedule during LS1.

To accommodate these constraints, a reduced one-dimensional parameter space source scan (referred to as the *HV source scan*) was conducted to identify a suitable starting point for a more detailed multi-parameter scan, to be performed later using the e^+e^- collisions of SuperKEKB after the PXD2 installation. This significantly reduces the future parameter space to scan. These starting points are found to serve already as acceptable DEPFET working points.

The HV source scan was conducted at DESY for the lower half-shell (*lower HS*) and at KEK for the second version of the upper half-shell (*upper HS*), as discussed in Section 7.5.2. The DEPFET working point parameters determined from the HV source scan, combined with the results from the series testing of the modules and subsequent improvements for the PXD2 operation, are discussed in Section 7.6.

7.1. Previous Optimization Efforts for PXD Modules During Series Testing

After the production process of the PXD modules, described in [62], each module underwent a functionality test, operational parameter characterization, and optimization procedure

7. PXD2 DEPFET Biasing Optimization

[117][63] at various sites: MPP, SiLab at Rheinische Friedrich-Wilhelms-Universität (Bonn), Georg-August-Universität (Göttingen), and DESY. At this stage, module grades were assessed to determine whether the module quality was sufficient for operation in the PXD.

During the optimization procedure, the operation voltages of the DEPFET pixel matrix were fine-tuned by measuring its response to ionizing radiation from a radioactive source, referred to as a *source scan*. Two types of sources were used: a ^{90}Sr β^- source or a ^{109}Cd γ source. The sensors were always illuminated from the top side. ^{90}Sr sources were preferred, as the low-energy γ radiation from the ^{109}Cd source was largely absorbed by the top-side metal layer structures of the sensor matrix.

The number of created e^-h^+ pairs is directly proportional to the energy loss of the traversing ionizing particle. For the ^{90}Sr source, the deposited energy follows a Landau-shaped distribution (see Section 2.3). According to Equation (5.4), the statistical distribution of the signal drain currents is also Landau-distributed.

The created e^-h^+ pairs may be distributed across several neighboring pixels. Consequently, neighboring pixel hits and pixel hits that share the same corner within one readout frame are combined into *pixel clusters*. The ADU values of individual pixels within a cluster are summed to compute the *cluster charge*, which represents the total energy loss of the ionizing particle as it traverses the sensor. A small fraction of the energy is lost in pixels whose charge does not exceed the ADU zero-suppression threshold¹.

Figure 7.1a shows a measured cluster charge distribution for the module W10-IF. The cluster charge distribution is fitted to a *LanGau* distribution, which is a convolution of a Landau distribution and a Gaussian readout noise distribution:

$$f_{\text{LanGau}}(Q_{\text{MPV}}, \eta, \sigma, A) = f_{\text{Landau}}(Q_{\text{MPV}}, \eta, A) \otimes f_{\text{Gaus}}(Q_{\text{MPV}}, \sigma), \quad (7.1)$$

where Q_{MPV} is the *most probable value (MPV)*, A is the amplitude of the MPV, η is the scale parameter for the Landau distribution f_{Landau} [118], and σ is the width of the Gaussian distribution f_{Gaus} . The LanGau distribution can be calculated using [119]. The fit in Figure 7.1a demonstrates good agreement in the peak region corresponding to the MPV. However, the tail of the measured cluster charge distribution deviates from the Landau distribution. These deviations are caused by: (a) the dynamic range of the DCD, where the sampling precision depends on the headroom between the pedestal ADU value and the maximum ADU value of 256, and (b) the path length of particles entering the silicon bulk at shallow angles, for which the energy loss probability density function (p.d.f.) no longer conforms to an ideal Landau distribution.

To evaluate the DEPFET working point for different biasing voltage settings, several techniques were used over time and depending on the testing site. They ranged from evaluating the Q_{MPV} value and hit maps by eye up to sophisticated studies evaluating the sensor matrix in small pixel groups [63], [117]. In 2021, the library for the source scan in the PXD software framework contained a simplified *figure of merit (FOM)* [120], the *signal-to-noise ratio (SNR)*:

$$SNR = \frac{Q_{\text{MPV}}}{\sigma_{\text{noise}}}, \quad (7.2)$$

where Q_{MPV} is extracted from the LanGau fit, and σ_{noise} is the median of the pedestal noise

¹For a pixel hit, the collected charge must exceed the threshold of 7 ADU to filter out noise hits

7.1. Previous Optimization Efforts for PXD Modules During Series Testing

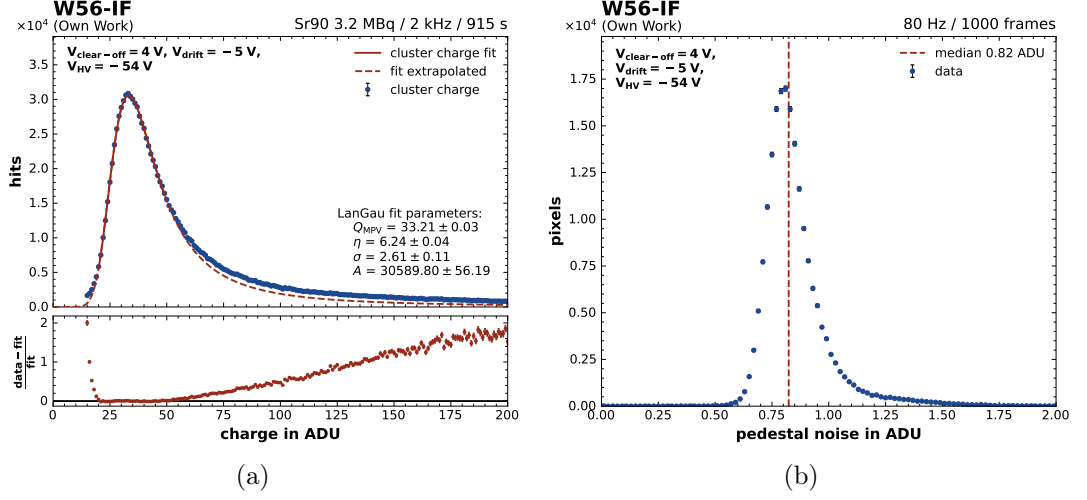


Figure 7.1.: (a) Measured cluster charge distribution from ionizing radiation exposed 915 s to an 3.2 MBq ^{90}Sr source with a trigger rate of 2 kHz. The peak region [15, 50] ADU (solid line) was used to fit a LanGau distribution (dashed line). The events with cluster charge < 15 ADU were removed to reduce further the noise contribution in the low ADU region. The onset of the removed peaking low ADU noise becomes visible around $\lesssim 20$ ADU. (b) Measured pedestal noise of the 192 k pixels from 1000 recorded frames with a trigger rate of 80 Hz, defined by the standard deviation of the mean pedestal value of each pixel. Indicated is the median noise value σ_{noise} .

of the DEPFET sensor matrix. Figure 7.1b shows a pedestal noise distribution measured for module W10-IF. The pedestal noise includes the ADC noise from the DCDs, which constitutes the dominant component of the readout noise. The higher the SNR value, the better are the working points of the DEPFET pixels in the sensor matrix optimized. The SNR is calculated for each PXD module separately.

The scanned parameter space was optimized over the years of series testing. The parameter space suggested in 2021 is listed in Table 7.1.

Voltage	Lower in V	Upper in V	Step in V
V_{HV}	-70	-60	2
V_{drift}	-5	-3	1
$V_{\text{clear-off}}$	2	5	1

Table 7.1.: Parameter space covered during the source scan in the series testing [120].

7.2. Revised Figure of Merit for DEPFET Biasing Optimization

For the pre-commissioning phase, the focus of the source scan is entirely on optimizing the DEPFET working points. The evaluation in this work will consider two criteria:

1. **SNR:** The signal-to-noise ratio, as described in Section 7.1.
2. **Signal Hits:** If certain regions of the sensor matrix are not properly depleted, they will appear as areas with a significantly lower number of pixel hits². This effect is expected to reduce the hit efficiency³. It also affects the measured *LanGau cluster charge distribution area*, where a larger area under the distribution would mean a better sensor configuration.

The cluster size (i.e., the number of pixels in a cluster) is correlated with the Q_{MPV} value and is therefore not considered as a separate criterion. A higher Q_{MPV} corresponds to a larger average cluster size.

To calculate the area under the measured charge distribution, the fitted cluster charge distribution is used since it is not directly affected by single noisy channels which can show up in single narrow noisy peaks in the charge spectrum. However, Equation (7.1) does not describe sufficiently the tail towards larger charge values. Therefore, a slightly modified distribution is defined, which overcomes this problem:

$$f_{\text{LanGauB}}(Q_{\text{MPV}}, \eta, \sigma, A, B) = f_{\text{LanGau}}(Q_{\text{MPV}}, \eta, \sigma, A) + B, \quad (7.3)$$

where B is a constant term that absorbs the effects of finite signal ADU precision and the increased path lengths of shallowly impinging ionizing particles (see Section 7.1). As a result, the fit range can be significantly extended, making the fit more robust across different cluster charge spectra measured for various module orientations on the half-shell relative to individual source positions (see Section 7.3 and Section 7.4).

Figure 7.2a shows an example of a LanGauB cluster charge distribution fit. A comparison between the seed pixel and cluster charge distributions is also shown in Figure 7.2b. For optimized DEPFET working points, pixel clusters typically consist of more than two pixels on average, causing the cluster charge distribution to shift toward higher charge values compared to the seed pixel charge distribution.

To incorporate the area under the curve in an FOM, Equation (7.2) is extended to define the *extended signal-to-noise ratio* (SNR_{ext}):

$$SNR_{\text{ext}} = \frac{Q_{\text{MPV}}}{\sigma_{\text{noise}}} \cdot \frac{F}{n_{\text{frames}}}, \quad (7.4)$$

where $F = \int f_{\text{LanGauB}} dq$ represents the area under the fitted cluster charge distribution, and n_{frames} is the number of recorded frames. The inclusion of n_{frames} normalizes the measurement.

Increasing F due to noise will still be penalized by a larger σ_{noise} value. Additionally, noise hits typically occur in the low ADU region, which can be excluded from the fit range (see Figure 7.2a).

²It was found, this does not necessarily hold for under-depletion (see Section 7.5.1).

³The ratio of the number of particles that traversed the detector to the number of clusters generated by the “hit” module.

7.2. Revised Figure of Merit for DEPFET Biasing Optimization

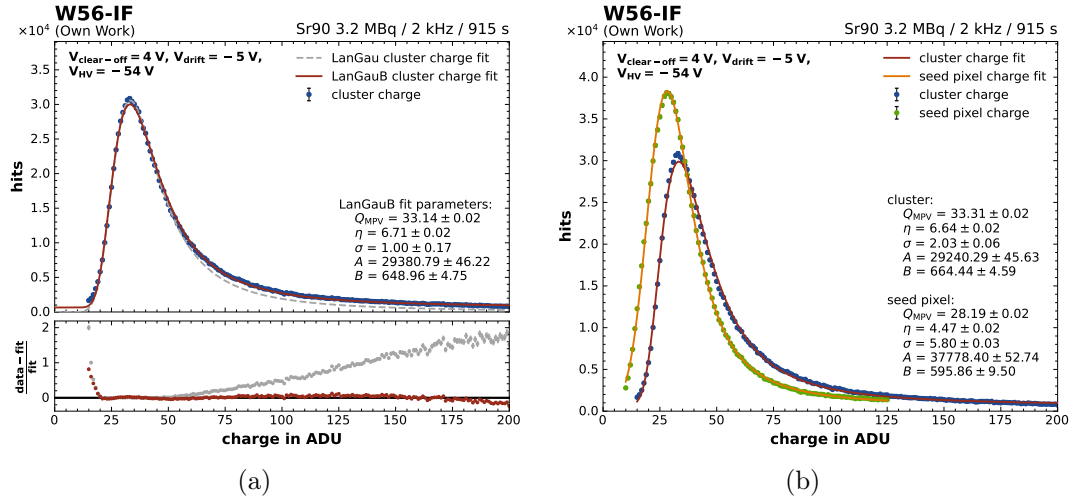


Figure 7.2.: (a) Comparison between a LanGau and LanGauB fit. The LanGau fit better describes the peak region but is primarily limited to that region. In contrast, the LanGauB fit provides a more accurate description of the overall distribution, making it more robust for automated fits across a wide range of cluster charge distributions. The onset of the removed low ADU noise peaking at < 15 ADU becomes visible around $\lesssim 20$ ADU. (b) Distribution of measured seed pixel charge and cluster charge values. In this example, the module was exposed to an $3.2 \text{ Bq } ^{90}\text{Sr}$ source for 915 s. The hit data was recorded with a trigger rate of 2 kHz.

Moreover, single pixels with significant higher hit rates can also be excluded during clustering, which removes isolated noise hits from F , counteracting possible optimization based on noise.

Based on the chosen FOM, either SNR or SNR_{ext} , the optimal DEPFET working point is defined by the maximum value of SNR or SNR_{ext} .

7.3. Charge Collection Dependency on Incident Angle

The path length through the sensor bulk increases for shallower ionizing e^- incident angles relative to the sensor surface. Consequently, the energy deposited in the sensor bulk increases. If the angle is sufficiently shallow relative to the pixel size, the cluster size also increases. A study was conducted in preparation for the construction of a half-shell test setup for the half-shell source scans to examine the dependency of the Q_{MPV} on the incident angle of ionizing particles from a ^{90}Sr source.

The ^{90}Sr source was positioned at a constant distance r of approximately 7 cm from the center of the DEPFET sensor matrix of a test PXD module. The incident angle of the source with respect to the DEPFET sensor matrix was varied by moving the source around a circle in the r - u plane, while maintaining a fixed center position in the v -direction. The DEPFET sensor matrix response to the ionizing radiation was measured for each respective incident angle.

The measured cluster charge and seed charge distributions were fitted using Equation (7.3). Figure 7.3a shows the measured Q_{MPV} values as a function of the incident angle. Additionally, Figure 7.3b shows the respectively measured cluster charge distributions.

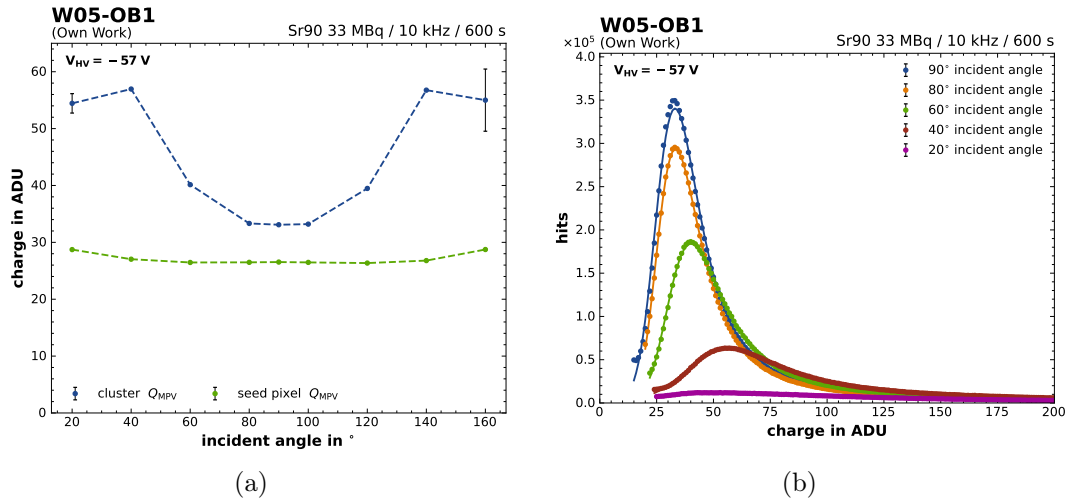


Figure 7.3.: (a) Measured seed pixel and cluster Q_{MPV} values depending on the incident angle of the ionizing radiation using PXD test module exposed to a 33 Bq ^{90}Sr source. (b) Measured cluster charge distributions depending on the respective incident angles. The solid lines show the LanGauB fit distributions. (Measurements performed in cooperation with SiLab Bonn)

While the seed pixel Q_{MPV} value shows only considerable variations at very shallow incident angles, a clear angular dependency is observed for the cluster charge Q_{MPV} values. A local minimal plateau occurs for a perpendicular incident angle (90°) with a spread of $\pm 10^\circ$. At shallower incident angles, the path length increases, raising the probability of additional pixel traversal. Consequently, the cluster charge Q_{MPV} values increase significantly. This behavior is further corroborated by the slightly decreasing seed charge Q_{MPV} toward shallower angles (prior to increasing again at very shallow angles), as the energy deposition becomes more likely spread across multiple pixels. The fitted cluster charge Q_{MPV} reaches a maximum at approximately 30° (150°).

7.3. Charge Collection Dependency on Incident Angle

The measured cluster charge distribution at 20° (160°) shows a very broad Landau distribution. Additionally, the cluster size distribution reveals an increased fraction of clusters containing only a single pixel. This is attributed to the shallow incident angle and multiple scattering effects, where even a small scattering angle can deflect the ionizing particle out of the silicon bulk. Moreover, the probability of larger scattering angles increases with the path length (see Section 2.3). This significantly broadens the Landau distribution, leading to greater fit uncertainties for these measurement points.

7.4. Simulation and Construction of a Half-Shell Source Setup

An aluminum (Al) BP mockup was specifically designed for the 2018 PXD1 pre-commissioning at DESY. This Al BP mockup remained available and served as the basis for the PXD2 pre-commissioning half-shell test setup. The previous pre-commissioning setup was extended by a source setup to facilitate source measurements with a PXD half-shell.

The new half-shell test setup was designed to provide space for a movable source holder to illuminate the half-shell. The project schedule had planned for the serial testing and optimization of the half-shells. The basic Al BP mockup setup is illustrated in Figure 7.4.



Figure 7.4.: The Al BP mockup was already utilized for the PXD1 commissioning. The thin, round section at the center represents the mockup of the actual beryllium (Be) component that covers the IP. This central section is enclosed by the PXD. The mockup BP is surrounded by Al profiles, which are mounted together with the mockup BP onto two end plates that support the entire setup.

7.4.1. Source Setup Simulation

Time constraints in the PXD2 commissioning project plan required the parallel planing and construction of the new half-shell test setup while in parallel the half-shells were serially assembled at MPP.

The optimal source positions were unknown parameters for the new half-shell test setup. Since the ionizing particle intensity of a radioactive source decreases with a $1/r^2$ dependency, where r is the distance, it was essential to ensure that the source positions were carefully chosen. A suitable particle intensity needed to be maintained while ensuring that all edges of the half-shell were adequately illuminated.

The geometry of the half-shells, characterized by the vertical L2.1 and L1.1 ladders on one side and the nearly vertical L2.6 and L1.4 ladders on the opposite side, required the use of at least two source positions. To determine and optimize these positions, an iterative simulation was set up to evaluate possible configurations. Figure 7.5 shows a simplified CAD model of the half-shell test setup, including two possible source positions to be tested using the simulation.

The **basf2** framework provides a Geant4 [72] based detector simulation of the entire Belle II detector, including the PXD, with subsequent event reconstruction. For the half-shell source setup simulation, this framework was utilized. Most of the Belle II detector geometry was removed, retaining only the fully populated PXD half-shell geometry. The SuperKEKB Be BP

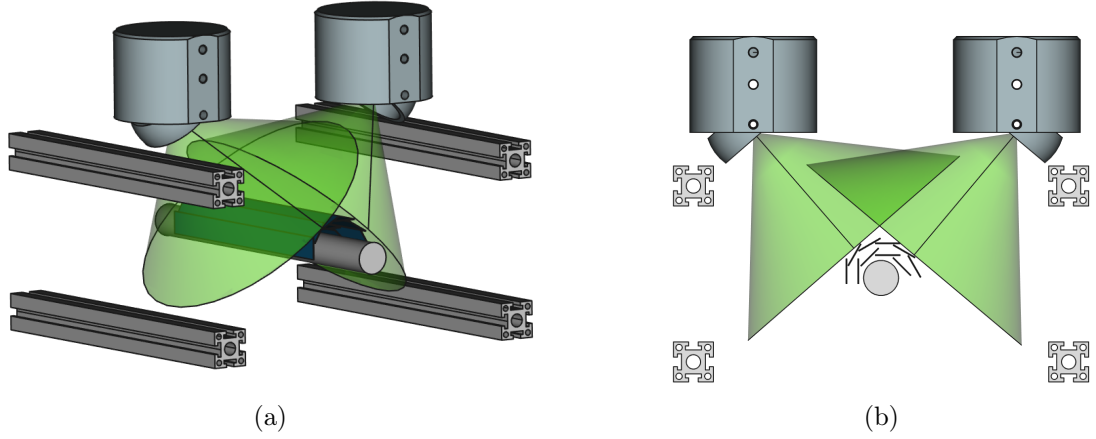


Figure 7.5.: Simplified CAD model of a mounted PXD half-shell on the central part of the Al BP mockup. Two source positions are illustrated along with their illumination cones. The source holders include a rotatable plate for adjusting the incident angle of the ^{90}Sr sources. Additionally, the holders feature a safety position, where the source is directed inside the aluminum holder for radiation safety. The aluminum profiles of the BP mockup support structure are considered to avoid collisions with the source holder. (a) 3D view, (b) section view.

geometry was replaced by a solid Al BP geometry. The Geant4 PXD half-shell geometry used in the simulation is shown in Figure 7.6.

In the simulation, e^- are generated using `basf2`'s `ParticleGun` module. The particle gun is configured with the potential source positions, incorporating the dimensions of the actual ^{90}Sr source into the simulation. The ^{90}Sr isotope undergoes a decay cascade, $^{90}\text{Sr} \rightarrow ^{90}\text{Y} \rightarrow ^{90}\text{Zr}$, through β^- decay processes. The e^- momentum distribution is generated using the `BxDecay0` library [121].

Only the higher-energy decay, $^{90}\text{Y} \rightarrow ^{90}\text{Zr}$, is considered, as it has an endpoint energy of 2.28 MeV. In contrast, the $^{90}\text{Sr} \rightarrow ^{90}\text{Y}$ decay has a lower endpoint energy of only 0.546 MeV and is therefore excluded. The resulting e^- momentum spectrum is shown in Figure 7.7.

To reduce computational costs, particles are generated only within the solid angle occupied by the detector half-shell geometry. This solid angle depends on the source position. The definition of the source position is shown in Figure 7.8a. The required azimuthal angle for the generated e^- to fully illuminate the half-shell is illustrated in Figure 7.8b. Along the z -axis, the source position is fixed at the center of the L2 ladders (glue gap), ensuring that the polar angle in the solid angle is symmetric in the forward and backward directions.

The planar angles required to define the solid angle are calculated based on the half-cylinder model depicted in Figure 7.9a and Figure 7.9b. While the azimuth angle φ_2 and the polar angle θ_1 are straightforward to compute, determining φ_1 requires solving a numerical equation⁴

⁴The numerical solution was obtained in this work using the `Wolfram Alpha API` [122].

7. PXD2 DEPFET Biasing Optimization

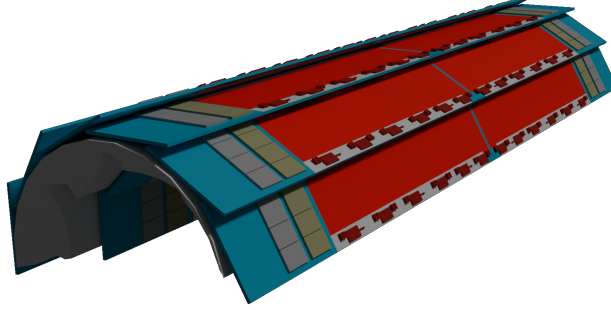


Figure 7.6.: PXD half-shell geometry used in Geant4 for the detector simulation. The Al mockup BP included in the simulation is not shown. Red indicates the DEPFET pixel matrix, and blue represents the Si support frame.

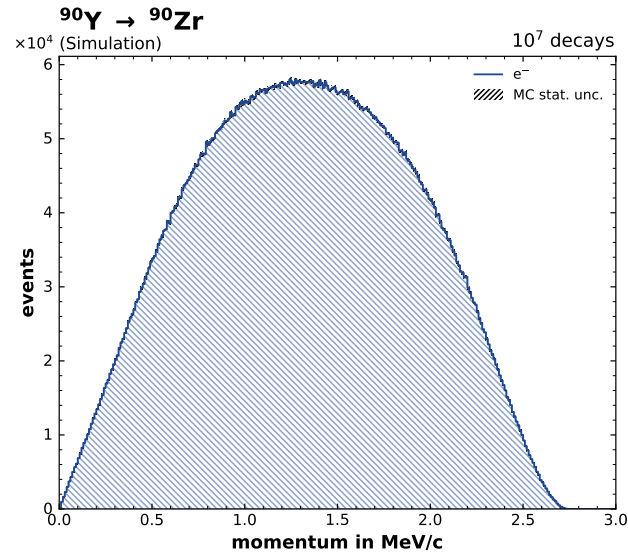


Figure 7.7.: Simulated e^- momentum spectrum expected from the ^{90}Sr source through the $^{90}\text{Y} \rightarrow ^{90}\text{Zr}$ β^- decay with an end point energy of 2.28 MeV. Mean e^- momentum is $1.32 \text{ MeV } c^{-1}$. The statistical uncertainties of the histograms are not visible.

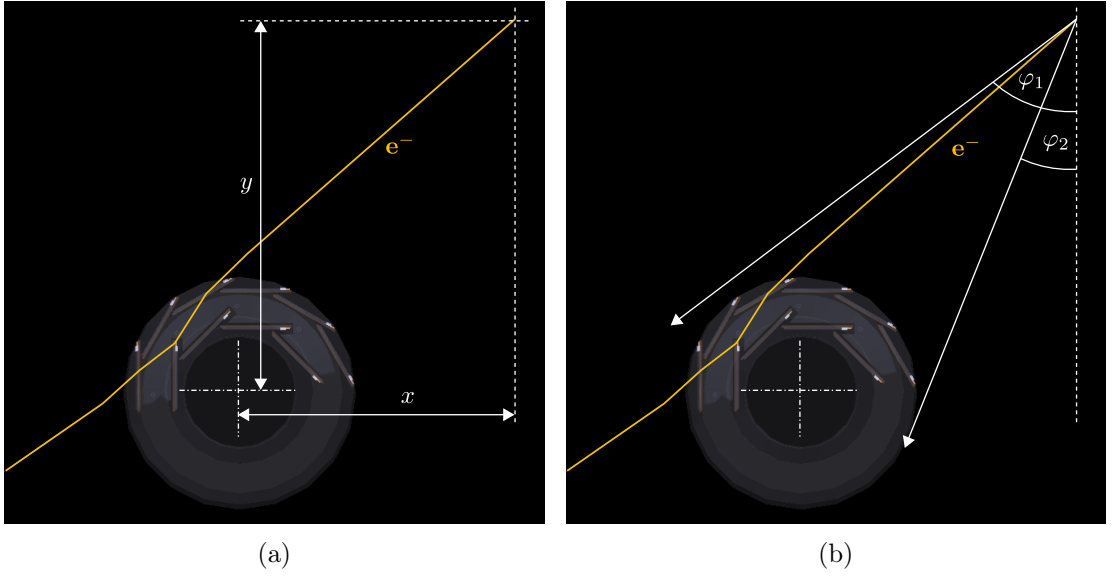


Figure 7.8.: PXD half-shell simulation in `basf2` showing a single generated e^- . The source position is located in the upper-right corner. The simulated track highlights the scattering of the e^- within the detector material, shown as kinks along the trajectory. (a) Displays the source position in terms of height (y) and horizontal distance (x). (b) Illustrates the opening angles that define the e^- generation window, $\varphi_1 - \varphi_2$, in the xy -plane.

7. PXD2 DEPFET Biasing Optimization

derived from the geometry:

$$\frac{\pi}{2} - \arctan\left(\frac{\sqrt{r^2 - y_T^2}}{y_T}\right) = \arctan\left(\frac{x + \sqrt{r^2 - y_T^2}}{y - y_T}\right), \quad (7.5)$$

where y_T is the height of the tangent defined by the angle φ_1 and the contour of the half-cylinder in the xy -plane.

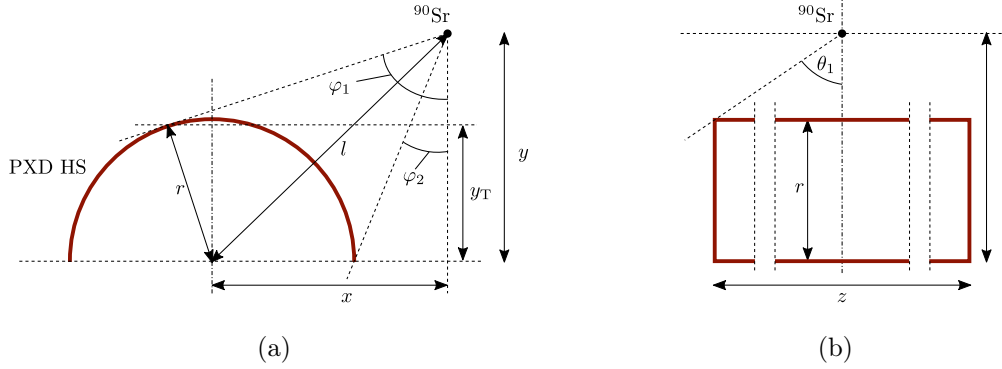


Figure 7.9.: Simplified half-cylinder model of the PXD half-shell used to calculate the solid angle occupied by the half-shell. (a) Shows the section view in the xy -plane, and (b) shows the section view in the lz -plane.

Once Equation (7.5) is solved, the planar angles defining the solid angle for the simulated illumination can be determined using the following expressions:

$$\varphi_1 = \arctan\left(\frac{x + \sqrt{r^2 - y_T^2}}{y - y_T}\right) \quad (7.6)$$

$$\varphi_2 = \arctan\left(\frac{x - r}{y}\right) \quad (7.7)$$

$$\theta_1 = \arctan\left(\frac{1}{2} \frac{z}{\sqrt{x^2 + y^2 - r}}\right). \quad (7.8)$$

It should be noted that Equation (7.8) provides only an approximate value for the optimal angle. However, due to the relatively large EOS regions, this approximation is sufficiently accurate to ensure coverage of the sensitive DEPFET sensor matrix regions.

Two source positions were identified through an iterative optimization process. These positions ensure full illumination of the half-shell while avoiding collisions with the Al profiles of the BP mockup support structure. For each of the two final source positions, a simulated dataset consisting of 1×10^7 e^- was generated. The optimized parameters for the source positions and the corresponding solid angles used in the simulation are listed in Table 7.2.

Position	x in cm	y in cm	$\frac{z}{2}$ in cm	r in cm	y_T in cm	φ_1 in $^\circ$	φ_2 in $^\circ$	θ_1 in $^\circ$
1	8.0	9.1	8.5	2.8	22.6	47.5	18.5	43.4
2	-6.0	9.1	8.5	2.8	20.6	-48.0	-19.4	43.7

Table 7.2.: Source positions and parameters used for the PXD half-shell source setup simulation.

7.4.2. Validation of the Simulation

Due to the complex geometry of the half-shell and its relative orientation to the source positions, computing the expected particle rate analytically is challenging. Instead, a prototype of the source setup was constructed, and a PXD half-shell mockup – used for transportation testing from MPP to DESY and to train the BP mounting procedure – was employed. This mockup featured a single working module installed on ladder L1.3.

To validate the simulation and estimate the expected hit rate, test measurements were conducted for the two favored source positions listed in Table 7.2. Figure 7.10a and Figure 7.10b show the normalized simulated and measured pixel hit projections for source position 1, while Figure 7.10c and Figure 7.10d show the same for source position 2.

The u projections for both source positions observed in the measurements align well with the simulation. Dips in the distributions, caused by shading from the overlaps of neighboring ladders or the Si support frames of the L2 ladders, are captured accurately. A slight shift along the u -axis is attributed to the alignment precision of the source but is negligible.

The v projections for both source positions exhibit a minor discrepancy in inclination between the simulation and the measurements. This suggests that the actual ^{90}Sr source is slightly more collimated than the simulated source. However, this effect is less than 20 % and is considered negligible, as the overall illumination at the edges of the half-shell remains sufficiently large.

From the measurement, normalization factors of 6.4890 for source position 1 and 6.285 for source position 2 were calculated based on the total number of hits measured. The measurement was conducted with a source of activity 3.2 MBq over a duration of 915 s, with a trigger rate of 5 kHz.

7.4.3. Expected Hitmap and Measurement Time

The expected hitmap for a measurement time of 915 s with a reduced trigger rate of 2 kHz is shown in Figure 7.11. Both source positions ensure full illumination of all regions of the PXD half-shell.

To scan the 3D parameter space described in Section 7.5.1 (Table 7.3), 156 measurement points are required. Each configuration requires a measurement time of 915 s, along with an additional configuration time of approximately 300 s per point. This results in an estimated measurement time of approximately 53 h.

Due to limited resources at the DESY PXD half-shell pre-commissioning setup, with only 10 of the required 20 power supplies available, the scan had to be performed twice for each half-shell. Consequently, to cover the full parameter space for both PXD half-shells, a total measurement time of approximately 212 h was anticipated. This extended measurement time was accounted for in the original commissioning project schedule, and also served to study the long-term operational behavior of the half-shells.

7. PXD2 DEPFET Biasing Optimization

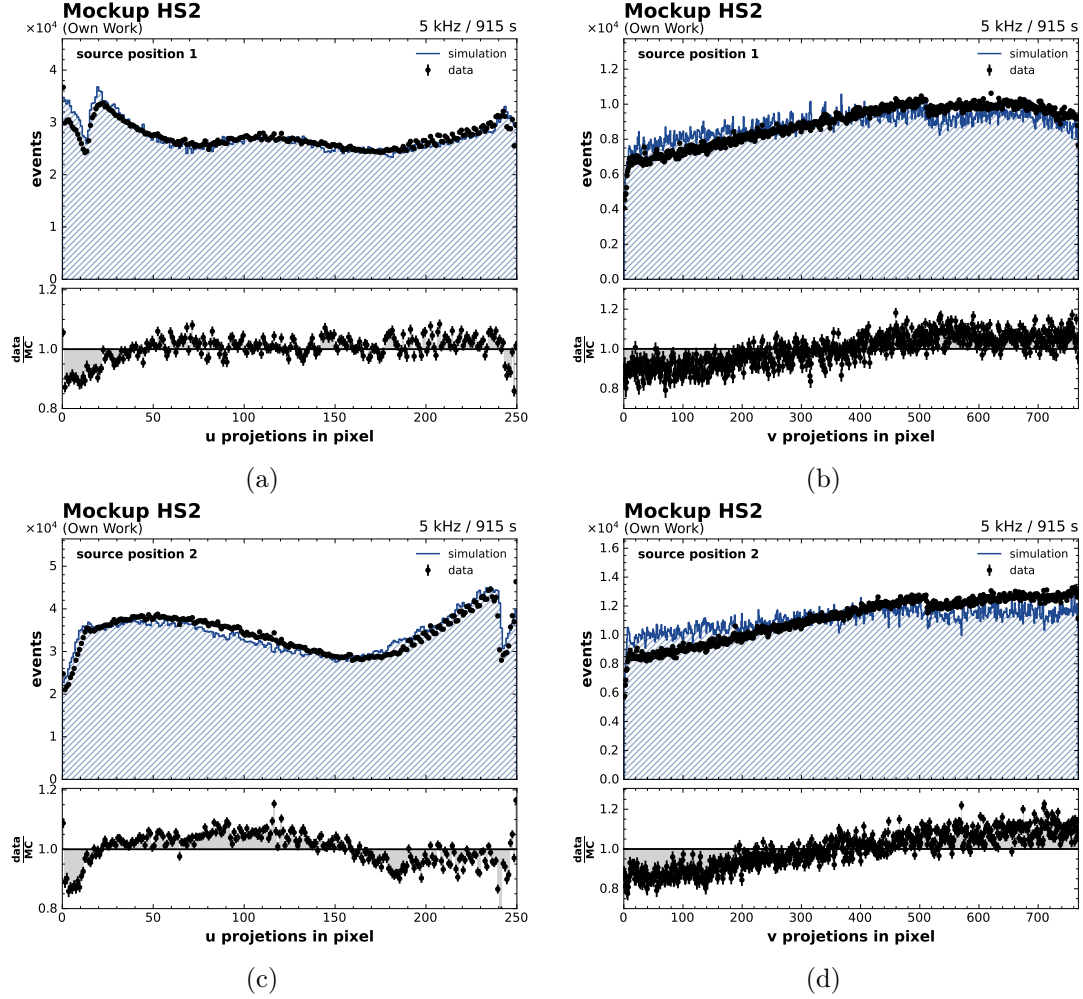


Figure 7.10.: Comparison of simulated and measured ionizing radiation for two source positions on L1.3, normalized to the total number of hits in the measurement. Pixel hits are projected onto the u -axis and v -axis of the DEPFET sensor matrix. The v -axis projections show a step at approximately 500 pixels, resulting from the change in pixel size. (a) and (b) correspond to source position 1, while (c) and (d) correspond to source position 2.

7.4. Simulation and Construction of a Half-Shell Source Setup

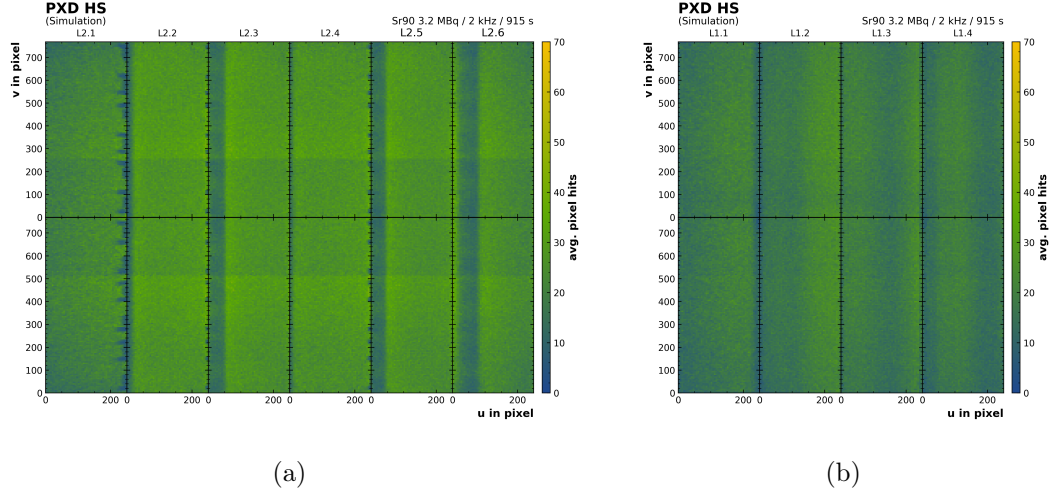


Figure 7.11.: Expected hitmap obtained from simulation, normalized for 915 s at a trigger rate of 2 kHz. The glue gap is located along the central horizontal axis. (a) The L2 hitmap reveals distinct shadow structures caused by overlapping ladders in the windmill arrangement. Shading from switcher ASICs and capacitors is visible due to the vertical placement of L2.1. Reduced hit numbers in rows 250 pixels symmetrically around the glue gap arise from the smaller pixel size in this region. (b) The L1 hitmap exhibits smeared shading due to multiple scattering in the outer L2 ladders. The expected hit rate is slightly lower for L1 compared to L2. L1.1, L1.2, and L2.1 to L2.3 are illuminated by source position 1, while L1.3, L1.4, and L2.4 to L2.6 are illuminated by source position 2.

7.4.4. DESY Half-Shell Test Setup

With the verifications gained from the simulations discussed above, the PXD half-shell test setup was constructed as illustrated in Figure 7.12. The setup provides essential connections from the module Kaptons to the power supplies, data readout, and configuration hardware, as well as the cooling system. A fully enclosing metal box serves multiple purposes: maintaining a dry volume, shielding against light and radiation, and integrating a four-axis movable source holder inside.

The enclosing metal box is mounted on a movable frame, enabling it to be displaced from the setup to allow placement and removal of the BP mockup with the mounted PXD half-shell. The dry volume is filled with gaseous N_2 to prevent condensation. A monitoring system, equipped with a camera, tracks the condition of the half-shell and records environmental parameters such as temperature and humidity. Additionally, a thermal interlock system is implemented to prevent the formation of condensed water or ice on the cooling structures during operation, especially in the event of a leakage in the dry volume.

After discovering mechanical issues with the first long-term operated upper half-shell, the camera and monitoring system was significantly extended to use the setup also for mechanical studies, which are not discussed in this work.

7. PXD2 DEPFET Biasing Optimization



Figure 7.12.: PXD half-shell test setup at DESY with the front panel opened. The magnified region highlights the source holder positioned above a PXD half-shell mounted on the Al BP mockup. A 50 μm thick polyethylene (PE) foil covers the half-shell to protect it from abrasions caused by the source holder mechanics.

7.4.5. KEK Commissioning Setup

Due to the adapted time schedule caused by the mechanical half-shell issues, the source scan for the repaired upper HS was relocated to the commissioning at KEK. Exploiting the knowledge of the source positions gained from the DESY half-shell source setup, a simplified static source setup was designed for operation at KEK within the final PXD2 commissioning setup. Figure 7.13 shows a CAD model of the source setup attached to a cylindrical metal cover. The source positions in the xy -plane are approximately aligned with those used at DESY. However, due to the less intense ^{90}Sr source available at KEK ($\sim 1.5\text{ MBq}$), the source positions were shifted to the center of the L2 modules instead of the center of the L2 ladders. This adjustment effectively doubled the number of source positions. The ^{90}Sr source was mounted in precast source holders, which included opening windows to allow ionizing radiation to enter the inner dry volume.

Figure 7.14 shows the KEK source setup in operation. The commissioning setup was enclosed within a dual-layer dry volume: an outer dry volume constructed with PE-foil and an inner dry volume defined by the cylindrical metal cover.

7.4. Simulation and Construction of a Half-Shell Source Setup

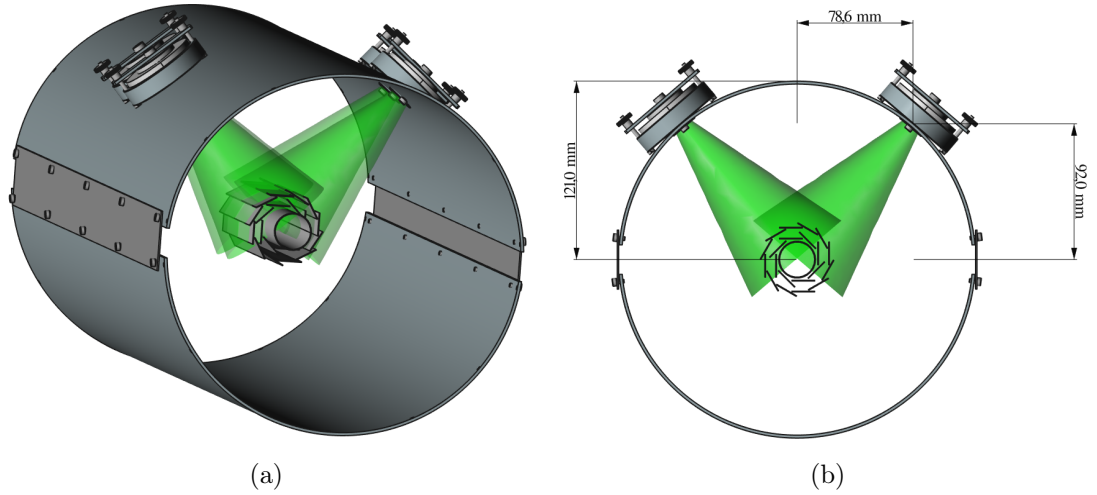


Figure 7.13.: Simplified CAD Model of the mounted PXD2 on the center part of the KEK BP. Illustrated are the four source positions with illumination cones. (a) 3D view, (b) section view.

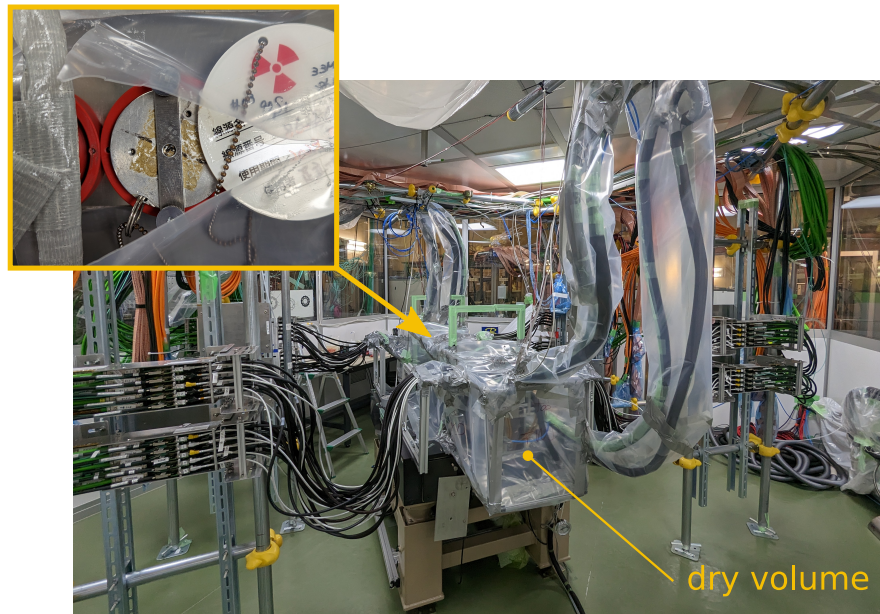


Figure 7.14.: PXD2 source setup at KEK enclosed within a N_2 -flooded dual-layer dry volume. Only the outer dry volume is visible. The magnified region highlights the ^{90}Sr source mounted in one of the source holders (red) attached to the cylindrical metal cover (inner dry volume).

7.5. Half-Shell Source Scans

The half-shell source scan is an automated measurement routine based on the module source scan during the series testing. It is designed to record hit data generated by the response to an ionizing ^{90}Sr source at various DEPFET biasing voltages. During the scan, all modules included in a measurement are configured with identical DEPFET voltage settings for V_{HV} , V_{drift} , $V_{\text{clear-off}}$.

At the start of each measurement, a pedestal calibration is performed, followed by the actual source measurement. Once the predefined measurement time is completed, the DEPFET biasing voltages are updated, and the next measurement is initiated, including a new pedestal calibration. These steps are repeated until the desired parameter space is covered.

The measurement process can be paused at any time and resumed by starting from the next measurement point. If a measurement is interrupted due to a detector operation error, the last measurement point can be repeated.

The recorded data are stored on a server and can be analyzed later offline. To analyze all module data, the analysis software was designed to be highly scalable and to run on the `htcondor` system on the NAF.

7.5.1. Multi-Parameter Source Scan

For the multi-parameter source scan, the parameter space outlined in Table 7.1 was refined based on previous findings from the series testing module source scans. One significant challenge was the considerable variation in the optimal DEPFET working points identified during the series testing. Since it was not feasible to arbitrarily expand the parameter space due to the long measurement times required, the chosen parameter space was carefully constrained.

The defined measurement points for the DEPFET biasing voltages are listed in Table 7.3. As explained in the beginning of this chapter, only the *upper HS v1*⁵ was subjected to this detailed source scan.

Voltage	Lower in V	Upper in V	Step in V
V_{HV}	-72	-48	2
V_{drift}	-6	-3	1
$V_{\text{clear-off}}$	2	4	1

Table 7.3.: Parameter space covered during the multi-parameter source scan in the half-shell test setup at DESY.

The individual analysis results for this measurement for all modules of upper HS v1 are summarized in Appendix A.12. In the following subsections, the findings are discussed for individual representative modules.

⁵The initial half-shell is denoted as “v1” since four ladders were replaced. All ladders from this initial half-shell are labeled with “v1” in their module naming scheme, e.g., L1.2v1-fwd.

Characteristic Q_{MPV} Curves

The measured Q_{MPV} curves of all upper HS v1 modules can be grouped into three distinct categories. For each category, measured Q_{MPV} curves of exemplary module are shown in Figure 7.15.

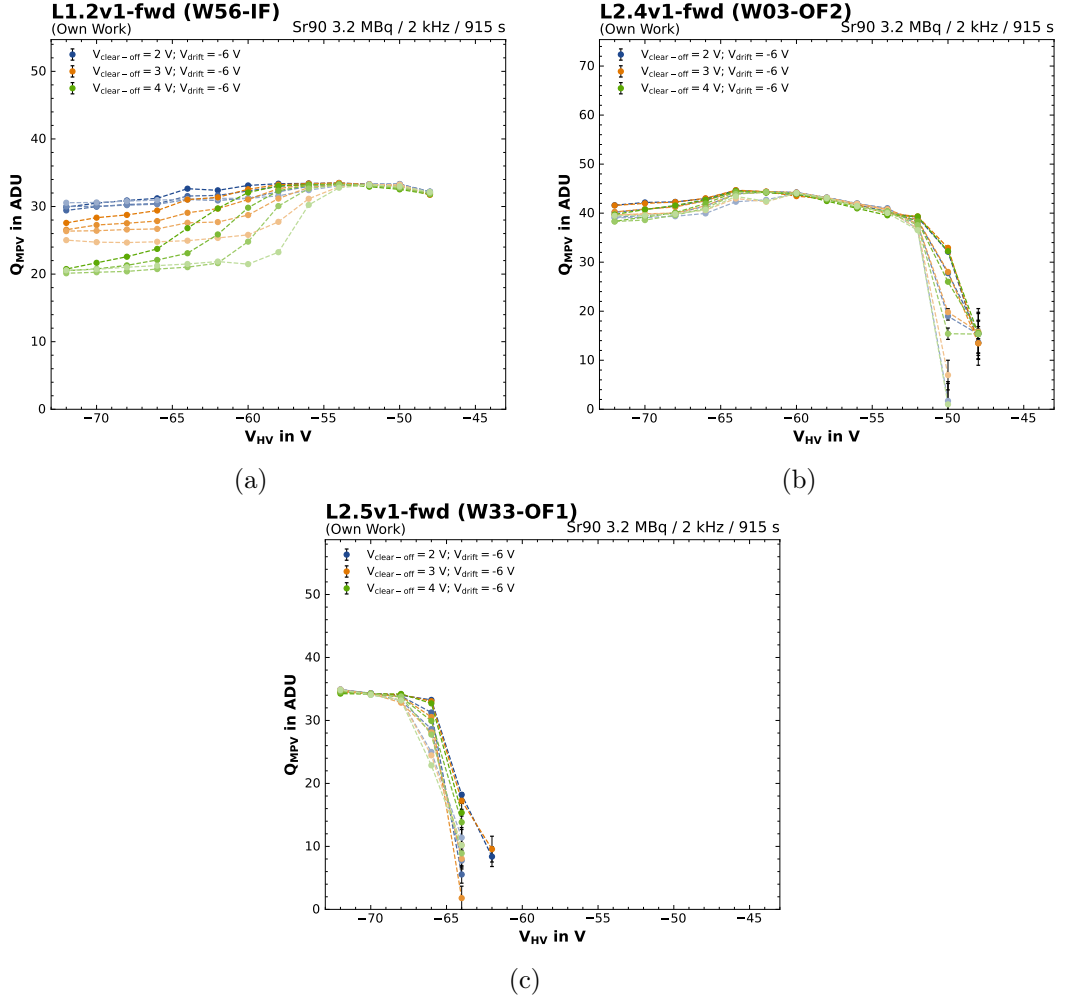


Figure 7.15.: Measured Q_{MPV} values for three characteristic modules. The different color intensities show a change in V_{drift} from the labeled dark (-6 V) to light (-3 V) in 1 V steps.

All Q_{MPV} curves span from the under-depleted region (low negative V_{HV}), characterized by lower Q_{MPV} values, to the fully depleted plateau region, where higher Q_{MPV} values are observed. This plateau represents a working point where the Q_{MPV} is minimally influenced by the V_{drift} and $V_{\text{clear-off}}$ configurations. Beyond the fully depleted regime, at excessively more negative V_{HV} settings, charge loss begins to set in.

In both the under-depleted regime and the excessively high negative V_{HV} regime, the e^- are

7. PXD2 DEPFET Biasing Optimization

not efficiently drifted into the internal gate (see Section 5.1.1). Consequently, Q_{MPV} values are expected to decrease in these regions.

The visibility of these transitions depends on the individual module characteristics. Additionally, the onset of the full depletion plateau is heavily module-dependent.

The Q_{MPV} curves of L1.2v1-fwd (W56-IF) and L2.4v1-fwd (W03-OF2) show a further characteristic: in the high negative V_{HV} region, Q_{MPV} values decrease as the charge loss sets in. These two module categories primarily differ in their behavior under excessively high negative V_{HV} . For modules such as L1.2v1-fwd (W56-IF), the Q_{MPV} values decrease more rapidly with increasingly negative V_{HV} , depending on specific V_{drift} and $V_{\text{clear-off}}$ settings. In this regime, less positive $V_{\text{clear-off}}$ configurations lead to significantly higher Q_{MPV} values. The impact of V_{drift} is smaller overall, but lower negative V_{drift} values also result in a faster decrease in Q_{MPV} as V_{HV} becomes more negative.

The shifted potential maximum toward the sensor surface in the excessively high negative V_{HV} regime can, to some extent, be pushed back deeper into the sensor bulk by increasing the negative V_{drift} and reducing the positive $V_{\text{clear-off}}$ voltages. This adjustment prevents the e^- from overcoming the deep p-well potential barrier to the clear implant or becoming trapped by the positive clear-gate potential along their drift path into the internal gate (see Figure 5.5).

In contrast, L2.4v1-fwd (W03-OF2) exhibits Q_{MPV} values that show little dependence on the V_{drift} and $V_{\text{clear-off}}$ settings, even in the high negative V_{HV} region. The origin of this difference in behavior between the two module types, particularly regarding the V_{drift} and $V_{\text{clear-off}}$ configurations, remains unclear.

The incident angle, determined by the orientation of the ladders relative to the ^{90}Sr source, can be ruled out as reason for differing of the Q_{MPV} characteristics despite the position and orientation do affect the absolute Q_{MPV} values (see Section 7.3). The modules L2.2v1-fwd and L2.2v1-bwd are located on the same ladder but exhibit two distinct Q_{MPV} characteristics (see Figure A.28 and Figure A.29). However, a similar Q_{MPV} characteristic is observed for modules of the same wafer, e.g. the modules of wafers W08, W32, W42, W46, W54, and W56 (compare Q_{MPV} curves in Appendix A.12). This variation between wafers hints to differences or variations in the wafer production.

The third type of characteristic Q_{MPV} curve is observed for modules like L2.5v1-fwd (W33-OF1), which exhibit significantly more negative depletion voltages compared to other modules. For these modules, the scanned parameter space may not have been wide enough to entirely reach the full-depletion regime. Moreover, V_{HV} did not become negative enough to enter the charge-loss regime.

The substantial difference in depletion voltage is attributed to the dissipated backside p^+ doping caused by the wafer bonding process (see Section 5.2.1). The wafer bonding was performed by two different companies, Shinetsu and ICEMOS. Wafers bonded at ICEMOS were subjected to unexpected higher temperatures, causing the backside p^+ doping to penetrate deeper into the n^- bulk region. This deeper penetration reduces the sensitive silicon volume and, as a result, lowers the required depletion voltage [123]. The majority of PXD modules are affected by this phenomenon. However, the third type modules, such as L2.5v1-fwd (W33-OF1), were bonded at Shinetsu and the observed onset of the bulk depletion aligns well with the design expectations (see Section 5.1.2).

All modules share a common feature: a plateau region with a high Q_{MPV} value that is minimally influenced by V_{drift} and $V_{\text{clear-off}}$. A working point within this region is expected to exhibit particularly stable behavior, referred to as the *stable working point*.

σ_{noise} Curves

The σ_{noise} curves for the three exemplary characteristic modules are shown in Figure 7.16. It is observed that the σ_{noise} levels are predominantly correlated with the $V_{\text{clear-off}}$ voltage and increase as $V_{\text{clear-off}}$ becomes less positive.

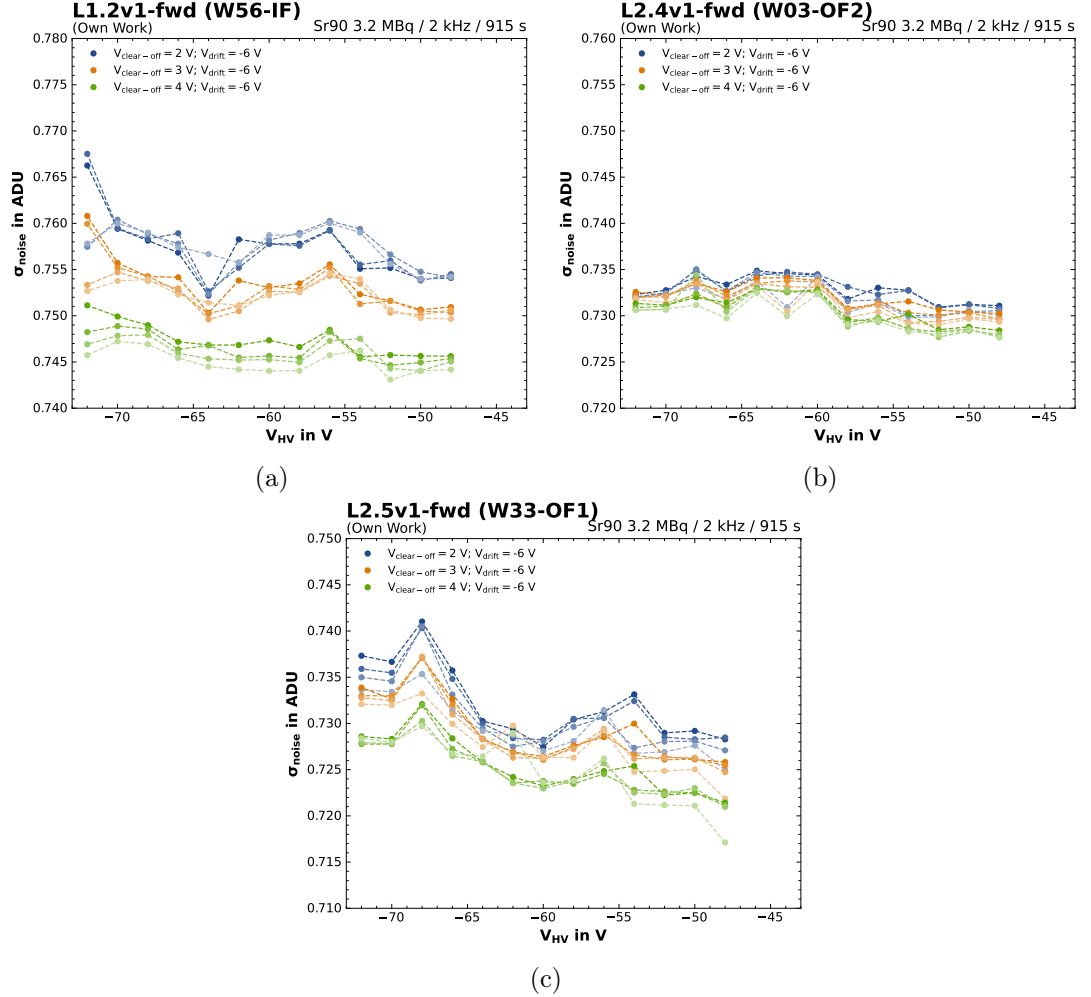


Figure 7.16.: Measured σ_{noise} values for three characteristic modules. The different color intensities show a change in V_{drift} from the labeled dark (-6 V) to light (-3 V) in 1 V steps.

For most modules, the σ_{noise} level increases with more negative V_{HV} values (see σ_{noise} curves in Appendix A.12). The splitting into sub- σ_{noise} levels for different V_{drift} voltages is on the order of its fluctuations and is therefore not significant.

The measured σ_{noise} levels across all modules on upper HS v1 range between 0.70 ADU and 0.82 ADU.

7. PXD2 DEPFET Biasing Optimization

V_{HV} Sweet Spot

A local Q_{MPV} maximum is observed in 12 out of the 20 modules at $V_{HV} = -64$ V (referred to as the “sweet spot”) for $V_{clear-off} = \{2, 3\}$ V and high negative V_{drift} voltages.

Additionally, for most of these 12 modules, a distinct dip in the σ_{noise} levels is evident under these conditions. For example, this behavior can be observed in Figure 7.15a(a) and Figure 7.16a for L1.2v1-fwd (W56-IF) and in Figure A.28 for L2.2v1-fwd (W46-OF2). The sweet spot for stable operation generally occurs at more negative V_{HV} voltages than the stable working point discussed above for the module. However, it may be more advantageous to operate the modules at the stable working point rather than at the localized sweet spot peak.

It is known from PXD1 that the optimal V_{HV} values shift with increasing TID due to avalanche effects caused by ineffective guard ring structures. This effect is currently under investigation and will be detailed in the PhD thesis of Georgios Giakoustidis (University of Bonn), to be published later this year. Higher negative V_{HV} voltages lead to stronger avalanche effects, resulting in increased bulk currents and, consequently, higher power loss.

SNR and SNR_{ext} Curves

The shapes of the calculated SNR and SNR_{ext} values follow closely the Q_{MPV} curves. Figure 7.17 (a), (c), and (e) show the calculated SNR and Figure 7.17 (b), (d), and (f) show the calculated SNR_{ext} values for the three exemplary characteristic modules discussed above. The SNR and SNR_{ext} curves of all 20 modules are shown in Appendix A.12.

The analysis of the SNR (Equation (7.2)) and SNR_{ext} (Equation (7.4)) values revealed that several modules exhibit significantly different optimized DEPFET working points compared to those identified during series testing. For instance, for L1.2v1-fwd (W56-IF), the optimized DEPFET working point determined by the maximum SNR and SNR_{ext} is $V_{HV} = -54$ V, $V_{drift} = -5$ V, and $V_{clear-off} = 4$ V, whereas the series testing identified a working point of $V_{HV} = -66$ V, $V_{drift} = -5$ V, and $V_{clear-off} = 3$ V. The series testing-optimized DEPFET working point lies in the over-depleted regime. The new DEPFET working point increased the SNR by approximately 20% and the SNR_{ext} by approximately 40%.

Figure 7.18 shows the improvement in number of pixel hits between the series testing-optimized DEPFET working point and the newly optimized working point(s) for module L1.2v1-fwd (W56-IF). Specifically, for the DEPFET working point defined by maximum SNR , the number of pixel hits increased by 13.8%, for the SNR_{ext} -based working point 14.4%. The projected pixel hits of all 20 modules are shown in Appendix A.12.

Table 7.4 shows the full result of the multi-parameter source scan analysis. For six out of the 20 modules a ≥ 4 V more positive V_{HV} voltage is found for the optimized DEPFET working point based on SNR and SNR_{ext} :

- L1.2v1-fwd (W56-IF)
- L1.3v1-fwd (W10-IF)
- L1.4v1-fwd (W59-IF)
- L1.4v1-bwd (W56-IB)
- L2.1v1-fwd (W45-OF1)
- L2.1v1-bwd (W42-OB2)

For six modules a ≥ -4 V more negative V_{HV} voltage is found for the optimized DEPFET working point based on SNR and/or SNR_{ext} :

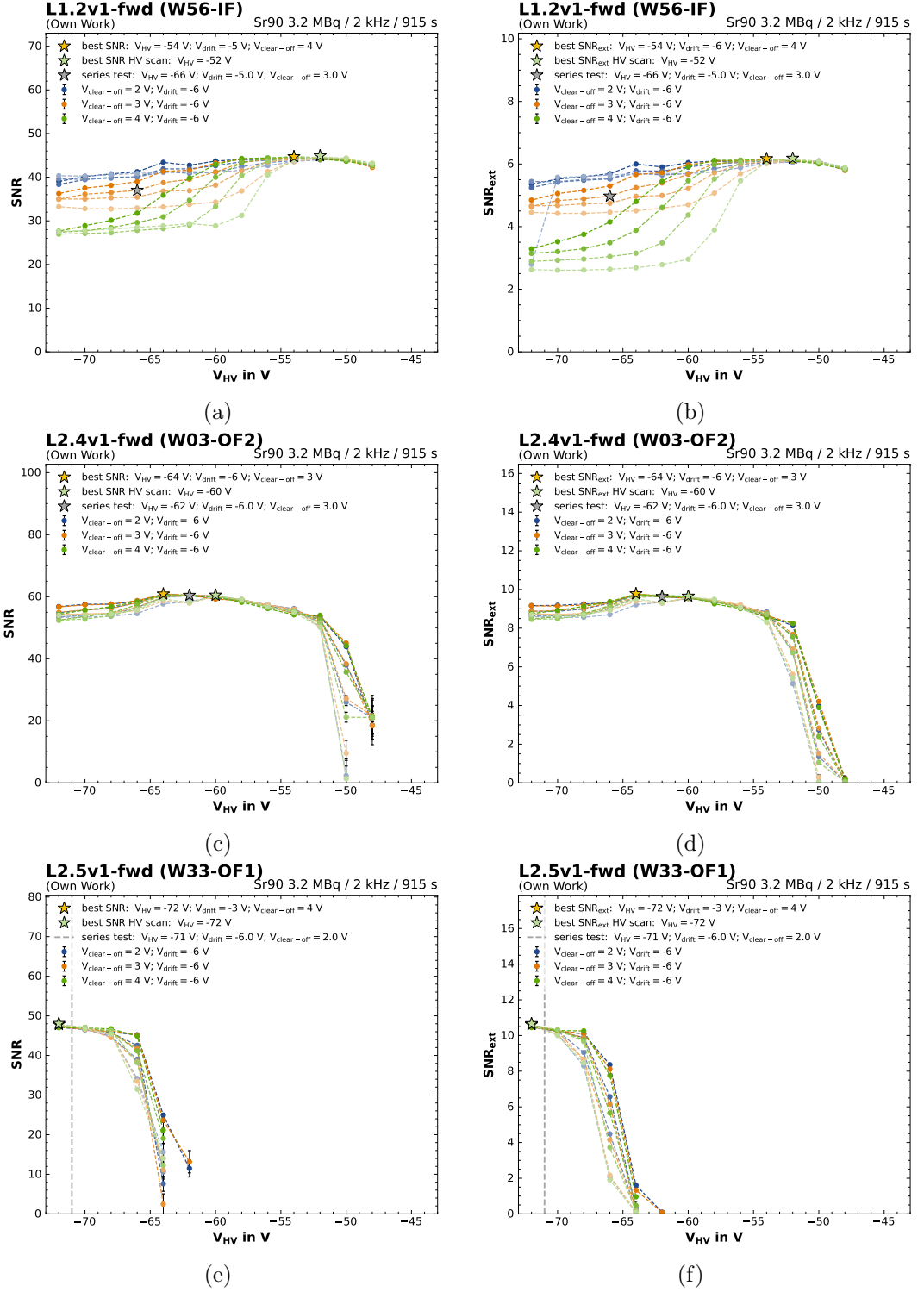


Figure 7.17.: Calculated SNR (left column) and SNR_{ext} (right column) values for three characteristic modules. The different color intensities show a change in V_{drift} from the labeled dark (-6 V) to light (-3 V) in 1 V steps. The best setting HV scan marker is for $V_{drift} = -3$ V and $V_{clear-off} = 4$ V.

7. PXD2 DEPFET Biasing Optimization

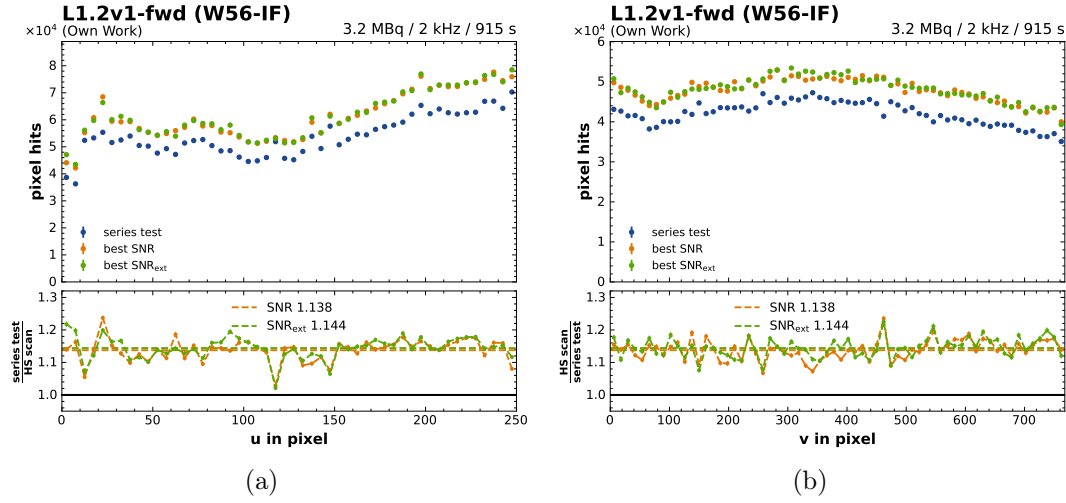


Figure 7.18.: Projected pixel hits are shown for (a) the u -axis and (b) the v -axis, comparing the newly optimized DEPFET working points with that identified during series testing.

- L1.1v1-bwd (W54-IB)
- L1.2v1-bwd (W52-IB)
- L2.2v1-fwd (W46-OF2)
- L2.2v1-bwd (W08-OB2) (not for SNR_{ext})
- L2.3v1-fwd (W08-OF2)
- L2.4v1-bwd (W46-OB1)

In total, a significantly better DEPFET working point was identified for 12 out of 20 modules. However, for certain modules, such as L1.2v1-bwd (W52-IB) (Figure A.21), the newly optimized SNR/SNR_{ext} -based DEPFET working point significantly deviates from the stable working point at $V_{\text{HV}} \sim -54$ V. In this case, the optimization identifies the sweet spot—discussed above—as the optimal configuration. The higher number of pixel hits measured for the stable working point configuration strongly suggests that the stable working point at $V_{\text{HV}} = -54$ V should be chosen. A similar situation is observed for L2.2v1-fwd (W46-OF2) (Figure A.28). The last column in Table 7.4 shows the identified stable working points. The location of the stable working points coincides well with the maximum of the $V_{\text{drift}} = -3$ V and $V_{\text{clear-off}} = 4$ V V_{HV} curve. Since no final conclusions can be drawn due to the non-uniform characteristics of the modules, the ideal configuration must be evaluated on a case-by-case basis. In Section 7.5.2, a simplified measurement is performed on all PXD2 modules to identify the stable working point; therefore, this deeper case-by-case analysis is omitted here.

For module L2.4v1-bwd (W46-OB1) (Figure A.33), the measurements exhibit several noisy frames with a significant number of noisy pixel patterns with $\mathcal{O}(1000)$ pixel hits in one readout frame. In this case, the SNR_{ext} value may have optimized for a voltage configuration where these noise patterns occur more frequently. Since the noise patterns appear only once every $\mathcal{O}(10000)$ frames, they are not reflected in the σ_{noise} calculations. As a result, the FOMs are not sensitive to these patterns. The Q_{MPV} , σ_{noise} , SNR , and SNR_{ext} curves for this module show considerable fluctuations, and the projected pixel hits clearly display different noise states

Module		Series testing in V			Q_{MPV} in V			SNR in V			SNR_{ext} in V			Stable WP in V	
Position	Wafer	V_{HV}	V_{drift}	$V_{clear-off}$	V_{HV}	V_{drift}	$V_{clear-off}$	V_{HV}	V_{drift}	$V_{clear-off}$	V_{HV}	V_{drift}	$V_{clear-off}$	V_{HV}	
Source Position 1	L1.1v1-fwd	W54-IP [†]	-60.0	-5.0	2.0	-58.0	-6.0	2.0	-58.0	-6.0	4.0	-58.0	-6.0	4.0	-54.0
	L1.1v1-bwd	W54-IB [†]	-54.0	-4.0	3.0	-58.0	-6.0	2.0	-58.0	-5.0	4.0	-58.0	-6.0	4.0	-54.0
	L1.2v1-fwd	W56-IP [†]	-66.0	-5.0	3.0	-54.0	-5.0	3.0	-54.0	-5.0	4.0	-54.0	-6.0	4.0	52.0
	L1.2v1-bwd	W52-IB [†]	-54.0	-5.0	2.0	-64.0	-6.0	2.0	-64.0	-6.0	2.0	-64.0	-6.0	2.0	-54.0
	L2.1v1-fwd	W45-OF1	-68.0	-3.0	4.0	-56.0	-6.0	3.0	-56.0	-4.0	4.0	-60.0	-6.0	3.0	-56.0
	L2.1v1-bwd	W42-OB2	-70.0	-5.0	5.0	-62.0	-6.0	3.0	-62.0	-6.0	3.0	-58.0	-4.0	4.0	-58.0
	L2.2v1-fwd	W46-OF2*	-58.0	-5.0	2.0	-64.0	-6.0	3.0	-64.0	-6.0	3.0	-64.0	-6.0	3.0	-58.0
	L2.2v1-bwd	W08-OB2*	-60.0	-5.0	3.0	-64.0	-6.0	2.0	-64.0	-6.0	2.0	-58.0	-6.0	4.0	-54.0
	L2.3v1-fwd	W08-OF2	-60.0	-6.0	3.0	-64.0	-6.0	2.0	-64.0	-6.0	2.0	-64.0	-6.0	2.0	-52.0
L2.3v1-bwd	W08-OB1	-64.0	-3.0	1.5	-64.0	-6.0	2.0	-64.0	-6.0	2.0	-64.0	-6.0	2.0	-54.0	
Source Position 2	L1.3v1-fwd	W10-IF	-70.0	-4.0	4.0	-64.0	-6.0	3.0	-64.0	-6.0	3.0	-64.0	-5.0	4.0	-60.0
	L1.3v1-bwd	W05-IB	-66.0	-5.0	3.0	-64.0	-6.0	3.0	-64.0	-5.0	4.0	-64.0	-5.0	4.0	-60.0
	L1.4v1-fwd	W59-IP ^{††}	-68.0	-5.0	2.0	-60.0	-6.0	2.0	-58.0	-6.0	4.0	-56.0	-5.0	4.0	-54.0
	L1.4v1-bwd	W56-IB ^{††}	-68.0	-5.0	2.0	-58.0	-6.0	2.0	-54.0	-5.0	4.0	-54.0	-4.0	4.0	-52.0
	L2.4v1-fwd	W03-OF2	-62.0	-6.0	3.0	-64.0	-6.0	3.0	-64.0	-6.0	3.0	-64.0	-6.0	3.0	-60.0
	L2.4v1-bwd	W46-OB1	-60.0	-5.0	2.0	-64.0	-6.0	2.0	-64.0	-6.0	3.0	-62.0	-6.0	2.0	-56.0
	L2.5v1-fwd	W33-OF1 ^{††}	-71.0	-6.0	2.0	-72.0	-4.0	2.0	-72.0	-3.0	4.0	-72.0	-3.0	4.0	-72.0
	L2.5v1-bwd	W42-OB1 ^{††}	-61.0	-6.0	2.0	-64.0	-6.0	3.0	-62.0	-6.0	4.0	-64.0	-6.0	3.0	-60.0
	L2.6v1-fwd	W32-OF2	-70.0	-5.0	5.0	-72.0	-5.0	2.0	-72.0	-4.0	3.0	-72.0	-4.0	3.0	-72.0
L2.6v1-bwd	W32-OB2	-70.0	-5.0	5.0	-70.0	-6.0	2.0	-68.0	-4.0	3.0	-72.0	-4.0	4.0	-70.0	

[†] Modules that were on a kinked ladder and were replaced.

^{††} Modules that were on a ladder that broke during the repair process and were replaced.

^{*} Modules which were on a ladder which changed position on the repaired half-shell.

Table 7.4.: New DEPFET biasing voltages identified through the multi-parameter source scan, optimized individually for maximizing Q_{MPV} , SNR , and SNR_{ext} . Stable WP identifies the stable working point determined by eye. For comparison are the settings included obtained during the series testing. The modules in the upper half of the table were exposed to source position 1 and the modules in the lower part were exposed to source position 2.

in the v -axis projection. As a result, noisy pixels are further suppressed in the analysis of the measurements performed in Section 7.5.2.

Hitmaps

Figure 7.19 and Figure 7.20 show the hitmaps of the upper HS v1 for the newly optimized DEPFET working points based on SNR and SNR_{ext} , respectively for L2 and L1. The shadow structures caused by module overlaps, switcher ASICs, and capacitors align with the expected positions from the simulation (see Figure 7.11).

Modules L2.5v1-fwd (W33-OF1), L2.6v1-fwd (W32-OF2), and L2.6v1-bwd (W32-OB2) exhibit ring structures, which indicate non-optimal DEPFET voltage settings (see below). This suggests that the depletion voltage for these modules is still not sufficiently negative and should be lowered further to optimize the bulk depletion.

Modules L2.4v1-bwd (W46-OB1), L2.5v1-bwd (W42-OB1), and L1.3v1-fwd (W10-IF) exhibit areas affected by noisy frames. These noisy frames are individual readout frames containing distinct noisy patterns. Similar noisy frames are also observed, though less prominently, in modules L2.1v1-fwd (W45-OF1) and L2.3v1-fwd (W08-OF2). Although the root cause remains unclear, these frames typically occur in only about one out of $\mathcal{O}(10000)$ frames and therefore do not pose a general issue. In Appendix A.13 it is shown, that the noise patterns are influenced by the DEPFET biasing voltages.

For modules L2.4v1-bwd (W46-OB1), L1.3v1-fwd (W10-IF), and L2.1v1-fwd (W45-OF1), the SNR_{ext} -based optimization results in a DEPFET working point with increased noise struc-

7. PXD2 DEPFET Biasing Optimization

tures. However, for module L2.5v1-bwd (W42-OB1), the SNR_{ext} -based optimization leads to a DEPFET working point with a slightly decreased noise structure. But the noise structure is significantly smaller compared to the other three significantly affected modules. The SNR_{ext} might be affected by the noisy frames; therefore, measures are adopted in Section 7.5.2 to mitigate this effect.

Some modules, such as L1.3v1-fwd (W10-IF), L1.4v1-fwd (W59-IF), and L2.4v1-bwd (W46-OB1), exhibit permanent dead drain lines. The hitmaps measured with the DEPFET working points identified during series testing are shown in Figure A.38.

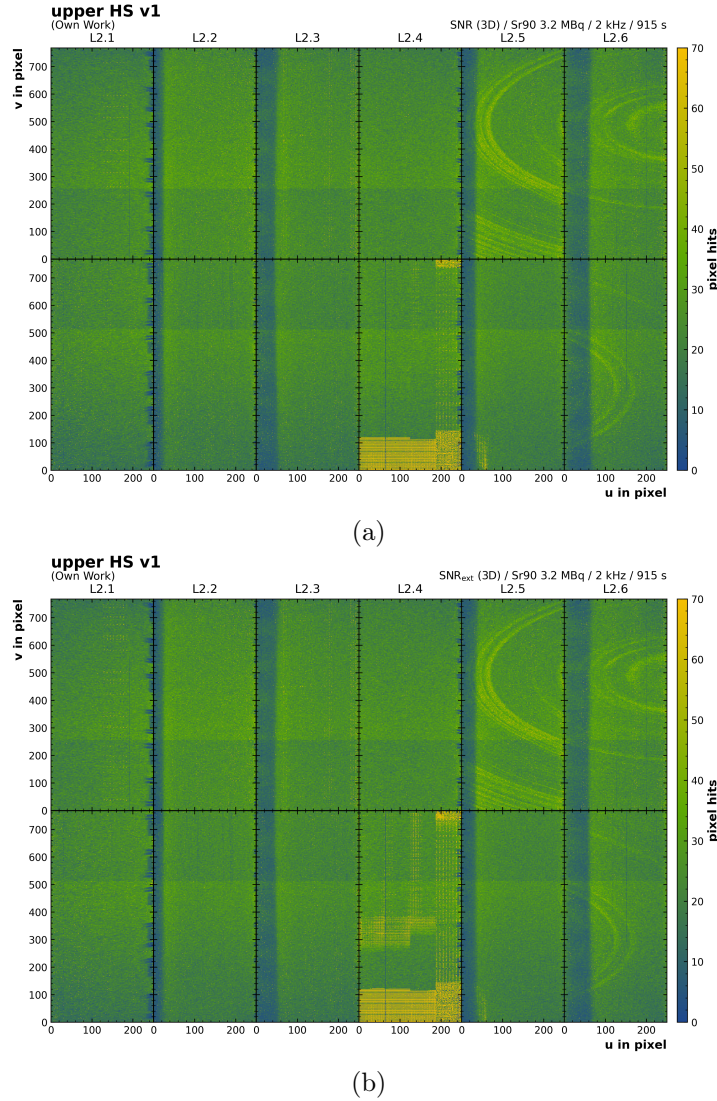


Figure 7.19.: Hitmaps for the upper HS v1 L2 modules with the DEPFET voltage configurations optimized for (a) maximal SNR , and (b) maximal SNR_{ext} .

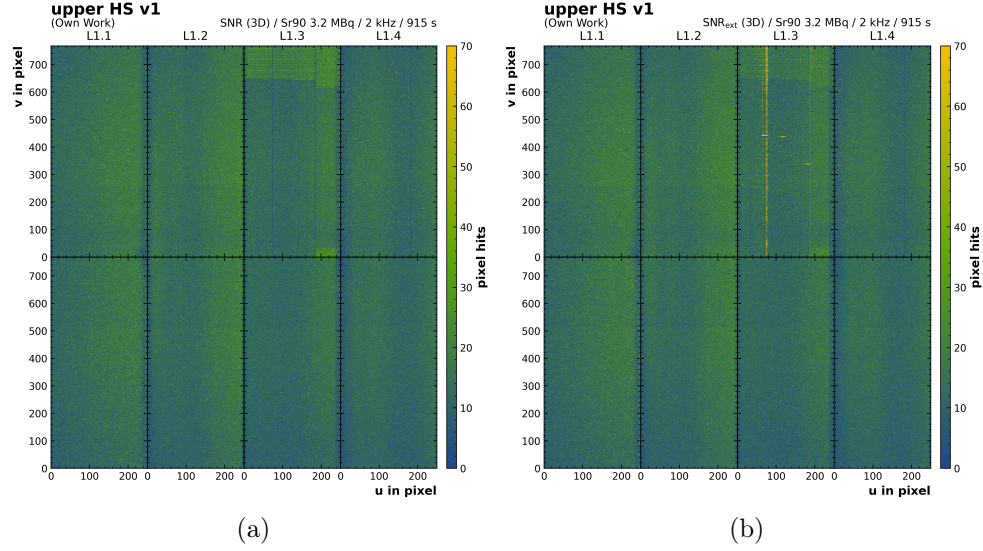


Figure 7.20.: Hitmaps for the upper HS v1 L1 modules with the DEPFET voltage configurations optimized for (a) maximal SNR , and (b) maximal SNR_{ext} .

Cluster Charge Distributions

If all modules exhibited similar properties, characteristics, and working points, the cluster charge distributions would depend solely on the incident angle of the e^- from the ^{90}Sr source. Consequently, one would expect similar cluster charge distributions and Q_{MPV} values for the fwd and bwd modules of the same ladder, given that the source is placed at the center of the ladder in the z -direction. However, as shown in Figure 7.21, which shows the cluster charge distributions sorted ladder-wise for the newly SNR optimized DEPFET working points, this is not uniformly the case.

It is evident that not all modules on the same ladder exhibit the same characteristic cluster charge distribution. While this holds true for L1.3v1, L2.1v1, and L1.4v1, the other seven ladders show significant differences in their cluster charge distributions.

This observation underscores the diverse properties of the modules, highlighting their complexity and variability, which makes deriving general conclusions challenging. It is also possible that, during the series testing phase when the module ASICs were calibrated, variations in the testing process led to differences in the working points of the ASIC chips. Additionally, the DEPFET sensor matrix biasing voltages (see Table 5.1) are not equal for all modules. All this could result in various effects, such as modules not operating with a homogeneous gain.

Ring Structures

Based on the current understanding, concentric bulk doping variations occurred during the production of the Si ingot from which the module wafers were cut. As shown in [124], the drain current pedestals of the DEPFET sensor matrix also exhibit these ring structures. DEPFET sensors from other experiments have also shown similar ring structures [125][126], which have been attributed to bulk doping variations or mobility variations of charge carriers caused by crystal quality fluctuations during the Si ingot growth process.

7. PXD2 DEPFET Biasing Optimization

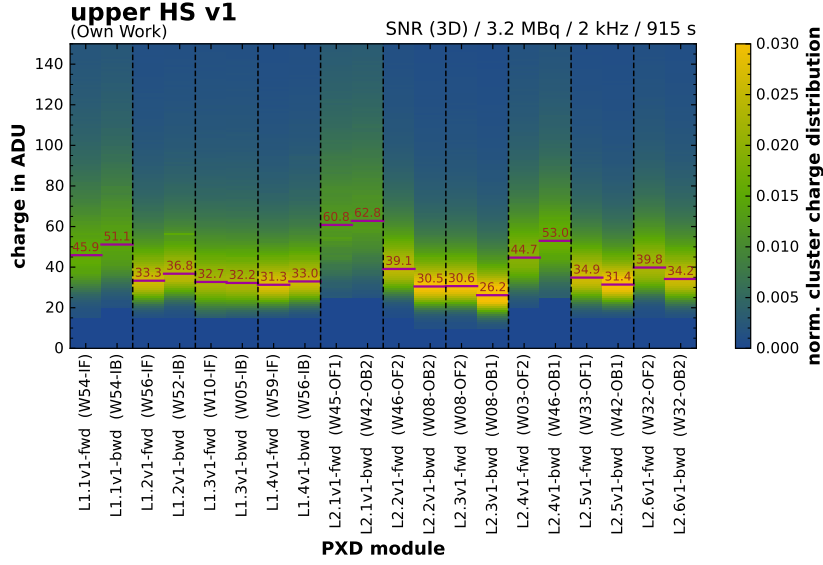


Figure 7.21.: Ladder-wise comparison of the measured cluster charge distributions from the multi-parameter source scan for the newly identified DEPFET working points based on SNR . Indicated in *dark pink* are the Q_{MPV} values. The lower range of the cluster charge distributions is defined by the Q_{MPV} fit window. Ladders L1.1v1, L2.1v1, and L2.4v1 exhibit broad cluster charge distributions, attributed to the shallow incident angles of the e^- from the ^{90}Sr source.

In cases of under-depletion or excessively high depletion voltages in a module, ring structures are observed in the hitmap. In the hitmaps (Figure 7.19) of the under-depleted L2.5v1-fwd and L2.6v1-fwd/-bwd modules, these ring structures show a higher concentration of pixel hits compared to the rest of the module or the hitmaps of other L2 modules.

Figure 7.22a shows two measurement hitmaps for L1.2v1-fwd: one corresponding to an under-depleted setting and the other to the optimal SNR setting. The hitmap for the under-depleted setting clearly shows ring structures with a higher concentration of hits compared to the optimal setting. This is further clarified in the projection shown in Figure 7.22b.

Figure 7.23a shows the cluster size distribution for the under-depleted and optimal SNR configurations. The cluster sizes increase significantly in the under-depleted configuration, with the mean cluster size rising from 2.349 ± 0.0016 to 2.972 ± 0.0020 , an approximate increase of 26.5 %.

Figure 7.23b and Figure 7.23c show that this increase occurs exclusively in the row direction (v -axis), where the mean cluster size grows by approximately 26.2 % (from 1.621 ± 0.0008 to 2.045 ± 0.0009). In contrast, the column direction (u -axis) shows a slight decrease in the mean cluster size of approximately 0.8 %, declining from 1.690 ± 0.0009 to 1.676 ± 0.0009 .

In [127], a laser scan setup was employed on a small 32×64 pixel DEPFET Hybrid 5 test structure to investigate signal generation when a narrow test laser beam illuminated specific areas of the pixels. At low depletion voltages, it was observed that two-pixel clusters began to respond when the laser beam struck a small area within a single pixel. This effect is demon-

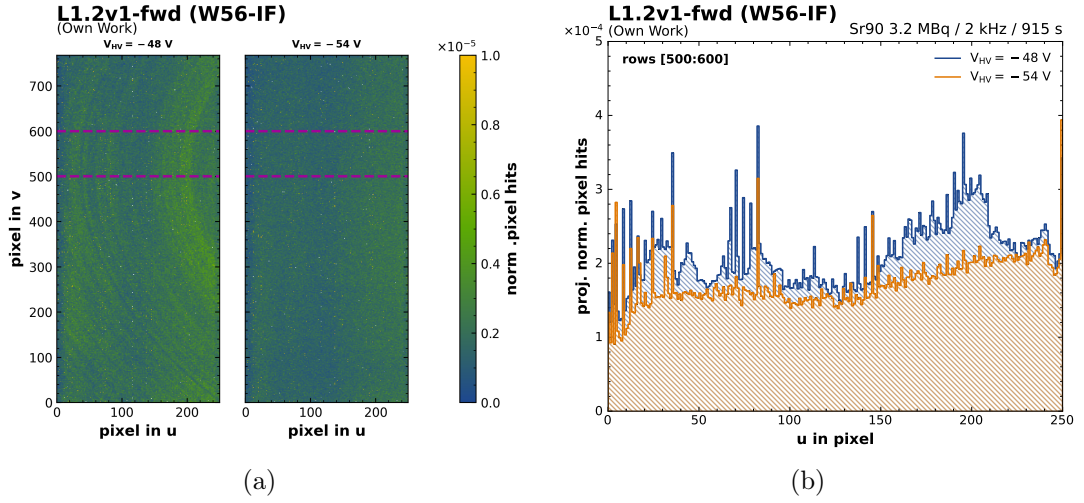


Figure 7.22.: Source measurements at $V_{\text{drift}} = -5$ V and $V_{\text{drift}} = 4$ V for two different V_{HV} settings: an under-depleted setting ($V_{\text{HV}} = -48$ V) and the setting corresponding to the maximum SNR ($V_{\text{HV}} = -54$ V). (a) Hitmaps for both settings, showing ring structures with increased number of hits in the under-depleted configuration. The dark pink dashed lines indicate the area used for the projection in (b). (b) Projections of pixel hits onto the u -axis for the selected rows in the hitmaps, highlighting the increased hit number in the ring structures. The measurement is normalized on number of recorded frames.

strated in Figure 7.23d. In [61], a similar effect was observed in analyzed PXD module test beam data.

Notably in Figure 7.23d, this phenomenon occurs exclusively between pixels in neighboring rows within the same column, with clusters consistently forming between pixels in lower even-numbered rows and higher odd-numbered rows. These *double-row clusters* appear to be grouped in a manner that suggests a connection to ring structures. This correlation is further supported by the fact that these DEPFET Hybrid 5 test structures were manufactured on the same wafers as the PXD modules.

The double-row cluster effect is attributed in [127] to the double-pixel structure, where two pixels share the same source implant (see Figure 5.4). If the bulk is not fully depleted, it is assumed that the potential maximum is not entirely confined within the internal gate of the pixel. Instead, it extends over a larger area. The generated signal e^- are still drifted toward the internal gate by the lateral drift field. However, a fraction of the e^- drifting beneath the clear implant (see Figure 5.5 and Figure 5.6) now follow a broader curved trajectory under the shared source implant [128]. Some of these e^- are attracted to the positive potential of the neighboring pixel's internal gate. As a result, both the neighboring pixel and the intended pixel cell create a signal.

Even though ring structures are observed when a module is operated at excessively high depletion voltages, the double-row cluster effect is not observed in such cases. Instead, only a decrease in number of pixel hits is measured.

7. PXD2 DEPFET Biasing Optimization

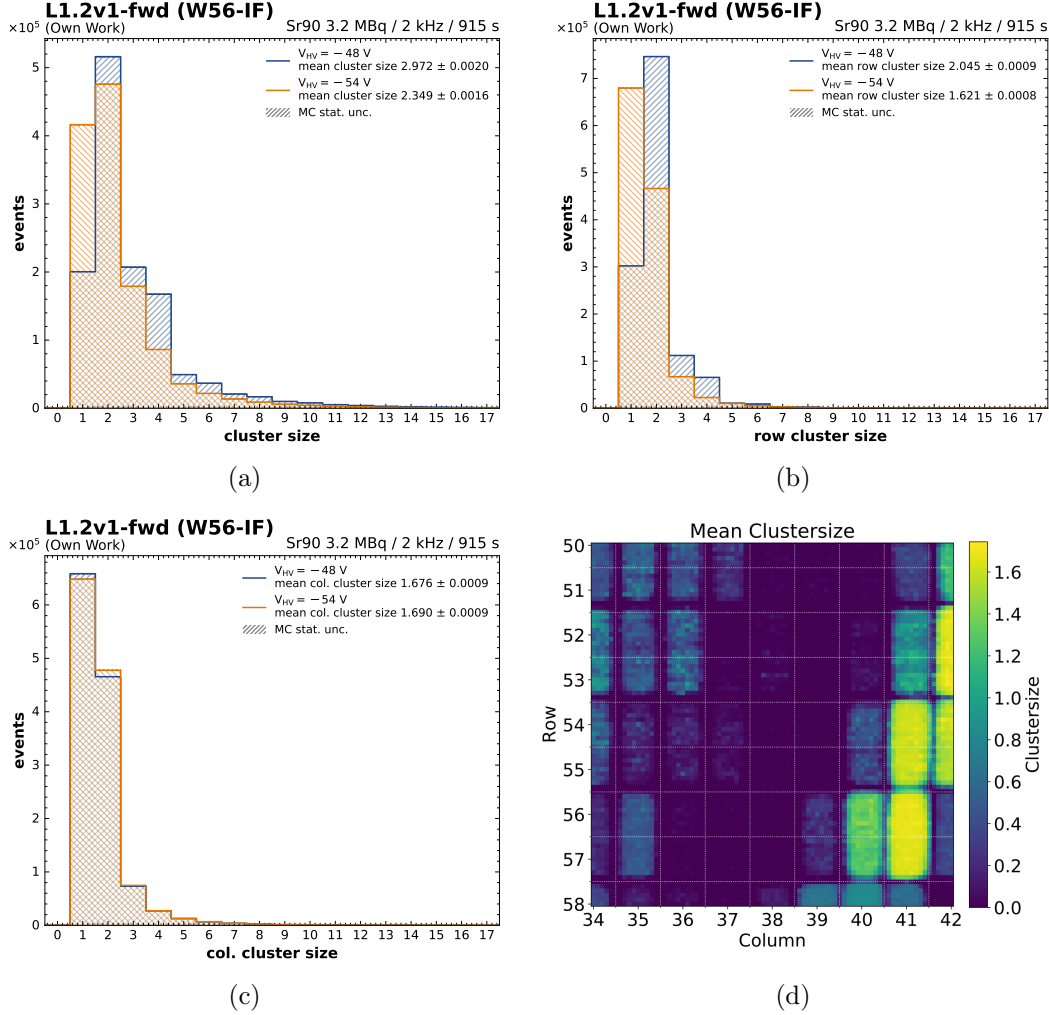


Figure 7.23.: Cluster size distributions measured for (a) the entire cluster size, (b) the cluster size in the row direction, and (c) the cluster size in the column direction at $V_{drift} = -5$ V and $V_{clear-off} = 4$ V. (d) The distribution of double-row clusters observed in under-depleted Hybrid 5 DEPFET test structures. The white dotted lines indicate the DEPFET pixel cell edges. The entire test structure was illuminated using a 680 nm diode laser, with 11 000 measurement points recorded at 2.1 s per point. Regions shown in green/yellow correspond to measurement points where illumination within a pixel resulted in a cluster size >1 pixel. The statistical uncertainties of the histograms (a)-(c) are not visible. (Figure (d) adapted from [127].)

7.5.2. HV Source Scan

As a result of the unforeseen abortion of the multi-parameter source scan, coupled with the significantly reduced available measurement time, a simplified scan approach became necessary. The multi-parameter scan described in Section 7.5.1 demonstrated that all modules exhibit a stable working point where the influence of V_{drift} and $V_{\text{clear-off}}$ voltages is significantly reduced while maintaining high SNR and SNR_{ext} values. The studies revealed, that for a good estimation of the stable working point, a scan of V_{HV} is sufficient.

It was therefore decided to defer the detailed multi-parameter scan to post-installation (into the Belle II detector), utilizing the e^+e^- beam at SuperKEKB (*beam scan*). Since beam time is both costly and experimentally valuable, it was essential to identify a suitable starting point for each module via the HV source scan (short: *HV scan*). These starting points should also ensure already sufficient detector performance.

Measurement

In the simplified source scan, only the V_{HV} configuration was scanned, keeping the V_{drift} and $V_{\text{clear-off}}$ voltages fixed, as summarized in Table 7.5. For certain module types, such as L1.2v2-fwd (W56-IF), the chosen V_{drift} and $V_{\text{clear-off}}$ settings led to a rapid decrease in SNR and SNR_{ext} values in the excessively high V_{HV} regime (see Section 7.5.1). Additionally, the maximum SNR and SNR_{ext} values along the chosen V_{HV} curve generally occurred at the stable working point. It is typically located at slightly more positive values than the maximum SNR and SNR_{ext} observed in the multi-parameter scan (see Appendix A.12). Consequently, this DEPFET working point serves as an optimal starting point for future voltage scans, with the V_{HV} value already suitable for detector operation in the Belle II experiment.

Voltage	Lower in V	Upper in V	Step in V
V_{HV}	-72	-44	2
V_{drift}	-3	-3	-
$V_{\text{clear-off}}$	4	4	-

Table 7.5.: V_{HV} range for the HV scan, while the V_{drift} and $V_{\text{clear-off}}$ voltages are fixed.

At DESY, the HV scan for the *lower HS* was conducted using two ^{90}Sr sources simultaneously placed in the x - y -plane at source positions 1 and 2. In z -direction, the sources were placed at the center of the modules, instead of the center of the ladders. Therefore, the fwd and bwd regions of the half-shell were scanned sequentially. This setup (together with the reduced parameter space) significantly decreased the nominal measurement time for the half-shell from 106 h to approximately 10 h.

At KEK, the weaker ^{90}Sr source required adjustments for the repaired *upper HS*. The measurement time per configuration was increased from 915 s to 1500 s, and the trigger rate was raised from 2 kHz to 4 kHz. As a result, the nominal measurement time extended to approximately 28 h for the half-shell, which was successfully integrated into the tight KEK commissioning schedule.

Analysis Results

Table 7.6 summarizes the optimized V_{HV} voltages for all PXD2 modules, determined by maximizing Q_{MPV} , SNR , and SNR_{ext} . With the exception of L1.2-fwd (W11-IF), L2.1-fwd (W45-OF1), and L2.5-fwd (W46-OF2), the optimized V_{HV} voltages for SNR and SNR_{ext} are consistent within 2 V. Notably, 17 out of 40 modules exhibit V_{HV} voltages at the maximum SNR that deviate by more than 4 V from the optimal V_{HV} configuration identified during the series testing. Moreover, seven modules show deviations of ≥ 10 V compared to the series testing results.

The HV scan results for all PXD2 modules are shown in Appendix A.13 Figure A.39 to Figure A.48. Notably, L2.12-bwd exhibits unforeseen instability in its operation. Figure A.49 and Figure A.50 show the module hitmaps of the upper HS and lower HS, respectively, obtained at the maximum SNR values. In Figure A.49, it is observed that the noisy patterns in L1.3-fwd (W10-IF) have disappeared (compare Figure 7.20). The analysis of the multi-parameter scan data from Section 7.5.1 revealed that the noisy patterns also disappeared for the $V_{\text{drift}} = -3$ V and $V_{\text{clear-off}} = 4$ V settings. This leads to the conclusion that the noisy patterns are influenced by the DEPFET biasing voltages.

The upper HS HV scan at KEK, performed with source positions A/B-bwd, was affected by the DAQ system operating in an “unstable state”, which led to unforeseen and random data truncation during module readout. Additionally, these measurements exhibited an increased rate of single noise hits. To mitigate the impact of noise and based on the observations in Section 7.5.1, pixels with significantly higher hit rates were excluded from the HV scan analysis. Figure A.51 shows the pixel hit distributions for all modules, along with the applied threshold for the maximum number of hits per pixel. Pixels that did not pass this selection were masked during the clustering process.

The affected truncated and noisy measurements resulted in fluctuating SNR_{ext} curves for the respective modules, as shown in Appendix A.13. These fluctuations were caused by significant variations in the measured number of clusters due to data truncation, while the total number of frames remained unaffected throughout the measurement. The root cause of this issue remains unclear. The SNR curves remain smooth. Consequently, the maximal SNR value appears to be the most reliable indicator for defining the desired preliminary V_{HV} voltage, serving as a starting point for future beam scans.

The ladder-wise cluster charge distributions corresponding to the maximum SNR are shown in Figure A.52. Modules L2.1, L1.5, and L1.6 exhibit nearly identical cluster charge distributions for the fwd and bwd modules. Additionally, reasonable agreement is observed for L1.1, L1.8, and L2.9. A comparison of L1.3 with itself from Figure 7.21 – representing the same module at the same position – reveals a decreased agreement between the forward and backward cluster charge distributions. This discrepancy is attributed to differences in the V_{HV} (for L1.3-fwd), V_{drift} and $V_{\text{clear-off}}$ configurations.

A direct comparison of the absolute cluster charge distribution values obtained from the multi-parameter source scan at DESY and the HV source scan at KEK is not feasible due to differing source positions, and environmental conditions, such as temperature. Specifically, the air temperature varied between the two setups, and the cooling system parameters at KEK were not identical to those used at DESY. It is well-known that temperature significantly impacts the DEPFET currents.

	Module		Series testing in V			Q_{MPV} in V	SNR in V	SNR_{ext} in V
	Position	Wafer	V_{HV}	V_{drift}	$V_{\text{clear-off}}$			
KEK Source Pos. A-fwd	L1.1-fwd	W68-IF	-54.0	-6.0	2.0	-52.0	-52.0	-52.0
	L1.2-fwd	W11-IF	-68.0	-3.0	2.0	-56.0	-56.0	-52.0
	L2.1-fwd	W45-OF1	-68.0	-3.0	4.0	-56.0	-56.0	-52.0
	L2.2-fwd	W56-OF1	-56.0	-6.0	2.0	-52.0	-52.0	-52.0
	L2.3-fwd	W08-OF2	-60.0	-6.0	3.0	-52.0	-52.0	-52.0
KEK Source Pos. B-fwd	L1.3-fwd	W10-IF	-70.0	-4.0	4.0	-62.0	-62.0	-62.0
	L1.4-fwd	W05-IF	-65.0	-6.0	2.0	-60.0	-60.0	-62.0
	L2.4-fwd	W03-OF2	-62.0	-6.0	3.0	-62.0	-62.0	-62.0
	L2.5-fwd	W46-OF2	-58.0	-5.0	2.0	-58.0	-58.0	-62.0
	L2.6-fwd	W32-OF2	-70.0	-5.0	5.0	-70.0	-70.0	-68.0
KEK Source Pos. A-bwd	L1.1-bwd	W61-IB	-54.0	-6.0	2.0	-50.0	-50.0	-50.0
	L1.2-bwd	W46-IB	-60.0	-4.0	5.0	-52.0	-52.0	-54.0
	L2.1-bwd	W42-OB2	-70.0	-5.0	5.0	-58.0	-58.0	-60.0
	L2.2-bwd	W53-OB2	-56.0	-6.0	2.0	-52.0	-52.0	-52.0
	L2.3-bwd	W08-OB1	-64.0	-3.0	1.5	-54.0	-54.0	-54.0
KEK Source Pos. B-bwd	L1.3-bwd	W05-IB	-66.0	-5.0	3.0	-62.0	-62.0	-62.0
	L1.4-bwd	W42-IB	-70.0	-5.0	5.0	-56.0	-56.0	-56.0
	L2.4-bwd	W46-OB1	-64.0	-3.0	2.0	-58.0	-58.0	-58.0
	L2.5-bwd	W08-OB2	-60.0	-5.0	3.0	-54.0	-54.0	-54.0
	L2.6-bwd	W32-OB2	-70.0	-5.0	5.0	-70.0	-70.0	-70.0
DESY Source Pos. 1	L1.5-fwd	W67-IF	-56.0	-6.0	2.0	-52.0	-52.0	-52.0
	L1.5-bwd	W67-IB	-54.0	-6.0	2.0	-50.0	-50.0	-50.0
	L1.6-fwd	W66-IF	-54.0	-6.0	2.0	-52.0	-52.0	-52.0
	L1.6-bwd	W58-IB	-58.0	-4.0	2.0	-52.0	-52.0	-52.0
	L2.7-fwd	W57-OF2	-50.0	-6.0	2.0	-50.0	-50.0	-50.0
	L2.7-bwd	W59-OB2	-52.0	-6.0	2.0	-50.0	-50.0	-50.0
	L2.8-fwd	W56-OF2	-54.0	-5.0	2.0	-52.0	-52.0	-52.0
	L2.8-bwd	W54-OB1	-52.0	-5.0	2.0	-52.0	-52.0	-52.0
	L2.9-fwd	W60-OF1	-51.0	-6.0	2.0	-52.0	-52.0	-52.0
DESY Source Pos. 2	L2.9-bwd	W56-OB1	-56.0	-5.0	2.0	-52.0	-52.0	-52.0
	L1.7-fwd	W69-IF	-56.0	-6.0	2.0	-52.0	-52.0	-52.0
	L1.7-bwd	W59-IB	-64.0	-4.0	3.0	-52.0	-52.0	-52.0
	L1.8-fwd	W53-IF	-66.0	-4.0	2.0	-52.0	-52.0	-52.0
	L1.8-bwd	W53-IB	-68.0	-5.0	3.0	-54.0	-54.0	-54.0
	L2.10-fwd	W45-OF2	-66.0	-3.0	3.0	-52.0	-52.0	-52.0
	L2.10-bwd	W10-OB1	-60.0	-5.0	3.0	-56.0	-56.0	-54.0
	L2.11-fwd	W05-OF1	-60.0	-5.0	2.0	-60.0	-60.0	-58.0
	L2.11-bwd	W04-OB1	-68.0	-5.0	4.0	-56.0	-54.0	-54.0
	L2.12-fwd	W43-OF1	-60.0	-5.0	2.0	-54.0	-54.0	-54.0
	L2.12-bwd	W33-OB1	-67.0	-6.0	2.0	-72.0	-68.0	-68.0

Table 7.6.: Optimized V_{HV} voltages identified through the HV source scan, based on Q_{MPV} , SNR , and SNR_{ext} . For comparison are the settings included obtained during the series testing.

7.6. First Run 2 PXD2 Hit Efficiency Improvements

After the installation of PXD2 into the Belle II detector, Belle II resumed operation in February 2024 (*Run 2*). At the very beginning of Run 2, the HV scan data had not yet been fully analyzed. As a result, the PXD2 modules were initially configured with the series testing DEPFET voltage parameters listed in Table 7.8. Once the HV source scan analysis results were available, the V_{HV} voltages for individual modules were adjusted accordingly. This section outlines the specific improvements achieved through these optimizations.

Online PXD Hit Efficiency

The Belle II experiment includes a data quality monitoring (DQM) system that provides information from a subset of online-analyzed events recorded during physics data acquisition. The analyzed data is not finally calibrated but for a modest performance analysis this is sufficient.

A convenient feature of DQM system is the *PXD hit efficiency* analysis. In this context, tracks reconstructed using SVD hits are analyzed to identify matching PXD clusters. Only tracks that satisfy the selection criteria outlined in Table 7.7 are considered. The PXD hit efficiency is defined as the fraction of tracks with associated PXD clusters relative to the total number of tracks defined by SVD hits.

Quantity	Symbol	Value/Range
distance to POCA in r - ϕ plane	$ d_0 $	$< 0.5 \text{ cm}$
z-coordinate of POCA	z_0	$< 1 \text{ cm}$
transverse momentum	p_T	$\geq 1 \text{ GeV}$
distance of the track to the center of gravity of the cluster	d	$< 500 \text{ }\mu\text{m}$

Table 7.7.: Track selection criteria for online PXD hit efficiency calculation.

Series Testing Configuration

In the early Run 2 data, when PXD2 was configured with the series testing parameters, the modules L1.4-bwd, L1.7-bwd, L1.8-bwd, and L2.1-bwd exhibited significantly lower hit efficiencies compared to the others, as clearly shown in Figure 7.24 (blue). For these modules, the HV scan indicates that the SNR maximum occurs at a V_{HV} value that is 12 V to 14 V more positive compared to the series testing V_{HV} voltages.

HV Scan Configuration

To improve the PXD2 hit efficiency, the V_{HV} voltages of individual modules were adjusted based on the values identified in Section 7.5.2. Table 7.8 lists the modules and their updated V_{HV} voltages, while the V_{drift} and $V_{\text{clear-off}}$ voltages were retained from the series testing configuration. The module hit efficiencies after the V_{HV} adjustments are shown in Figure 7.24 (red). It is evident that the working points for modules with significantly lower efficiencies have improved. Their hit efficiencies increased to approximately 98 %, aligning now with the performance of the other modules.

For modules L1.2-bwd, L1.8-fwd, and L2.11-bwd, the hit efficiencies also showed slight im-

7.6. First Run 2 PXD2 Hit Efficiency Improvements

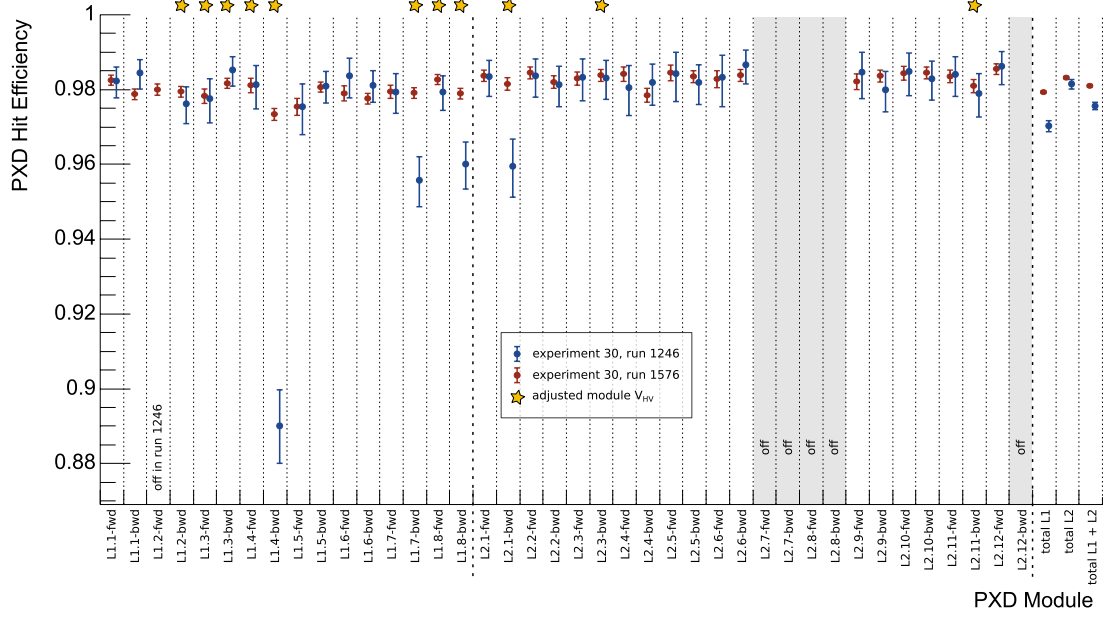


Figure 7.24.: The hit efficiencies of individual PXD2 modules, combined efficiencies for L1 and L2, as well as the total PXD2 hit efficiency, are shown. The hit efficiency from run 1246 corresponds to the configuration where all modules were operated using the series testing parameters. In contrast, the hit efficiency from run 1576 reflects the configuration where the V_{HV} voltages of individual modules (yellow stars) were adjusted (see text for explanation). The modules on ladders L2.7 and L2.8 are turned off due to significant thermal bowing, while L2.12-bwd is disabled due to unstable operation.

7. PXD2 DEPFET Biasing Optimization

provements. In contrast, the hit efficiency of module L1.3-bwd decreased slightly, though the change remains within the uncertainties. No significant changes were observed in the hit efficiencies of modules L1.3-fwd, L1.4-fwd, and L2.3-bwd.

The optimization of these individual modules led to an overall increase in the PXD2 hit efficiency from $97.55 \pm 0.1\%$ to $98.13 \pm 0.03\%$, corresponding to an improvement of approximately 0.5 %. The most significant improvement was observed for module L1.4-fwd, with its efficiency increasing from $89 \pm 1\%$ to $97.38 \pm 0.16\%$, representing an approximate 8 % gain.

Module		Series testing in V			SNR in V	new in V
Position	Wafer	V_{HV}	V_{drift}	$V_{\text{clear-off}}$	V_{HV}	V_{HV}
L1.3-fwd	W10-IF	-70.0	-4.0	4.0	-62.0	-60.0
L1.4-fwd	W05-IF	-65.0	-6.0	2.0	-60.0	-60.0
L1.2-bwd	W46-IB	-60.0	-4.0	5.0	-52.0	-52.0
L1.3-bwd	W05-IB	-66.0	-5.0	3.0	-62.0	-60.0
L1.4-bwd	W42-IB	-70.0	-5.0	5.0	-56.0	-56.0
L2.1-bwd	W42-OB2	-70.0	-5.0	5.0	-58.0	-58.0
L2.3-bwd	W08-OB1	-64.0	-3.0	1.5	-54.0	-54.0
L1.8-fwd	W53-IF	-66.0	-4.0	2.0	-52.0	-52.0
L1.7-bwd	W59-IB	-64.0	-4.0	3.0	-52.0	-52.0
L1.8-bwd	W53-IB	-68.0	-5.0	3.0	-54.0	-54.0
L2.11-bwd	W04-OB1	-68.0	-5.0	4.0	-54.0	-56.0

Table 7.8.: Single modules with adjusted V_{HV} voltages during the early phase of Run 2 (see explanation in the text). The *SNR* column indicates the V_{HV} voltage at which the maximum *SNR* was measured during the HV source scan. The “new” column shows the newly applied V_{HV} voltages. For L1.3-fwd and L1.3-bwd, an earlier stage of the HV scan analysis yielded slightly different *SNR* maxima, leading to the selection of slightly more positive V_{HV} values.

8. Summary and Outlook

In this work, a novel method for measuring the τ -lepton lifetime using a template fitting approach is presented. The decay length of 3x1-prong $\tau^+\tau^-$ decays is measured in the xy -plane, from the precisely known SuperKEKB nano-beam IP to the 3-prong τ -lepton decay vertex.

A robust software framework has been developed to unify and integrate all related studies, enabling seamless implementation and testing of new features. This framework establishes a clear pipeline for data reprocessing and result reproduction.

A key aspect of the measurement is the reconstruction of the τ -lepton decay vertex. Its performance is evaluated through an additional vertex fit using two out of the three tracks, combined with the measurement of the DOCA between this two-track vertex and the third track. Using the information from the PXD, a vertex resolution of $31.43\,\mu\text{m} \pm 0.01\,\mu\text{m}$ is achieved.

A likelihood model has been developed to determine the best fitting lifetime template. This model is validated through 5000 individual pseudo-data fits, where the pseudo-data bin contents are fluctuated according to their expected statistical experimental uncertainties. The results demonstrate that the fit accurately estimates the correct lifetime value and scaling parameter within the expected statistical precision.

To model different lifetime hypotheses, a re-weighting method has been implemented to create decay length templates from one simulated $\tau^+\tau^-$ sample with a nominal lifetime. This method is validated using four additional $\tau^+\tau^-$ samples generated with shifted τ -lepton lifetimes. The validation study showed no significant deviations when fitting the shifted lifetime samples as pseudo-data in two independent fit configurations, each based on templates derived from different generator lifetime samples.

Systematic uncertainties are incorporated as NPs in the likelihood model. Comprehensive studies to mitigate and reduce mismodeling of specific observable distributions have been conducted. The most impactful mismodeling effects are identified in the $p_{T,\tau_{3p}}$ and $\theta_{\tau_{3p}}$ distributions. A 2D re-weighting template correction approach reduces the impact of these mismodeling NPs in a dedicated likelihood fit study with a preliminary fit setup from 0.36 fs to 0.21 fs.

The fit stability and correlations of the NPs are analyzed in single-template fit setups. NPs that show no impact on the fit result are pruned to reduce correlations and improve fit stability. While certain template fits exhibit instabilities caused by strong NP correlations, the overall fit stability remains robust, supported by the stable curvature of the $2\Delta\text{NLL}$.

A significant improvement in precision compared to the previous Belle experiment measurement ($290.17\,\text{fs} \pm 0.53\,\text{fs stat.} \pm 0.33\,\text{fs syst.}$) is expected, despite using a smaller experimental dataset. The measurement presented in this work is projected to be dominated by systematic uncertainties, with an overall expected precision of 0.2 fs, including a statistical precision of 0.08 fs and a systematic precision of 0.18 fs.

Since September 2024, further work is ongoing in parallel by the analysis team to address the remaining challenges and advance further the analysis toward publication. In particular, the $c\bar{c}$

8. Summary and Outlook

contribution has been further examined to reduce the associated uncertainty and mitigate the observed (anti-)correlations. The parameter μ_{bkg} in the normalization fit has been decomposed into $q\bar{q}_{uds}$ and $c\bar{c}$ components, each with characteristic decay length distributions. Additionally, the single-bin side region has been divided into two side regions with binned decay length distributions¹. This modification enhances the differentiation between individual background contributions and enables more controlled normalization of the distinct $c\bar{c}$ process groups.

In the meantime, it has also been verified that the $\tau^+\tau^-$ backgrounds are adequately simulated. These include 1-prong decays incorrectly identified as 3-prong decays, as well as the $e^+e^-\tau^+\tau^-$ contribution in the $\ell^+\ell^-X^+X^-$ sample. The uncertainty on the $e^+e^-\tau^+\tau^-$ contribution is incorporated as an NP, following the approach used for the K^\pm contribution in Section 6.8.9. If necessary, a tighter χ^2_{prob} selection can be applied (see Figure 6.22), for example, $\chi^2_{\text{prob}} > 0.05$, to further reduce the $e^+e^-\tau^+\tau^-$ contribution.

The misalignment study should be repeated with a larger dataset to confirm, using a more precise NP envelope, that the fit uncertainty does not increase. A simulated dataset size similar to that used in the material budget study, 500 fb^{-1} , is likely sufficient for this purpose. The misalignment scenario with the largest impact will be kept as NP in the final likelihood model.

For the material budget study, it is crucial to confirm whether the observed higher material variation of the BP compensates for the unstudied impact of the VXD Si density variation. If not, such a feature must be implemented in **basf2**, and the study must be repeated.

The next step towards publication is to conduct the fit without uncovering the best-fitting lifetime value. This ensures a “blinded study” of the fit’s true behavior and its final uncertainties. If this step is successful, the fit can then be performed in multiple phase space regions, comparing the relative deviations of the best-fit lifetime values without revealing their absolute value. For instance, executing the study in four regions of the azimuthal angle $\phi_{\tau_{3p}}$ of the reconstructed τ_{3p} can help to identify any uncovered impact from the IP, vertex fit, or other uncovered sources.

Once all remaining studies and checks are successfully completed, the final unblinded fit can be performed to obtain the world’s most precise τ -lepton lifetime measurement.

This work highlights the crucial role of the PXD in the τ -lepton lifetime measurement. Section 6.5.2 demonstrated that events in which at least one track lacks a PXD hit exhibit a 30 % degradation in vertex resolution, emphasizing the necessity of optimal PXD performance.

During the PXD1 commissioning, it was observed that the application of nonuniform measurement and evaluation criteria during the series testing phase led to suboptimal PXD module configurations. To address this for the final PXD2, an advanced half-shell pre-commissioning ^{90}Sr test setup was designed to ensure uniform optimization of the DEPFET sensor working points. The implementation of such a test setup was guided by a simulation based on a modified **basf2** detector simulation. This simulation determined the source positions for optimal illumination and, consequently, the setup dimensions.

As part of the pre-commissioning phase at DESY, comprehensive multi-parameter ^{90}Sr source scans were planned. Although not all initially intended measurements could be completed, valuable insights were obtained from the first long-term operation of a double-layer PXD half-shell. In particular, the identification of mechanical deformations, such as ladder bending, proved to be critical. Without the timely detection of these structural issues and subsequent design

¹The decay length distribution in the side region is independent of the τ -lepton lifetime value due to the low signal contribution.

improvements to the half-shell, there would have been a substantial risk of severe mechanical failures during post-installation operation.

Despite these challenges, a uniform evaluation of the DEPFET working points across all modules was successfully implemented in this work. Valuable information was obtained by characterizing all modules under consistent measurement conditions. Two figures of merit (SNR and SNR_{ext}) were employed to evaluate the DEPFET working points. While SNR_{ext} offers up to twice the differentiation capability of SNR , it is more susceptible to noise. SNR_{ext} was defined to prevent ring structures in the optimal DEPFET working point. However, the analysis revealed that SNR inherently avoids these issues when the correct V_{HV} range is scanned. Consequently, evaluating the scan results using only the SNR FOM is sufficient.

A stable working point was observed for all modules, exhibiting a high SNR value with minimal dependence on V_{drift} and $V_{\text{clear-off}}$. However, this stable working point does not necessarily correspond to the maximum SNR value in the multi-parameter source scan. Selecting the optimal DEPFET setting remains challenging due to the complexity and variability of the modules, making it difficult to derive general conclusions. Therefore, case-by-case considerations are still required.

For under-depleted module configurations, ring structures with an increased number of pixel hits were observed. A double-row cluster effect was identified, which is responsible for degradation of PXD hit resolution in under-depleted modules. This highlights the necessity of operating the modules at optimal working points.

A simplified HV scan was performed during (pre-)commissioning to identify the stable working point for each PXD2 module, based on the maximum SNR value along the V_{HV} curve at constant V_{drift} and constant $V_{\text{clear-off}}$. The detailed multi-parameter source scan for all PXD2 modules was deferred to the post-installation phase, utilizing e^+e^- beam collisions at SuperKEKB. Consequently, the HV scan results will serve as the starting points for the future beam scans.

The analysis of the half-shell source scan data revealed that the DEPFET working points were not optimally identified for all modules during the series testing phase. Optimization through the multi-parameter scan in the pre-commissioning phase led to hit efficiency improvements of up to 14 %. This finding was further supported by early Run 2 experimental data. The V_{HV} parameter settings determined from the HV source scan resulted in significant improvements in PXD hit efficiency, particularly for four modules, with efficiency gains of up to 8 %.

The next step involves modifying the source scan measurement to operate in conjunction with SuperKEKB e^+e^- collisions. This modification should extend the scan to allow individual voltage adjustments for each module, as the starting points identified with the HV source scan vary between modules. Furthermore, the clusterizer can be modified so that single noisy frames, which exceed a certain occupancy, are discarded and not counted. This will increase the robustness of SNR_{ext} towards noisy frames.

Experience with PXD1 operation showed that radiation damage in the guard ring structures during SuperKEKB operation necessitated adjustments to the V_{HV} voltages. For all modules, an adjustment of at least -2 V at the end of Run 1 was required to maintain full depletion. The exposed TID between Aug. 2019 and Apr. 2022 was estimated to be $< 10\text{ kGy}$ [129], with the actual value depending on the module's position. This is a small fraction of the expected TID of 200 kGy over 10 yr of operation. Based on this observation, it is recommended to develop a scan procedure to evaluate the DEPFET performance during physics data collection. This would allow small DEPFET bias voltage adjustments and direct evaluation of the SNR values,

8. *Summary and Outlook*

enabling regular optimization of performance. This approach would facilitate early detection of shifts in DEPFET working points, allowing for timely compensation to maintain maximal performance.

Bibliography

- [1] C. Campagnari and M. Franklin, “The discovery of the top quark,” *Rev. Mod. Phys.*, vol. 69, pp. 137–212, 1 Jan. 1997. DOI: 10.1103/RevModPhys.69.137 (cit. on p. 13).
- [2] ATLAS Collaboration, “Observation of a new particle in the search for the Standard Model Higgs boson with the ATLAS detector at the LHC,” *Phys. Lett. B*, vol. 716, pp. 1–29, 2012. DOI: 10.1016/j.physletb.2012.08.020 (cit. on p. 13).
- [3] CMS Collaboration, “Observation of a new boson at a mass of 125 GeV with the CMS experiment at the LHC,” *Phys. Lett. B*, vol. 716, pp. 30–61, 2012. DOI: 10.1016/j.physletb.2012.08.021 (cit. on p. 13).
- [4] M. L. Perl *et al.*, “Evidence for Anomalous Lepton Production in e^+e^- Annihilation,” *Phys. Rev. Lett.*, vol. 35, no. 22, pp. 1489–1492, 1975. DOI: 10.1103/PhysRevLett.35.1489 (cit. on p. 13).
- [5] T. Abe *et al.*, “Belle II technical design report,” 2010. arXiv: 1011.0352 [physics.ins-det] (cit. on pp. 13, 45, 47–53).
- [6] K. Akai, K. Furukawa, and H. Koiso, “SuperKEKB collider,” *Nucl. Instrum. Meth.*, vol. A907, p. 188, 2018. DOI: 10.1016/j.nima.2018.08.017. arXiv: 1809.01958 [physics.acc-ph] (cit. on pp. 13, 41).
- [7] P. W. Higgs, “Broken symmetries and the masses of gauge bosons,” *Physical Review Letters*, vol. 13, no. 16, pp. 508–509, Oct. 1964. DOI: 10.1103/PhysRevLett.13.508 (cit. on p. 15).
- [8] S. Weinberg, “A model of leptons,” *Physical Review Letters*, vol. 19, pp. 1264–1266, 1967. DOI: 10.1103/PhysRevLett.19.1264 (cit. on p. 15).
- [9] C. Burgard, *Standard model of physics*, <http://www.texample.net/tikz/examples/model-physics/>, Accessed: 2025-02-27 (cit. on p. 16).
- [10] S. Navas *et al.*, “Particle Data Group,” *Phys. Rev. D*, vol. 110, no. 3, p. 030001, 2024. DOI: 10.1103/PhysRevD.110.030001 (cit. on pp. 16, 17, 20–22, 31–33, 36, 41).
- [11] M. Thomson, *Modern Particle Physics*. Cambridge University Press, 2013. DOI: 10.1017/CB09781139525367 (cit. on p. 17).
- [12] M. D. Schwartz, *Quantum Field Theory and the Standard Model*. Cambridge University Press, 2014. DOI: 10.1017/9781139540940 (cit. on p. 17).
- [13] H. Bichsel, “Straggling in thin silicon detectors,” *Rev. Mod. Phys.*, vol. 60, pp. 663–699, 3 Jul. 1988. DOI: 10.1103/RevModPhys.60.663 (cit. on p. 20).

Bibliography

- [14] G. R. Lynch and O. I. Dahl, “Approximations to multiple Coulomb scattering,” *Nuclear Instruments and Methods in Physics Research Section B: Beam Interactions with Materials and Atoms*, vol. 58, no. 1, pp. 6–10, 1991. DOI: 10.1016/0168-583X(91)95671-Y (cit. on p. 21).
- [15] S. M. Sze, *Semiconductor Devices: Physics and Technology*, 2nd. Wiley, 1985. DOI: 10.1002/0470068329 (cit. on p. 23).
- [16] G. Lutz, *Semiconductor Radiation Detectors, Device Physics*, 2nd ed. Springer Berlin, Heidelberg, 2007. DOI: 10.1007/978-3-540-71679-2 (cit. on pp. 23, 25, 58, 59).
- [17] H. Kolanoski and N. Wermes, *Particle Detectors*. Oxford University Press, Jun. 2020. DOI: 10.1093/oso/9780198858362.001.0001 (cit. on pp. 23–25, 27).
- [18] J. Schwank, M. Shaneyfelt, D. Fleetwood, *et al.*, “Radiation effects in MOS oxides,” *Nuclear Science, IEEE Transactions on*, vol. 55, pp. 1833–1853, Sep. 2008. DOI: 10.1109/TNS.2008.2001040 (cit. on p. 26).
- [19] The Belle II Collaboration, “Measurement of the τ -lepton mass with the Belle II experiment,” *Phys. Rev. D*, vol. 108, p. 032006, 3 Aug. 2023. DOI: 10.1103/PhysRevD.108.032006 (cit. on pp. 32, 93, 103).
- [20] A. Lusiani, *Status and Plans of Tau Fits for HFLAV/PDG*, Presented on behalf of the BABAR Collaboration, Louisville, Kentucky, USA: University of Louisville, Dec. 2023 (cit. on pp. 32, 147).
- [21] J. Erler and M. Luo, “Precision Determination of Heavy Quark Masses and the Strong Coupling Constant,” *Physics Letters B*, vol. 558, pp. 125–131, Apr. 2003. DOI: 10.1016/S0370-2693(03)00276-4 (cit. on pp. 32, 33).
- [22] P. Baikov, K. Chetyrkin, and J. H. Kuhn, “Hadronic Z - and τ -Decays in Order α_s^4 ,” *Physical Review Letters*, vol. 101, p. 012002, 2008. DOI: 10.48550/arXiv.0801.1821 (cit. on p. 33).
- [23] E. Braaten and C. S. Li, “Electroweak radiative corrections to the semihadronic decay rate of the τ lepton,” *Physical Review D*, vol. 42, 3888(R), Dec. 1990. DOI: 10.1103/PhysRevD.42.3888 (cit. on p. 33).
- [24] J. Erler, α_s with GAPP, 2011. DOI: 10.48550/arXiv.1102.5520. arXiv: 1102.5520 [hep-ph] (cit. on p. 33).
- [25] J. Erler, *Private communication*, Email conversation, October 28, 2024 (cit. on p. 33).
- [26] A. Stahl, *Physics with Tau Leptons*. Berlin, Heidelberg: Springer, 2000. DOI: 10.1007/BFb0109618 (cit. on p. 34).
- [27] G. J. Feldman *et al.*, “Measurement of the τ Lifetime,” *Phys. Rev. Lett.*, vol. 48, p. 66, 1982. DOI: 10.1103/PhysRevLett.48.66 (cit. on p. 35).
- [28] K. Belous, M. Shapkin, A. Sokolov, *et al.*, “Measurement of the τ -lepton Lifetime at Belle,” *Phys. Rev. Lett.*, vol. 112, p. 031801, 3 Jan. 2014. DOI: 10.1103/PhysRevLett.112.031801 (cit. on pp. 35, 38, 39).

- [29] R. Balest *et al.*, “Measurement of the tau lepton lifetime,” *Phys. Lett. B*, vol. 388, pp. 402–408, 1996. DOI: 10.1016/S0370-2693(96)01163-X (cit. on p. 36).
- [30] OPAL Collaboration, “Improved measurement of the lifetime of the τ lepton,” *Physics Letters B*, vol. 374, no. 4, pp. 341–350, May 1996. DOI: 10.1016/0370-2693(96)00255-9 (cit. on p. 36).
- [31] ALEPH Collaboration, “Updated measurement of the tau lepton lifetime,” *Physics Letters B*, vol. 414, no. 3-4, pp. 362–372, Oct. 1997. DOI: 10.1016/S0370-2693(97)01116-7 (cit. on p. 37).
- [32] D. Buskulic *et al.*, “A precise measurement of the τ lepton lifetime,” *Physics Letters B*, vol. 297, no. 3, pp. 432–448, 1992. DOI: 10.1016/0370-2693(92)91283-F (cit. on p. 37).
- [33] D. Decamp *et al.*, “Measurement of the tau lepton lifetime,” *Physics Letters B*, vol. 279, no. 3, pp. 411–421, 1992. DOI: 10.1016/0370-2693(92)90413-X (cit. on p. 37).
- [34] D. Buskulic *et al.*, “Measurement of the τ lepton lifetime,” *Z. Phys. C*, vol. 70, pp. 549–560, 1996. DOI: 10.1007/s002880050132 (cit. on p. 37).
- [35] L3 Collaboration, “Measurement of the lifetime of the tau lepton,” *Physics Letters B*, vol. 479, pp. 67–78, Mar. 2000. DOI: 10.1016/S0370-2693(00)00347-6 (cit. on p. 37).
- [36] DELPHI Collaboration, “A precise measurement of the tau lifetime,” *The European Physical Journal C*, vol. 36, no. 3, pp. 283–296, Aug. 2004. DOI: 10.1140/epjc/s2004-01953-7 (cit. on p. 38).
- [37] Belle II Collaboration, *Luminosity*, <https://www.belle2.org/research/luminosity>, Accessed: 2024-06-30, 2024 (cit. on p. 41).
- [38] K. Oide, “KEKB B-Factory, The Luminosity Frontier,” *Progress of Theoretical Physics*, vol. 122, no. 1, pp. 69–80, Jul. 2009. DOI: 10.1143/PTP.122.69. eprint: <https://academic.oup.com/ptp/article-pdf/122/1/69/5393234/122-1-69.pdf> (cit. on p. 41).
- [39] W. Altmannshofer *et al.*, “The Belle II physics book,” *PTEP*, vol. 2019, no. 12, E. Kou and P. Urquijo, Eds., p. 123C01, 2019. DOI: 10.1093/ptep/ptz106. arXiv: 1808.10567 [hep-ex] (cit. on pp. 41, 50, 199).
- [40] H. Svidras, “Measurement of the photon energy spectrum in inclusive radiative B meson decays using the hadronic-tagging method,” English, PhD thesis, University of Hamburg, Mar. 2023 (cit. on p. 42).
- [41] A. Baur, *ZMQ Implementation for a Reliable Parallel Processing Framework on the High Level Trigger at the Belle II Experiment*, 2018 (cit. on p. 42).
- [42] Tadeas Bilka, “Time-dependent CP violation in $B^0 \rightarrow \eta_c K_S^0$ decays at the Belle experiment, Alignment of the Belle II detector,” Ph.D. thesis, Belle II, 2022 (cit. on pp. 43, 111, 135).
- [43] Y. Funakoshi *et al.*, “The SuperKEKB Has Broken the World Record of the Luminosity,” *JACoW*, vol. IPAC2022, pp. 1–5, 2022. DOI: 10.18429/JACoW-IPAC2022-MOPLXGD1 (cit. on p. 44).

- [44] KEK, *Belle II Detector 3D model*, <https://www.belle2.org/archives/> (cit. on p. 45).
- [45] T. Hara, T. Kuhr, and Y. Ushiroda, “Belle II Coordinate System and Guideline of Belle II Numbering Scheme,” Belle II Collaboration, Tech. Rep., 2011, Belle II Note, BELLE2-NOTE-TE-2015-009 (cit. on pp. 45, 46).
- [46] L. Zani, K. Adamczyk, L. Aggarwal, *et al.*, “The silicon vertex detector of the Belle II experiment,” *Nuclear Instruments and Methods in Physics Research Section A*, vol. 1038, p. 166 952, 2022. DOI: 0.1016/j.nima.2022.166952 (cit. on p. 46).
- [47] A. Baur, P. Ahlburg, L. Andricek, *et al.*, “The Belle II Pixel Vertex Detector,” Jun. 2024, p. 009. DOI: 10.22323/1.448.0009 (cit. on p. 46).
- [48] L. Burmistrov, I. Adachi, F. Le Diberder, *et al.*, “Belle II aerogel RICH detector,” *Nuclear Instruments and Methods in Physics Research Section A: Accelerators, Spectrometers, Detectors and Associated Equipment*, vol. 958, p. 162 232, 2020, Proceedings of the Vienna Conference on Instrumentation 2019. DOI: 10.1016/j.nima.2019.05.073 (cit. on p. 49).
- [49] T. Aushev *et al.*, “A scintillator based endcap KL and muon detector for the Belle II experiment,” *Nuclear Instruments and Methods in Physics Research Section A: Accelerators, Spectrometers, Detectors and Associated Equipment*, vol. 789, p. 134, 2015. DOI: 10.1016/j.nima.2015.03.060 (cit. on p. 52).
- [50] R. Itoh, A. Baur, S. Park, *et al.*, “Improved HLT Framework for Belle II Experiment,” *EPJ Web of Conferences*, vol. 295, May 2024. DOI: 10.1051/epjconf/202429502016 (cit. on p. 53).
- [51] T. Kuhr, C. Pulvermacher, M. Ritter, *et al.*, “The Belle II Core Software,” *Comput. Softw. Big Sci.*, vol. 3, no. 1, p. 1, 2019. DOI: 10.1007/s41781-018-0017-9. arXiv: 1809.04299 [physics.comp-ph] (cit. on p. 54).
- [52] The Belle II Collaboration, *Belle II Analysis Software Framework (basf2)*, 2022. DOI: 10.5281/zenodo.5574115 (cit. on p. 54).
- [53] V. Bertacchi *et al.*, “Track finding at Belle II,” *Comput. Phys. Commun.*, vol. 259, p. 107 610, 2021. DOI: 10.1016/j.cpc.2020.107610. arXiv: 2003.12466 [physics.ins-det] (cit. on p. 54).
- [54] J.-F. Krohn *et al.*, “Global decay chain vertex fitting at Belle II,” *Nucl. Instrum. Meth.*, vol. A976, p. 164 269, 2020. DOI: 10.1016/j.nima.2020.164269. arXiv: 1901.11198 [hep-ex] (cit. on p. 55).
- [55] W. D. Hulsbergen, “Decay chain fitting with a Kalman filter,” *Nuclear Instruments and Methods in Physics Research Section A: Accelerators, Spectrometers, Detectors and Associated Equipment*, vol. 552, pp. 566–575, 2005. DOI: 10.1016/j.nima.2005.06.078. arXiv: physics/0503191 [physics] (cit. on p. 55).
- [56] R. Bock and W. Kirscher, *The Data Analysis BriefBook*. Berlin, Heidelberg, New York: Springer-Verlag, 1998. DOI: 10.1007/978-3-662-03725-6 (cit. on p. 55).

- [57] J. Kemmer and G. Lutz, “New detector concepts,” *Nuclear Instruments and Methods in Physics Research Section A: Accelerators, Spectrometers, Detectors and Associated Equipment*, vol. 253, no. 3, pp. 365–377, Jan. 1987. DOI: 10.1016/0168-9002(87)90518-3 (cit. on p. 57).
- [58] R. Richter, *Private communication*, Email conversation, November 30, 2024 (cit. on p. 58).
- [59] R. Richter, L. Andricek, P. Fischer, *et al.*, “Design and technology of DEPFET pixel sensors for linear collider applications,” *Nuclear Instruments and Methods in Physics Research Section A: Accelerators, Spectrometers, Detectors and Associated Equipment*, vol. 511, no. 1, pp. 250–256, 2003, Proceedings of the 11th International Workshop on Vertex Detectors. DOI: 10.1016/S0168-9002(03)01802-3 (cit. on p. 58).
- [60] S. Stadler, A. Bähr, J. Ninković, *et al.*, “First insights on super-gq DePFET: An improved high performance sensor with increased gain and sub-electron noise levels capabilities,” *Nuclear Instruments and Methods in Physics Research Section A: Accelerators, Spectrometers, Detectors and Associated Equipment*, vol. 1069, p. 169 945, 2024. DOI: 10.1016/j.nima.2024.169945 (cit. on p. 59).
- [61] P. Ahlburg, “Development of a Laboratory Readout System for DEPFET Pixel Detector Modules and Investigation of Radiation Backgrounds at the SuperKEKB Accelerator,” PhD thesis, Rheinische Friedrich-Wilhelms-Universität Bonn, Jan. 2023 (cit. on pp. 59, 177).
- [62] F. Müller, “Characterization and optimization of the prototype DEPFET modules for the Belle II Pixel Vertex Detector,” PhD thesis, Jul. 2017. DOI: 10.5282/edoc.21071 (cit. on pp. 60–62, 66, 149).
- [63] P. Wieduwilt, “Characterisation, optimisation and performance studies of pixel vertex detector modules for the Belle II experiment,” PhD thesis, May 2021. DOI: 10.53846/goediss-8871 (cit. on pp. 63, 150).
- [64] M. Koch, “Development of a Test Environment for the Characterization of the Current Digitizer Chip DCD2 and the DEPFET Pixel System for the Belle II Experiment at SuperKEKB,” Presented 05 Sep 2011, Rheinische Friedrich-Wilhelms-Universität Bonn, 2011 (cit. on p. 65).
- [65] D. Levit, I. Konorov, D. Greenwald, *et al.*, “FPGA Based Data Read-Out System of the Belle II Pixel Detector,” *IEEE Transactions on Nuclear Science*, vol. 62, no. 3, pp. 1033–1039, 2015. DOI: 10.1109/TNS.2015.2424713 (cit. on p. 66).
- [66] D. Levit, “Search for $D^+ \rightarrow K^- K_s^0 \pi^+ \pi^- \pi^0$ at the Belle Experiment and Development of the Read-Out System for the Pixel Detector of the Belle II Experiment,” PhD thesis, Technische Universität München, 2019, p. 201 (cit. on p. 66).
- [67] Gefler, Thomas and Kühn, Wolfgang and Lange, Jens Sören and Liu, Zhen’An and Münchow, David and Spruck, Björn and Zhao, Jingzhou, “The ONSSEN Data Reduction System for the Belle II Pixel Detector,” *IEEE Transactions on Nuclear Science*, vol. 62, no. 3, pp. 1149–1154, 2015. DOI: 10.1109/TNS.2015.2414713 (cit. on p. 66).

- [68] S. P. Reiter, “Implementation, Operation and Monitoring of the Data Acquisition System of the Belle II Pixel Detector during Physics Data Taking in 2019-2022,” PhD thesis, Justus-Liebig-Universität Gießen, Feb. 2023. DOI: 10.22029/jlupub-18382 (cit. on p. 66).
- [69] S. Rummel, “The power supply system for the DEPFET pixel detector at BELLE II,” *Nuclear Instruments and Methods in Physics Research Section A: Accelerators, Spectrometers, Detectors and Associated Equipment*, vol. 699, pp. 51–55, 2013, Proceedings of the 8th International “Hiroshima” Symposium on the Development and Application of Semiconductor Tracking Detectors. DOI: 10.1016/j.nima.2012.04.041 (cit. on p. 66).
- [70] Y. Han, *Performance with 2-layer PXD*, Tracking Meeting, Jan. 2022 (cit. on p. 69).
- [71] S. Gentile and M. Pohl, “Physics of tau leptons,” *Physics Reports*, vol. 274, no. 5, pp. 287–374, 1996. DOI: 10.1016/0370-1573(96)00002-6 (cit. on p. 72).
- [72] S. Agostinelli *et al.*, “GEANT4: A simulation toolkit,” *Nucl.Instrum.Meth.*, vol. A506, pp. 250–303, 2003. DOI: 10.1016/S0168-9002(03)01368-8 (cit. on pp. 71, 156).
- [73] S. Jadach, B. F. L. Ward, and Z. Was, “The precision Monte Carlo event generator KK for two-fermion final states in e^+e^- collisions,” *Comput. Phys. Commun.*, vol. 130, p. 260, 2000. DOI: 10.1016/S0010-4655(00)00048-5. arXiv: hep-ph/9912214 [hep-ph] (cit. on p. 72).
- [74] S. Banerjee, D. Biswas, T. Przedzinski, *et al.*, *Monte Carlo Event Generator updates, for tau pair events at Belle II energies*, <https://arxiv.org/abs/2111.05914>, 2021. DOI: 10.48550/arXiv.2111.05914. arXiv: 2111.05914 [hep-ph] (cit. on p. 72).
- [75] S. Banerjee and A. Pathak, “Update of TAUOLA Monte Carlo for Belle II software,” Jul. 2020, BELLE2-NOTE-PH-2020-05, (Restricted Access) (cit. on pp. 72, 139).
- [76] T. Sjöstrand, S. Ask, J. R. Christiansen, *et al.*, “An Introduction to PYTHIA 8.2,” *Comput. Phys. Commun.*, vol. 191, pp. 159–177, 2015. DOI: 10.1016/j.cpc.2015.01.024. arXiv: 1410.3012 [hep-ph] (cit. on p. 72).
- [77] D. J. Lange, “The EvtGen particle decay simulation package,” *Nucl. Instrum. Meth.*, vol. A462, p. 152, 2001. DOI: 10.1016/S0168-9002(01)00089-4 (cit. on p. 72).
- [78] G. Balossini, C. M. Carloni Calame, G. Montagna, *et al.*, “Matching perturbative and parton shower corrections to Bhabha process at flavour factories,” *Nucl. Phys. B*, vol. 758, pp. 227–253, 2006. DOI: 10.1016/j.nucphysb.2006.09.022 (cit. on p. 73).
- [79] G. Balossini, C. Bignamini, C. M. C. Calame, *et al.*, “Photon pair production at flavour factories with per mille accuracy,” *Phys. Lett. B*, vol. 663, pp. 209–213, 2008. DOI: 10.1016/j.physletb.2008.04.007 (cit. on p. 73).
- [80] C. M. Carloni Calame, G. Montagna, O. Nicrosini, *et al.*, “The BABAYAGA event generator,” *Nucl. Phys. B Proc. Suppl.*, vol. 131, M. Incagli and G. Venanzoni, Eds., pp. 48–55, 2004. DOI: 10.1016/j.nucphysbps.2004.02.008 (cit. on p. 73).
- [81] C. M. Carloni Calame, “An improved parton shower algorithm in QED,” *Phys. Lett. B*, vol. 520, pp. 16–24, 2001. DOI: 10.1016/S0370-2693(01)01108-X (cit. on p. 73).

- [82] C. M. Carloni Calame, C. Lunardini, G. Montagna, *et al.*, “Large angle Bhabha scattering and luminosity at flavor factories,” *Nucl. Phys. B*, vol. 584, pp. 459–479, 2000. DOI: 10.1016/S0550-3213(00)00356-4 (cit. on p. 73).
- [83] F. Berends, P. Daverveldt, and R. Kleiss, “Radiative corrections to the process $e^+e^- \rightarrow e^+e^-\mu^+\mu^-$,” *Nucl. Phys. B*, vol. 253, pp. 421–440, 1985. DOI: 10.1016/0550-3213(85)90540-1 (cit. on p. 73).
- [84] F. Berends, P. Daverveldt, and R. Kleiss, “Complete lowest-order calculations for four-lepton final states in electron-positron collisions,” *Nucl. Phys. B*, vol. 253, pp. 441–463, 1985. DOI: 10.1016/0550-3213(85)90541-3 (cit. on p. 73).
- [85] F. Berends, P. Daverveldt, and R. Kleiss, “Monte Carlo simulation of two-photon processes: II: Complete lowest order calculations for four-lepton production processes in electron-positron collisions,” *Comp. Phys. Commun.*, vol. 40, no. 2, pp. 285–307, 1986. DOI: 10.1016/0010-4655(86)90115-3 (cit. on p. 73).
- [86] S. Uehara, “TREPS: A Monte-Carlo Event Generator for Two-photon Processes at e^+e^- Colliders using an Equivalent Photon Approximation,” Jul. 1996. DOI: 10.48550/arXiv.1310.0157. arXiv: 1310.0157 [hep-ph] (cit. on p. 73).
- [87] PHOKAHARA collaboration, *PHOKHARA version 9.1*, <https://looptreeduality.csic.es/phokhara/phokhara9.1.pdf>, Aug. 2014 (cit. on p. 73).
- [88] Belle II Collaboration, *Belle II Luminosity - Total recorded integrated luminosity before Long Shutdown 1*, <https://confluence.desy.de/pages/viewpage.action?pageId=349466209>, Accessed: 2025-03-01 (Restricted Access) (cit. on p. 76).
- [89] Belle II Collaboration, *Offline luminosity page*, <https://confluence.desy.de/pages/viewpage.action?pageId=278242419>, Accessed: 2024-07-08 (Restricted Access) (cit. on p. 76).
- [90] The Belle II Collaboration, *Measurement of the integrated luminosity of data samples collected during 2019-2022 by the Belle II experiment*, <https://arxiv.org/abs/2407.00965>, 2024. arXiv: 2407.00965 [hep-ex] (cit. on p. 76).
- [91] S. Moneta, F. Forti, and E. Paoloni, “A novel method for tau-lepton lifetime measurement with early Belle II data,” Presented on 29 10 2020, Master’s thesis, Pisa, Università di Pisa, Pisa, 2020 (cit. on p. 77).
- [92] G. Cowan, *Statistical Data Analysis*. Oxford, UK: Oxford University Press, 1998. DOI: 10.1093/oso/9780198501565.001.0001 (cit. on p. 79).
- [93] K. Cranmer, G. Lewis, L. Moneta, *et al.*, “HistFactory: A tool for creating statistical models for use with RooFit and RooStats,” New York U., New York, Tech. Rep., 2012. DOI: 10.17181/CERN-OPEN-2012-016 (cit. on p. 79).
- [94] L. Heinrich, M. Feickert, G. Stark, *et al.*, “pyhf: pure-Python implementation of HistFactory statistical models,” *Journal of Open Source Software*, vol. 6, no. 58, p. 2823, 2021. DOI: 10.21105/joss.02823 (cit. on pp. 79, 82, 127).

Bibliography

- [95] K. Cranmer and A. Held, *Building and steering template fits with cabinetry*, Mar. 2021. DOI: 10.5281/zenodo.4627038 (cit. on pp. 79, 127).
- [96] G. Zech, *Analysis of distorted measurements – parameter estimation and unfolding*, 2016. arXiv: 1607.06910 [physics.data-an] (cit. on p. 83).
- [97] Z. Gruberová, Z. Dolezal, P. Rados and A. Rostomyan, “Study of the τ lepton decays at the Belle II experiment,” *BELLE2-MTHESIS-2021-007.*, 2021 (cit. on pp. 89, 201).
- [98] R. Hoppe and D. Pitzl, *Correction for tracking momentum and energy bias based on $D0$ invariant mass peak for proc13 and prompt processing of buckets 26-36*, <https://docs.belle2.org/record/4027/?>, BELLE2-NOTE-PH-2023-069, (Restricted Access), Dec. 2023 (cit. on pp. 92, 141).
- [99] Q. Ji, S. Jia, and C. Shen, “Energy resolution and bias with E_γ 2.0 GeV using symmetric decays of $\pi^0 \rightarrow \gamma\gamma$ and $\eta \rightarrow \gamma\gamma$ at Belle-II,” May 2021, BELLE2-NOTE-PH-2020-073, (Restricted Access) (cit. on p. 92).
- [100] L. Cao and K. Tackmann, *Calibration of photon detection efficiency of the Belle II electromagnetic calorimeter using radiative muon pair events*, <https://docs.belle2.org/record/4072/?>, BELLE2-NOTE-TE-2024-002, (Restricted Access), Jan. 2023 (cit. on p. 92).
- [101] J. P. Lees *et al.*, “Production of charged pions, kaons, and protons in e^+e^- -annihilations into hadrons at $\sqrt{s}=10.54$ GeV,” *Physical Review D*, vol. 88, no. 3, Aug. 2013. DOI: 10.1103/physrevd.88.032011 (cit. on p. 95).
- [102] T. Bilka *et al.*, “Alignment for the first precision measurements at Belle II,” *EPJ Web Conf.*, vol. 245, C. Doglioni, D. Kim, G. A. Stewart, *et al.*, Eds., p. 02023, 2020. DOI: 10.1051/epjconf/202024502023 (cit. on p. 111).
- [103] Python Software Foundation, *Python: A programming language*, <https://www.python.org>, Version 3.8, 1991 (cit. on p. 127).
- [104] M. E. Nils Braun *et al.*, *B2Luigi: A workflow management system for Belle II analyses*, <https://github.com/belle2/b2luigi>, Version 1.0, 2018 (cit. on p. 127).
- [105] Apache Software Foundation, *Apache Parquet: An open source, column-oriented data file format designed for efficient data storage and retrieval*, <https://parquet.apache.org>, Version 1.3.1, 2013 (cit. on p. 127).
- [106] R. Brun and F. Rademakers, “ROOT – an object oriented data analysis framework,” *Nucl. Inst. & Meth. in Phys. Res. A*, vol. 389, pp. 81–86, 1997, Proceedings AIHENP’96 Workshop, Lausanne, Sep. 1996. DOI: 10.1016/S0168-9002(97)00048-X (cit. on p. 128).
- [107] J. Pivarski and contributors, *Uproot: Root i/o in pure python and numpy*, <https://github.com/scikit-hep/uproot>, Version 5.3.9, 2023 (cit. on p. 129).
- [108] The pandas development team, *Pandas: Python data analysis library*, <https://pandas.pydata.org>, Version 2.0.3, 2008 (cit. on p. 129).

- [109] A. Haupt and Y. Kemp, “The NAF: National Analysis Facility at DESY,” *J. Phys. Conf. Ser.*, vol. 219, J. Gruntorad and M. Lokajicek, Eds., p. 052007, 2010. DOI: 10.1088/1742-6596/219/5/052007 (cit. on p. 131).
- [110] T. Kluyver, B. Ragan-Kelley, F. Pérez, *et al.*, *Jupyter Notebooks—a publishing format for reproducible computational workflows*, 2016. DOI: 10.3233/978-1-61499-649-1-87 (cit. on p. 131).
- [111] D. Thain, T. Tannenbaum, and M. Livny, “Distributed computing in practice: the Condor experience: Research Articles,” *Concurrency - Practice and Experience*, vol. 17, pp. 323–356, Feb. 2005. DOI: 10.1002/cpe.938 (cit. on p. 131).
- [112] Belle II Collaboration, *Misalignments*, <https://xwiki.desy.de/xwiki/bin/view/BI/Belle~IIIInternal/Software/SoftwareAlignMent/Misalignments/>, Accessed: 2024-10-08 (Restricted Access) (cit. on p. 135).
- [113] D. Pitzl, *Material Budget from Nuclear Interactions*, Tracking & Vertexing Weekly Meeting, Belle II Collaboration, Event date: November 23, 2023, Online Event, <https://indico.belle2.org/event/10683/> (Restricted Access) (cit. on p. 136).
- [114] P. Rados *et al.*, *Tracking Efficiency with Taus: Update on MC15rd*, https://indico.belle2.org/event/10572/contributions/68899/attachments/25231/37323/ta_u_eff_mc15rd_update_9Nov23.pdf, Presented at Tracking & Vertexing Meeting, 9 November 2023, HEPHY (Restricted Access), Nov. 2023 (cit. on p. 141).
- [115] P. Rados *et al.*, *Tracking Efficiency with Taus*, https://indico.belle2.org/event/8043/contributions/51113/attachments/20577/30471/tau_eff_f2f_31jan23.pdf, Presented at Face 2 Face Tracking Meeting, 31 January 2023, DESY (Restricted Access), Jan. 2023 (cit. on p. 141).
- [116] R. L. Workman *et al.*, “Review of Particle Physics,” *PTEP*, vol. 2022, p. 083C01, 2022. DOI: 10.1093/ptep/ptac097 (cit. on p. 147).
- [117] H. Schreeck, “Commissioning and First Data Taking Experience with the Belle II Pixel Vertex Detector,” PhD thesis, PhD thesis, Georg-August-Universität Göttingen, May 2020. DOI: 10.53846/goediss-8060 (cit. on p. 150).
- [118] L. Landau, “On the energy loss of fast particles by ionization,” *J. Phys. (USSR)*, vol. 8, pp. 201–205, 1944. DOI: 10.1016/b978-0-08-010586-4.50061-4 (cit. on p. 150).
- [119] SiLab-Bonn, *pylandau - A simple Landau definition to be used in Python...* <https://github.com/SiLab-Bonn/pylandau>, Accessed: 2024-12-12, 2024 (cit. on p. 150).
- [120] PXD Collaboration, *PXD SC Lab Framework - Source Scan Library*, https://gitlab.desy.de/belle2/detector/pxd/pxd_sc_lab_framework/-/blob/3f47b59ec3c3ec51b9ec99a2b4de326520356375/calibrations/source_scan/source_scan_lib.py, Commit hash: 3f47b59ec3c3ec51b9ec99a2b4de326520356375, 2021 (cit. on pp. 150, 151).
- [121] F. Mauger and V. Tretyak, *BxDecay0 - C++ port of the legacy Decay0 FORTRAN library*, <https://github.com/BxCppDev/bxdecay0>, 2017 (cit. on p. 157).

Bibliography

- [122] J. Coombs *et al.*, *Python Client built against the Wolfram Alpha API*, <https://github.com/jaraco/wolframalpha>, Accessed: 2024-12-11, 2024 (cit. on p. 157).
- [123] R. Richter, *Private communication*, Online Meeting, July 3, 2024 (cit. on p. 168).
- [124] Botho Paschen, “Characterization and Operation of Final DEPFET Pixel Detector Modules for the Belle II Experiment,” PhD thesis, Rheinische Friedrich-Wilhelms-Universität Bonn, Oct. 2024 (cit. on p. 175).
- [125] P. Majewski, L. Andricek, A. Bahr, *et al.*, “DEPFET Macropixel Detectors for MIXS: Integration and Qualification of the Flight Detectors,” *IEEE Transactions on Nuclear Science*, vol. 59, no. 5, pp. 2479–2486, 2012. DOI: 10.1109/TNS.2012.2211616 (cit. on p. 175).
- [126] M. Bonholzer, R. Andritschke, V. Emberger, *et al.*, “Drain current characteristics of Athena WFI flight-like DEPFETs,” in *Space Telescopes and Instrumentation 2022: Ultraviolet to Gamma Ray*, J.-W. A. den Herder, S. Nikzad, and K. Nakazawa, Eds., International Society for Optics and Photonics, vol. 12181, SPIE, 2022, p. 121813V. DOI: 10.1117/12.2628862 (cit. on p. 175).
- [127] S. Schnitzius, *Charakterisierung von DEPFET-Pixel-Teststrukturen mit einem Laser-Setup*, Bachelor thesis, Rheinische Friedrich-Wilhelms-Universität Bonn, 2021 (cit. on pp. 176–178).
- [128] R. Richter, *Private communication*, Email conversation, January 28, 2025 (cit. on p. 177).
- [129] Y. Buch, “Total Ionizing Dose Measurement of the Belle II Pixel Detector,” Master’s thesis, Master’s thesis, Georg-August-Universität Göttingen, Oct. 2022 (cit. on p. 187).
- [130] Belle II Collaboration, *Data Format from ETM to GDL*, <https://confluence.desy.de/display/BI/Data+Format+from+ETM+to+GDL>, Accessed: 2024-08-19, (Restricted Access), 2024 (cit. on p. 200).

A. Appendix

A.1. Production Cross-Section

Physics Process	Cross Section in nb	Selection Criteria
$\Upsilon(4S)$	1.110 ± 0.008	
$u\bar{u}(\gamma)$	1.61	-
$d\bar{d}(\gamma)$	0.40	-
$s\bar{s}(\gamma)$	0.38	-
$c\bar{c}(\gamma)$	1.30	-
$e^+e^-(\gamma)$	300 ± 3 (MC stat.)	$10^\circ < \theta_e^* < 170^\circ$, $E_e^* > 0.15$ GeV
$e^+e^-(\gamma)$	74.4	$p_e > 0.5$ GeV/c and e in ECL
$\gamma\gamma(\gamma)$	4.99 ± 0.05 (MC stat.)	$10^\circ < \theta_\gamma^* < 170^\circ$, $E_\gamma^* > 0.15$ GeV
$\gamma\gamma(\gamma)$	3.30	$E_\gamma > 0.5$ GeV in ECL
$\mu^+\mu^-(\gamma)$	1.148	-
$\mu^+\mu^-(\gamma)$	0.831	$p_\mu > 0.5$ GeV/c in CDC
$\mu^+\mu^-\gamma(\gamma)$	0.242	$p_\mu > 0.5$ GeV in CDC, $\geq 1 \gamma$ ($E_\gamma > 0.5$ GeV) in ECL
$\tau^+\tau^-(\gamma)$	0.919	-
$\nu\bar{\nu}(\gamma)$	0.25×10^{-3}	-
$e^+e^-e^+e^-$	39.7 ± 0.1 (MC stat.)	$W_{\ell\ell} > 0.5$ GeV/c ²
$e^+e^-\mu^+\mu^-$	18.9 ± 0.1 (MC stat.)	$W_{\ell\ell} > 0.5$ GeV/c ²

Table A.1.: Production cross-section at $\sqrt{s} = 10.58$ GeV. (Table adapted from [39])

A.2. Scaling of Simulated Data Samples

Assuming, the simulated dataset has a luminosity $\mathcal{L}_{\text{int}}^{\text{MC}}$ and needs to be scaled to the corresponding luminosity of the experimental data $\mathcal{L}_{\text{int}}^{\text{data}}$ (Equation (6.1)), the luminosity scaling factor η is defined by

$$\eta = \frac{\mathcal{L}_{\text{int}}^{\text{data}}}{\mathcal{L}_{\text{int}}^{\text{MC}}}. \quad (\text{A.1})$$

In the case of higher statistics in the simulated dataset, this leads to smaller statistical uncertainty in the simulation. The statistical uncertainty has to be propagated following the Gaussian

A. Appendix

propagation laws:

$$\frac{\sigma_{\text{stat}}^{\text{MC}}}{N_{\text{MC}}} = \frac{\sigma_{\text{stat}}^{\text{MC}}}{\eta N_{\text{MC}}}, \quad (\text{A.2})$$

$$\sigma_{\text{stat}}^{\text{MC}} = \eta \sqrt{N_{\text{MC}}}, \quad (\text{A.3})$$

where $\sigma_{\text{stat}}^{\text{MC}}$ is the statistical uncertainty on the nominal simulated data sample, and $\sigma_{\text{stat}}^{\text{MC}}$ is the statistical uncertainty on the scales simulated data sample. To obtain eq. (A.3), the relation $\sigma_{\text{stat}} = \sqrt{N}$ is used, which expresses the uncertainty of observing N events under a discrete Poisson probability density distribution.

A.3. ECL Trigger Bits

The trigger bits used for the τ -lepton lifetime analysis are defined as (the information is taken from [130]):

- **hie**
 - total ECL energy > 1 GeV
 - no ECL Bhabha veto signal
- **lm10** (prescaled since experiment 20)
 - $N_{\text{cluster}} \geq 3$, one with $E_{\text{lab}} \geq 300$ MeV
 - $1 \leq \theta_{\text{id}} \leq 17 \equiv 12.4^\circ < \theta_{\text{lab}} < 154.7^\circ$
 - not an ECL 3D Bhabha
- **lm11**
 - one cluster with ≥ 2 GeV(CM) with $\theta_{ID} = 4^\circ - 14^\circ$
- **lm12**
 - one cluster with ≥ 2 GeV(CM) with $\theta_{ID} = 2^\circ, 3^\circ, 15^\circ$ or 16°
 - not an ECL 3D Bhabha
- **lm14**
 - one $CL \geq 2$ GeV(CM) with $\theta_{ID} = 1^\circ$ or 17°
 - not an ECL 3D Bhabha
- **lm16**
 - only one cluster with $E_{\text{CM}} \geq 1$ GeV, $4 \leq \theta_{\text{id}} \leq 15$
 - no other cluster with $E_{\text{lab}} \geq 300$ MeV anywhere
- **lm17**
 - only one cluster with ≥ 1 GeV(CM) with $\theta_{ID} = 2^\circ, 3^\circ$, or 16°
 - no other cluster with ≥ 300 MeV(Lab) anywhere
- **lm18**
 - two clusters with $170^\circ < \Delta\phi_{\text{CM}} < 190^\circ$ and $E_{\text{lab}} > 250$ MeV

- no other cluster with $E_{\text{CM}} \geq 2$ GeV anywhere
- 1m19
 - two clusters with $170^\circ < \Delta\phi_{\text{CM}} < 190^\circ$
 - one cluster with $E_{\text{lab}} > 250$ MeV, the other with $E_{\text{lab}} < 250$ MeV
 - no other cluster with $E_{\text{CM}} \geq 2$ GeV anywhere
- 1m110
 - two clusters with $160^\circ < \Delta\phi_{\text{CM}} < 200^\circ$ and $160^\circ < \sum\theta_{\text{CM}} < 200^\circ$
 - no other cluster with $E_{\text{CM}} \geq 2$ GeV anywhere
- 1m112 (tighter selection of 1m110)
 - $N_{\text{cluster}} \geq 3$, one with $E_{\text{lab}} \geq 500$ MeV
 - $2 \leq \theta_{\text{id}} \leq 16 \equiv 18.5^\circ < \theta_{\text{lab}} < 139.3^\circ$
 - not an ECL 3D Bhabha
- 1m113 (modified trigger bit of 1m16)
 - only one cluster with ≥ 0.5 GeV(CM) with $\theta_{\text{ID}} = 6^\circ - 11^\circ$
 - no other $CL \geq 300$ MeV(Lab) anywhere

The ECL 3D Bhabha veto is defined as:

- ec1_3dbha (3D Bhabha veto since Experiment 10 the general Bhabha veto)
 - $165^\circ < \Sigma\theta_{\text{CM}} < 190^\circ$, where $\Sigma\theta_{\text{CM}}$ is the sum of polar angles of 2 clusters in CM
 - $160^\circ < \Delta\phi_{\text{CM}} < 200^\circ$, where $\Delta\phi_{\text{CM}}$ is the difference of phi angles of 2 clusters in CM
 - $E(\text{CL1}) > 3$ GeV && $E(\text{CL2}) > 3$ GeV && ($E(\text{CL1}) > 4.5$ GeV or $E(\text{CL2}) > 4.5$ GeV)
where $E(\text{CLX})$ is the energy of cluster number X ($X = 1, 2$) in CM

A.4. π^0 Efficiency Correction

The π^0 detection efficiency ε_{π^0} is studied in [97], where the number of reconstructed π^0 from experimental and simulated data is compared and ε_{π^0} is extracted. The π^0 count is fitted to the two-photon mass peak from the $\tau \rightarrow 3\pi\pi^0\nu$ decay, where the two photons originate from the π^0 decay.

The ε_{π^0} correction factors are provided in bins of π^0 momentum p and polar angle $\cos\theta$. However, the provided 2D bins do not cover the phase space necessary for this analysis. The ε_{π^0} correction factors are applied as event weights and for the uncovered regions, a weight of one is applied. Table A.2 shows the used ε_{π^0} correction weights. Figure A.1 shows the number of π^0 s in bins of p and $\cos\theta$. The red box indicates the phase space with the available ε_{π^0} correction factors.

Figure A.2a shows the distribution of the number of π^0 on the 1-prong side $n_{\pi^0,1p}$ without ε_{π^0} correction. The normalized ratio plot indicates that the overestimation is particularly significant for events with one or two π^0 s, while events without π^0 s are underestimated.

A. Appendix

		$\cos \theta$					
		$[-0.65, -0.3]$	$[-0.3, 0.0]$	$[0.0, 0.3]$	$[0.3, 0.5]$	$[0.5, 0.7]$	$[0.7, 1.0]$
p in GeV	$[0.6, 0.8]$	0.895 ± 0.031	1.005 ± 0.047	1.011 ± 0.027	1.006 ± 0.043	0.999 ± 0.036	0.885 ± 0.040
	$[0.8, 1.0]$	0.897 ± 0.021	1.036 ± 0.024	1.066 ± 0.021	1.032 ± 0.023	1.053 ± 0.023	0.993 ± 0.026
	$[1.0, 1.5]$	0.966 ± 0.017	1.034 ± 0.015	1.055 ± 0.023	1.057 ± 0.015	1.044 ± 0.013	0.993 ± 0.015
	$[1.5, 2.0]$	0.992 ± 0.026	1.011 ± 0.020	1.018 ± 0.015	1.050 ± 0.017	1.037 ± 0.014	0.990 ± 0.016
	$[2.0, 3.0]$	0.972 ± 0.031	1.008 ± 0.028	1.066 ± 0.029	1.017 ± 0.018	1.040 ± 0.015	1.011 ± 0.017

Table A.2.: ε_{π^0} correction weights of the red boxed region in Figure A.1

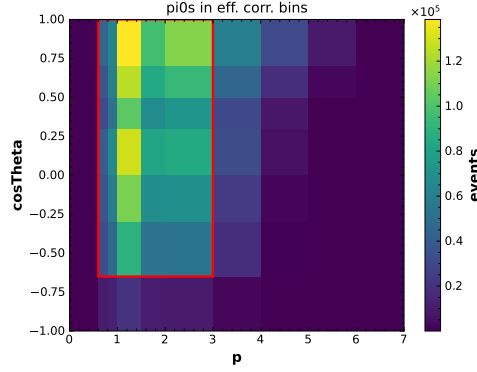


Figure A.1.: 2D π^0 p - $\cos \theta$ phase space. Red box indicates the phase space region with available ε_{π^0} correction factors. Outside that box region the weights are set to one.

After applying the ε_{π^0} correction weights to the simulated samples, the data/MC discrepancy in the distribution of the $n_{\pi^0,1p}$ increased, as shown in Figure A.2b. It is visible in both figures (a) and (b), the simulation overestimates the number of π^0 s. The exact source of the $n_{\pi^0,1p}$ migration across bins cannot be determined.

The data/MC agreement for the τ_{3p} transverse momentum $p_{T,\tau_{3p}}$ does not improve with the direct π^0 ε_{π^0} correction approach (Figure A.3a and Figure A.3b). However, for $p_{T,\tau_{3p}} < 2.5$ GeV, a significant shape-shift is observed in the normalized ratio plot.

Since the $p_{T,\tau_{3p}}$ data/MC agreement does not improve, and the $n_{\pi^0,1p}$ data/MC agreement decreased, the ε_{π^0} correction is performed through the general photon efficiency ε_γ correction as described in Section 6.4.2.

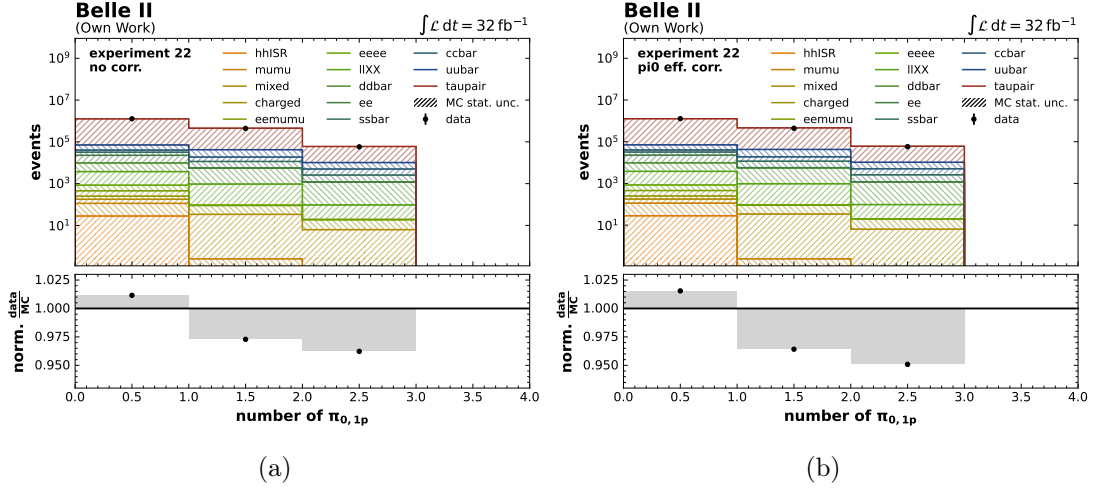


Figure A.2: $n_{\pi^0, 1p}$, (a) without any ε_{π^0} correction applied and (b) with ε_{π^0} correction weights applied, studied on the Experiment 22 dataset. The statistical uncertainties of the histograms are not visible.

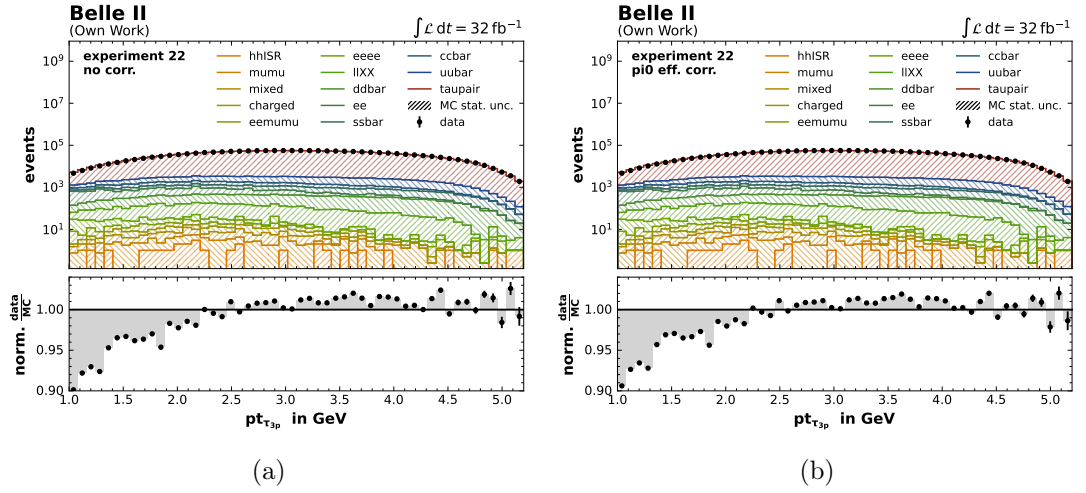


Figure A.3: τ_{3p} p_T distributions with a significant data/MC disagreement (a) without any ε_{π^0} correction applied and (b) with ε_{π^0} correction weights applied, studied on the Experiment 22 dataset. The statistical uncertainties of the histograms are not visible.

A.5. Applying Event Selection

A.5.1. Observable Distributions with All Selections Applied

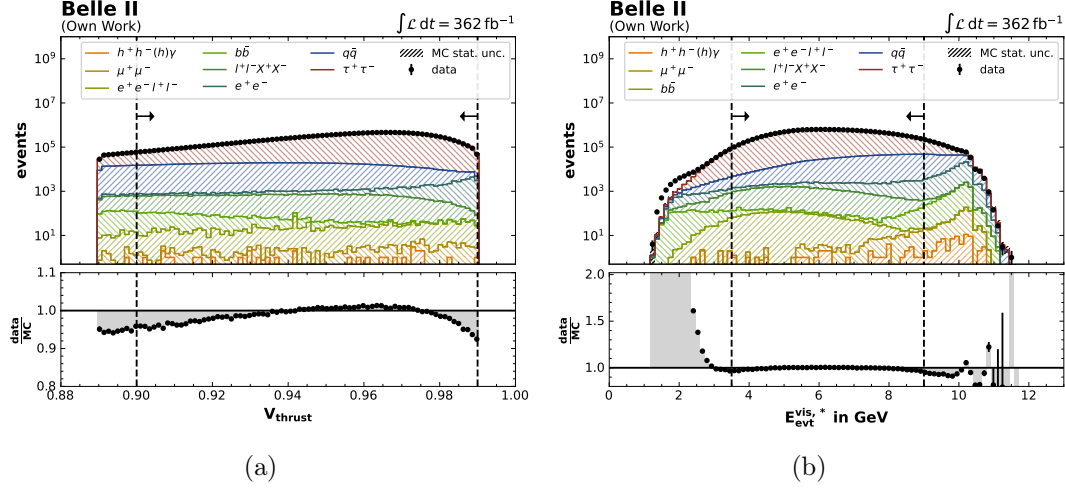


Figure A.4.: Distribution after event selection (Table 6.8) but without the indicated selection of: (a) V_{thrust} and (b) $E_{\text{vis},*}$. The statistical uncertainties of the histograms are not visible within the selection window.

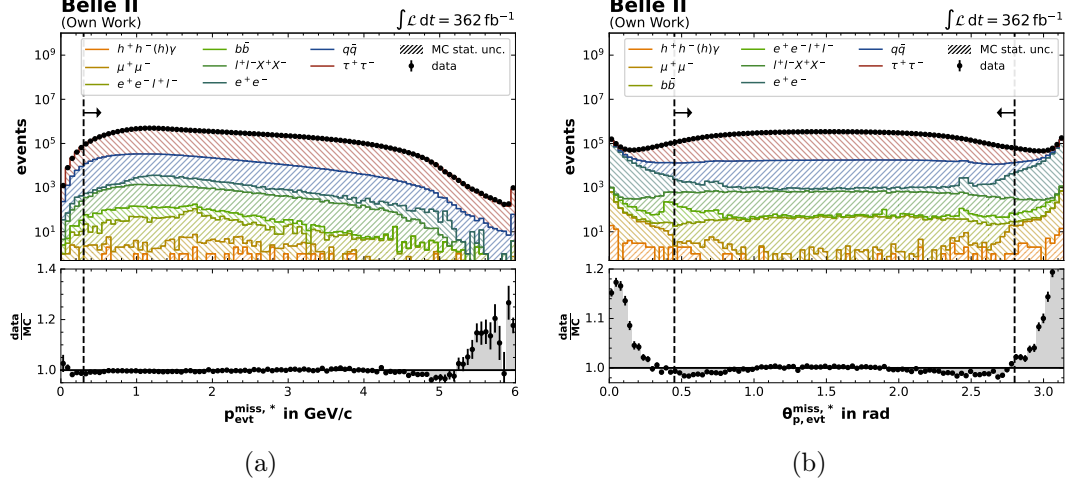


Figure A.5.: Distribution after event selection (Table 6.8) but without the indicated selection of: (a) $p_{\text{miss},*}$ and (b) $\theta_{\text{miss},*}$. The statistical uncertainties of the histograms are not visible.

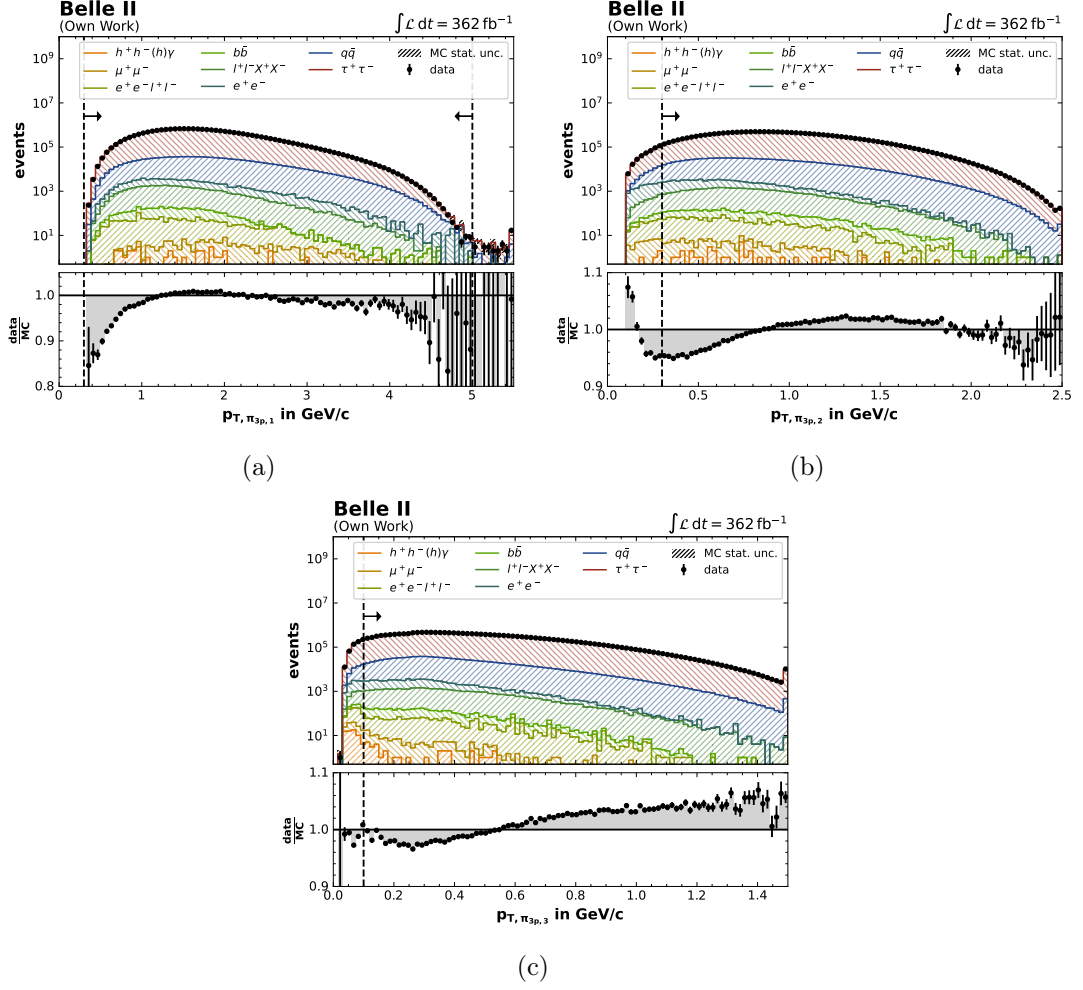


Figure A.6.: Distribution after event selection (Table 6.8) but without the indicated selection of: (a) $p_{T, \pi_{3p,1}}$, (b) $p_{T, \pi_{3p,2}}$, and (c) $p_{T, \pi_{3p,3}}$. The statistical uncertainties of the histograms are not visible within the selection window.

A. Appendix

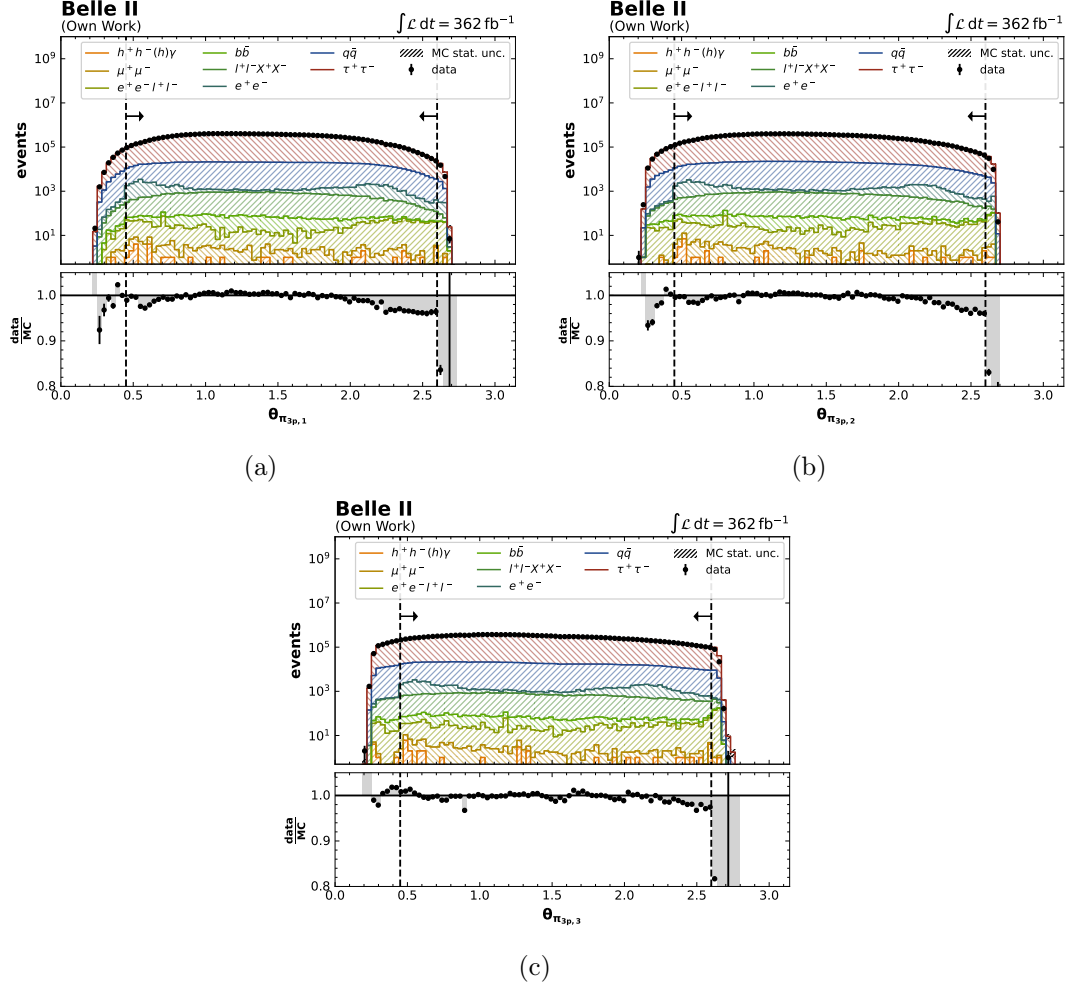


Figure A.7.: Distribution after event selection (Table 6.8) but without the indicated selection of: (a) $\theta_{\pi_{3p,1}}$, (b) $\theta_{\pi_{3p,2}}$, and (c) $\theta_{\pi_{3p,3}}$. The statistical uncertainties of the histograms are not visible within the selection window.

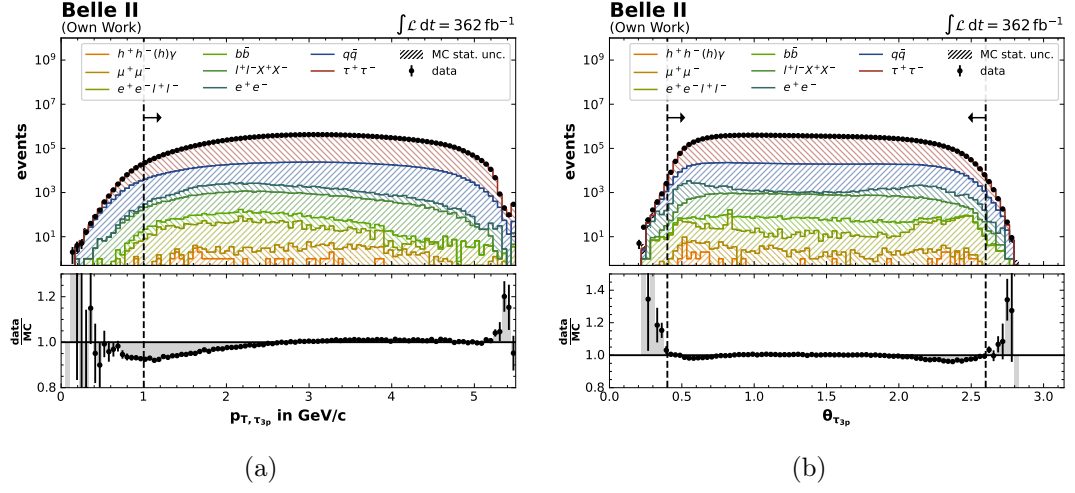


Figure A.8.: Distribution after event selection (Table 6.8) but without the indicated selection of: (a) $p_{T, \tau_{3p}}$ and (b) $\theta_{\tau_{3p}}$. The statistical uncertainties of the histograms are not visible.

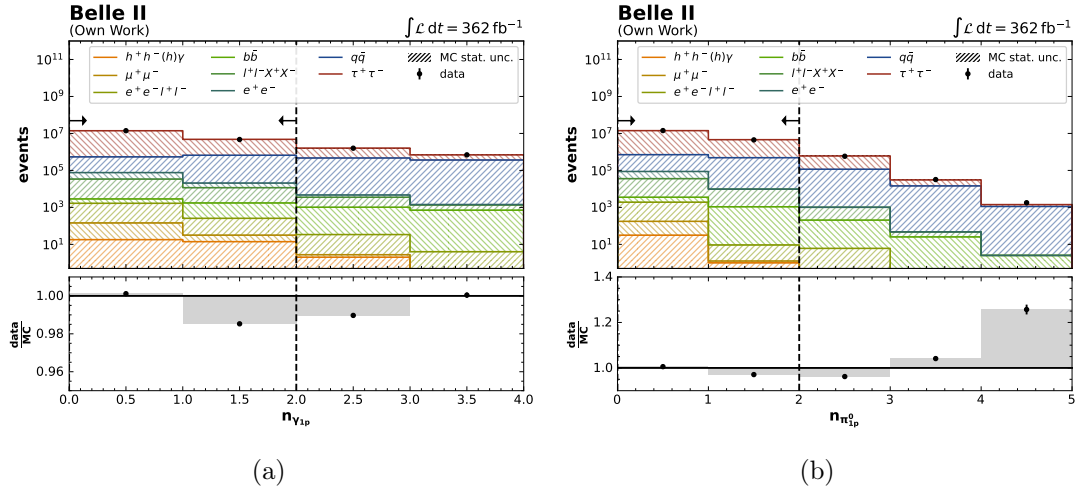


Figure A.9.: Distribution after event selection (Table 6.8) but without the indicated selection of: (a) $n_{\gamma_{1p}}$ and (b) $n_{\pi_{1p}^0}$. The statistical uncertainties of the histograms are not visible.

A. Appendix

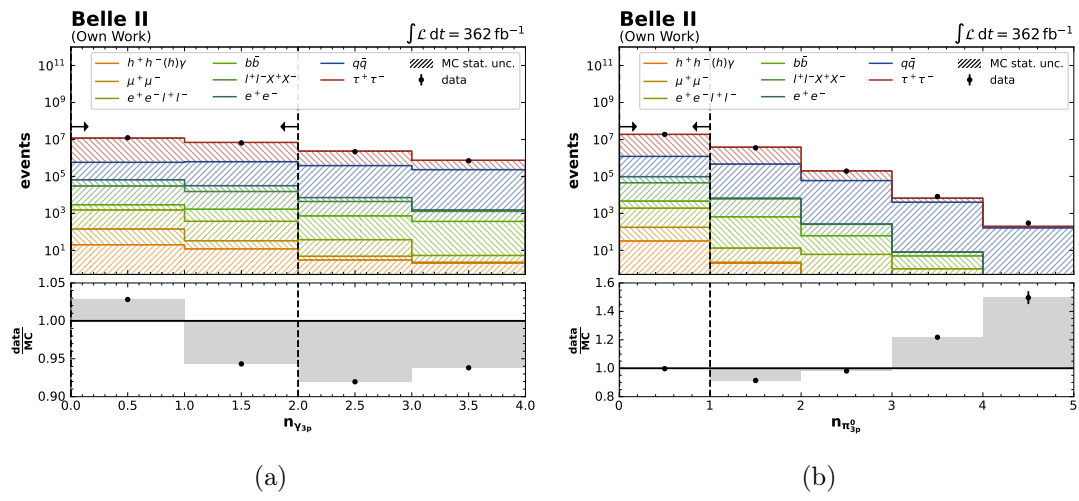


Figure A.10.: Distribution after event selection (Table 6.8) but without the indicated selection of: (a) $n_{\gamma_{3p}}$ and (b) $n_{\pi_{3p}^0}$. The statistical uncertainties of the histograms are not visible.

A.6. π_{3p}^{\pm} Momentum

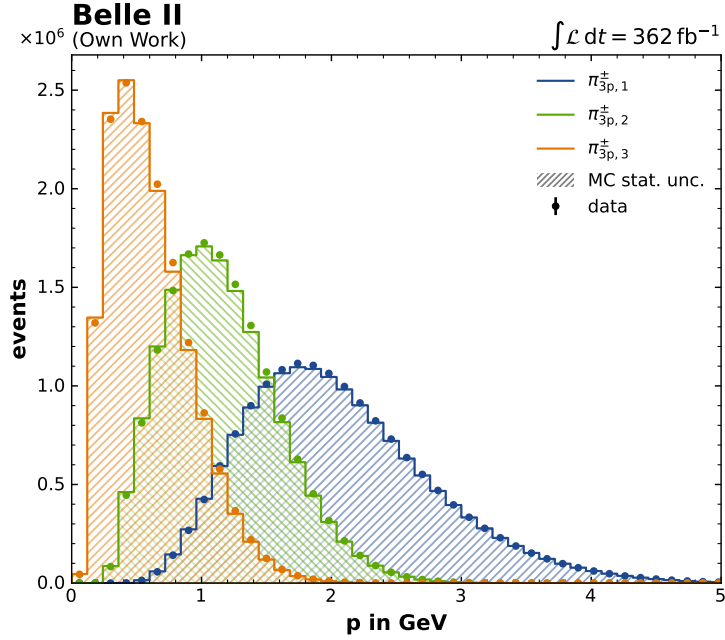


Figure A.11.: Momentum of the leading p_T , sub-leading p_T , and low p_T π_{3p}^{\pm} . The statistical uncertainties of the histograms are not visible.

A.7. Analysis Framework Task Trees

A.7.1. Template Creation Task Tree

Figure A.12 shows the Task tree for the signal region template creation including the mismodeling shape systematics. Each box represents a Task, and the arrows show the input dependencies of the Tasks. Each Task starts only if the output of the previous dependent Task is created.

If no Template is available, the Task tree execution starts with `CreateWeightsFile`, creating the weights for the template correction (if no template correction is applied, this is skipped). If the correction weights are available, the nominal signal region instanced Template object is created in the `CreateNominalSignalRegionTemplate` Task, and the nominal template histogram is added. Using the nominal template histogram, all the shifted lifetime histograms are created in parallel in the `CreateOffsetSignalRegionTemplates` Tasks, and the Template attributes are stored in pickle files for each Task. They are then combined in the `CombineSignalRegionTemplates` Task to a single instanced Template object.

If the pickle file with all the template histograms is available, the shape systematics are created and the instanced Systematic objects are added. In case of the mismodeling shape systematics, the `CreateMCMismodelingSyst` Tasks are executed after their inputs are created in the `CreateReWeightedHistogram` Tasks. There, the weights are calculated, to obtain the variation histograms. For all mismodeling shape systematics the Tasks are executed in parallel.

A. Appendix

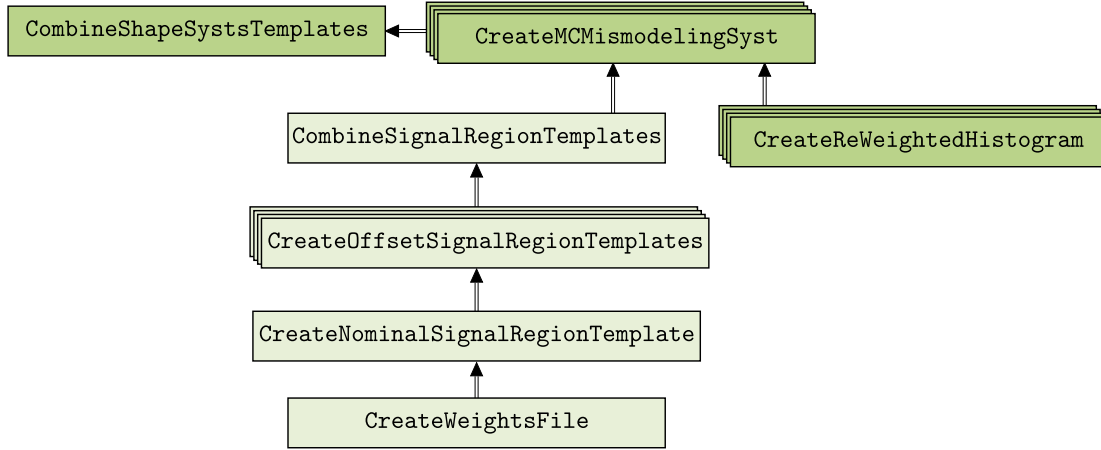


Figure A.12.: Task tree created with `b2luigi` for the signal fit region template creation in the framework.

Finally, the instanced `Systematic` objects are combined in the `CombineShapeSystsTemplates` Task.

The same schema is also applied similarly for all the other shape systematics. In the end, a single instanced `Template` object, comprising all template histograms and shape systematics remains, stored in a pickle file.

A.7.2. Lifetime Fit Task Tree

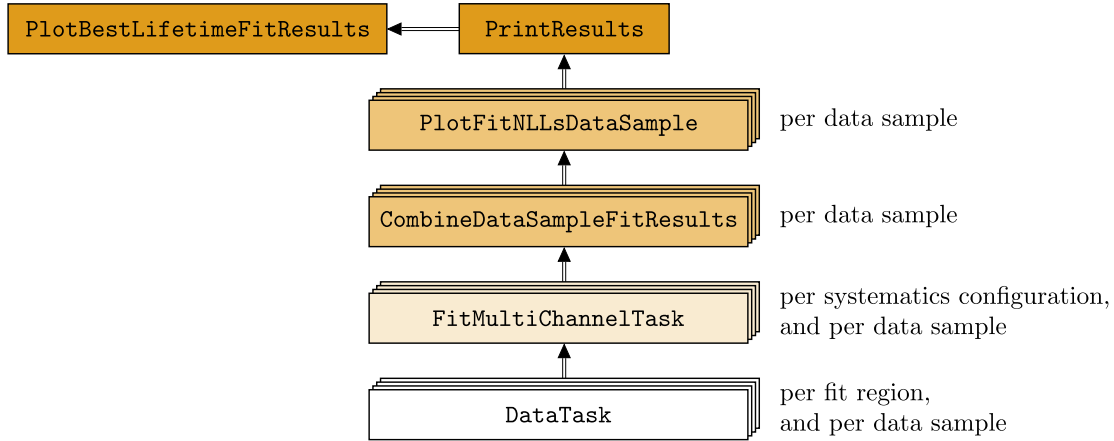


Figure A.13.: Task tree created with `b2luigi` for the lifetime fit in the framework.

Figure A.13 shows the `b2luigi` Task tree of the fitting pipeline. The `DataTask` ensures, that the data samples (pseudo data or experimental data) for the lifetime fit are compatible to the templates (e.g. correct binning). The data histograms are stored in `pickle` files, which are loaded in the `FitMultiChannelTask` together with the `Template` object attributes. The individual fit configurations are performed in several parallel Tasks. The output of these Tasks

are the fit results for each data sample, and each individual fit configuration. In the subsequent **CombineDataSampleFitResults Task**, the fit results for all different systematic configurations, are combined, respectively for each data sample fed into the fit. This allows to study the impact of single systematics and fit configurations simultaneously.

For each data sample put into the fit, the $2\Delta\text{NLL}$ curves of each systematic configuration is plotted in the **PlotFitNLLsDataSample Task**. The best lifetime fit values and the 68 % CL are written by the **PrintResults Task** for all data samples and all NP configurations in a text file. This enables fast access to the main fit results, and provides a direct comprehensive overview. A final plot, visualizing these results is created, showing the best lifetime fit values and their 68 % CL.

A.8. Full Uncertainty Breakdown

Source	σ in fs
Systematic	0.19
MC stat.	0.07
template correction ($\theta_{\pi_{3p}}$ & $p_{T\pi_{3p}}$)	0.06
$c\bar{c}$ contribution ($\pm 50\%$)	0.09
$\Delta x_{\text{PromptProc}}$	0.06
$\Delta x_{\text{IntrSyst},1}$	0.02
$\Delta x_{\text{Day2Day}}$	0.00
$\Delta x_{\text{IntrSyst},2}$	0.05
$\mathcal{Q}_{\text{BP},\pm 5\%}$	0.10
$\varepsilon_{\text{trig}}$	0.04
K^\pm	0.00
$\varepsilon_{\text{track}}$	0.00
luminosity	0.00
ε_γ	0.02
E_γ	0.00
$E_{\text{loss,PDG}}^{\text{PDG}}$	0.00
$E_{\text{loss,bias}}^{\text{data}}$ & $E_{\text{loss,stat}}^{\text{data}}$	0.00
$E_{\text{loss,bias}}^{\text{MC}}$ & $E_{\text{loss,stat}}^{\text{MC}}$	0.00
$p_{\text{PDG}}^{\text{PDG}}$	0.00
$p_{\text{bias}}^{\text{data}}$	0.00
$p_{\text{bias}}^{\text{MC}}$	0.00
$p_{\tau_{3p}}$	0.00
$M_{\tau_{3p}}$	0.08
$d_{2\times 1}$	0.00
V_{thrust}	0.01
$E_{\text{evt}}^{\text{vis},*}$	0.00
$M_{\text{evt}}^{2\text{ miss},*}$	0.00
$\theta_{p,\text{evt}}^{\text{miss},*}$	0.03
$n_{\pi_{0,1p}}$	0.00
$n_{\gamma_{1p}}$	0.00
$n_{\gamma_{3p}}$	0.00
$M_{\text{evt}}^{2\text{ miss},*}$	0.00
Total	0.20

Table A.3.: Table of all uncertainty NPs, before pruning.

A.9. MC Stat. NP Correlations

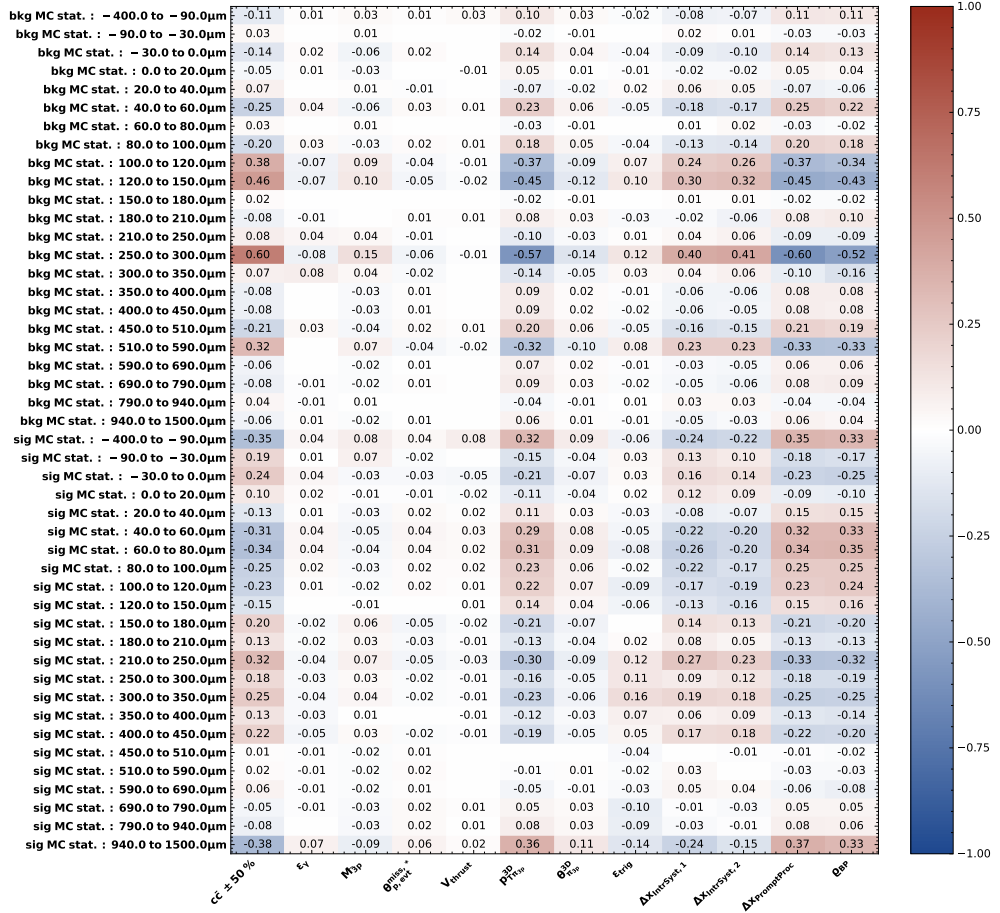


Figure A.14.: Correlation matrix of the MC stat. NPs with the shape uncertainty NPs of the pruned pseudo data fit for the nominal template.

A. Appendix

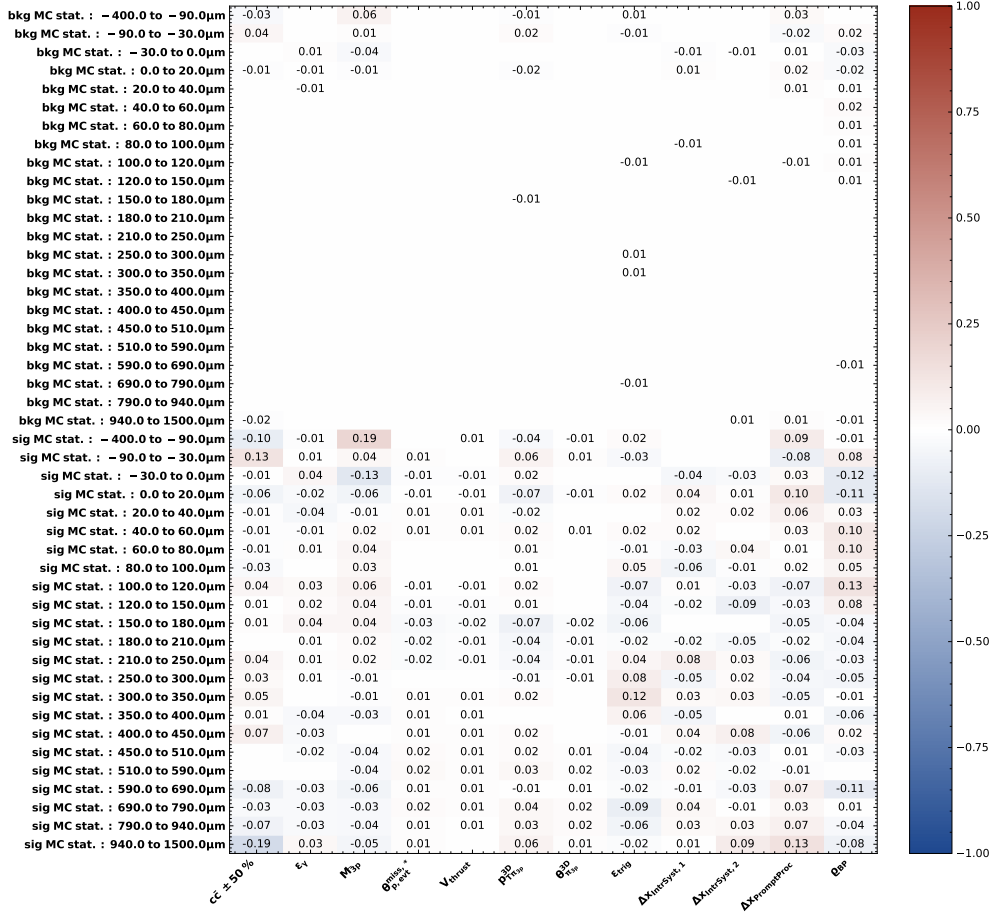


Figure A.15.: Correlation matrix of the MC stat. NPs with the shape uncertainty NPs of the pruned pseudo data fit for the $+0.01\text{fs}$ template.

A.10. Pseudo Data Fit Pulls

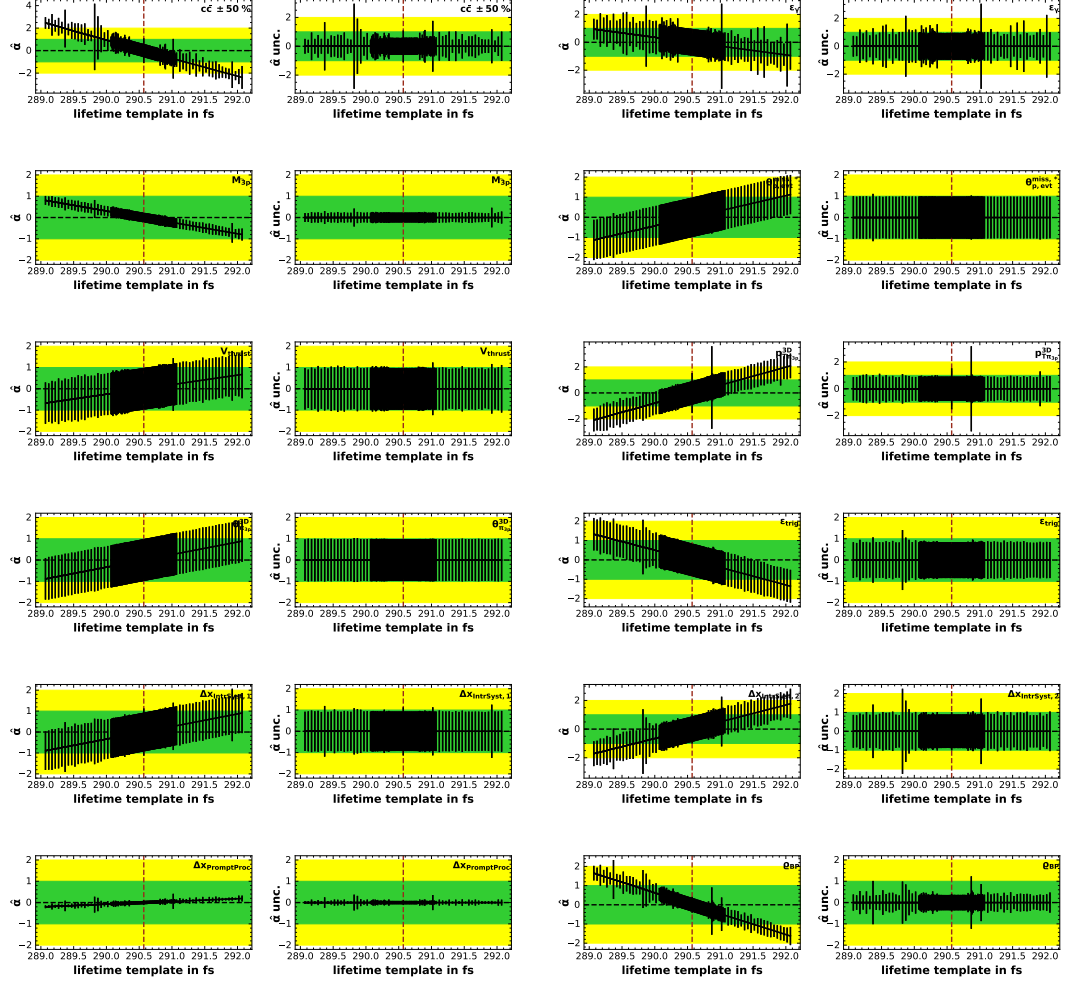


Figure A.16.: Post fit pull plots for the nominal template pseudo data Likelihood scan with the pruned NPs. Red dashed line indicates the nominal template. Two columns are always associated. The left of the two columns always show the parametrized post fit NP values with their fit uncertainties, and the right columns always show only the parametrized fit uncertainties of the post fit values for better comparison within the single template fits.

A.11. Mechanical Issues Observed with PXD2

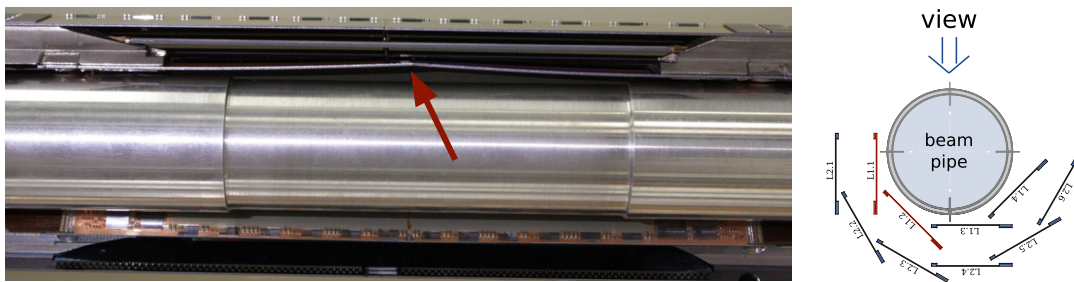


Figure A.17.: Kinked L1 ladders (red arrow, red ladders) due to thermal stress.

A.12. Multi-Parameter Source Scan Results

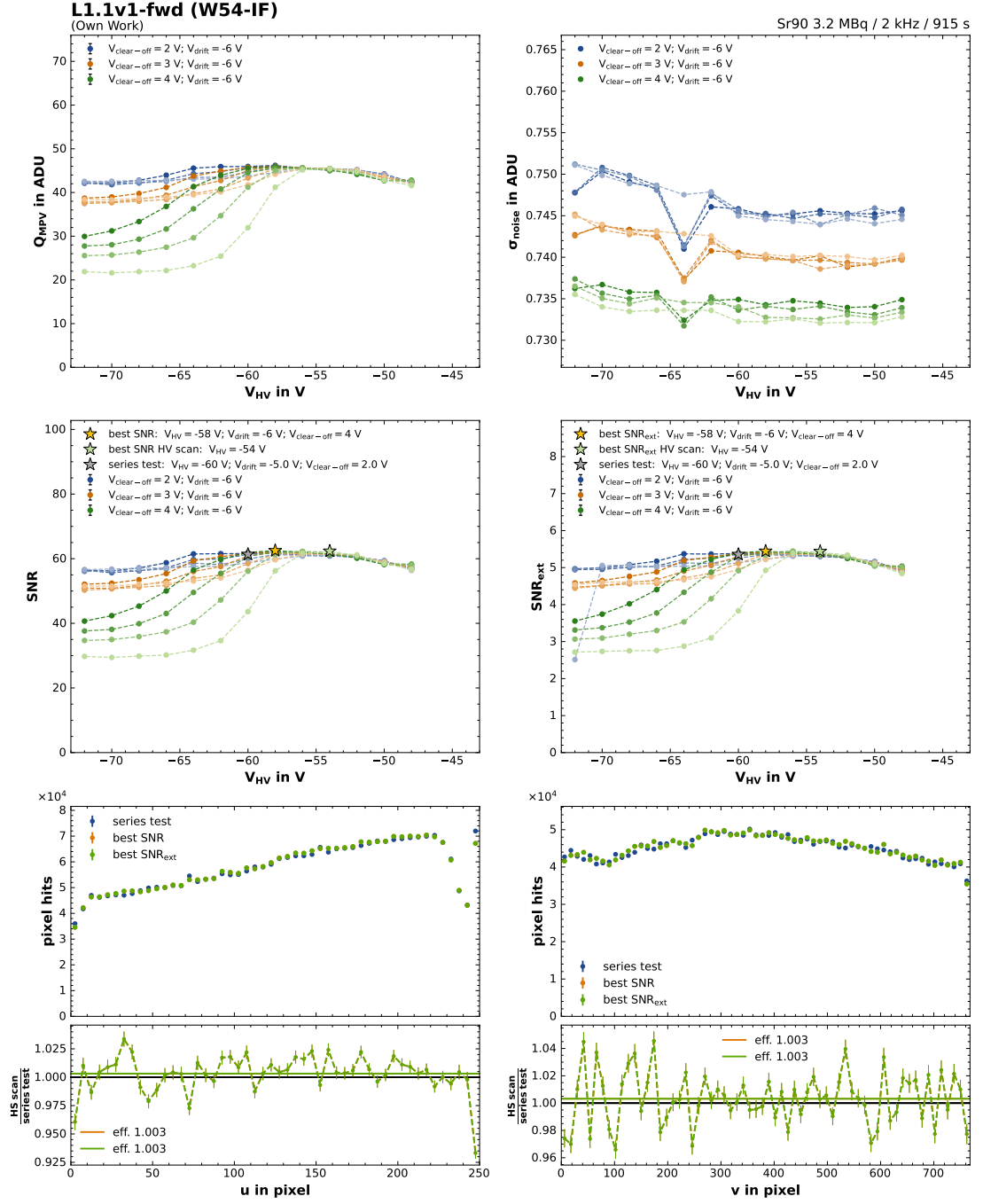


Figure A.18.: 3D source scan results for module L1.1v1-fwd (W54-IF). The different color intensities show a change in V_{drift} from the labeled dark (-6 V) to light (-3 V) in 1 V steps.

A. Appendix

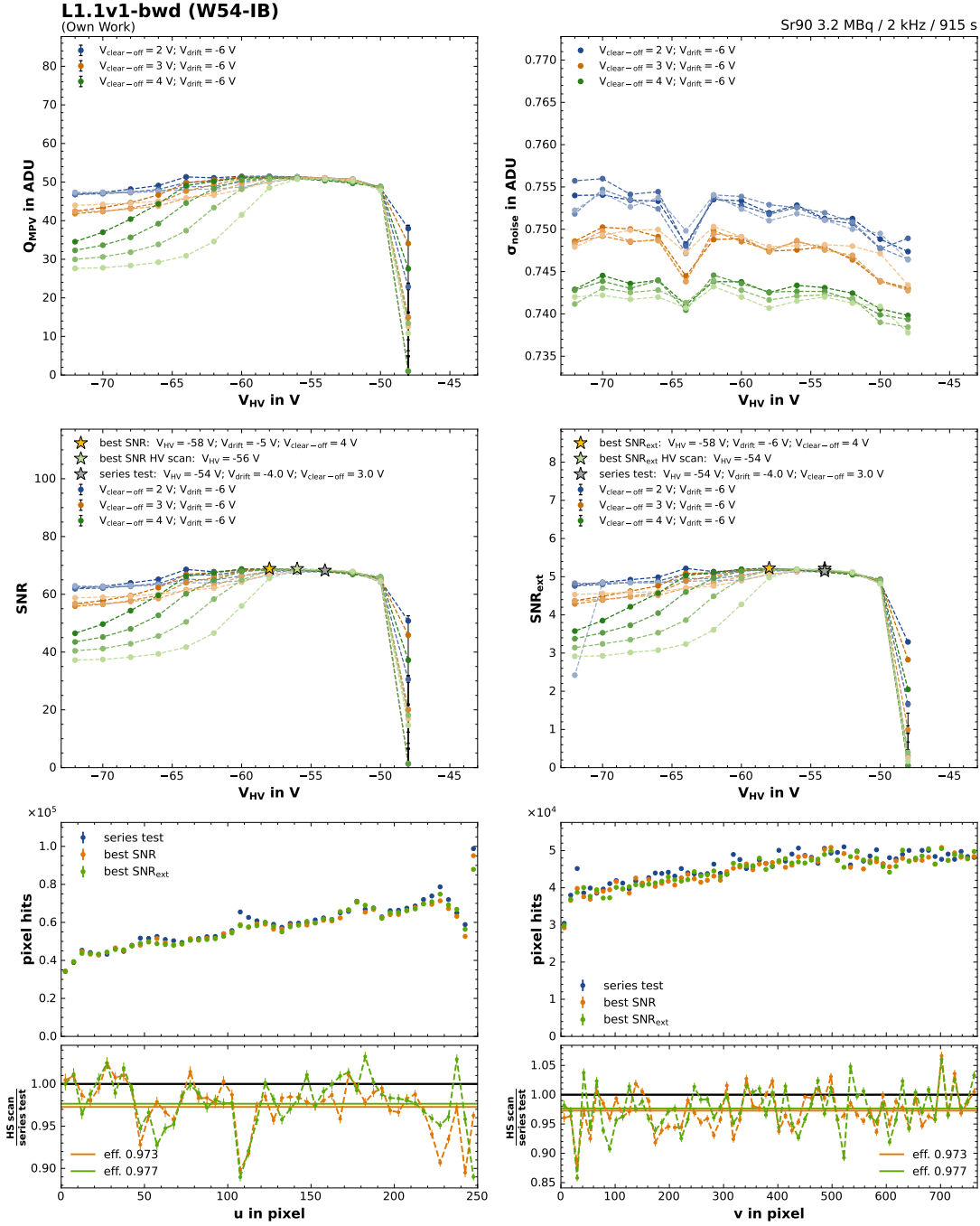


Figure A.19.: 3D source scan results for module L1.1v1-bwd (W54-IB). The different color intensities show a change in V_{drift} from the labeled dark (-6 V) to light (-3 V) in 1 V steps.

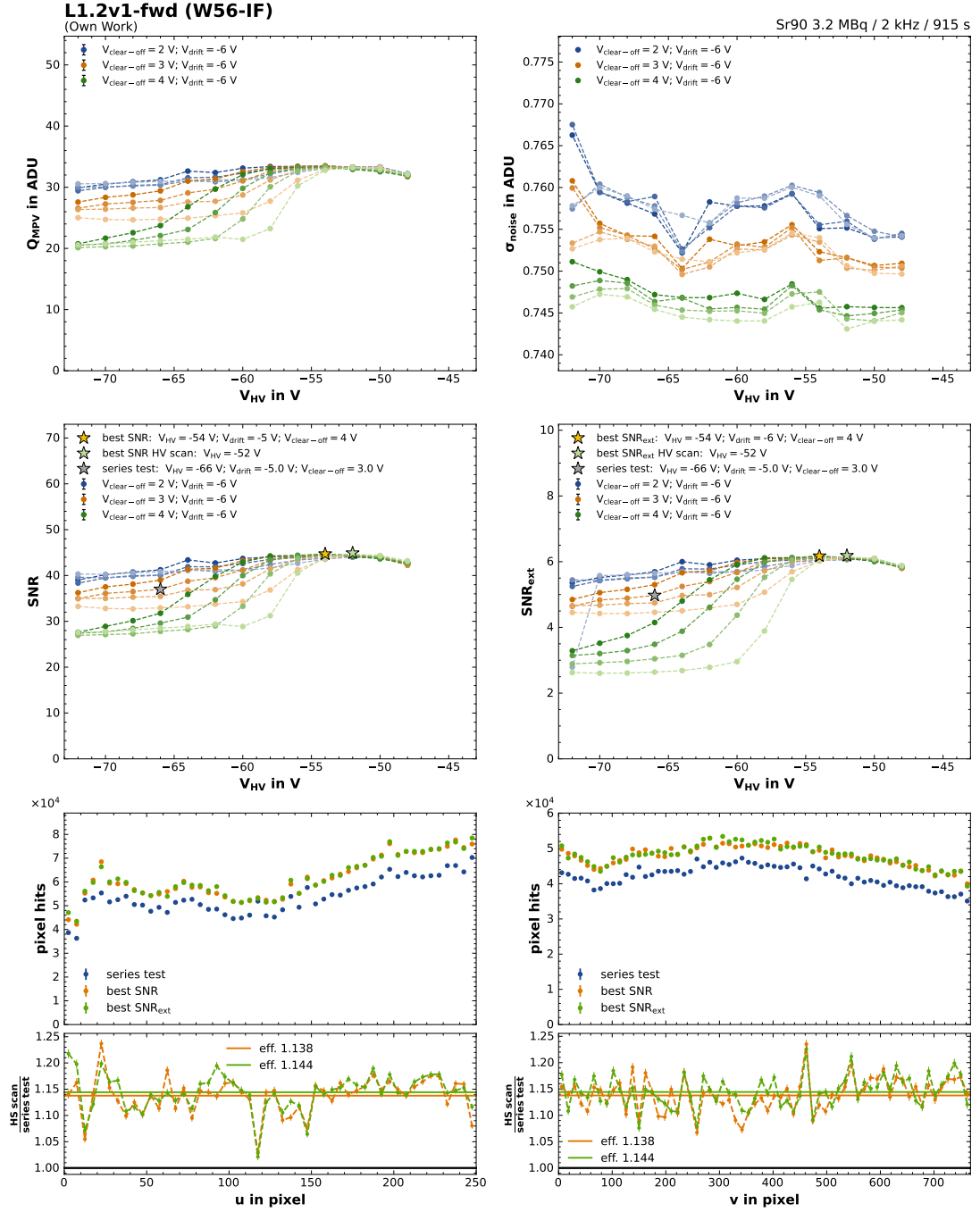


Figure A.20.: 3D source scan results for module L1.2v1-fwd (W56-IF). The different color intensities show a change in V_{drift} from the labeled dark (-6 V) to light (-3 V) in 1 V steps.

A. Appendix

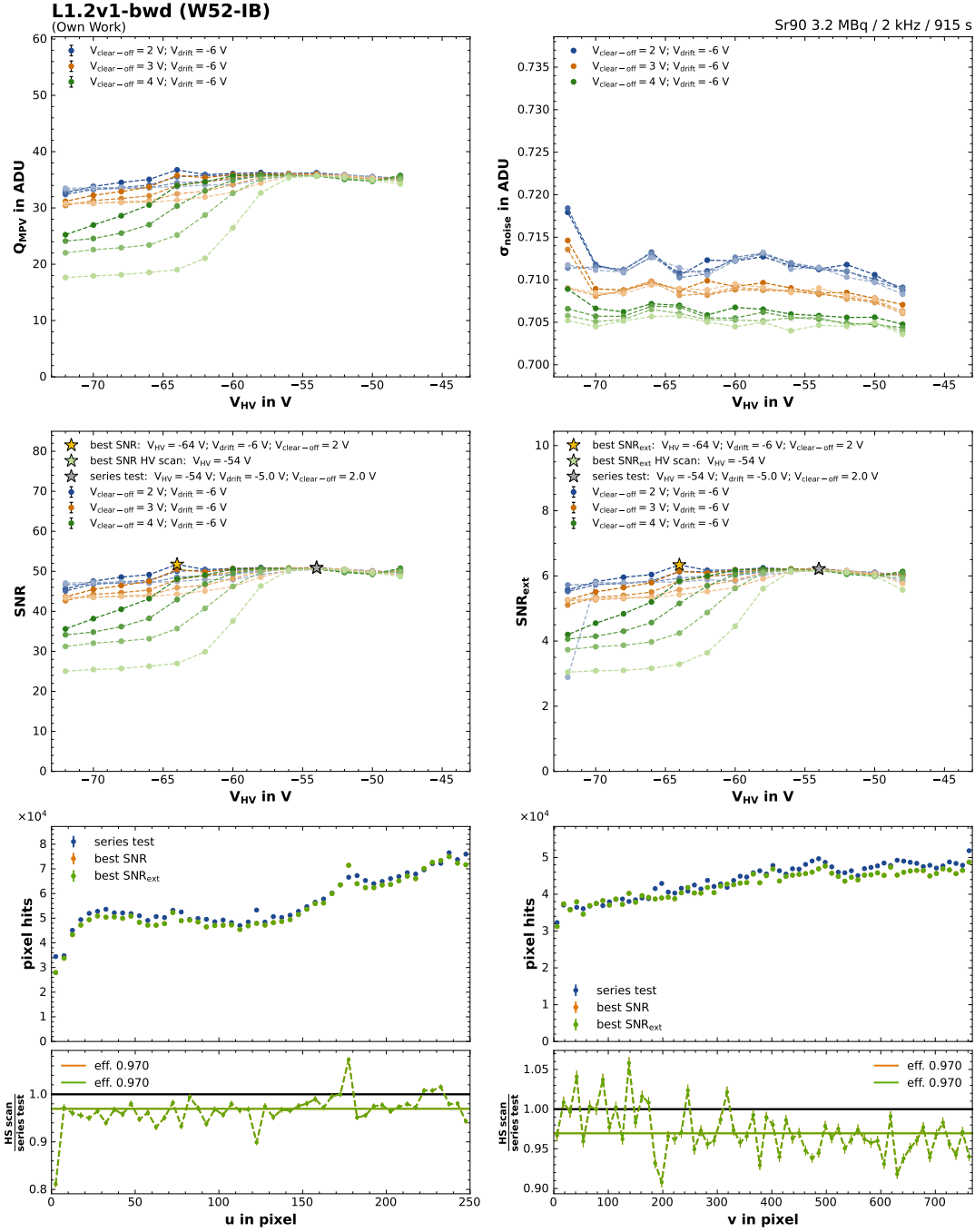


Figure A.21.: 3D source scan results for module L1.2v1-bwd (W52-IB). The different color intensities show a change in V_{drift} from the labeled dark (-6 V) to light (-3 V) in 1 V steps.

A.12. Multi-Parameter Source Scan Results

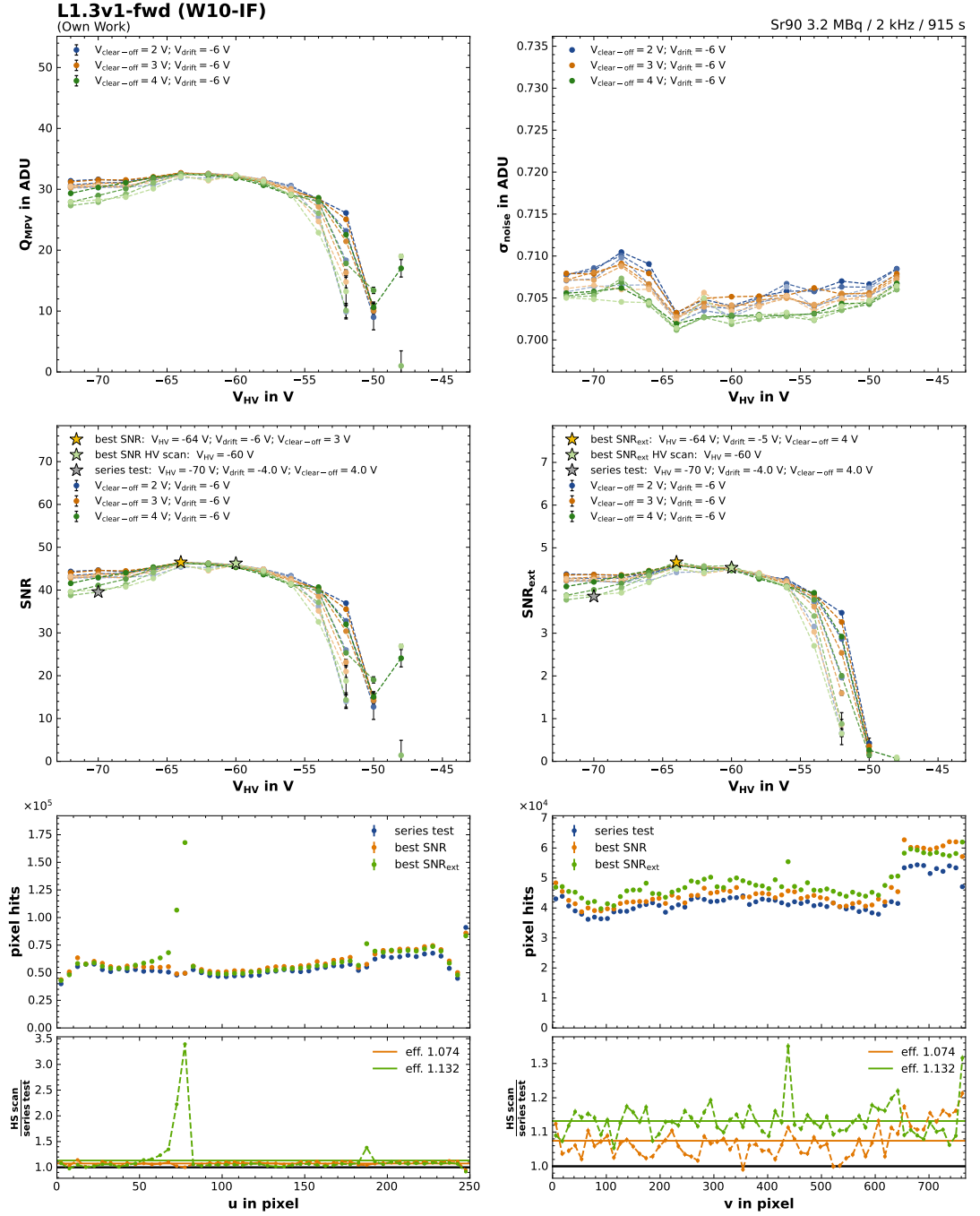


Figure A.22.: 3D source scan results for module L1.3v1-fwd (W10-IF). The different color intensities show a change in V_{drift} from the labeled dark (-6 V) to light (-3 V) in 1 V steps.

A. Appendix

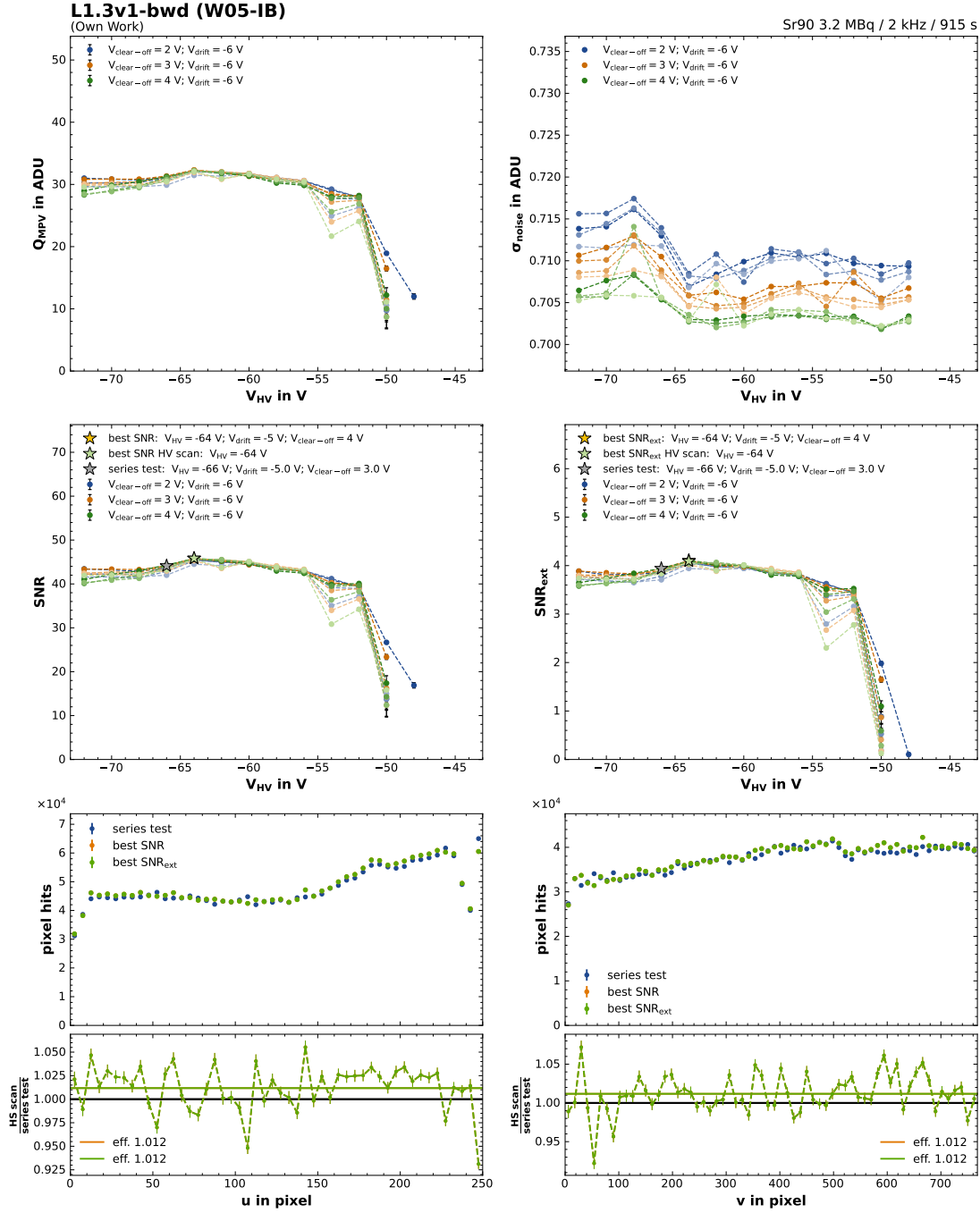


Figure A.23.: 3D source scan results for module L1.3v1-bwd (W05-IB). The different color intensities show a change in V_{drift} from the labeled dark (-6 V) to light (-3 V) in 1 V steps.

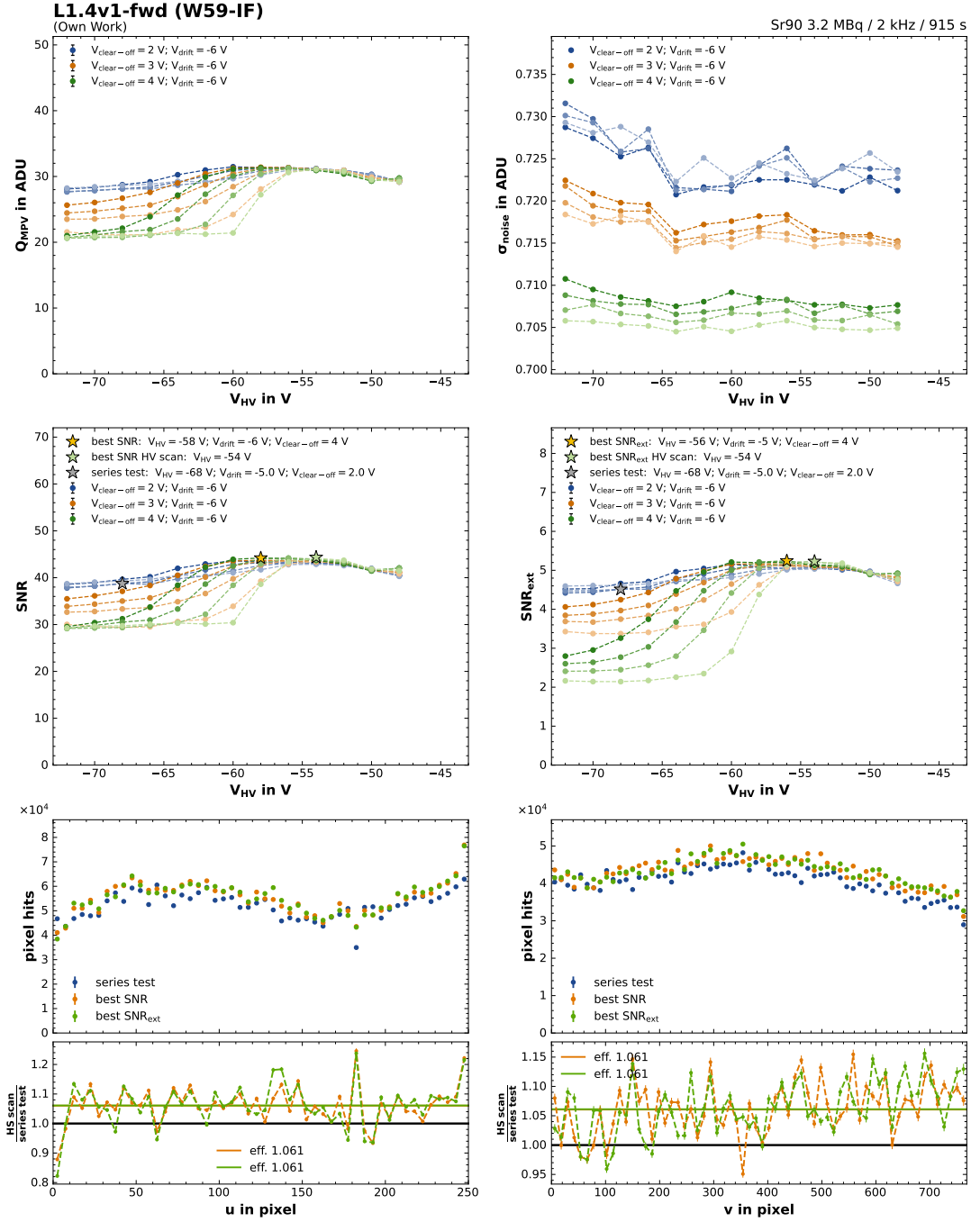


Figure A.24.: 3D source scan results for module L1.4v1-fwd (W59-IF). The different color intensities show a change in V_{drift} from the labeled dark (-6 V) to light (-3 V) in 1 V steps.

A. Appendix

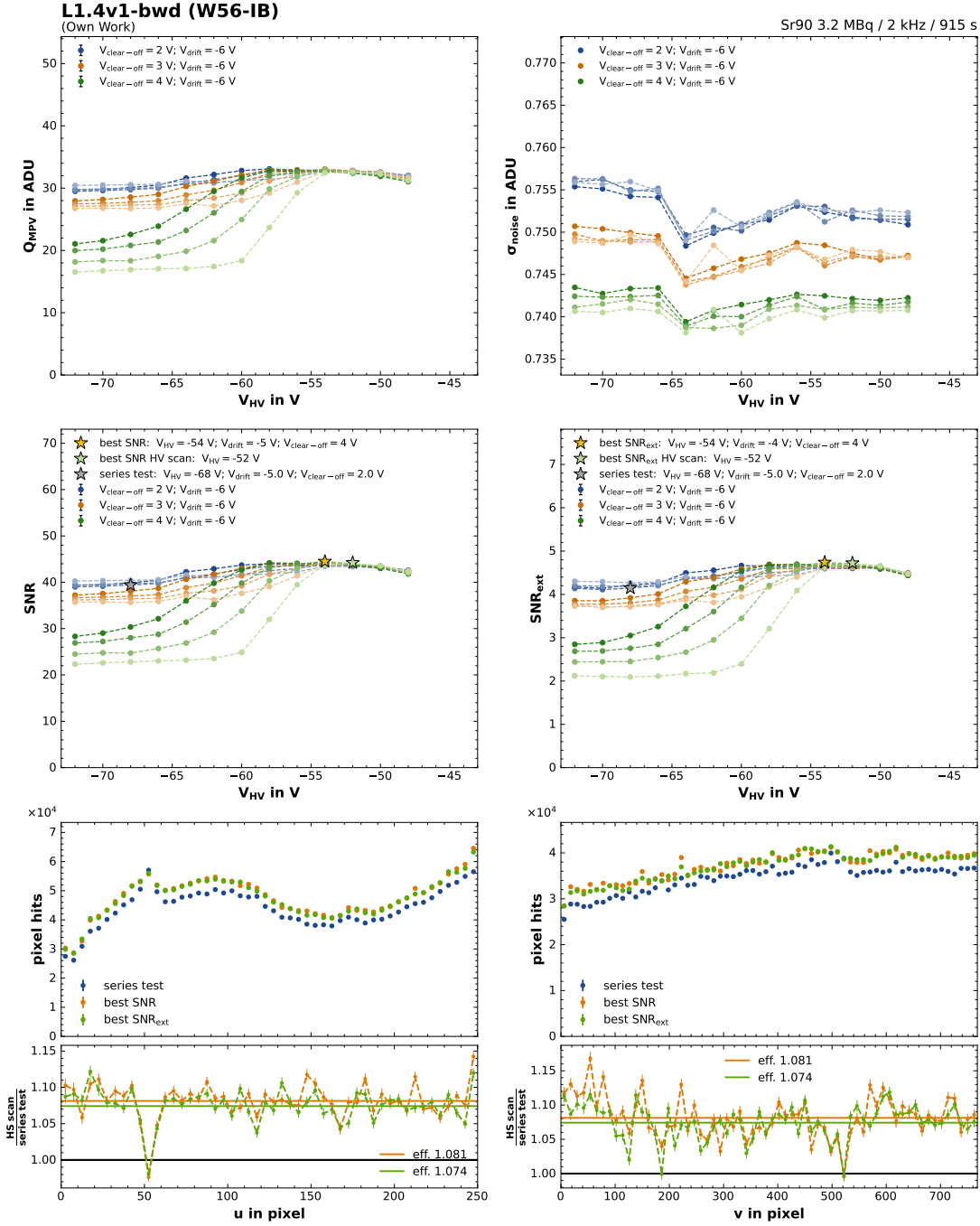


Figure A.25.: 3D source scan results for module L1.4v1-bwd (W56-IB). The different color intensities show a change in V_{drift} from the labeled dark (-6 V) to light (-3 V) in 1 V steps.

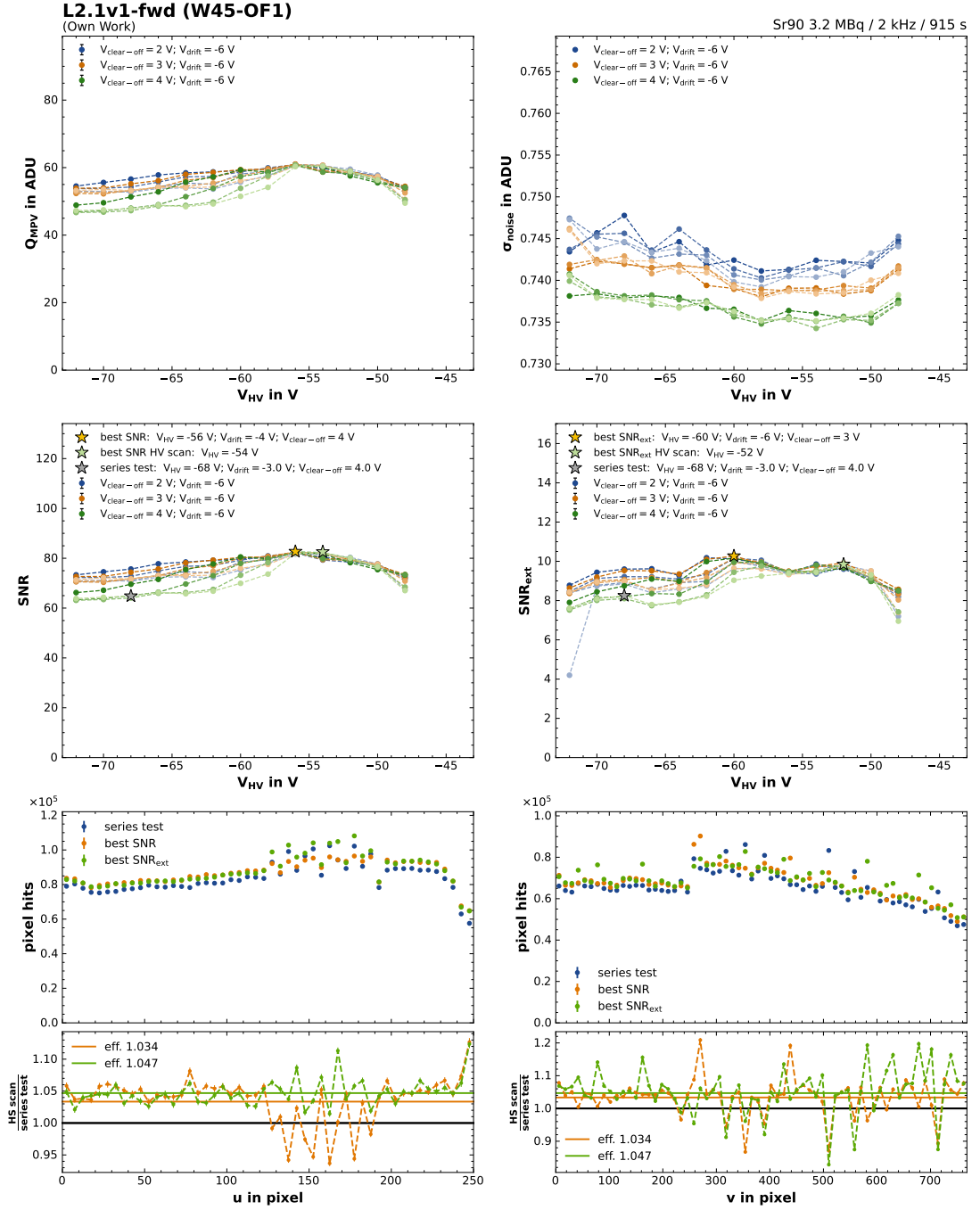


Figure A.26.: 3D source scan results for module L2.1v1-fwd (W45-OF1). The different color intensities show a change in V_{drift} from the labeled dark (-6 V) to light (-3 V) in 1 V steps.

A. Appendix

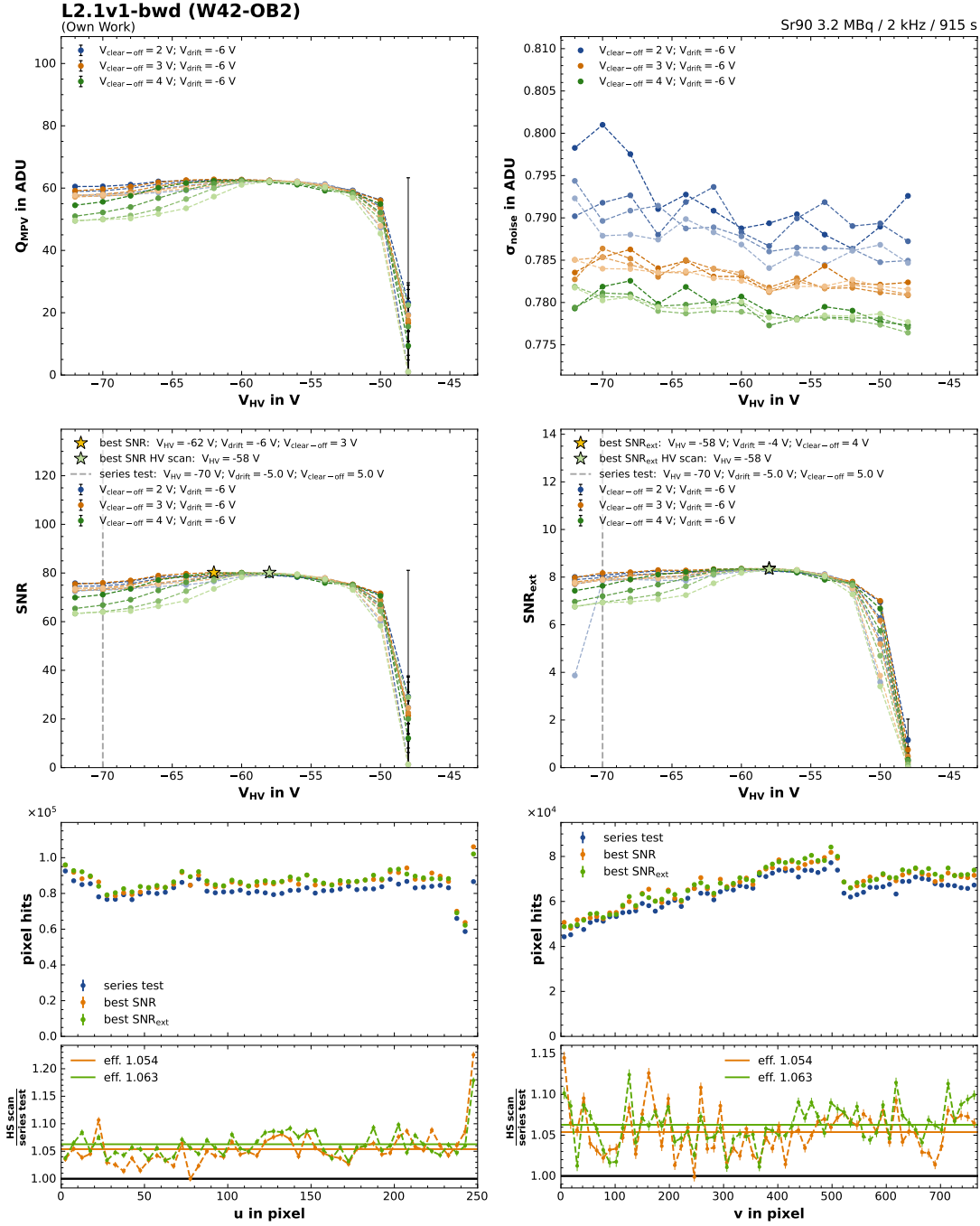


Figure A.27.: 3D source scan results for module L2.1v1-bwd (W42-OB2). The different color intensities show a change in V_{drift} from the labeled dark (-6 V) to light (-3 V) in 1 V steps.

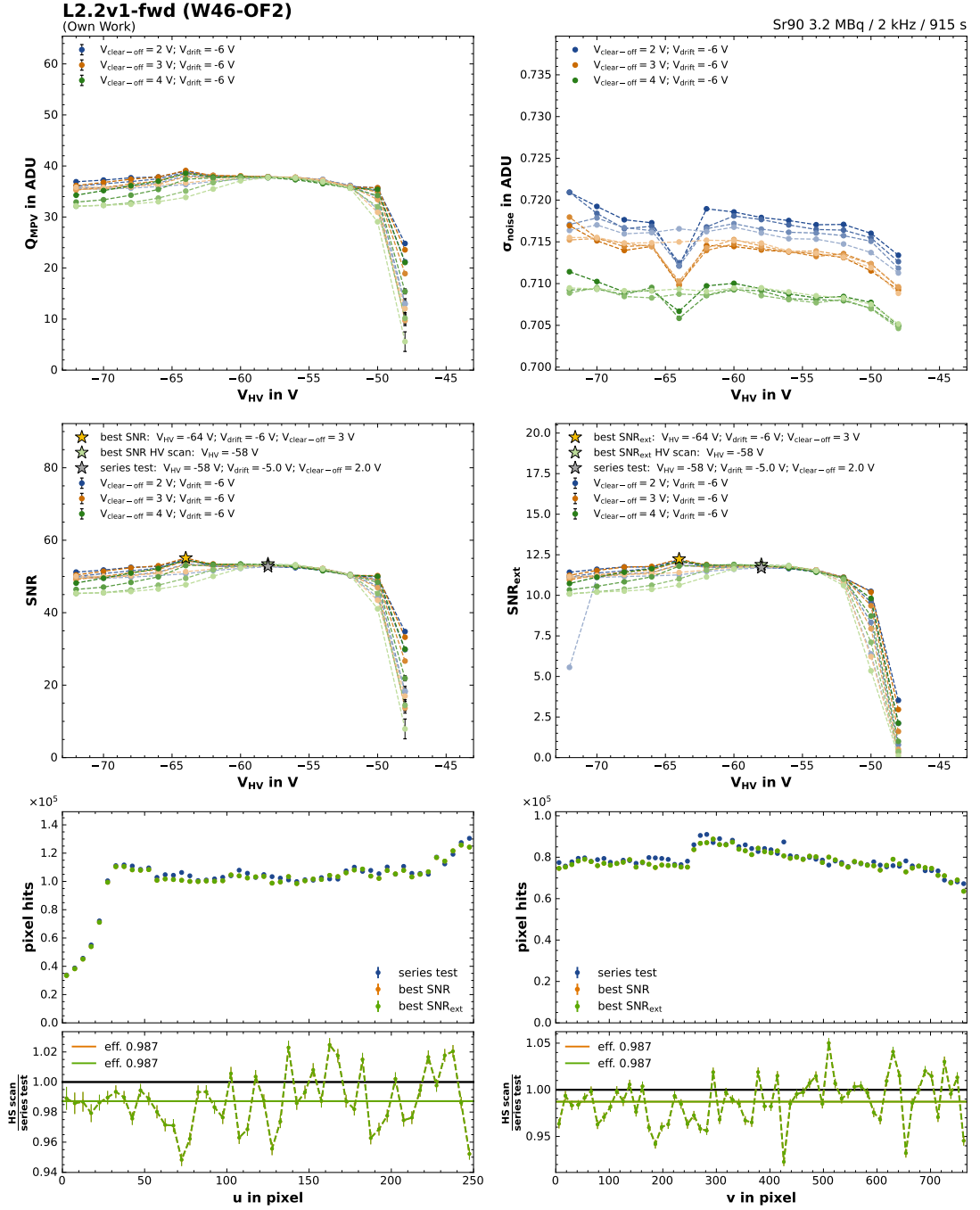


Figure A.28.: 3D source scan results for module L2.2v1-fwd (W46-OF2). The different color intensities show a change in V_{drift} from the labeled dark (-6 V) to light (-3 V) in 1 V steps.

A. Appendix

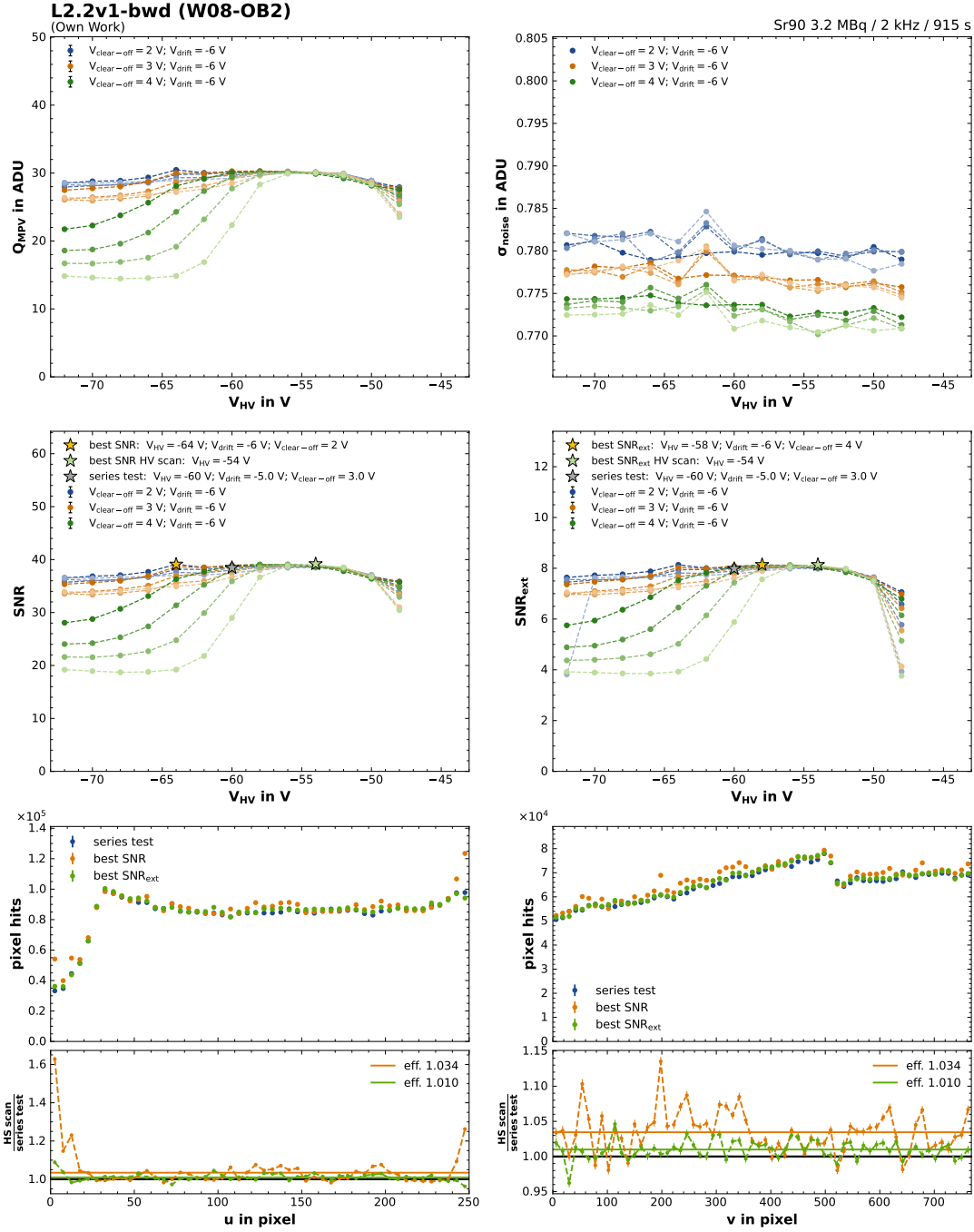


Figure A.29.: 3D source scan results for module L2.2v1-bwd (W08-OB2). The different color intensities show a change in V_{drift} from the labeled dark (-6 V) to light (-3 V) in 1 V steps.

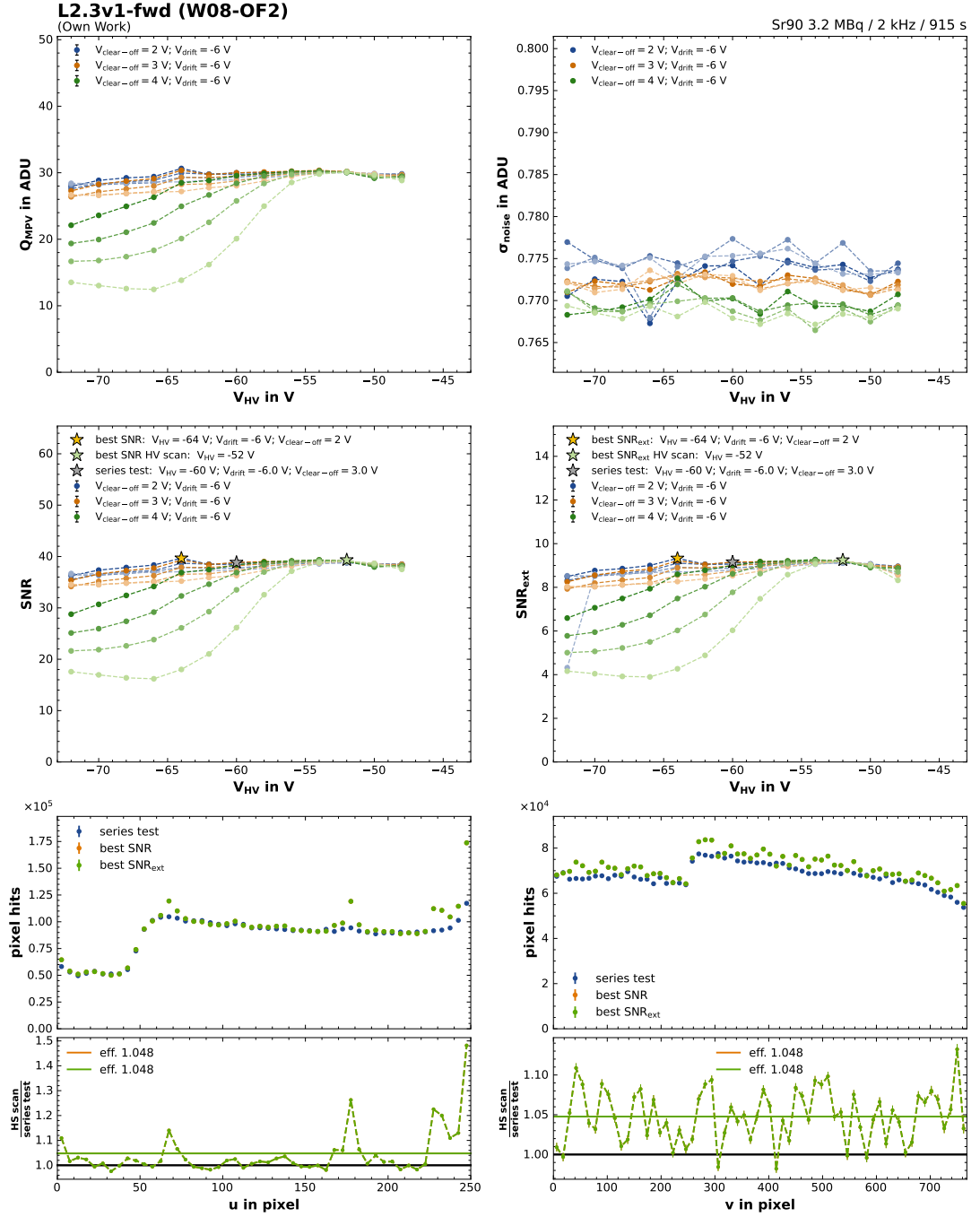


Figure A.30.: 3D source scan results for module L2.3v1-fwd (W08-OF2). The different color intensities show a change in V_{drift} from the labeled dark (-6 V) to light (-3 V) in 1 V steps.

A. Appendix

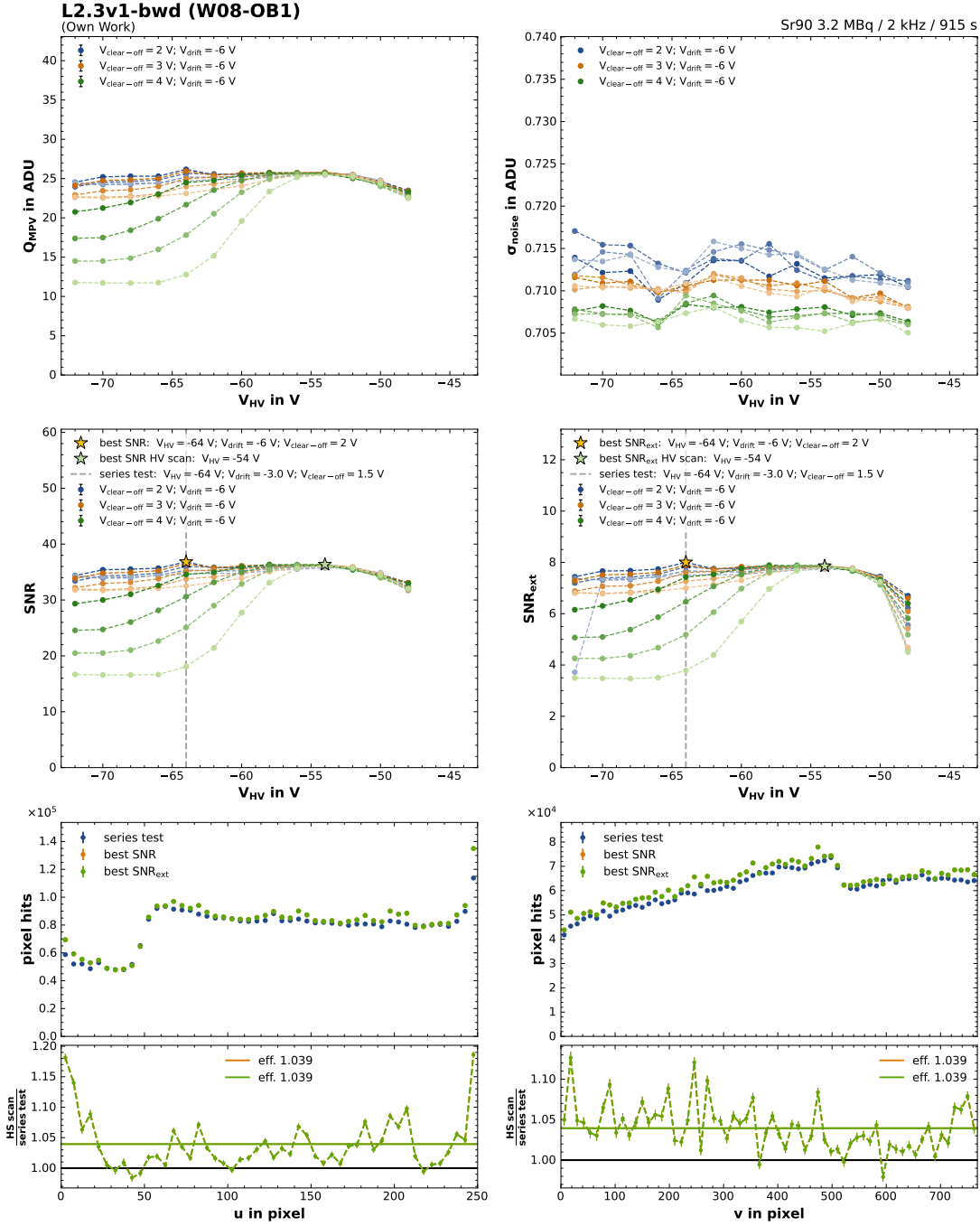


Figure A.31.: 3D source scan results for module L2.3v1-bwd (W08-OB1). The different color intensities show a change in V_{drift} from the labeled dark (-6 V) to light (-3 V) in 1 V steps.

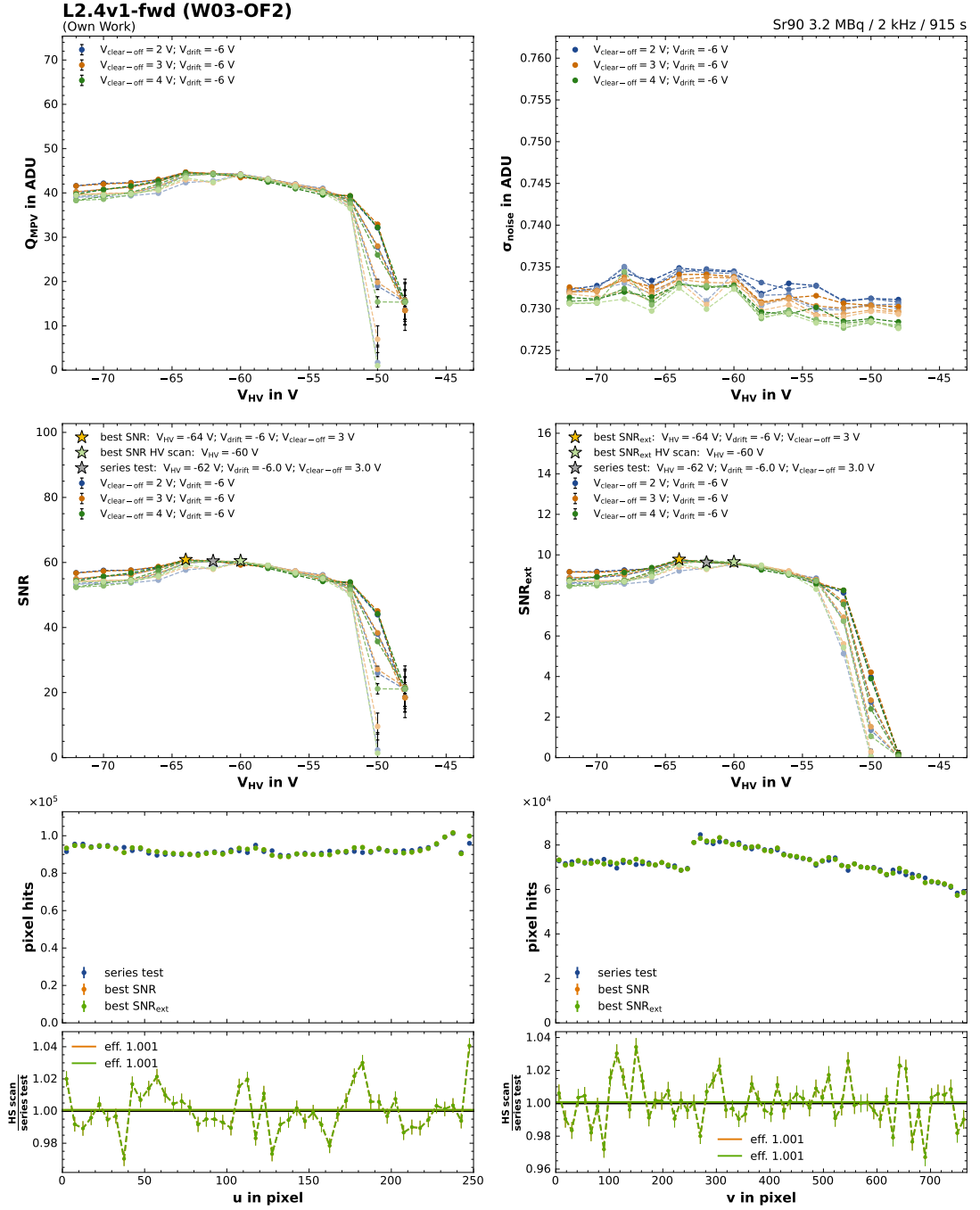


Figure A.32.: 3D source scan results for module L2.4v1-fwd (W03-OF2). The different color intensities show a change in V_{drift} from the labeled dark (-6 V) to light (-3 V) in 1 V steps.

A. Appendix

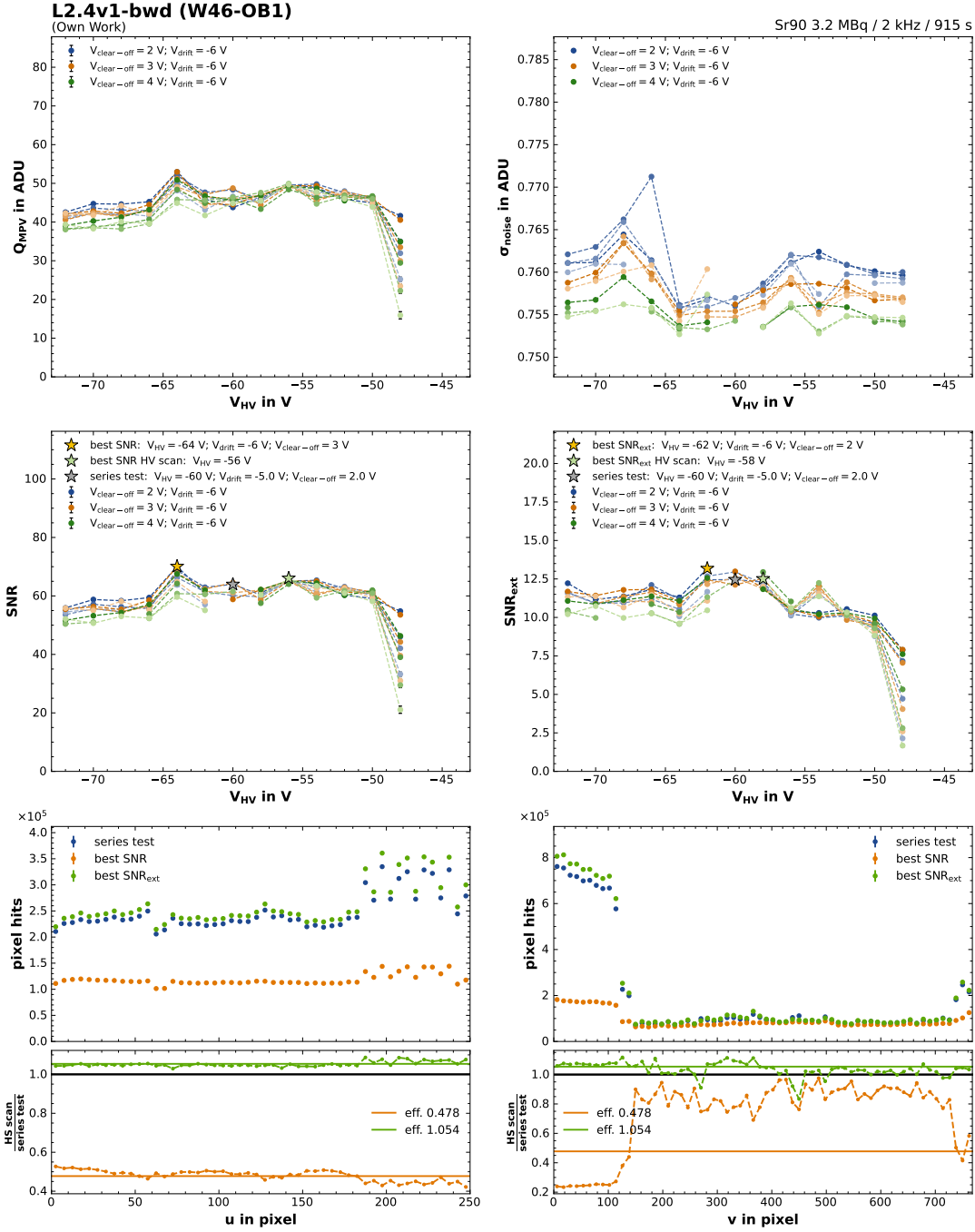


Figure A.33.: 3D source scan results for module L2.4v1-bwd (W46-OB1). The different color intensities show a change in V_{drift} from the labeled dark (-6 V) to light (-3 V) in 1 V steps.

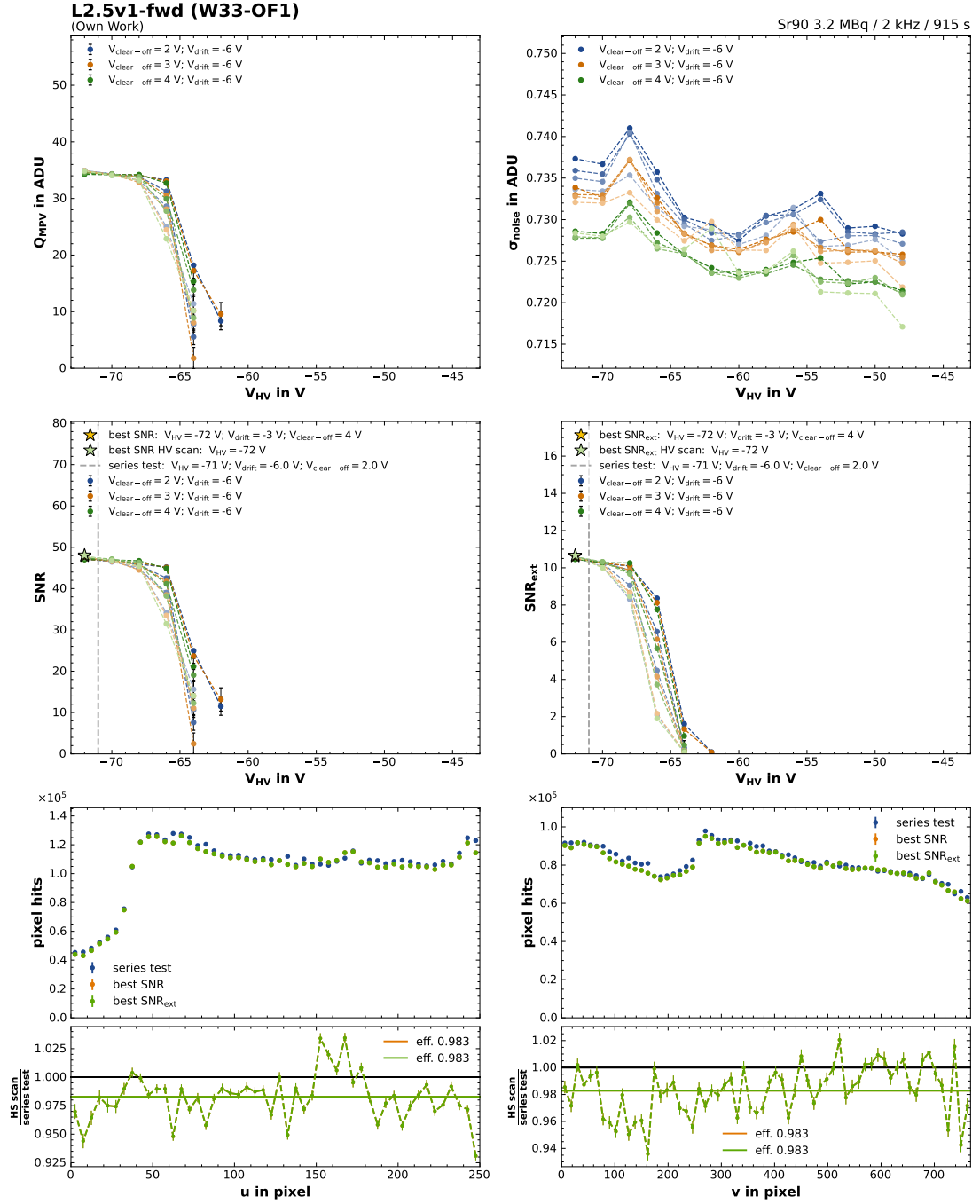


Figure A.34.: 3D source scan results for module L2.5v1-fwd (W33-OF1). The different color intensities show a change in V_{drift} from the labeled dark (-6 V) to light (-3 V) in 1 V steps.

A. Appendix

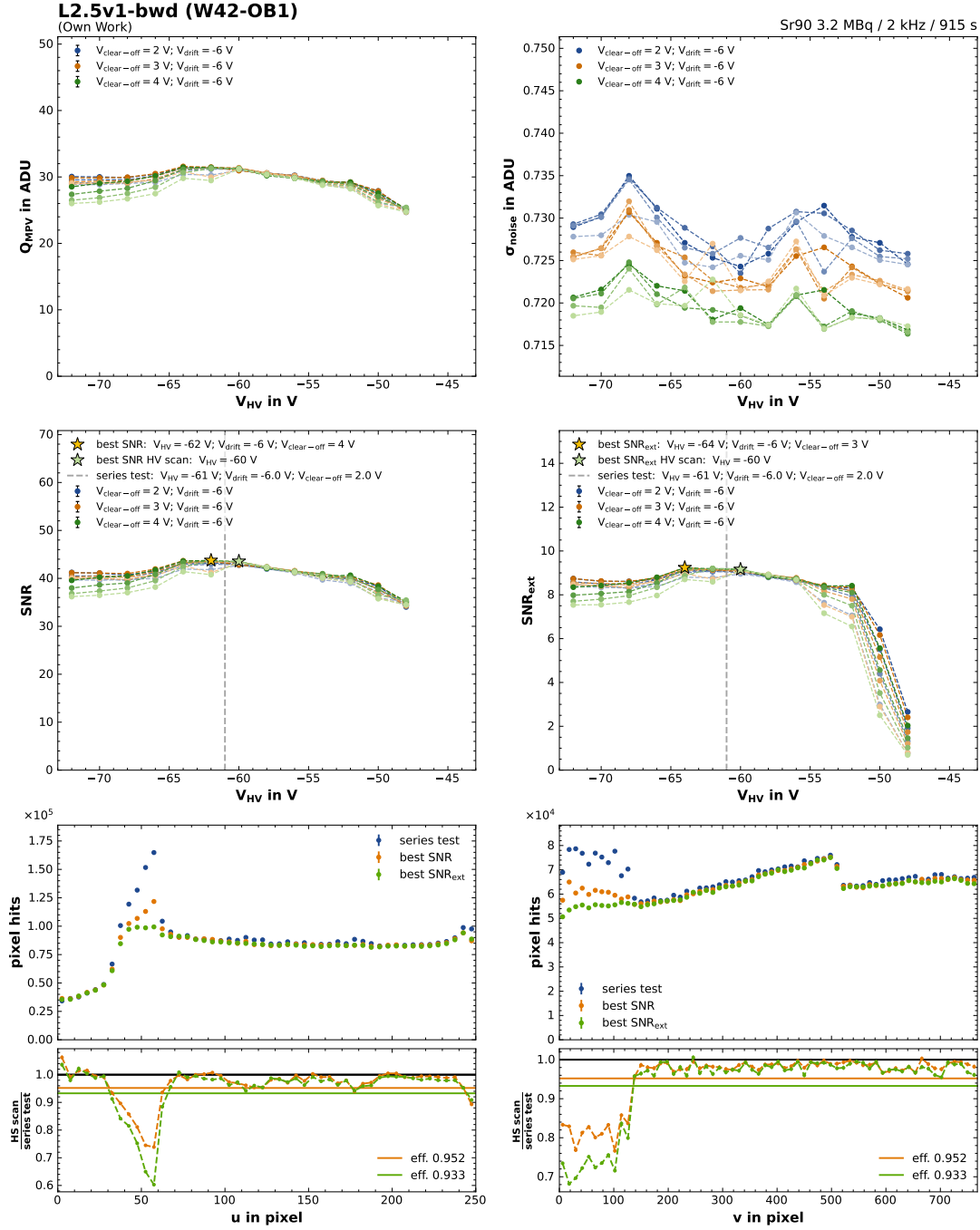


Figure A.35.: 3D source scan results for module L2.5v1-bwd (H2052, W42-OB1). The different color intensities show a change in V_{drift} from the labeled dark (-6 V) to light (-3 V) in 1 V steps.

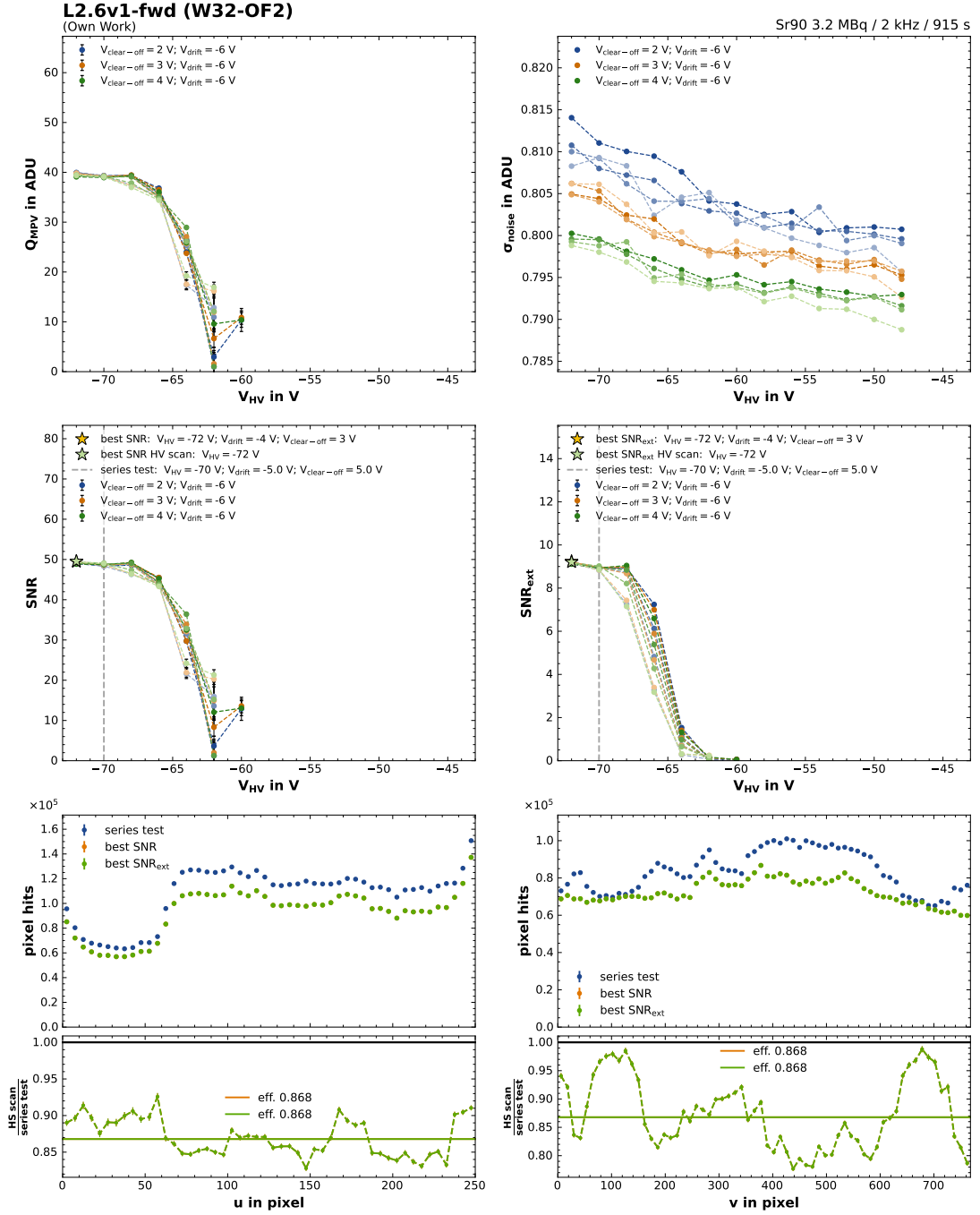


Figure A.36.: 3D source scan results for module L2.6v1-fwd (W32-OF2). The different color intensities show a change in V_{drift} from the labeled dark (-6 V) to light (-3 V) in 1 V steps.

A. Appendix

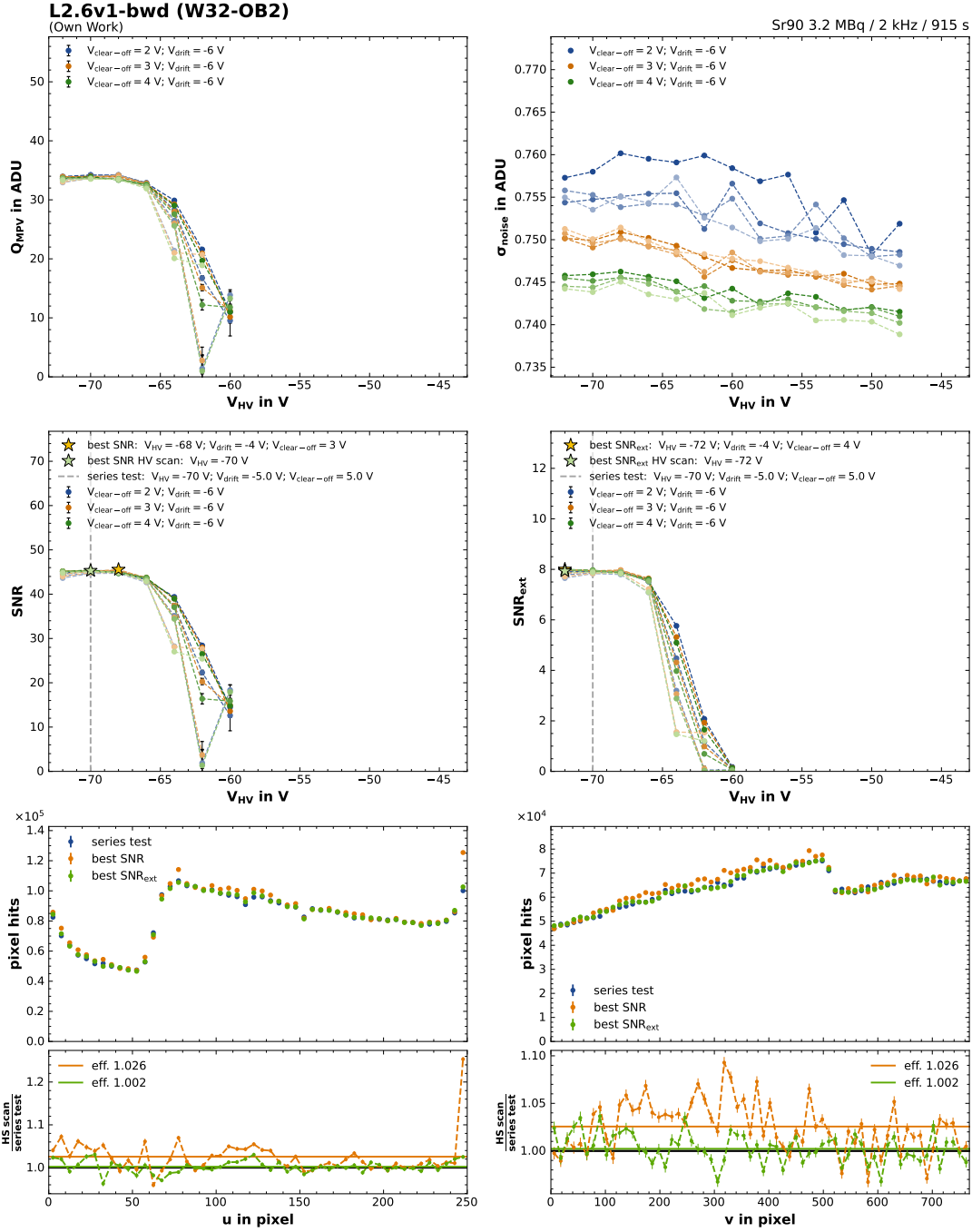


Figure A.37.: 3D source scan results for module L2.6v1-bwd (W32-OB2). The different color intensities show a change in V_{drift} from the labeled dark (-6 V) to light (-3 V) in 1 V steps.

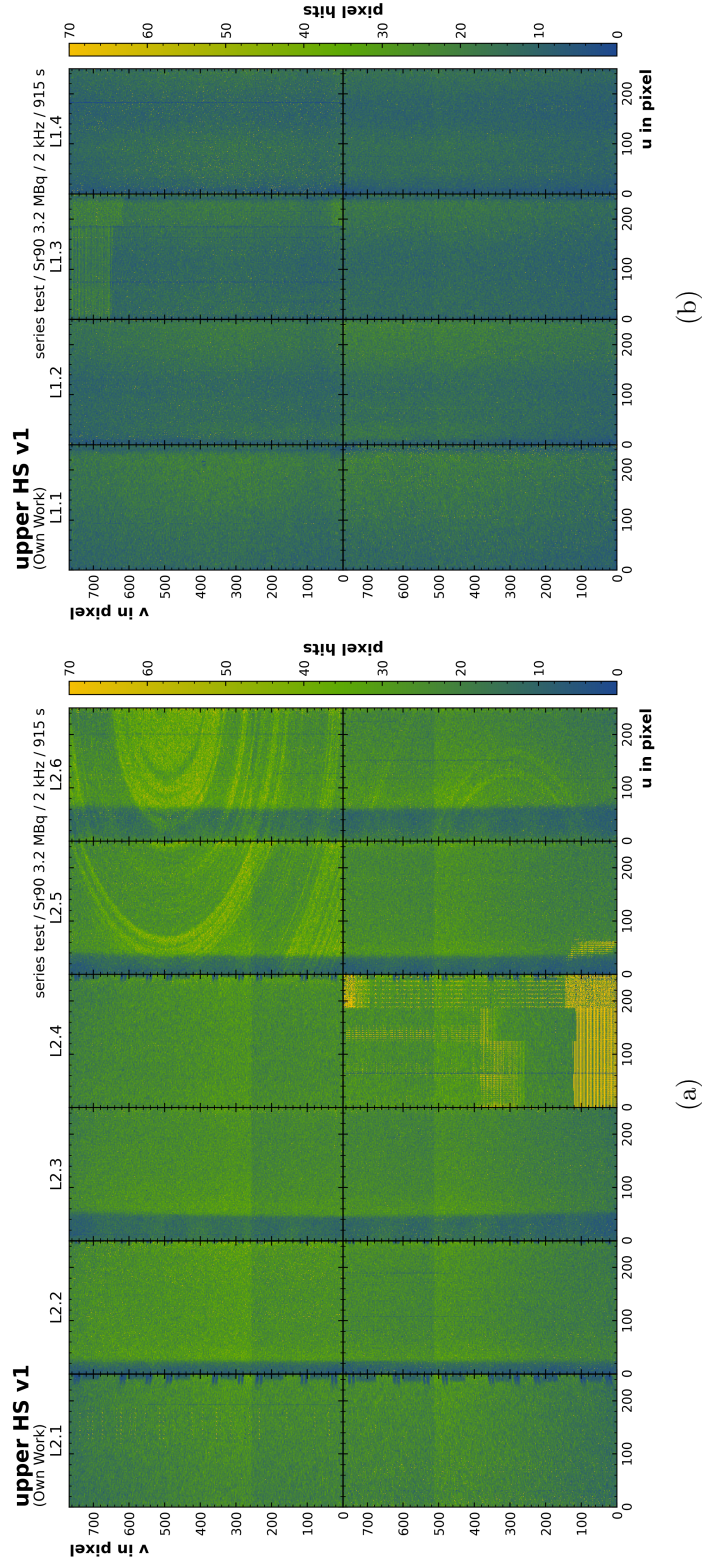


Figure A.38.: Hitmaps for the upper HS v1 modules with the DEPFET voltage configurations optimized during series testing. For module L2.1-bwd, L2.3-bwd, L2.5-fwd, L2.6-fwd, and L2.6-bwd either slightly different V_{HV} or $V_{clear-off}$ configurations were selected (max. ± 1 V) for the plotting, which were covered by a measurement point of the HS multi-parameter source scan. (a) L2, (b) L1.

A.13. HV Scan Results

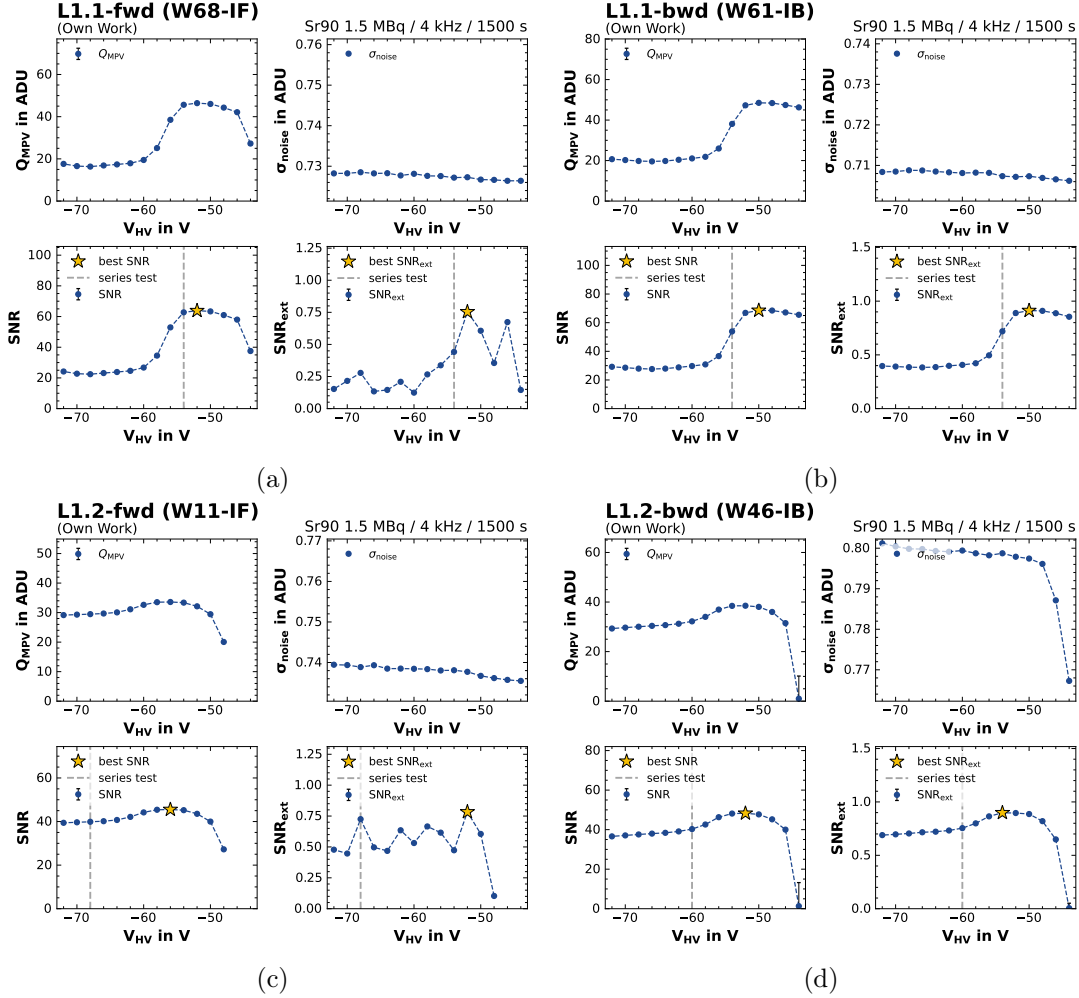


Figure A.39.: HV scan results for $V_{drift} = -3$ V and $V_{clear-off} = 4$ V showing the Q_{MPV} , σ_{noise} , SNR and SNR_{ext} distributions for modules: (a) L1.1-fwd (W68-IF), (b) L1.1-bwd (W61-IB), (c) L1.2-fwd (W11-IF), and (d) L1.2-bwd (W46-IB).

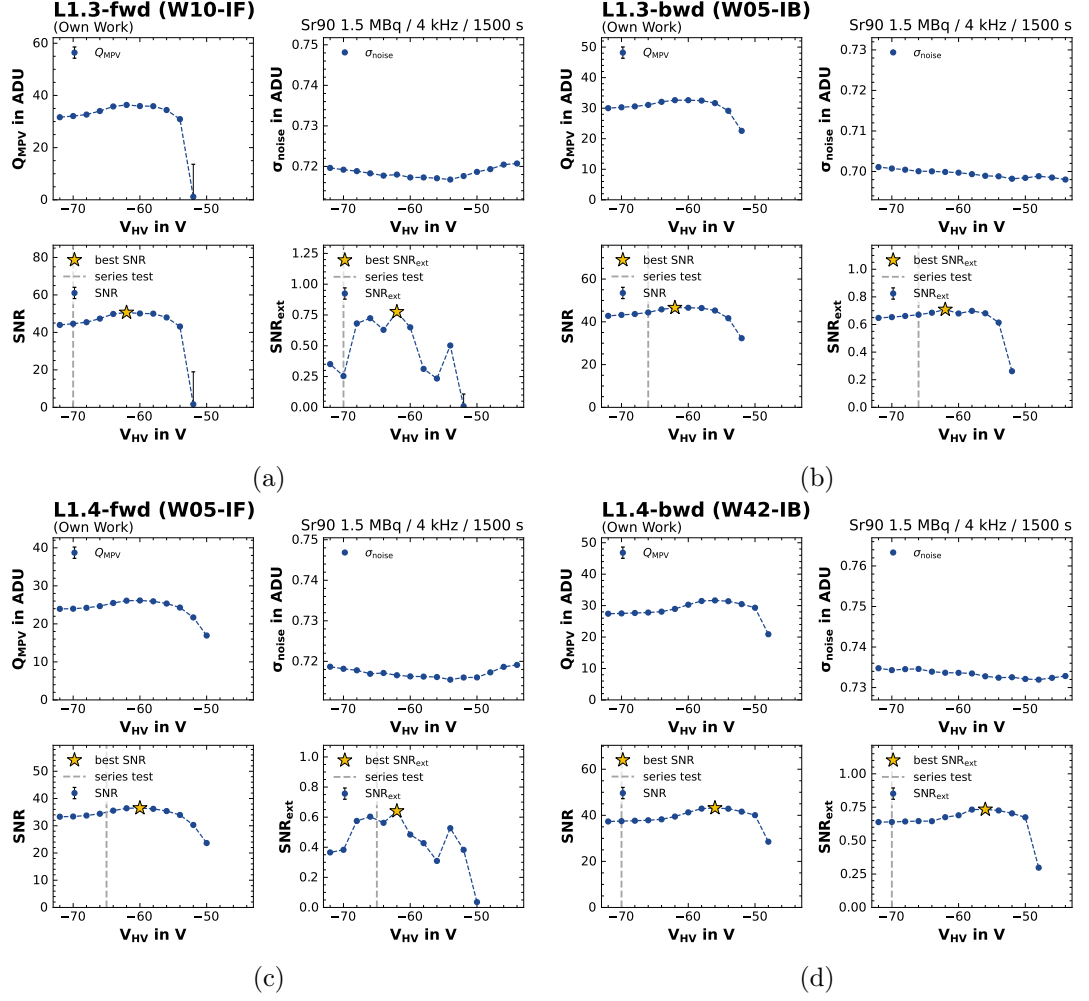


Figure A.40.: HV scan results for $V_{drift} = -3$ V and $V_{clear-off} = 4$ V showing the Q_{MPV} , σ_{noise} , SNR and SNR_{ext} distributions for modules: (a) L1.3-fwd (W10-IF), (b) L1.3-bwd (W05-IB), (c) L1.4-fwd (W05-IF), and (d) L1.4-bwd (W42-IB).

A. Appendix

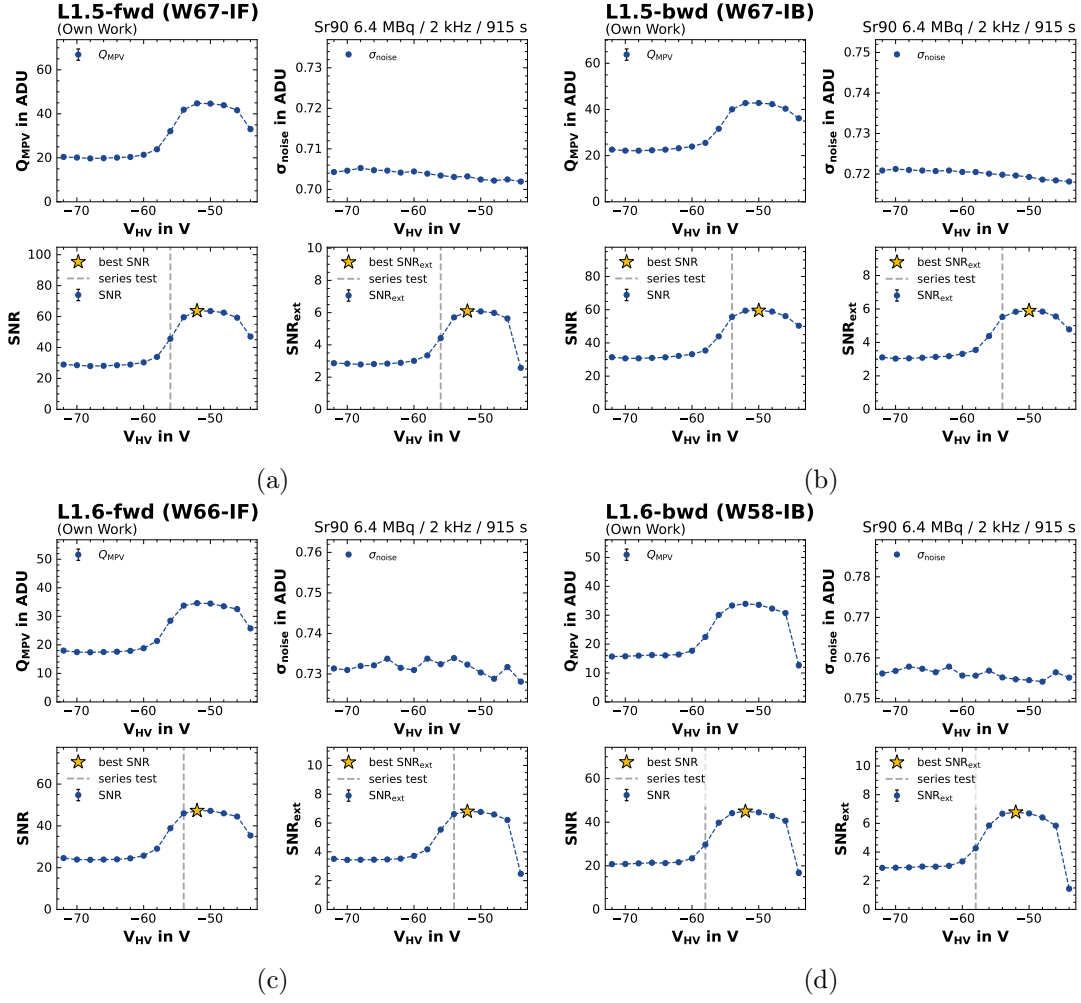


Figure A.41.: HV scan results for $V_{\text{drift}} = -3 \text{ V}$ and $V_{\text{clear-off}} = 4 \text{ V}$ showing the Q_{MPV} , σ_{noise} , SNR and SNR_{ext} distributions for modules: (a) L1.5-fwd (W67-IF), (b) L1.5-bwd (W67-IB), (c) L1.6-fwd (W66-IF), and (d) L1.6-bwd (W58-IB).

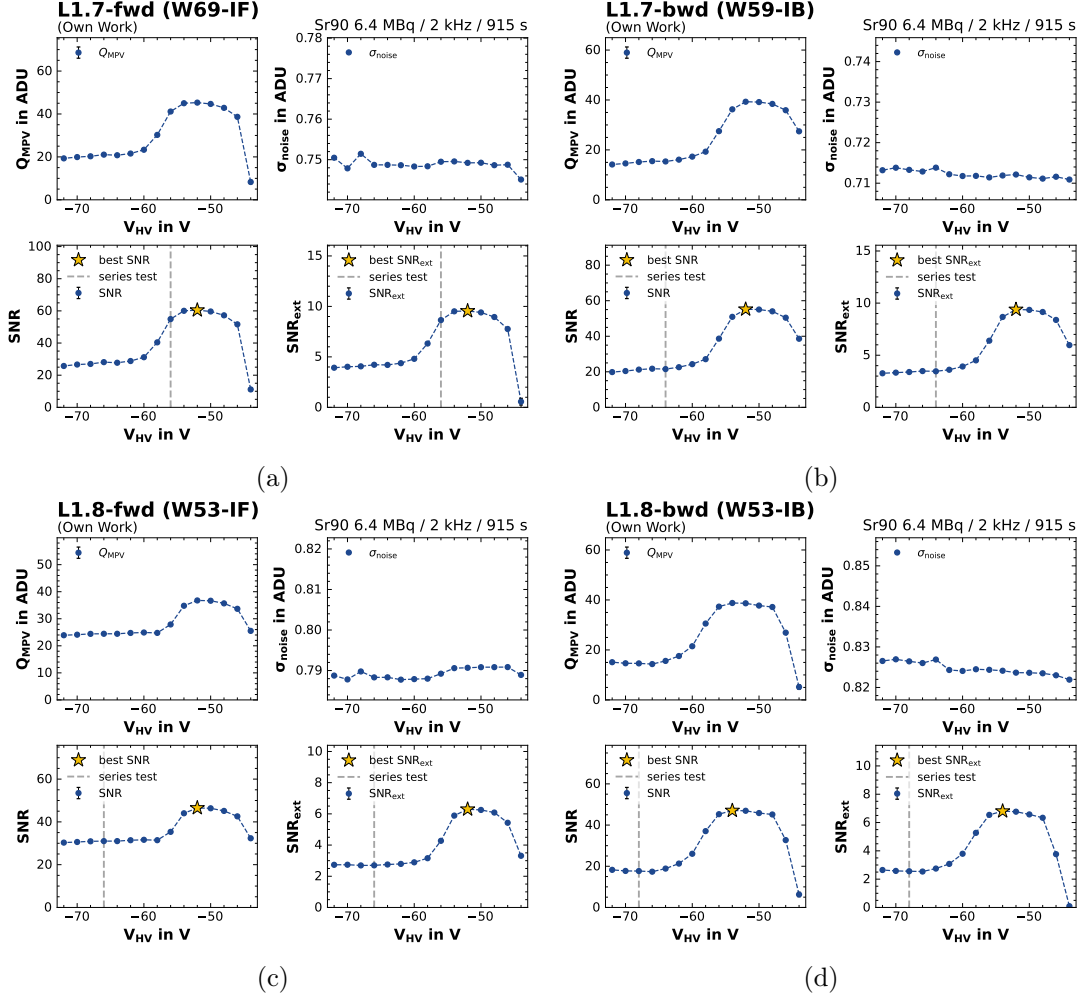


Figure A.42.: HV scan results for $V_{drift} = -3$ V and $V_{clear-off} = 4$ V showing the Q_{MPV} , σ_{noise} , SNR and SNR_{ext} distributions for modules: (a) L1.7-fwd (W69-IF), (b) L1.7-bwd (W59-IB), (c) L1.8-fwd (W53-IF), and (d) L1.8-bwd (W53-IB).

A. Appendix

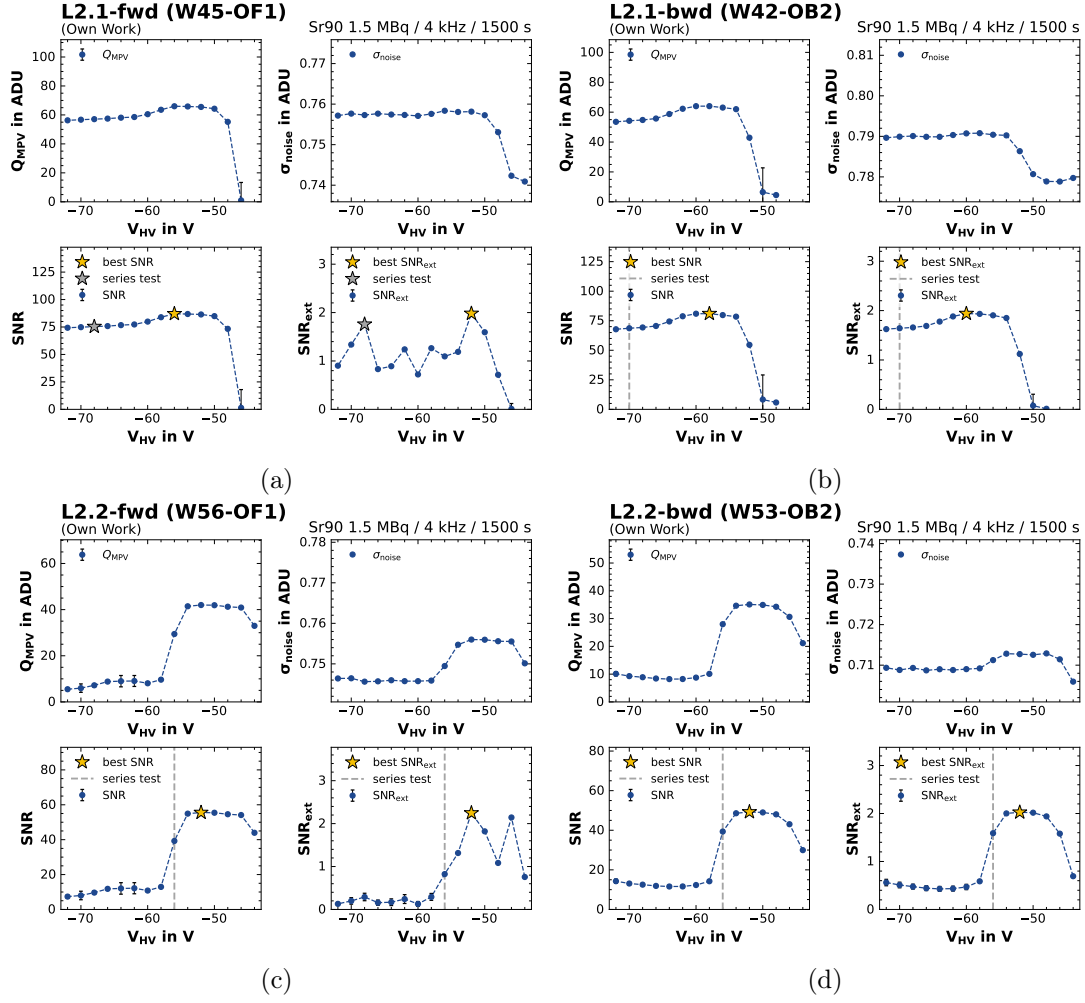


Figure A.43.: HV scan results for $V_{drift} = -3$ V and $V_{clear-off} = 4$ V showing the Q_{MPV} , σ_{noise} , SNR and SNR_{ext} distributions for modules: (a) L2.1-fwd (W45-OF1), (b) L2.1-bwd (W42-OB2), (c) L2.2-fwd (W56-OF1), and (d) L2.2-bwd (W53-OB2).

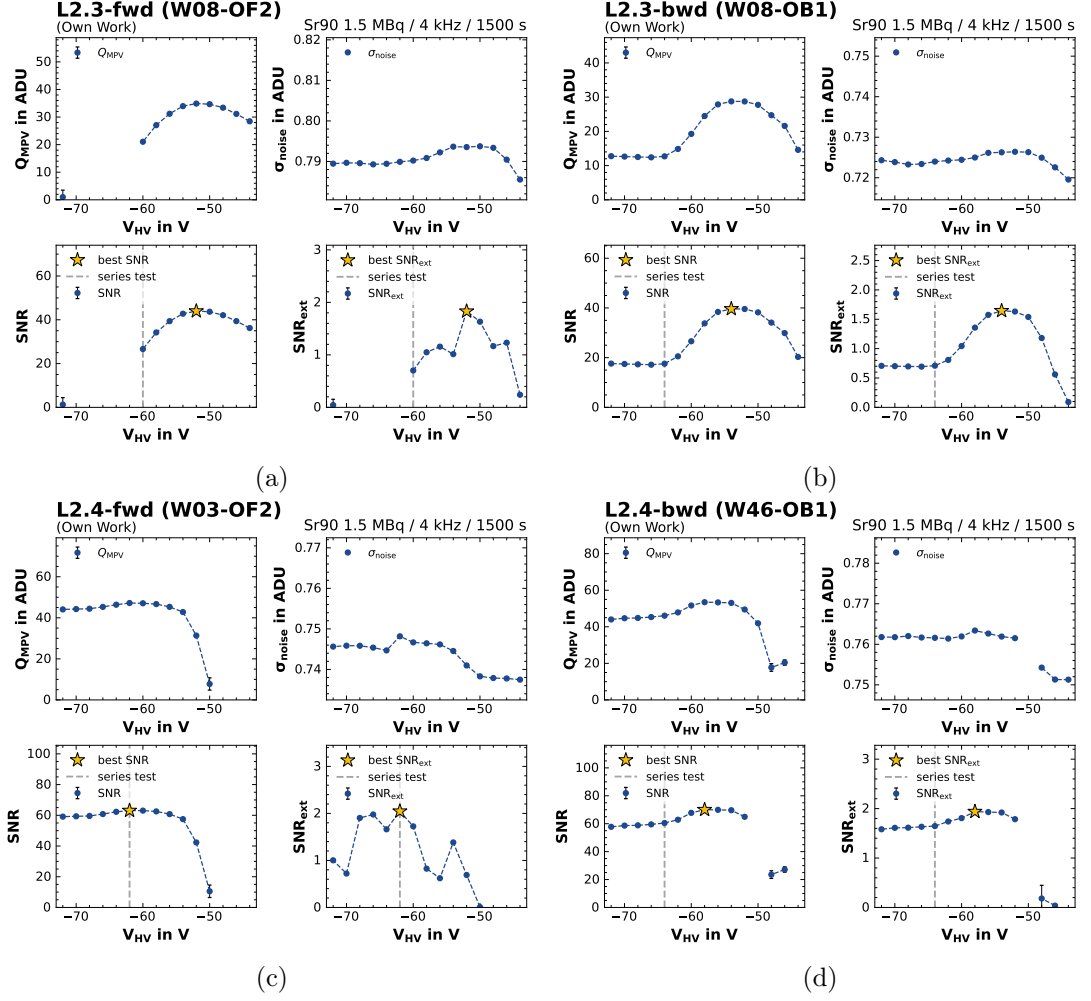


Figure A.44.: HV scan results for $V_{drift} = -3$ V and $V_{clear-off} = 4$ V showing the Q_{MPV} , σ_{noise} , SNR and SNR_{ext} distributions for modules: (a) L2.3-fwd (W08-OF2), (b) L2.3-bwd (W08-OB1), (c) L2.4-fwd (W03-OF2), and (d) L2.4-bwd (W46-OB1).

A. Appendix

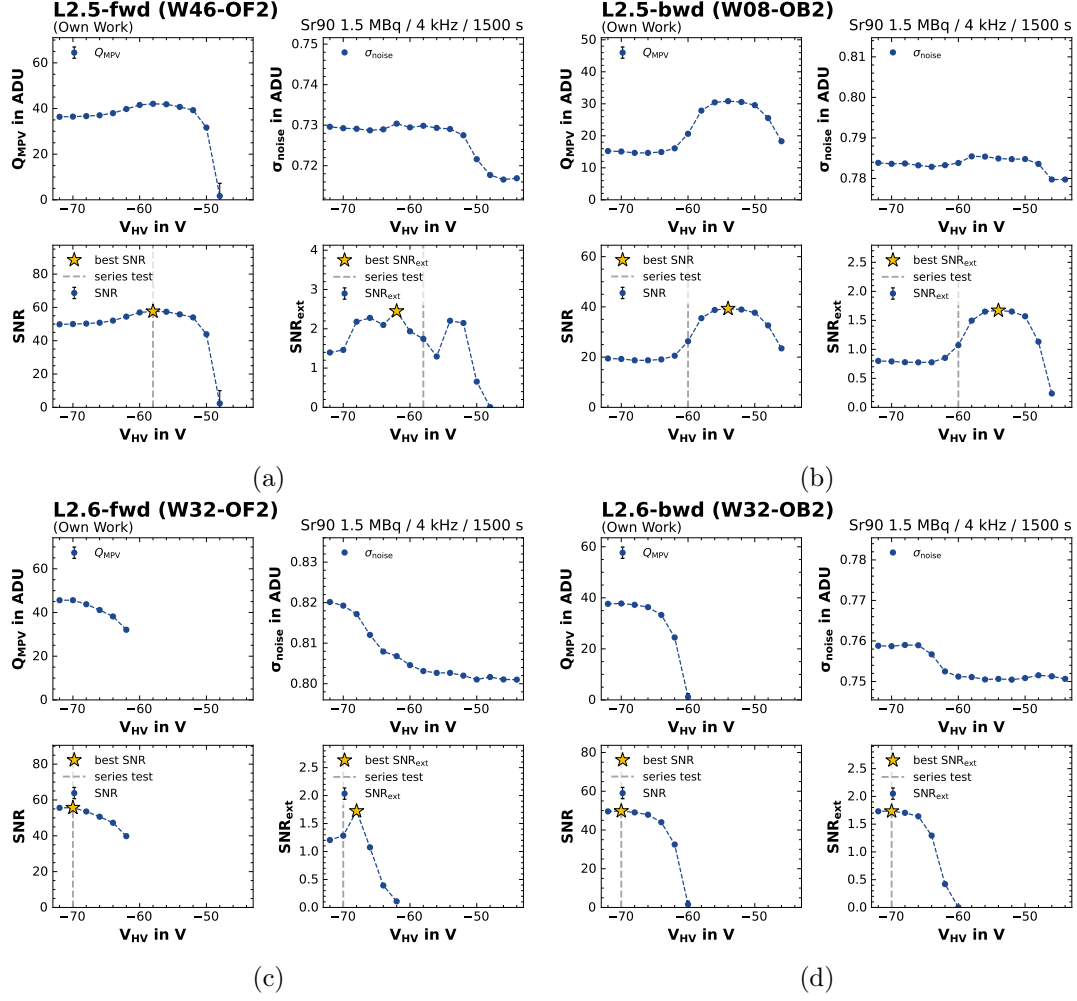


Figure A.45.: HV scan results for $V_{drift} = -3$ V and $V_{clear-off} = 4$ V showing the Q_{MPV} , σ_{noise} , SNR and SNR_{ext} distributions for modules: (a) L2.5-fwd (W46-OF2), (b) L2.5-bwd (W08-OB2), (c) L2.6-fwd (W32-OF2), and (d) L2.6-bwd (W32-OB2).

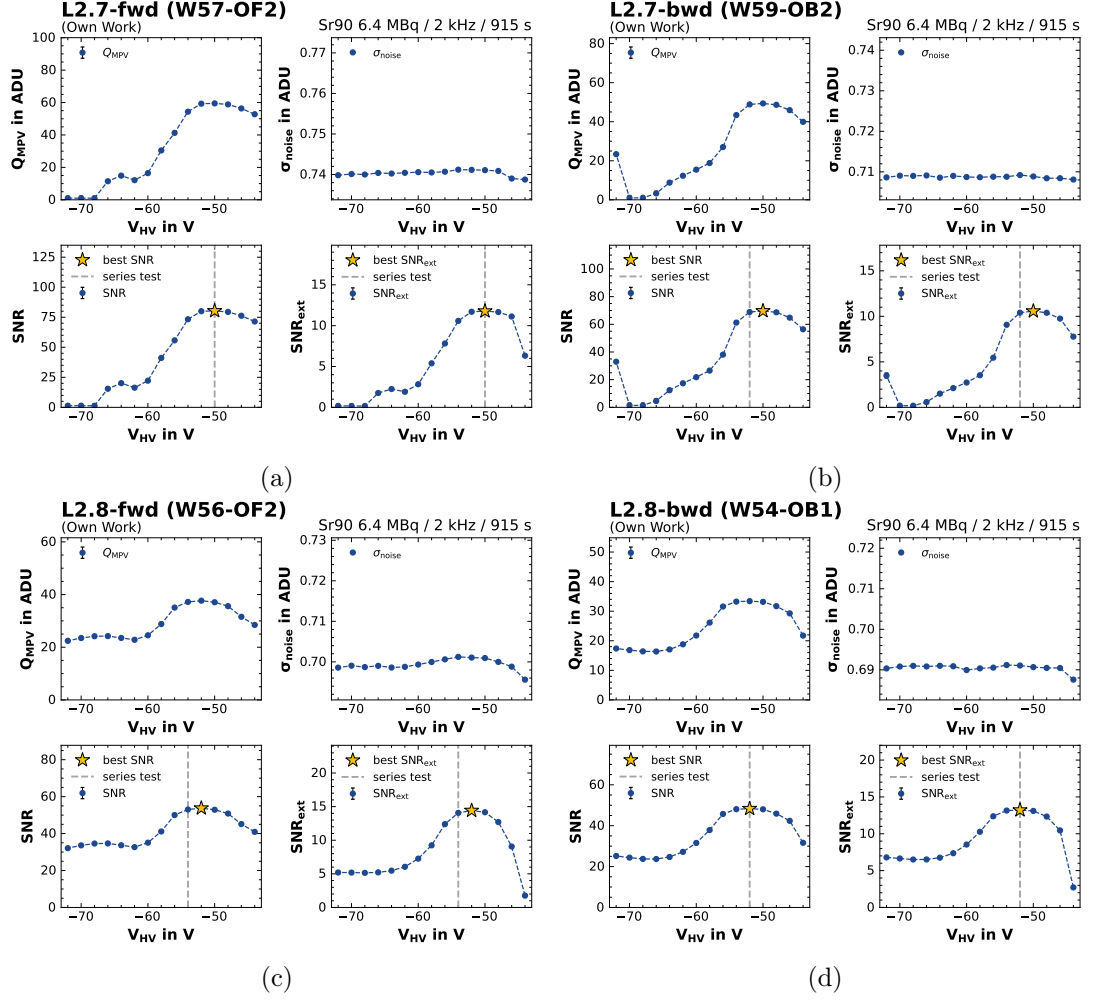


Figure A.46.: HV scan results for $V_{drift} = -3$ V and $V_{clear-off} = 4$ V showing the Q_{MPV} , σ_{noise} , SNR and SNR_{ext} distributions for modules: (a) L2.7-fwd (W57-OF2), (b) L2.7-bwd (W59-OB2), (c) L2.8-fwd (W56-OF2), and (d) L2.8-bwd (W54-OB1).

A. Appendix

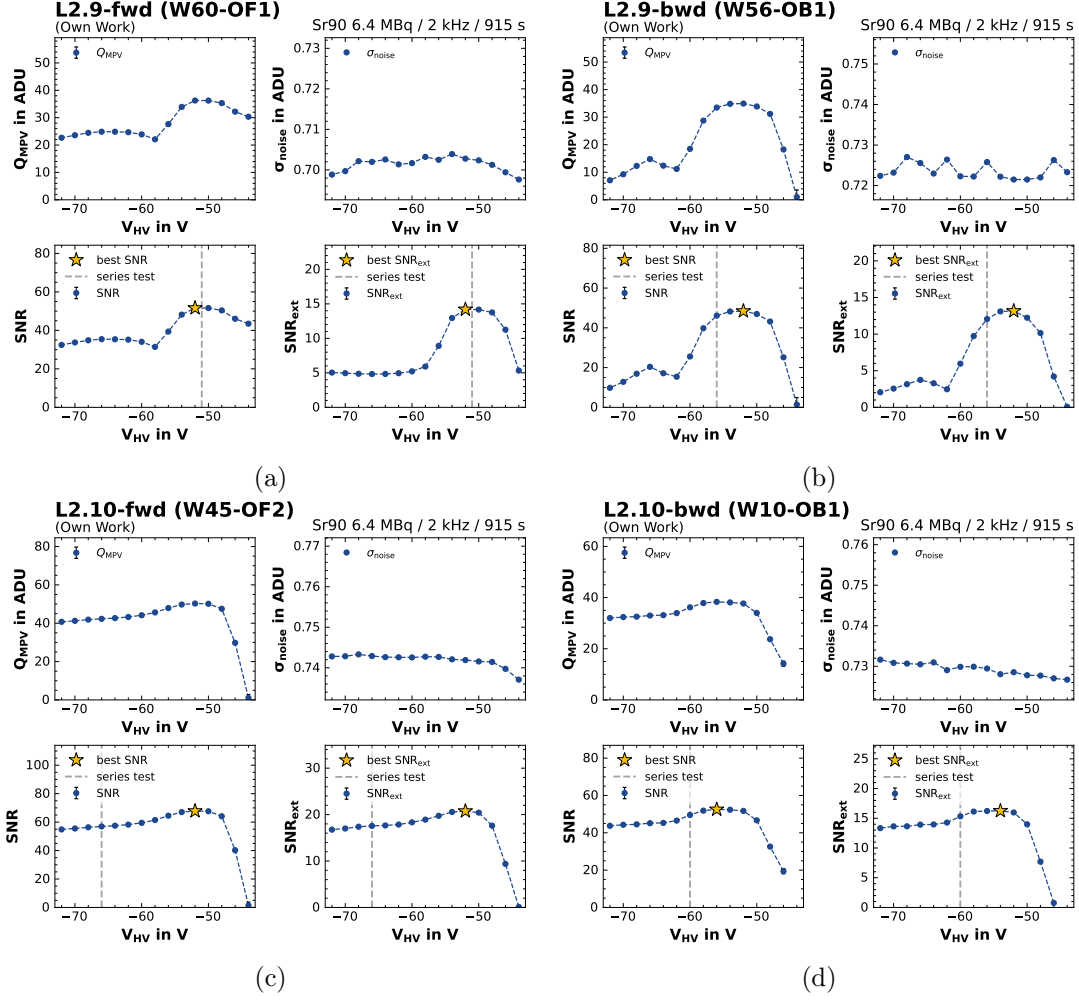


Figure A.47.: HV scan results for $V_{drift} = -3$ V and $V_{clear-off} = 4$ V showing the Q_{MPV} , σ_{noise} , SNR and SNR_{ext} distributions for modules: (a) L2.9-fwd (W60-OF1), (b) L2.9-bwd (W56-OB1), (c) L2.10-fwd (W45-OF2), and (d) L2.10-bwd (W10-OB1).

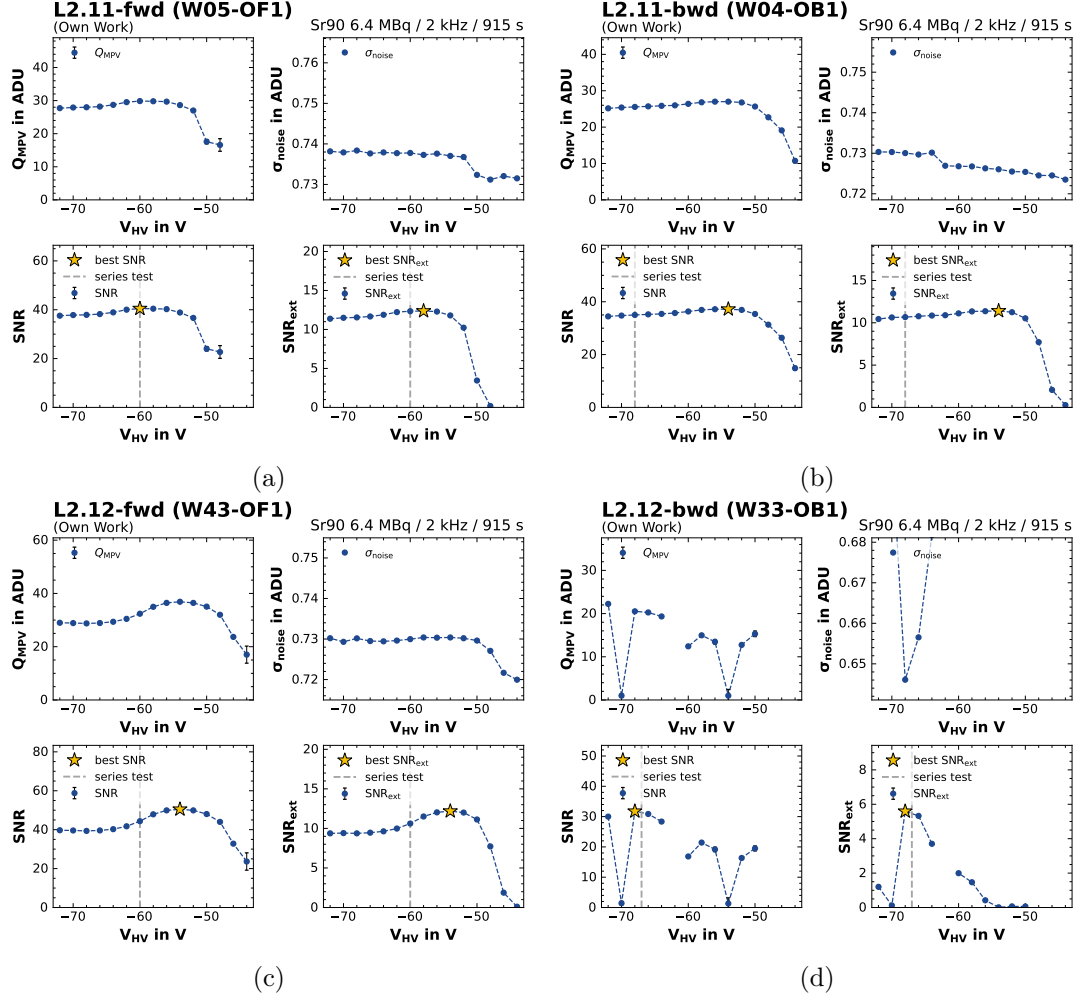


Figure A.48.: HV scan results for $V_{drift} = -3$ V and $V_{clear-off} = 4$ V showing the Q_{MPV} , σ_{noise} , SNR and SNR_{ext} distributions for modules: (a) L2.11-fwd (W05-OF1), (b) L2.11-bwd (W04-OB1), (c) L2.12-fwd (W43-OF1), and (d) L2.12-bwd (W33-OB1).

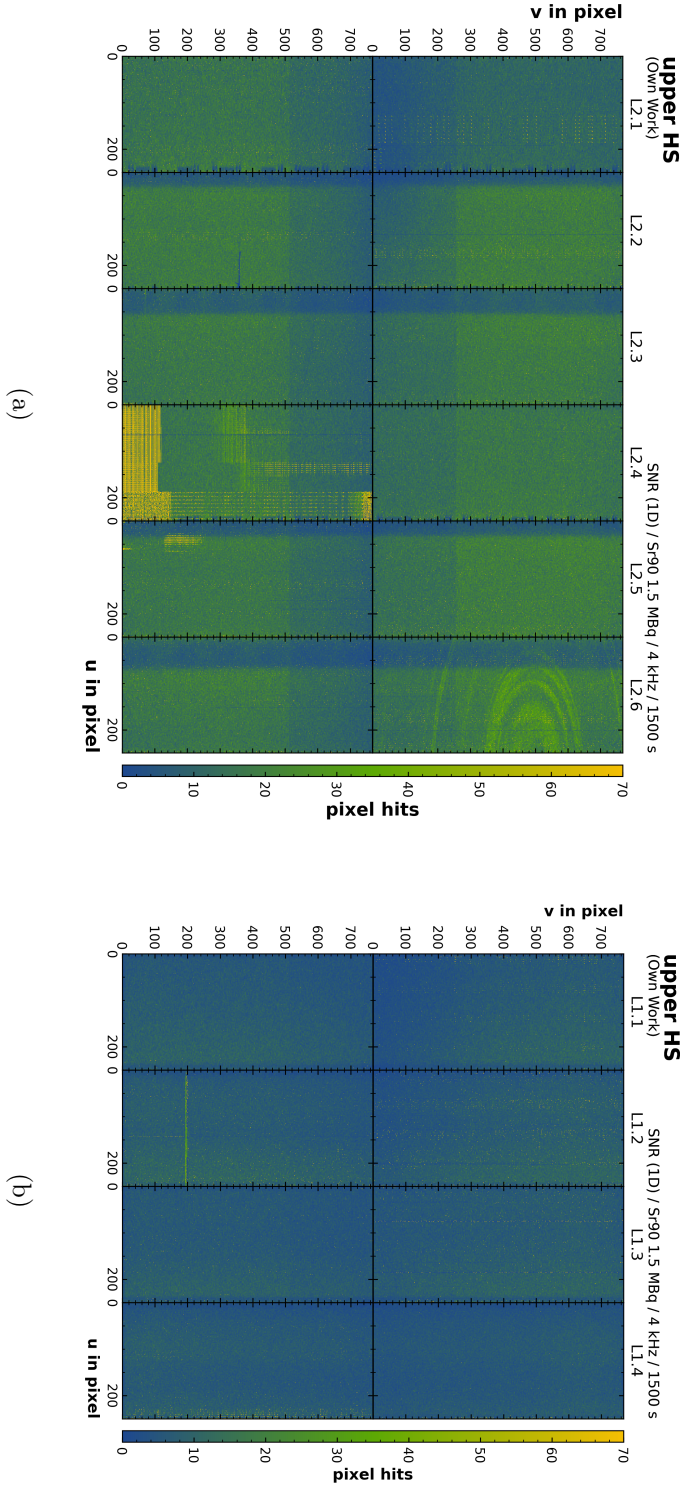


Figure A.49.: Hitmaps of the repaired upper HS HV scan at the KEK commissioning source setup. For each module, the V_{HV} configuration is shown, which maximizes the SNR value. Consecutively, the same source was placed at four different positions (A-fwd/-bwd, B-fwd/-bwd, see Table 7.6) centered above the fwd and bwd modules. The measurements were performed for each position independently. The L2 hitmaps (a) show noisy frames for L2.4-bwd, a small noisy corner for L2.5-bwd, and significant ring structures for L2.6-fwd. The L1 hitmaps (b) look smooth and uniform apart from a noisy/inefficient gate at L1.2-bwd at row 200.

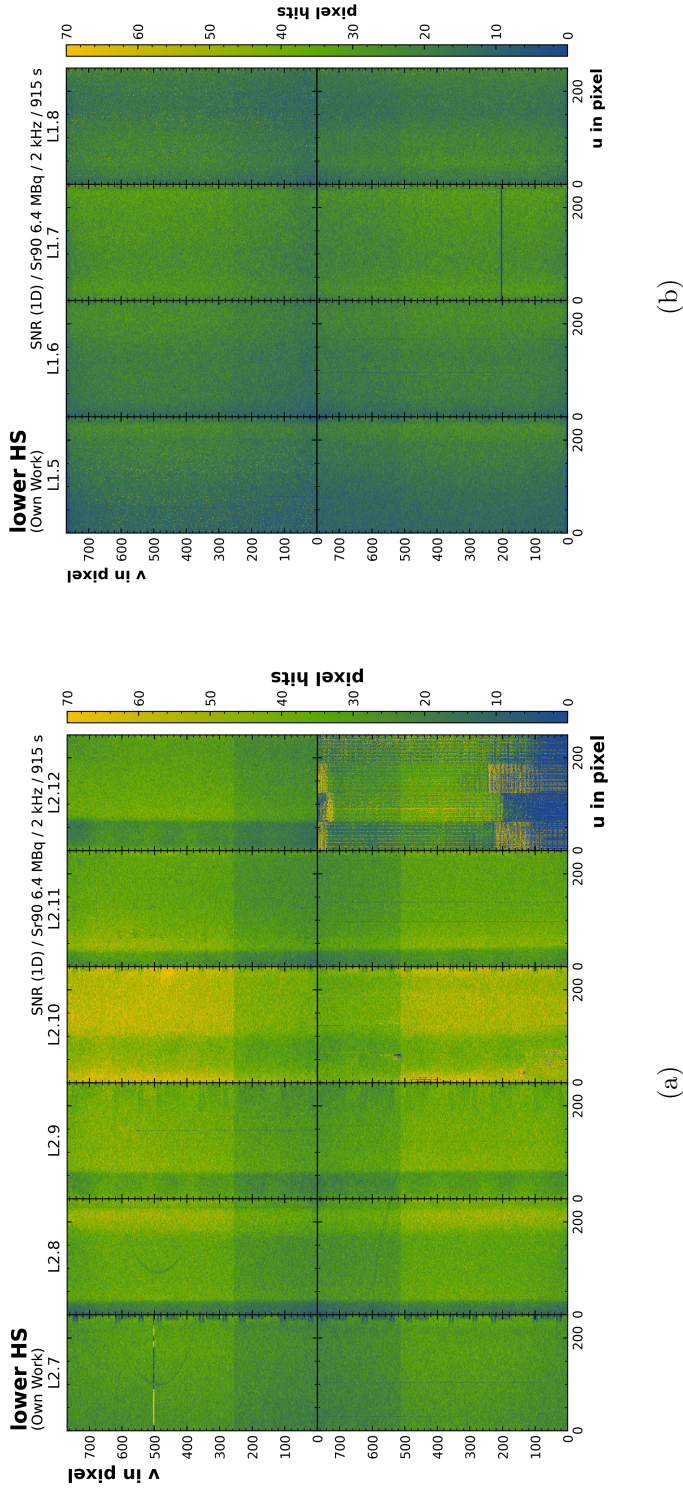


Figure A.50.: Hitmaps of the lower HS HV scan from the DESY half-shell test setup. For each module, the V_{HV} configuration is shown, which maximizes the SNR value. The measurement was performed with two ^{90}Sr sources simultaneously (position 1 and position 2). The measurements were performed for the fwd and bwd modules independently (see Table 7.6). Therefore, the z (v) positions of the sources were adjusted respectively to the center of the modules (instead of the center of the ladder). Owing to the two sources, the L2 hitmaps (a) show reduced shadow structures compared to the multi-parameter scan. L2.10 benefits the most from the two sources in terms of number of measured hits. L2.12-bwd shows a significant amount of noisy frames and inefficient regions (blue). The hit level for L2.1-fwd was somewhat decreased since the source was at position A-fwd probably slightly misaligned. The L1 hitmaps (b) show no clear shadows anymore and additionally feature an increased hit level compared to the multi-parameter scan. L2.7-fwd and L1.7-bwd show a non-functional gate at row 500 and 200 respectively. L2.10-bwd show some inefficient regions, and L2.7-fwd and L2.8-fwd show some small ring structures.

A. Appendix

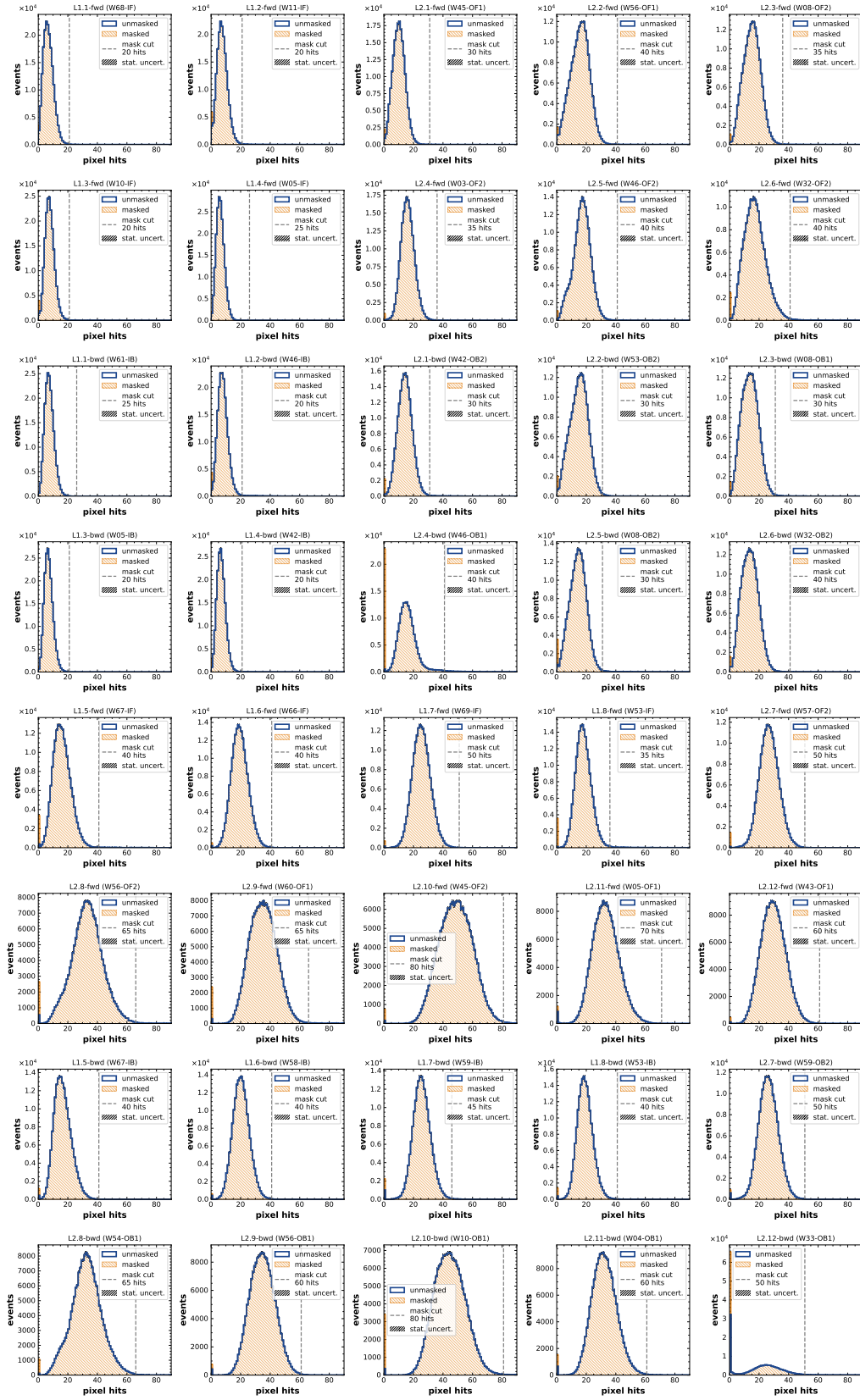
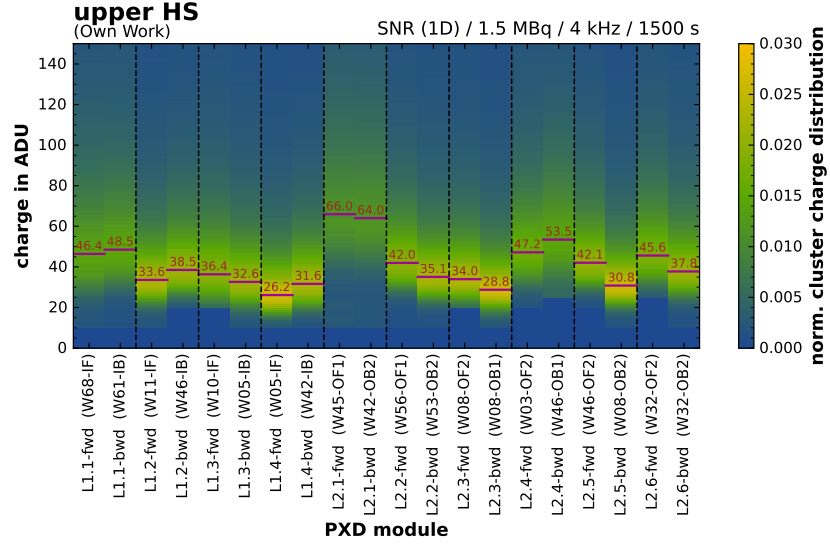
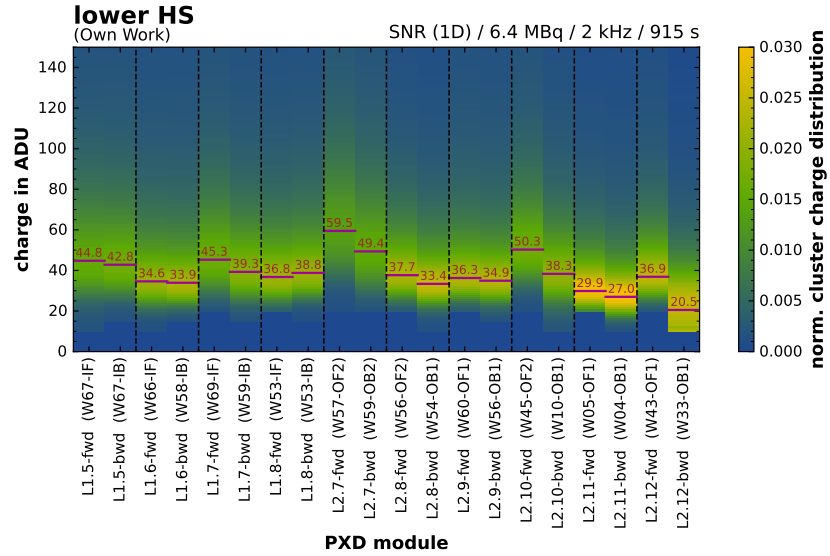


Figure A.51.: Selection cut for number of pixel hits.



(a)



(b)

Figure A.52.: Ladder-wise comparison of the measured cluster charge distributions from the HV source scan for the newly identified V_{HV} voltages based on SNR . (a) shows the upper HS, and (b) the lower HS.

Acronyms

ADU	Analog-to-digital units
ADC	Analog-to-digital converter
Al	Aluminum
ARICH	Aerogel ring-imaging Cherenkov counter
ASIC	Application-specific integrated circuit
BP	Beam pipe
CDC	Central drift chamber
CKM	Cabibo-Kobayashi-Maskawa
CM	Center of mass
DAQ	Data acquisition
DCD	Drain current digitizer
DEPFET	Depleted p-channel field effect transistor
DHH	Data handling hub
DHP	Data handling processor
DOCA	Distance of closest approach
EM	electromagnetic
EOS	End of stave
EW	Electroweak
FOM	Figure of merit
FSR	Final state radiation
HEP	High energy physics
HER	High-energy ring
HLT	High level trigger

A. Appendix

HS Half-shell

HV High voltage

IF/IB Inner forward/inner backward

IP Interaction point

ISR Initial state radiation

KLM K_L^0 and μ detector

L Layer or ladder

LER Low-energy ring

LS Long shutdown

MIP Minimum ionizing particle

MPV Most-probable value

OF/OB Outer forward/outer backward

ONSEN Online selector node

p.d.f. Probability density function

(P)(N)MOS-FET (p-channel)(n-channel) metal oxide semiconductor field effect transistor

POCA Point of closest approach

PXD Pixel vertex detector

QCD Quantum chromodynamics

QED Quantum electrodynamics

SCB Support and cooling block

Si Silicon

SM Standard Model

SNR Signal-to-noise ratio

SVD Silicon vertex detector

VXD Vertex detector

W Wafer or Watt

Acknowledgments

I would like to express my deepest gratitude to all those without whom this work, and my achievements in recent years, would not have been possible. First and foremost, I am immensely grateful to my family, my girlfriend, and my friends. Your constant moral support has been an invaluable pillar throughout this journey.

I am also sincerely thankful to the many incredible people I have had the privilege to work with over the past years. I would like to thank Kerstin Tackmann and Daniel Pitzl for their supervision and guidance. Special thanks go to Armine Rostomyan, Carsten Niebuhr, Arthur Bolz, and Fabian Becherer for their continuous support and for always having an open door whenever I had questions. I am also grateful to the entire DESY Belle II group, including former members, for the collaborative and welcoming working environment. I would like to thank Andreas Gellrich and the DESY UCO team for their invaluable assistance with the NAF and HTCondor systems.

I am equally grateful to Sascha Dreyer, Henrikas Svidras, Marcel Hohmann, Filippo Dattola, Tommy Martinov, Navid Rad, Alberto Martini, Varghese Babu, Abtin Narimani, Eldar Ganiev, Cyrille Praz, Raimundo Hoppe, and Michel Hernández Villanueva for the many enjoyable moments and activities we shared beyond work.

Special thanks also go to the Bonn SiLab PXD team, particularly Botho Paschen, Georgios Giakoustidis, Jannes Schmitz, and Munira Kahn, for their essential support during the PXD2 detector commissioning.

I am very grateful to the many colleagues from the PXD and DEPFET collaborations who generously shared their expertise and insights, including Simon Reiter, Huha Ye, Björn Spruck, Philipp Leidl, Rainer Richter, Enrico Töpper, David Kittlinger, and Michal Ritzert.

I would also like to thank the DESY technicians Karsten Gadow, Rainer Stevers, Michelle Klotz, and Jasper Kehl for their outstanding support during the PXD2 pre-commissioning and commissioning phases. Without your know-how and dedication, this work would not have been possible.

Furthermore, I want to thank Sally, Armine Rostomyan, Carsten Niebuhr, Arthur Bolz, Fabian Becherer, Simon Reiter, Rainer Richter, and Marcel Hohmann for carefully reading (parts of) this thesis and providing valuable feedback and comments.

Finally, I would like to thank everyone I may have unintentionally omitted here. Your support and contributions have been just as important and sincerely appreciated.

Eidesstattliche Versicherung

Hiermit versichere ich an Eides statt, die vorliegende Dissertationsschrift selbst verfasst und keine anderen als die angegebenen Hilfsmittel und Quellen benutzt zu haben.

Sofern im Zuge der Erstellung der vorliegenden Dissertationsschrift generative Künstliche Intelligenz (gKI) basierte elektronische Hilfsmittel verwendet wurden, versichere ich, dass meine eigene Leistung im Vordergrund stand und dass eine vollständige Dokumentation aller verwendeten Hilfsmittel gemäß der Guten wissenschaftlichen Praxis vorliegt. Ich trage die Verantwortung für eventuell durch die gKI generierte fehlerhafte oder verzerrte Inhalte, fehlerhafte Referenzen, Verstöße gegen das Datenschutz- und Urheberrecht oder Plagiate.

6. März 2025

A. Baur

Unterschrift des Doktoranden

Declaration

I hereby declare upon oath that I have not submitted a dissertation with the same research topic to an academic higher education institution that had been already accepted or evaluated as insufficient in an earlier doctoral procedure.

Ich versichere, dass ich keine Dissertation mit dem gleichen Forschungsthema schon einmal in einem fruheren Promotionsverfahren an einer wissenschaftlichen Hochschule eingereicht habe, die angenommen oder als ungenugend beurteilt worden ist.

I hereby declare upon oath that I have written the present dissertation independently and have not used further resources and aids than those stated in the dissertation.

Hiermit erkläre ich an Eides statt, dass ich die vorliegende Dissertationsschrift selbst verfasst und keine anderen als die angegebenen Quellen und Hilfsmittel benutzt habe.

I hereby declare upon oath that the dissertation submitted in electronic form and the printed bound copy of the dissertation submitted for archiving are identical.

Ich versichere an Eides statt, dass die in elektronischer Form eingereichte Dissertation und das zur Archivierung eingereichte gedruckte gebundene Exemplar der Dissertation identisch sind.

A. Baur

Anselm Baur

Hamburg, 06 March 2025